INTERNATIONAL DOCTORAL
SCHOOL OF THE USC

Antía
Graña González

PhD Thesis

Fission of ^{238}U investigated using proton-induced knockout collisions in inverse kinematics

Santiago de Compostela, 2024

Doctoral Programme in Nuclear and Particles Physics

ESCOLA DE DOUTORAMENTO
INTERNACIONAL DA USC

PhD Thesis

Fission of ^{238}U investigated using proton-induced knockout collisions in inverse kinematics

Author

Antía Graña González

Supervisors
José Luis Rodríguez Sánchez and José Fernando Benlliure Anaya

Tutor
José Fernando Benlliure Anaya

PhD Programme in Nuclear and Particle Physics

Santiago de Compostela
28 june 2024

Abstract

This thesis focuses on the analysis of the fission experiment performed at the GSI facilities (Germany) in March 2021 within the international collaboration framework R^3B (Reactions with Relativistic Radioactive beams).

In the research presented in this work, proton-induced knockout reactions are combined for the first time with the study of fission in inverse kinematics. To do so, ^{238}U beams are accelerated to imping on a liquid hydrogen target (LH_2) at 540MeV/u. This experimental technique would provide full kinematics measurements by obtaining the excitation energy for the fissioning nuclei and identifying the mass, charge, and TKE of the two fission fragments on an event-by-event basis. Such data can be obtained by combining the SOFIA (Studies Of FIssion with Aladin) experimental setup with a silicon tracker based on AMS-type detectors [1] and the calorimeter CALIFA (CALorimeter for In-Flight detection of γ rays and high energy charged pArticles) [2] developed by the R^3B collaboration. Proton-induced spallation reactions, and in particular, the few nucleon-knockout collisions, are very versatile because they cover a wide range of excitation energies, enabling the study of fission at both low and high excitation energies by selecting specific reaction channels.

Pre- and post-saddle dynamics were investigated. For the study of the pre-saddle dynamics, the partial fission yields and the width of the charge distribution were calculated for different fissioning systems and compared with previous experimental data. Several theoretical de-excitation models such as ABLA, GEMINI, and SMM were benchmarked. For the study of post-saddle dynamics, the evolution of the fission yields with the excitation energy was evaluated. Several suppression functions were tested, and the combination of two exponentials proved to reproduce the data better. The neutron excess and the even-odd effect were studied for different excitation energies, as well as the total kinetic energies.

Acknowledgements

I wish to thank the help provided by all the people who participated in this work or have participated in my journey to reach this point in my life.

I would like to thank my thesis tutor José Benlliure Anaya and also Dolores Cortina Gil for choosing me for this work. You placed that trust in me and gave me thereby the opportunity to learn about the fascinating world of nuclear physics. Thank you for welcoming me so openly when I asked for the FPI, and thank you of course for all the meetings and useful discussions about physics we had through these four years.

I would like to especially acknowledge the help provided by José Luis Rodríguez Sánchez, my thesis supervisor. Because if I have to thank someone above all, that is you. Thank you for explaining to me how R3BRoot works. Thank you for your constant supervision of my analysis and your guidance through the different stages of the thesis. Thank you for being always there, any time, any place, for any doubt. Thank you for your patience. Thank you for being such a good teacher and at the same time still treat me like a partner. Thank you for making everyone's day by always having the office full of chocolate, cakes, cookies, and other products rich in fully hydrogenated palm oil. And grapes, let's not forget that from time to time were also grapes.
I have been really lucky to have you as a thesis supervisor, I hope you also enjoyed having me as a student. I think you are both a great person and a great scientist. As a person, you are kind, helpful and caring. As a scientist, you are sharp as a tack, and best of all, constant and thorough. I wish you the best in both physics and personal life. You deserve to be the happiest a person can be.

I want to thank my best friend Gabriel García Jiménez, who did his Ph.D. at the same time as I did. We shared experimental campaigns at GSI, data analysis, data suffering, and long office days. You are great both as a co-worker and as a friend. As a co-worker, thank you for all the coding advices, the calibration discussions, and the support. As a friend, thank you for being such a good person, so loyal and so kind. Thank you for being a constant supplier of dad jokes and pranks, having the office full of useless prints, changing the keys of my keyboard, doing cakes on Saturdays and always being up to watch cartoons with an eternal kid like myself. Thank you for the tons of fun I had with you since we met on a plane to Germany four years ago, talking about The Name of the Wind and the Twilight saga. GSI days would have never been the same without you as a partner, riding the bike at 5 degrees at 7 AM after a night shift. Thanks to your sister Irene too, who I met more recently and is just as kind and good at heart as you are. You are such a fighter, I hope you finish your degree successfully very soon and start living a less stressful life (and of course, greetings to David too!). Starting to share the apartment with you two was the best that happened to me this last year, you made me feel as if I had a family in Santiago.

Thanks to another Ph.D. buddy, Martina Feijoo Fontán. We shared the office and a lot of unforgettable experiences at GSI, like the game nights, the Queimadas, and the excursions. Despite all the hard work we went through, sometimes we could even imagine we were in a summer camp. You are funny, charming, and a continuous source of good vibes. Never let anything take that from you!

Thanks to Juan Lois Fuentes, who I met early in the degree. You were there at one of the most important and challenging stages of my life and supported me more than anyone else. Thank you for that, and for the great times we had together that I will treasure in my heart forever. Part of who I am now is from your legacy.

Thanks to everyone else in Santiago's physics groups, from GENP, FICA and also the technical and administrative staff. Thanks to Daniel Fernández Fernández, for sharing this nice thesis template and for all the funny topics at lunch times. Thanks to our great technician, David González Caamaño, whose work was crucial to build Califa. Thank to Marcos Seco, for dealing with the intricate mechanisms of the Cluster's computing, and for taking me to the CiTIUS during the Cluster shutdwon so I could back up my files. Thanks to Ricardo Rodríguez for helping me with all the bureaucracy of the thesis, always in the best mood, and for all the permissions for entering the IGFAE at non-working hours. Thanks to Beatriz Fernández Domínguez, full of energy, and a moral reference. Your capacity to shoulder responsibilities and execute them efficiently, all while maintaining a smile, is truly admirable. Thanks to Hector Álvarez Pol, father of R3BRoot and Great Lord of Uncertainties Calculation. Thank you for all the rigorous discussions about physics, calibrations, and uncertainties. Thanks to Manuel Caamaño Fresco, probably the most thorough and punctilious person I have ever met. I love how you never settle for a superficial explanation about anything, how you dig deep into reasoning until reaching the barest truth underneath. In general, thanks to the 3 of you for being the kind of scientist who despite having reached far in the world of physics does not hesitate to 'get down into the mud' with long calculations or coding. Thank you for explaining physics with so much passion, in difficult times it is a good reminder of why we all are here.

Greetings to Alicia and Lílit too! Thank you for your recommendations on TV series and films, especially Hazbin Hotel and Helluva Boss. I had a lot of fun sharing some lunches with you. Despite the age gap, I'm sure I would have gotten along really well with you two at high school!

Thanks to the SOFIA people who shared the experiment with us at GSI, namely Julien Taieb, Audrey Chatillon, Pierre Morfouace, and Guillaume. It was a real pleasure to share experiments with such a group as you are, so hardworking, efficient, and motivated. Watching you working reminds me to one of those documentaries of super-well-organized ants, where each one has a task but they all work together as a team to reach a common goal. Thank you for explaining me so many things about the experiment and the detectors while I was there. Also thanks for all the nice dinners you invited me to at GSI, I remember that sometimes you even cooked vegetarian for me. After the COVID-19 hardest times, it felt really wholesome when I saw you all for the first time having dinner all together at the Gastehaus kitchen, celebrating and laughing. And you invited me to join. And I thought, yes, of course, you are the kind of people I would love to be around.

Thanks to Konstanze Boretsky and Andreas Heinz for, in a purely altruistic way, sending me such detailed and polite corrections of my Proceedings, and in the case of the latter, also for the thesis corrections. They were truly useful, and I appreciate the effort. Thanks to Valerii Panin, who taught us how to assemble the AMS with the delicacy necessary for a detector that seemed like it could break just by looking at it very closely. Thanks to Philipp and Leyla, the local people responsible for keeping the 'Caliph' on his throne. Special thanks to Daniel Körper, organized and firm, I enjoyed a lot working with you in the cave. Thank you for all your valuable lessons about technical tasks, you are a great foreman. Thanks a lot to all the Ph.D./post-doc friends I met at GSI: Silvia, Andrea L., Ivana, Eleonora, Manuel, Tomás, Enis, Luke, Andrea J. and many more. I enjoyed a lot fighting together to set up an experiment, and also the hilarious game nights and evenings we spent together. I wish you all good luck in your respective thesis defenses or in your postdocs. Special thanks to Hans Toshihide Törnqvist, probably the most both intelligent and humble person I have ever met, which is a very uncommon combination of qualities. Watching you work meticulously and doing everything with your characteristic care and elegance is a source of inspiration. You have an incredibly bright and warm aura, as I told you once. Just like the white origami angel you made for me. I feel truly fortunate that I found you on my way.

Y ahora, en castellano.

Un buen profesor no es sólo aquel que sabe mucho, sino aquel que sabe cómo transmitirlo, y sobre todo, aquel que realmente se preocupa porque sus alumnos aprendan y no sólo por cubrir sus horas de docencia. Quisiera agradecer especialmente a un par de profesores que he tenido en 2º de bachillerato, ambos los dos apasionados de la ciencia y de la enseñanza, y que cada uno a su manera sabía hacer de su clase una auténtica 'performance'. Gracias, Mariano Durán, profesor de física, por tu amor por la ciencia y por ser un showman. Quien crea que la física es aburrida, monótona o predecible, es porque nunca ha estado en tu clase. Gracias, Luis Puig, de matemáticas. Durante tus clases, creo que me reí y aprendí a partes iguales. Lo cual es muy importante, porque como tú bien dices, 'no hay nada más valioso que el arte de hacer reír'. Eres sin lugar a dudas el mejor profesor que he tenido nunca. Y desde luego, el único profesor que por voluntad propia nos daba clases particulares de forma puramente altruista las tardes antes de los exámenes. Recuerdo que en el primer examen de mátematicas que tuve contigo no saqué muy buena nota. Sinceramente, aunque ya sabía que quería hacer física, no me había esforzado tanto como pudiera para ese examen en concreto. No fue por pereza, seguramente fuera porque me estaba chapando palabra por palabra el libro de biología, otra de mis ciencias favoritas (gracias también a ti, Luisa Hebia) o haciendo cuestionarios de química (gracias también a ti, Ramón Rico). Cuando fui a tu mesa a la revisión del examen, me miraste muy fijamente a los ojos y me dijiste, señalándome con el dedo acusador: '¡Antía!' -pausa dramática- '¡tú puedes hacerlo mucho mejor que esto!' -otra pausa dramática- '¡¡y lo sabes!!'. Creo desde ese día contigo sólo saqué nueves y dieces. Ese recuerdo de ti se ha quedado grabado para siempre en mi memoria y lo utilizo cada vez que necesito recordarme, que, si quiero, puedo hacerlo mejor.

Gracias a mi amiga Uxía, probablemente de todos mis amigos eres aquella con la que he conseguido mantener un contacto más sólido a través de los años. Y no creo que sea sólo porque seamos vecinas, es porque eres de esas personas que nunca se olvidan de ti, ni aunque estén estresadas ni aunque estén lejos, ni aunque sean tiempos difíciles. Eres la viva imagen de la lealtad. Me encanta poder hacer planes contigo de todo tipo, ir a la playa, ir de caminata, ir a tomar un café al Camping, celebrar Halloween por todo lo alto o ver una peli en tu casa (saludos

también a Luísa y a Manuel!). Me encanta además el hecho de poder quedar contigo y con mi hermana, incluso desde que ella era muy pequeña. Nunca te ha importado romper las barreras intergeneracionales, y eso es fantástico. Por último, espero que tu también puedas alcanzar tu vocación y ser profesora, creo honestamente que has nacido para ello.

Gracias a mis amigas que conocí en el Atios. Formáis parte de mi infancia, la cual es una piedra angular en el desarrollo de una persona. Aunque con los años perdiéramos el contacto, guardo un recuerdo muy especial de cada una de vosotras. Gracias a Isa, precursora de buena parte de nuestras anécdotas más divertidas. Brindo por aquellos días de comer juntas, ir a particulares de Begoña y coronar el día con largas charlas sobre dramas románticos (tuyos). Gracias a Ana Belén, con la cual compartí gran parte de mi infancia ya antes de que llegase al colegio. Gracias por las tardes de verano en la playa y las tardes de espiritismo en invierno. Por todas las veces que rogábamos y rogábamos para que nuestros padres nos dejasen quedarnos a dormir la una en casa de la otra. Gracias a Yoli, con la que compartí mesa en clase por muchos años y muchas tardes de entrenamiento en La Malata. Gracias por iniciarme en el mundo del kayak-polo y por todo lo que luchamos codo con codo como compañeras de equipo. En general, gracias a las tres, porque a pesar de los intrincados y misteriores mecanismos de la relación social entre adolescentes, guardo un recuerdo increíble con vosotras en el Atios, cuyos pasillos fueron parte de nuestra casa durante la mitad de nuestras vidas (a día de hoy). Gracias también a nuestras amigas del Terra de Trasancos con las que hicimos grupo, Alba y Sofía. Me lo pasé genial con todas vosotras cuando estábamos en el grupo de 'Perrechas'. También del Terra, gracias a Fiz, nos has dado un año inolvidable en primero de bachillerato. Gracias por los trucos de magia, las canciones improvisadas, los malabares y las bromas. Cuando te fuiste, el mundo perdió varias unidades de brillo, contraste y saturación. No te ha dado tiempo de llegar a donde podría haber llegado alguien con tu talento y tu creatividad. Ojalá estés haciendo malabares en el Circo del Sol del Más Allá.

Y hablando de Kayak-polo, gracias a nuestra entrenadora, Paula, por la paciencia, el arrojo, y la esperanza depositada en nosotras. Gracias también a nuestro entrenador Víctor, sin tus consejos seguramente me hubiese ahogado en el mundial de kayak-surf. No obstante, gracias a ti, hasta lo llevé a cabo con cierto arte. Y por supuesto, gracias a todo el equipo de Copacabana de Ferrol, con los que compartí una adolescencia preciosa de campeonatos por España y quedadas en la playa, en el cine o en las casas de cada uno de nosotros.

De kayak-polo, y también del Atios, gracias a mi amigo Martín y también a su familia, Kalki, Samu, Carlos y Helena. Los mejores recuerdos que guardo de vacaciones son con vosotros, y saber que vamos a quedar para una comida siempre es un motivo de alegría durante la semana. Sois una familia estupenda, espero que podamos seguir reuniéndonos durante muchos años, ya sea para comidas de domingo, terracitas en la playa o para algún viaje como los que ya hicimos.

Gracias a mis amig@s que conocí en mi etapa en el Sofía Casanova, especialmente a Jessica, Andrea, Paula, Irene y Helena. También a Álvaro, pero a ti ya te conocía de compartir una infancia feliz de andar en bici, jugar al *'Pillaesconditebuscalaberintoaoscuras'* y construír jaimas en el estudio. Gracias a todos, porque aunque sea la desaparecida del grupo, cuando volvemos a tener tiempo libre y nos juntamos, sigue siendo igual de divertido que siempre. Es genial poder rememorar con vosotros todas las anécdotas de fiestas y veranos cada vez que nos vemos, espero que todavía nos queden muchas más anécdotas por vivir. Gracias especialmente a Pablito, por estar ahí en 2º de bachillerato, que fue incluso más intenso que la carrera. No hubiera sido lo

mismo sin tu apoyo, mandándonos mensajes a las 4 de la mañana del tipo 'yo me voy a acostar ahora', 'ah, pues yo me acabo de levantar'. Enhorabuena, tras muchos años luchando por ello, ya eres doctor! Ahora me toca a mí.

Gracias a mis amigos de carrera, especialmente Iván y Sara. Me lo he pasado siempre genial con vosotros y os he querido (y os quiero) muchísimo. Recuerdo con mucho cariño la etapa en la que prácticamente vivíamos los cuatro juntos. Durante esos años fuisteis como mi familia en Santiago. Si bien la carrera fue una etapa muy dura a nivel de agobios y estrés, el haber podido compartir esos años con vosotros ha hecho que sean recuerdos dorados. Daba igual que estuviéramos en un piso de estudiantes un poco hacinados en torno a una mesa pequeña, durante el poco rato que no estábamos trabajando nos lo pasábamos como si estuviésemos en el mejor lugar del mundo. Os echo de menos todos los días. Por supuesto, gracias también a mis amigas de carrera con las que tengo recuerdos inolvidables, tanto de estar en la biblioteca hasta las 4 de la mañana como de fiesta: Amparo, Vicky y Carolina. Para esta última, especialmente a ti, 2 cosas: 1 eres la persona más graciosa que he conocido nunca, guarda esa cualidad para siempre. Y 2: gracias por haberme enseñado Gravity Falls, creo me la he visto tantas veces y se la he enseñado a tanta gente que ya forma parte de mi ADN.

Gracias a mis amig@s de Tenerife, en especial a Laura y Raquel, con las que siento una conexión especial. Con vosotras siempre me he sentido comprendida y apoyada, puesto que compartimos ilusiones, preocupaciones e intereses como la ciencia, la escalada o las aventuras por la naturaleza. Hemos disfrutado de momentos fantásticos cuando estábamos juntas en Tenerife, y después de eso lo hemos seguido haciendo quedando en diferentes puntos, como en Valencia y Galicia. Estoy muy contenta de haber sido capaz de mantener el contacto con vosotras, lo cual a veces puede ser complicado con la distancia y el ajetreo del día a día. Espero que podamos mantener esto para siempre y seguir quedando en diferentes partes del mundo para irnos de aventuras y quedarnos hasta la 3 de la mañana hablando como metralletas en nuestro Consejo de Sabias. Por supuesto, gracias también al resto de mis amigos de Tenerife, con especial cariño a Andreu, Óscar, Fernando y Carles. Los dos años que estuve haciendo el máster en Tenerife fueron como si me hubiese teletransportado a otra dimensión. Una dimensión donde existía descansar los fines de semana. No, mejor que eso, donde existía irse de EXCURSIÓN los fines de semana. Muchísimas gracias a todos por esos dos años de fantasía y aventuras por lugares increíbles.

Un saludo también para mis amigos del roco, con especial cariño para Pequi, Pablo y Alex, nuestro sensei. Al final de un largo día de trabajo, cuando *estás que te subes por las paredes*, no hay nada mejor para desestresarse como luchar por alcanzar una presa a 10 m del suelo colgado de una cuerda (por extraño que suene, es completamente cierto). Y sobre todo, con vosotros como compañeros. Desde luego, os echaré mucho de menos en los próximos años. Espero que nos podamos seguir juntando para ir a escalar al aire libre de vez en cuando!

Se me parte el corazón al pensar en muchas amistades que he dejado por el camino de todos los sitios por los que he pasado. A veces siento que voy todo el rato de un lado para otro, como si mi vida fuese una colección de campamentos de verano (en este último se han pasado con las gymkanas). Cada vez que llego a un sitio nuevo tengo que forjarme una vida nueva, amistades nuevas, rutinas nuevas. Y parece ser que siempre acabo consiguiéndolo, acabo por conocer a gente maravillosa a la que adoro, y cuando mejor estamos, sopla el viento del norte y me tengo que ir para otro lado. Ojalá pudiera llevaros a todos en mi bolsillo. Como no puedo, por lo menos trato de llevaros a todos en el corazón.

Menos mal que por lo menos, creo que podré tener por siempre un enclave en el mejor lugar del mundo, al cual quiero casi como se quiere a una persona: Valdoviño. El portal al Atlántico, cuya bahía azul recibe con los brazos abiertos los más salvajes temporales de invierno y los más bellos atardeceres de verano. Guardado por imponentes acantilados y cubierto de praderas verdes, al fondo de la colina está mi hogar, donde crecí mirando fijamente esa línea que une el cielo con el mar, esperando a ver el rayo verde cuando el Sol la acaba de cruzar.

Gracias a mi familia. Tengo la suerte de haber nacido en una familia muy unida y que siempre me ha apoyado. Gracias a mi madre Isa, por su herencia, tanto genética como inculcada: gracias por la creatividad, el optimismo, la inspiración y el temperamento. Tú me has dado el fuego. Gracias por enseñarme a pintar, leer, escribir historias y hacer obras de teatro. Gracias por todas las fiestas y cumpleaños que me organizaste cuando era niña. De la misma forma, gracias a mi padre Juan, por la constancia, la fuerza, la paciencia y el sentido del humor. Tú me has dado la tierra. Gracias por preguntarme durante tantos años historia y biología, traerme cafés al estudio, estar siempre dispuesto a ir a pasear aunque durmieras 4 horas, llevar las maletas al coche, poner el 'Nadie Sabe Nada' y por venir a buscarme al fin del mundo si hace falta. Gracias a los dos por financiarme los estudios, soportarme cuando estoy estresada y sobre todo, gracias por instruírme en el valor más importante de todos: ser buena persona. Gracias por esperarme con los brazos abiertos cada vez que vuelvo a casa. Subir por la pista y ver encendido el candil de la cocina, y a Nala y a Gru en la entrada (y a Balto en su día) es una de las mejores sensaciones que caben en mi corazón. Gracias también a mis abuelos, que han sido como mis segundos padres desde que soy pequeña. Gracias a mi abuelo Ángel, por inculcarme la curiosidad y el ingenio, por enseñarme a trepar a los árboles y a hacer flautas con las plantas, por contarme todos los días el Cuento de la Música Improvisada. Gracias a mi abuela Concha, por ser siempre tan comprensiva conmigo, por enseñarme a coser, por contarme cuentos cuando no me quería ir a la cama y por los inumerables botes de mermelada, membrillo y caldo gallego que me ha hecho durante todos estos años. Y perdón a todos, porque nada de lo que escriba hará justicia a todo lo que os debo.

Y por supuesto, la joya de la corona, gracias a mi hermana Mencía, mi persona favorita en el mundo. Divertida y apasionada, gracias por ser un punto de conexión con el lado más brillante de la vida. Eres como un Sol radiante, capaz de alegrar el día a todo aquel que te rodea. Allá por donde pasas, tras tu rastro de purpurina los árboles brotan, las flores se abren y las sonrisas se ensanchan. Eres el chocolate de la tarta, el punto focal del cuadro, el estribillo de la canción, la gracia del chiste y el beso de la película. Y a pesar de serlo, no dejas que la vanidad corrompa tu buen corazón. Una de las cosas que más me gusta es llegar a casa los viernes por la noche y que tengas mil cosas que contarme. Que no pares, no pares, no pares y no pares de hablar, que todo te guste, todo sea divertido y todo te haga ilusión. Y que a pesar de que seas la chica más guay del mundo, sigas queriendo venir a dormir con tu hermana mayor por las noches. Te quiero.

Por último, si se me permite dejar de lado la humildad por un momento, gracias, Antía. Porque sin ti nada de esto hubiera sido posible. Porque la vida tiene muchos colores a través de tus ojos. Soy muy afortunada de saber que voy a poder estar contigo hasta el último día de mi vida.

Thanks to the strength, the resistance, and the inspiration,
thanks to my friends, my family, and the love of my life,
to not to forget thanking anyone in this enumeration
I might have thanked someone more than twice!

VINCENT: *"Hold my hand, Doctor. Try to see what I see. We are so lucky we are still alive to see this beautiful world. Look at the sky. It's not dark and black without character. The black is in fact deep blue. And over there, lighter blue. And blowing through the blueness and the blackness, the wind swirling through the air and then, shining, burning, bursting through, the stars. Can you see how they roar their light? Everywhere we look, the complex magic of nature blazes before our eyes."*

DOCTOR WHO: *"I've seen many things, my friend. But you're right. Nothing quite as wonderful as the things you see. "*

Vincent Van Gogh and Doctor Who while looking at the starry night, from the television series 'Doctor Who', 10th episode of the 5th season. Dedicated to all those who when they look up at the night sky see more than white dots, to those for whom life has many colors through their eyes.

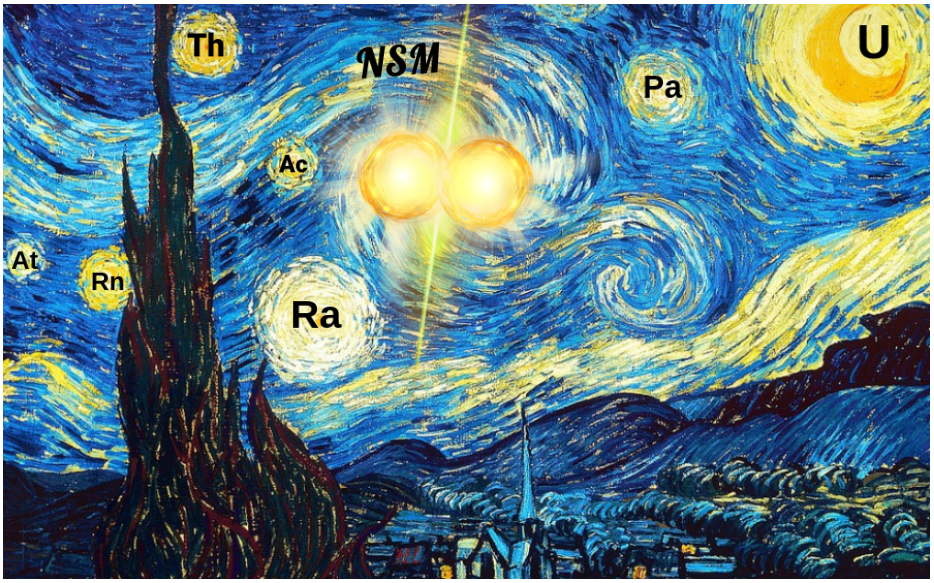

Figure 1: *Artistic adaptation by the author of the painting 'The Starry Night' by Vincent van Gogh, open access. The two stars colliding at the center correspond to a Neutron Star Merger (NSM), suggested as one of the astrophysical sites with the highest production of heavy elements.*

Contents

List of Figures

All figures in this work are the creation of the author, unless otherwise noted. References and permissions for reproduced figures are provided.

List of Tables

Introduction

Once upon a time, the fission

"Nuclear fission is, at the same time,
a rather simple and a rather complex notion.
When a nucleus becomes too heavy it just divides,
but it's not so easy to parameterize such motion"

If I had to choose a beginning of this story without going back to the discovery of fire, I would say this story begins in the winter of 1932 at the Cavendish Laboratory in England, with James Chadwick discovering the neutron [3], already predicted in 1920 by Ernest Rutherford. The discovery of the neutron not only allowed a better understanding of the nuclear structure but also enabled a new world of possibilities in the field of nuclear reactions. Before the discovery of the neutron, reactions were produced using positively charged particles as protons or α particles. It was the physicist Enrico Fermi who started using the recently discovered neutrons to induce reactions. Since neutrons were not electrostatically repelled by the target, there was no need to accelerate them to high energies before they could undergo a nuclear reaction. Enrico Fermi and his collaborators bombarded most of the elements in the periodic table with neutrons since they had discovered a method to artificially induce atomic transformations just as though they were alchemists: the target elements captured the neutrons and transformed into heavier elements through β^- decay. In 1934 the time came for Uranium, the heaviest element in nature, to be bombarded with neutrons, to see if the same method could reach beyond the limits of nature and produce heavier nuclei. Since by irradiating uranium, Fermi verified the presence of artificial atomic species, he suggested the formation of one or several elements with atomic numbers higher than 92 [4] that were labeled as 'transuranics' by the scientific community. Despite the idea was widely accepted, those elements were not yet identified, and the presence of lighter nuclei in the samples encouraged the scientist Ida Noddack to first mention the idea of the nucleus breaking into smaller fragments [5]. However, Idda Noddack did not have experimental evidence, and around that time the idea of a neutron having energy enough to break a heavy nucleus was inconceivable. During those years numerous experiments were performed

bombarding heavy nuclei with neutrons to identify these transuranics, among whom were the scientists Lise Meitner and Otto Hahn. In 1938 Otto Hahn and Fritz Strassmann identified Barium in their samples, and Lise Meitner together with Otto Robert Frisch regarded this as evidence of the nucleus breaking: nuclear fission had been discovered [6](1939). Although fission was discovered 85 years ago, still lacks a satisfactory and complete description. In the beginning, it was parameterized on the basis of the liquid-drop model, but soon the necessity to include microscopic quantum phenomena as the nuclear shell structure became evident. Nowadays, it is known that nuclear fission is a complex dynamical process, whose description involves a time-dependent approach based on the coupling of the intrinsic and collective excitations of the nuclear constituents.

Chapter 1

Introduction

The introductory chapter has a first section where the objectives of this research are stated so that the reader has a clear vision from the beginning about the topic of this study. This section briefly mentions concepts that will be explained in more detail throughout the thesis. After describing the objectives, the two next sections are a bibliographic review of fission and the different studies carried out on it. These two last sections are especially dedicated to most novice readers, so if a more advanced reader prefers entering directly into the subject matter of this study, the author recommends continuing through the methodology chapter.

1.1 Objectives

In the last decade, unprecedented fission experiments have been carried out at the GSI/FAIR facility using the inverse-kinematics technique in combination with state-of-the-art detectors developed by the R^3B (Reactions with Relativistic Radioactive Beams) collaboration. For the first time in the history of fission, it was possible to measure and identify both fission fragments simultaneously in terms of their mass and atomic numbers [7, 8] and to extract correlations between fission observables sensitive to the dynamics of the fission process [9] and the nuclear structure at the scission point [10, 11].

The introduction of inverse kinematics was a great advance for fission studies, by allowing the identification of the fission fragments in charge and mass with good resolution, until then impossible through direct kinematics [12]. Fission induced by inverse kinematics through mechanisms such as Coulomb excitation [8], transfer, or fusion-fission [13, 14] is highly useful for studying fission at low excitation energies, including investigations of fission barriers, neutron excess, and pairing effects. These reaction mechanisms give rise to fissioning systems well-defined in energy, charge, and mass. However, they are often limited to low-energy studies, and in the case of fusion-fission and transfer to nuclei close to the stability valley. Hence, other phenomena that manifest predominantly at high excitation energies, such as dissipation or transient times, need to induce

fission at higher energies and with lower angular momentum [15, 16]. Spallation reactions are very versatile, since they allow a wide range of energies to be covered, depending on the number of nucleons removed in the reaction. Therefore, by using this reaction mechanism it is possible to carry out studies on both low and high-energy fission by selecting specific reaction channels, and they are also not limited to stable nuclei. Specifically, the quasi-free (p, 2p) collisions have been proven to be very useful in studying single-particle properties in nuclei by reconstructing the excitation energy with the missing mass method.

In the research presented in this work, proton-induced knockout reactions are combined for the first time with the study of fission in inverse kinematics. To do so, ^{238}U beams are accelerated to imping on a liquid hydrogen target (LH_2) at 540 MeV/u. This experimental technique would provide full kinematics measurements by obtaining the excitation energy for the fissioning nuclei and identifying the mass, charge, and TKE of the two fission fragments on an event-by-event basis. Such data can be obtained by combining the SOFIA (Studies Of FIssion with Aladin) experimental setup with a silicon tracker based on AMS-type detectors [1] and the calorimeter CALIFA (CALorimeter for In-Flight detection of γ rays and high energy charged pArticles) [2] developed by the R^{3}B collaboration. Studies for both high and low excitation energies could be conducted, as well as experiments with exotic nuclei. With all these ideas in mind, the main objectives of this study are reunited in the list below.

- This experiment is the first of its kind, so it has been conducted with a stable beam as a proof of concept for the proton-knockout-induced fission line of research. Therefore, one of the main objectives is to test its ability to obtain complete kinematic measurements and its versatility by studying fission at both low and high energies.

- Study the evolution with the fissioning system of observables sensitive to the pre-saddle dynamics, such as the partial fission yields and the widths of the charge distributions.

- Study the evolution of fission yields and fission modes with the excitation energy. The gradual weakening of the influence of shell structure on the fission yields with the increase of excitation energy can be quantified with the so-called suppression function [17], which minimizes the microscopic term of the energy-dependent effective potential. However, model parameters used in this approach are still not constrained due to the lack of data at different excitation energies. Thus, this research line could provide a new dataset very valuable to constrain the suppression function parameters.

- Another interesting question is the possible dependence of the energy sorting of the fission fragments on the excitation energy of the compound nucleus, since in direct kinematics studies with neutrons, the well-known saw-tooth shape shows higher neutron multiplicities for higher incident neutron energies [18]. To do so, observables sensitive to the post-saddle dynamics such as the neutron excess and the even-odd effect are studied for different excitation energy ranges.
- The experiment was performed using a stable ^{238}U beam to test the experimental setup, but the long-term objective is to perform experiments with more neutron-rich isotopes, to obtain fission yields and fission barrier heights to improve the predictions of the r-process calculations in the field of Astrophysics.

1.2 Introduction to fission

The next section will explain the nuclear fission process and how the understanding of it has evolved from the traditional liquid drop model to the complex dynamical models used nowadays.

1.2.1 General overview

Fission is a nuclear reaction that consists of the division of a heavy nucleus into two lighter nuclei, in addition to some other light particles such as neutrons, protons, and α particles. It is an exothermic reaction that can release large amounts of energy in both as γ rays and kinetic energy of the reaction products, for example, a typical uranium fission event releases around 200 MeV. Fission can happen naturally as a decay of heavy nuclei or can be produced artificially by inducing some excitation energy in the heavy nucleus through different methods, such as particle-induced fission [19], electromagnetic-induced fission ('Coulex') [20], β-delayed fission [21], and fusion-fission [22] among others. Historically, the first used method was particle-induced fission, when the uranium was bombarded with neutrons. The term 'compound nucleus' was first introduced by Bohr in his 1936 paper [23] (when fission was still not discovered) to define the intermediate system formed by the union of the accelerated neutron and the heavy nucleus. He suggested that the de-excitation process of this nucleus would be independent of its formation, and the different de-excitation channels such as particle and photon emission (or as it would be discovered 3 years later, fission) would compete with each other. Still, there would be a dependence on the initial excitation energy, angular momentum, and parity. From now on within this manuscript, both terms

'compound nucleus' and 'fissioning system' will be used indistinctly to refer to the heavy nucleus that has been excited and that will eventually de-excite via fission or another channel.
Fission can be divided into two stages. The first stage goes from the formation of the compound nucleus to the so-called saddle point, where the fission process becomes irreversible. Before this point, the compound nucleus could choose another channel rather than fission to de-excite, but if the saddle is reached, fission is decided. The second stage goes from the saddle to the scission point, where the neck joining the two nascent fragments breaks and they become separate nuclei (the so-called fission fragments). After the scission, Coulomb repulsion accelerates the fragments away from each other, and the excitation energy available at the scission point is shared by the fission fragments.
At the beginning of the process, the movement of the excited nucleons makes the compound nucleus deform, evolving from the spherical shape to a more elongated one. Any deformation away from a sphere will result in a larger surface, directly increasing the surface energy of the nucleus and therefore decreasing the binding energy of the system, as it can be seen in the classic liquid drop model (LDM) formula shown in Eq. (1.1). The binding energy is a form of potential energy, and it is defined as the minimum energy required to separate a nucleus into its constituents. Therefore, the lower the binding energy, the less bounded the system is.

$$\mathrm{B} = \mathrm{E_{Volume}} - \mathrm{E_{Surface}} - \mathrm{E_{Coulomb}} - \mathrm{E_{Asymmetry}} + \delta(\mathrm{Z,A})_{\mathrm{pairing}} \tag{1.1}$$

But on the other hand, the increasing elongation makes the average distance between protons bigger, decreasing the Coulomb energy and increasing the binding energy of the nucleus, making it more stable. Since the other terms contributing to the binding energy do not suffer appreciable changes during the deformation, the evolution of the system will be solely decided by the balance between surface ($\mathrm{E_S}$) and Coulomb ($\mathrm{E_C}$) terms. Eq. 1.2 shows the calculation of the Q value for the transition between the spherical shape ($\epsilon = 0$) to a nucleus with a distortion ϵ_1 from the sphere radius. The first term in brackets in Eq. 1.2 will be negative when moving towards larger deformations, and the second term will be positive (since the surface increases with deformation and the Coulomb repulsion decreases). But what will define the potential energy shape will be the rate of growth/decrease of one to the other.

$$\mathrm{Q} = \mathrm{B}(\epsilon_1) - \mathrm{B}(0) = \underbrace{[\mathrm{E_S}(0) - \mathrm{E_S}(\epsilon_1)]}_{<0} + \underbrace{[\mathrm{E_C}(0) - \mathrm{E_C}(\epsilon_1)]}_{>0} \tag{1.2}$$

In the first stage, the surface energy increases faster than the Coulomb energy decreases, making the first term in Eq. 1.2 larger than the second one and thus leading to a $Q < 0$ value. This corresponds with the potential energy maximum drawn in Fig. 1.1, known as the 'fission barrier'. This maximum potential energy corresponds to a minimum binding energy where the compound nucleus is highly unstable, the so-called 'saddle point'. In order to overcome the saddle point, the excitation energy of the compound nucleus must exceed the height of the barrier or pass through it via tunnel effect, as happens in spontaneous fission.

$$Q = B(\epsilon_2) - B(\epsilon_1) = \underbrace{[E_S(\epsilon_1) - E_S(\epsilon_2)]}_{<0} + \underbrace{[E_C(\epsilon_1) - E_C(\epsilon_2)]}_{>0} \tag{1.3}$$

For the second stage of fission, the energy balance formula is written in Eq. 1.3, totally analogous to the previous one but now between the deformation ϵ_1 reached at the saddle point and a larger deformation ϵ_2. Immediately after surpassing the saddle point, the Coulomb energy starts to decrease much faster than the surface energy increases, making the first term in Eq. 1.3 smaller than the second one and thus leading to a $Q > 0$ value. This implies that the transition to more deformed states will be energetically favourable, since the binding energy of the system increases with deformation until the scission point. After the scission point, the two newborn fragments will have a larger binding energy than the deformed nucleus.

The resulting fission fragments are emitted with high kinetic and excitation energies, as a consequence of the energy changes involved in the process and sketched in Fig. 1.1. The total available energy is defined at the beginning of the process by the potential energy of the fissioning system in the ground state (Ep^{GS}) and its initial excitation energy (Ei^*). Since surpassing the fission barrier requires part of this excitation energy, after the saddle the system has an excitation energy left of $E^*_{Bf} = Ei^* - Ep^{GS}$. Then, in the journey from the saddle towards the scission, the potential energy that is decreasing transforms into excitation energy and a small fraction can also be converted into pre-scission kinetic energy (E_k^{pre}). The excitation energy of the system is classified into two modes according to the degrees of freedom involved. When the degrees of freedom are small, such as single-particle excitations, the excitation energy is stored in the so-called intrinsic modes (E^*_{int}). However, when the number of degrees of freedom involved is higher, which implies deformations and rotational or vibrational movements, the excitation energy is stored in the so-called collective modes (E^*_{col}). Besides, the energy can be dissipated from the collective modes to the intrinsic excitations.

After the scission, part of the potential energy previously held by the fissioning

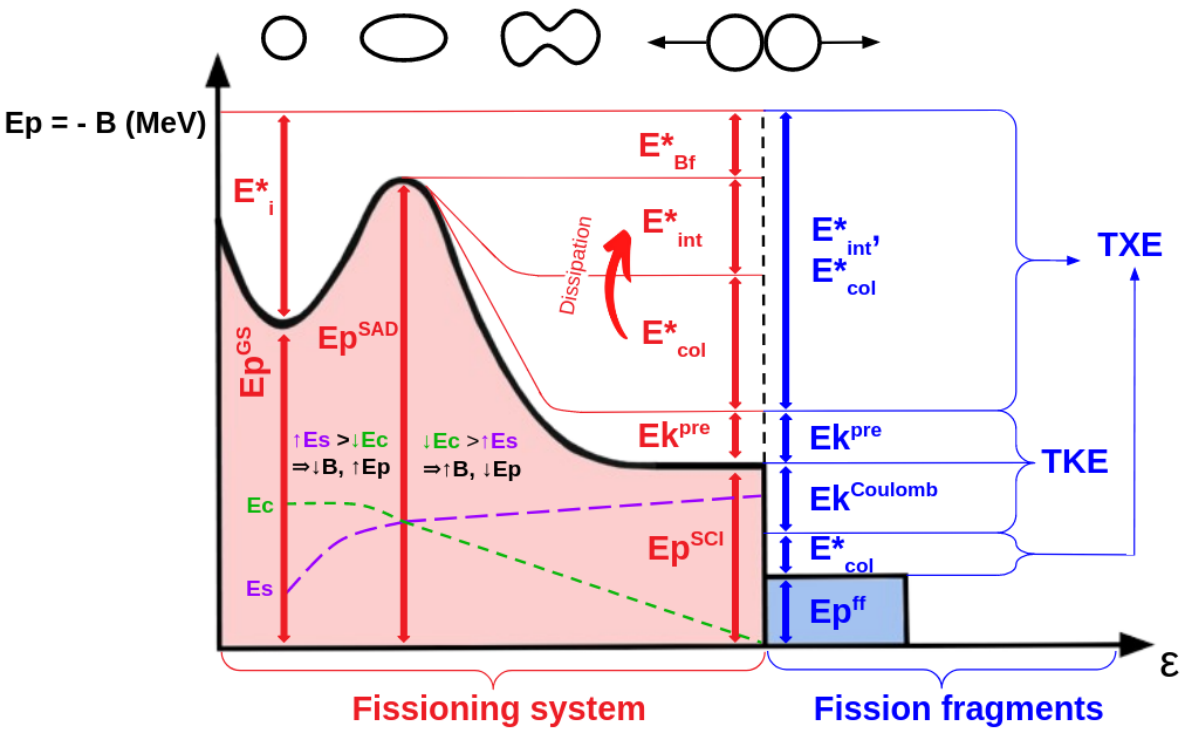

Figure 1.1: *Schematic diagram of the potential energy evolution with the deformation parameter ϵ, indicating the different energies involved. In the upper part, the evolution of the fissioning system is illustrated according to the different stages.*

system will be transferred into kinetic energy ($E_k^{Coulomb}$), due to the Coulomb repulsion between the two fission fragments, and collective excitation modes, as deformations of the fission fragments. Finally, all the energy stored in intrinsic and collective excitation modes constitutes the total excitation energy of the fission fragments (TXE), and the addition of the pre-scission and Coulomb kinetic energies constitutes the total kinetic energy (TKE).

1.2.2 Liquid drop model

In 1939, a little after the discovery of fission, the scientists Niels Bohr and John Archibald Wheeler parameterized the fission process on the basis of the LDM formula, shown in Eq. [19]. This model treats the nucleus macroscopically as if it behaved as a charged drop of liquid, therefore they considered that in the ground state, the heavy nucleus would be spherical. Due to the excitation, the initial radius of the sphere would be deformed up to the value described in Eq. 1.4, where R(0) is the initial radius value, θ the angle of the radius respect to the longitudinal axis, P_i Legendre Polinomials and ϵ_i are small quantities that express the extent of the deformation.

$$R(\theta) = R(0)[1 + \epsilon_0 + \epsilon_2 P_2(\cos\theta) + \epsilon_3 P_3(\cos\theta) + ...] \tag{1.4}$$

Approximating the formula up to the quadrupole term, the change in the surface and Coulomb energy terms due to the deformation can be described as shown in Eq. 1.5.

$$\begin{aligned} E_S(\epsilon) &= E_S(0) \cdot (1 + \frac{2}{5}\epsilon_2^2) \\ E_C(\epsilon) &= E_C(0) \cdot (1 - \frac{1}{5}\epsilon_2^2) \end{aligned} \tag{1.5}$$

Substituting these terms in the equation 1.2 an expression to estimate the probability that the nucleus undergoes fission is obtained in 1.6, since if $E_C(0) > 2E_S(0)$ then $Q > 0$ and the nucleus evolves towards higher deformations.

$$Q = E_C(0)\frac{1}{5}\epsilon_2^2 - E_S(0)\frac{2}{5}\epsilon_2^2 \tag{1.6}$$

This leads to the definition of the fissility parameter in formula 1.7. Therefore, if $x > 1$ the nucleus would undergo fission, while if $x < 1$, it would be stable against deformations. The limiting obtained ratio Z^2/A is about a 17% greater than the ratio for the ^{238}U. Nuclei as the uranium that are close to this limit are stable against small deformations. But a larger deformation could lead the nucleus to surpass the fission barrier and give the long range Coulomb repulsion more advantage over the short-range attractions responsible for the surface tension, leading the system to fission.

$$x = \frac{E_C(0)}{2E_S(0)} \approx \frac{1}{50}\frac{Z^2}{A} \tag{1.7}$$

The LDM offers a good first interpretation of the fission process and predicts the appearance of the fission barrier. But it fails to describe several properties of the process and nuclear structure. It predicts that all nuclei are spherical in the ground state, which is not in agreement with observations. It also cannot explain the appearance of the magic numbers, and therefore cannot explain the asymmetric fission.

1.2.3 Shell model

Already in 1934 W. Elsasser following the ideas of J.H. Bartlett suggested that certain numbers of neutrons or protons in the nucleus seemed to form particularly stable configurations [24], similar to the way the electrons close shells in atoms. In 1948 M.Geoppert-Mayer published a paper [25] summarising experimental facts that supported this idea for nuclei with 20, 50, 82, or 126 number of neutrons or protons, which would later be coined as 'magic numbers'.

Among those experimental facts was asymmetric fission, something that had been observed since the very beginning of the fission studies. Even though the LDM formula suggests that the most likely partition is the one that leads to two fission fragments similar in charge and mass, the observations demonstrated that most of the time the nucleus splits into a heavier and a lighter fragment. The isotope ^{235}U contains 143 neutrons that could be split as $143 = 82 + 50 + 11$. The most probable fission are those in which one fragment has at least 82 neutrons and the other at least 50, supporting the existence of the closed shells of 50 and 82 neutrons. The calculations to develop this model were conducted by both the group of Haxel, Jensen, and Suess [26] and M.Geoppert-Mayer [27].

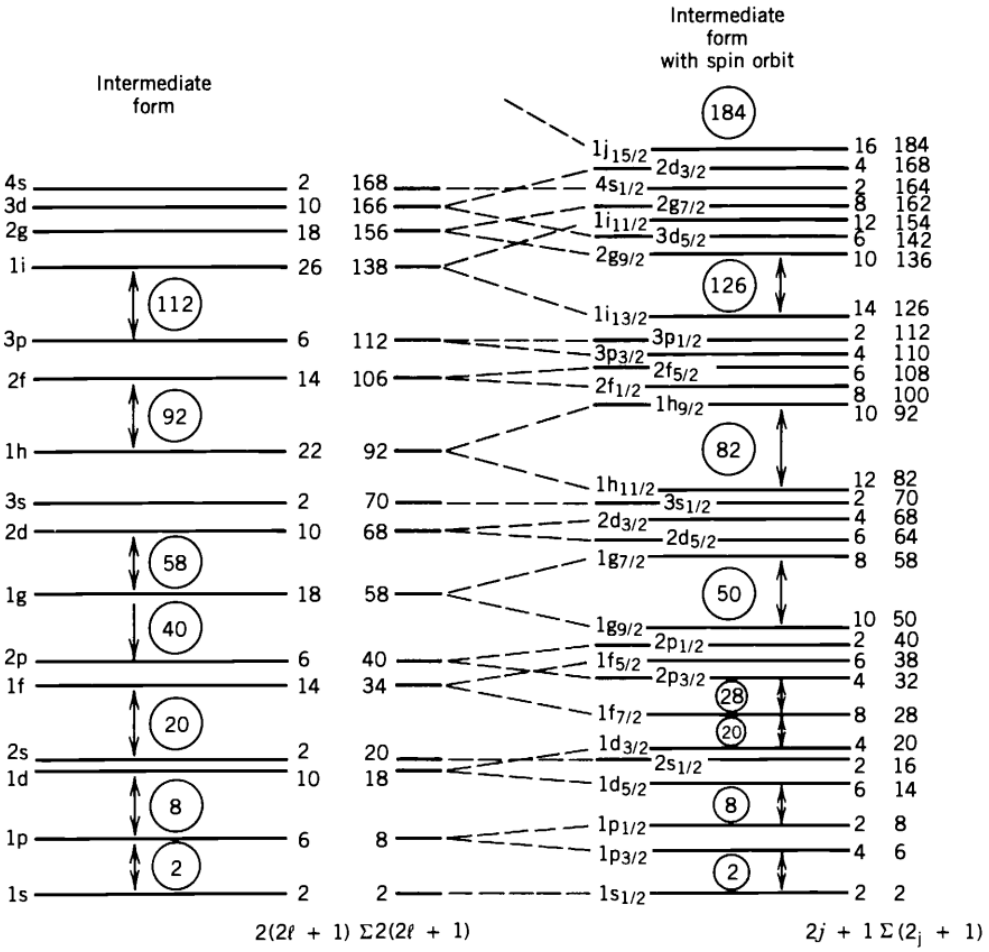

Figure 1.2: *Energy levels in the atomic nucleus. Left: energy levels calculated using the Woods-Saxon potential. Right: Splitting of the levels due to the introduction of the spin-orbit interaction, which splits levels with* $l > 0$ *into two new levels. The numbers to the right of each level show how many nucleons it can hold and the encircled numbers show the cumulative number of nucleons. Adapted with permission from Ref. [28]. Copyright (1991) by Wiley.*

In the atom, electronic energy levels appear when solving Schrodinger's equation for the Coulomb potential between the electron and the nucleus. It

depends inversely on the distance between the electron and the nucleus and does not depend on any angles. Such a potential is called a 'central potential'. In the case of the nucleus, the shell model assumes the nucleons are also under the influence of a central potential, but in this case, the potential is created by the nucleons themselves. This can be described by a potential that has a shape between that of a square well potential and a three-dimensional harmonic oscillator, which would be improved later and named by the authors as Woods-Saxon potential [29]. Still, the eigenvalues obtained did not match the observed magic numbers until M.Geoppert-Mayer and Jansen [26, 27] introduced, independently from each other, the spin-orbit coupling in the potential. Since neutrons and protons are both fermions, they have a magnetic momenta associated with their intrinsic angular momenta (the spin) apart from the magnetic momenta from their movement inside the nucleus. These two momenta can interact in a way that reminds the electromagnetic spin-orbit of the coupling of the crust electrons with the nucleus. Using this mean field potential plus the spin-orbit effect, the experimental magic numbers are exactly reproduced up to 126. The resulting energy level scheme is illustrated in Fig. 1.2.

Even though this model represents a great improvement, it was observed that nuclei having a number of protons and neutrons very far from the closed shells would have deformed shapes in the ground state. This deformed shape would change the nuclear potential and affect the motion of the nucleons. Therefore, in 1955 S.G. Nilsson modified the shell model to include deformed nuclei [30]. To do so, he introduced a non-spherical mean field where the nuclear shape and orientation were considered dynamical variables that were associated with the collective motion of the nucleons inside the nucleus. Within this model, he developed diagrams of the single-particle energy levels as a function of the nuclear deformation (see Fig. 1.3). However, the calculation of the total energy was less precise than the one obtained with the classic LDM.

In 1966, V.M. Strutinski developed a macroscopic-microscopic method [31] which consisted of correcting the macroscopic LDM potential (U_{LDM}) by the microscopic contributions (U_{Micro}) such as nucleon shells and pairing effects, as seen in Eq. 1.8. To do so, the microscopic term U_{Micro} was calculated as the difference of the single-particle energies between the Nilsson model and the uniform LDM.

$$U = U_{LDM} + U_{Micro}; \tag{1.8}$$

This method was called the 'Shell correction method'(SCM). As it can be seen

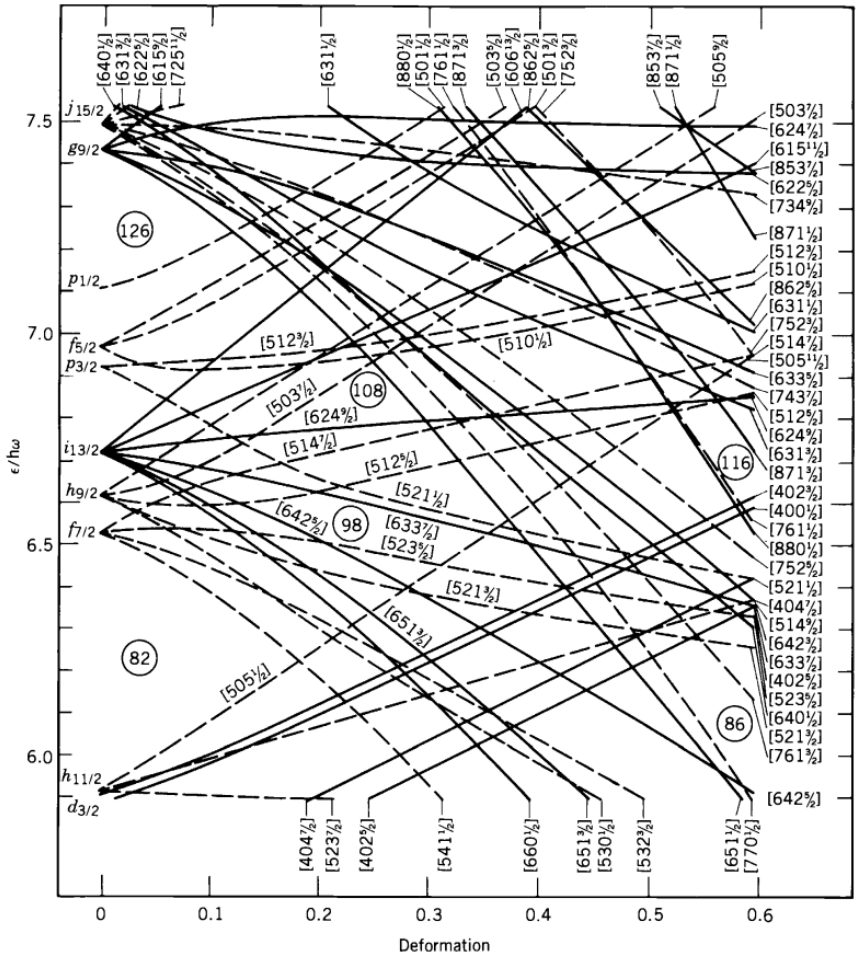

Figure 1.3: *Energy levels as a function of the deformation. Adapted with permission from Ref. [28]. Copyright (1991) by Wiley.*

in Fig. 1.3, some of the single-particle levels increase energy with deformation, and some of them decrease. The valence nucleon will therefore change from one state to the other, and modify the total potential by increasing or decreasing the barrier under or above the LDM. Therefore, the fission barrier calculated with the SCM has an oscillating behaviour as seen in Fig. 1.4, showing two or more minimums few MeV's above the ground state. This explained the observations of fission isomers (deformed metastable states that decay by spontaneous fission) done by Polikanov et al 1962 [32], and introduced the idea of deformed magic numbers. Since the energy levels change with deformation, deformed nuclei will present different nucleon numbers for which stability is enhanced in comparison with the spherical shapes.

The shell effects also play a key role in the final mass distribution of the fission fragments, since the formation of two fragments with a nucleon number close to a magic number will be enhanced over other configurations. Therefore, the best way to display the potential energy landscape is as a function of the deformation (the quadrupole moment) and the mass asymmetry of the two fragments. An

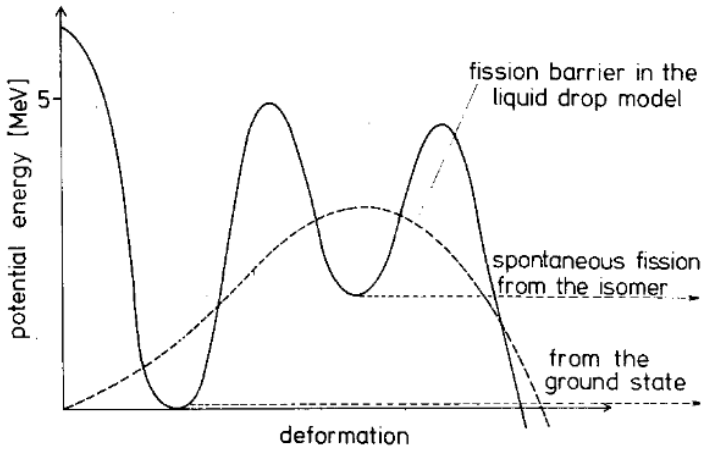

Figure 1.4: *Potential energy comparison between LDM and SCM. Adapted with permission from Ref. [33]. Copyright (1980) by Elsevier B.V.*

example of this dependence in both variables can be seen in Fig. 1.5 for the ^{236}U, showing several saddle points (which indicates the existence of isomeric states) and three fission valleys resulting in different possible mass asymmetry of the fission fragments. The middle one centered at zero, represents the case where the two fission fragments have similar charge and mass (symmetric fission), and the two valleys at the edges, correspond to the cases where one fission fragment is bigger than the other (asymmetric fission).

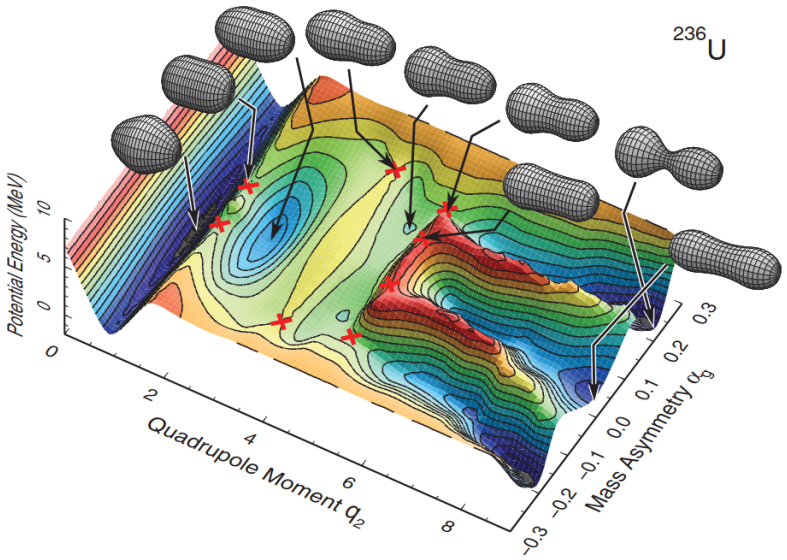

Figure 1.5: *Potential energy landscape as a function of deformation and mass asymmetry. Two red crosses show the saddle points. Adapted with permission from Ref. [34]. Copyright (2012) by the American Physical Society.*

1.2.4 Fission dynamics

Until now, fission has been discussed within the framework of the potential energy landscape. However, this only accounts for the static properties of the fission, while the process also presents important dynamic features such as the energy release in the coupling between degrees of freedom and the typical timescales along the process. This section will present a review of the evolution of the models used to estimate the fission probability, which competes with different particle evaporation channels. Decay probability is calculated based on statistical models as displayed in Eq. 1.9, where Γ_j is the decay width of a specific channel j (fission in this work) divided by the addition of all the possible decay widths, $\sum_i \Gamma_i$.

$$P_j(N,Z,E) = \frac{\Gamma_j(N,Z,E)}{\sum_i \Gamma_i(N,Z,E)} \tag{1.9}$$

The first description of the fission decay width was purely statistical, performed by Bohr and Wheeler [19]. Following the Weisskopf-Ewing formalism [35], the Bohr and Wheeler decay width is described as shown in Eq. 1.10. It is directly proportional to the temperature (T) and the ratio between the nuclear level densities at the saddle point ρ_{sd} and the ground state ρ_{gs}. Level densities are dependent on the excitation energy (E) and angular momentum (J). In the case of the level density at the saddle point, its energy would be the difference between the initial energy and the fission barrier height (B_f). The level densities were parametrized based on the Fermi gas model [36].

$$\Gamma_f^{BW} = \frac{T}{2\pi}\frac{\rho_{sd}(E - B_f,J)}{\rho_{gs}(E,J)} \tag{1.10}$$

The Bohr-Wheeler approach worked rather well for excitation energies close to the fission barrier. However, at higher excitation energies, the statistical method overestimated fission rates. In 1940 Kramers [37] published a paper suggesting that the movement of the nucleons inside the nucleus follows a Brownian motion. Within this context, the self-generated nuclear potential is regarded as an external field of force. The nucleons constitute a heat bath with thermal fluctuations that introduce a random component regarded as a viscosity parameter that opposes deformation. Therefore, when the fissioning system evolves towards the saddle point, even though there is a net energy transfer from the intrinsic modes (excitation) to the collective modes (deformation), this frictional force dissipates energy the other way around. This phenomenon is known as 'coupling between collective and intrinsic modes' and causes the slowing down in the motion towards the saddle point, enhancing other de-excitation channels, and therefore, decreasing

the overestimated LDM fission rates. To parameterize this phenomenon, Kramers employed the Fokker-Planck equations (FPE) [38] used in transport theories and reached a stationary solution (assuming density does not change with time) dependent on a dissipation parameter. Therefore, the fission decay width can be described as the Bohr-Wheeler decay width corrected by a factor that takes dissipation into account, as can be seen in Eq. 1.11. In the formula, β is the dissipation coefficient and w_0 is the frequency of an harmonic oscillator describing the potential at the saddle point deformation.

$$\Gamma_f^K = \left[\sqrt{1+\left(\frac{\beta}{2\omega_0}\right)^2} - \frac{\beta}{2\omega_0}\right]\Gamma_f^{BW}. \tag{1.11}$$

In 1981 Gavron and collaborators [39] measured a large number of pre-scission neutrons that they were not able to interpret within the framework of standard statistical-model calculations, implying a transition time of the order of 10^{-20} s or longer. This pointed out the necessity to take into account the temporal evolution of the fissioning system. Following the previous work performed by Kramers, Weidenmüller [40], Grangé [41], and Bhatt [42] developed a time-dependent approach using transport models based on the Langevin or FPE. They found that the fissioning system needs a certain time before it reached Kramer's stationary flux, and even some time before it starts to deform. This time becomes noticeable only at high excitation energies, which is why the statistical and stationary approaches worked rather well for low-energy fission. The reason why it appears at high energies is that if the available excitation energy is greater than the barrier but the time needed to deform to the saddle is longer than for particle evaporation, this channel will be favoured and fission rates will decrease. To take into account this new feature, the fission decay width can be parameterized as the stationary fission width from Kramer's but corrected by a time-dependent factor. The work performed by Jurado and collaborators [43, 44, 45] obtained an analytical solution of the FPE and the resulting time-dependent fission decay width can be expressed as shown in Eq. 1.12.

$$\Gamma_f(t) = \frac{W_n(x = x_{sd}; t, \beta)}{W_n(x = x_{sd}; t \to \infty, \beta)}\Gamma_f^K, \tag{1.12}$$

The factor $W_n(x; t, \beta)$ is the normalized probability distribution at the saddle-point deformation x_{sd}. For a nuclear potential described by a parabola, the Fokker-Planck equation has a Gaussian solution for the probability distribution at the saddle point which has a time-dependent width $\sigma(t)$, as shown in Eq.1.13

$$W_n(x = x_{sd}; t, \beta) = \frac{1}{\sqrt{2\pi\sigma(t)}} \exp\left(\frac{-x_{sd}^2}{2\sigma^2(t)}\right) \tag{1.13}$$

Fig. 1.6 shows the comparison of different approaches to calculate the escape rate functions, which are related to the fission decay width as $\lambda_f(t) = \Gamma_f(t)/\hbar$. In the plot, it can be seen that the FPE-like escape rate functions do not start to grow immediately. This time before the rate starts to increase is the so-called 'relaxation time'. When they start to grow, they do it in an exponential-like manner during a certain time, the so-called 'transient time' until the stationary flux described by Kramers is reached.

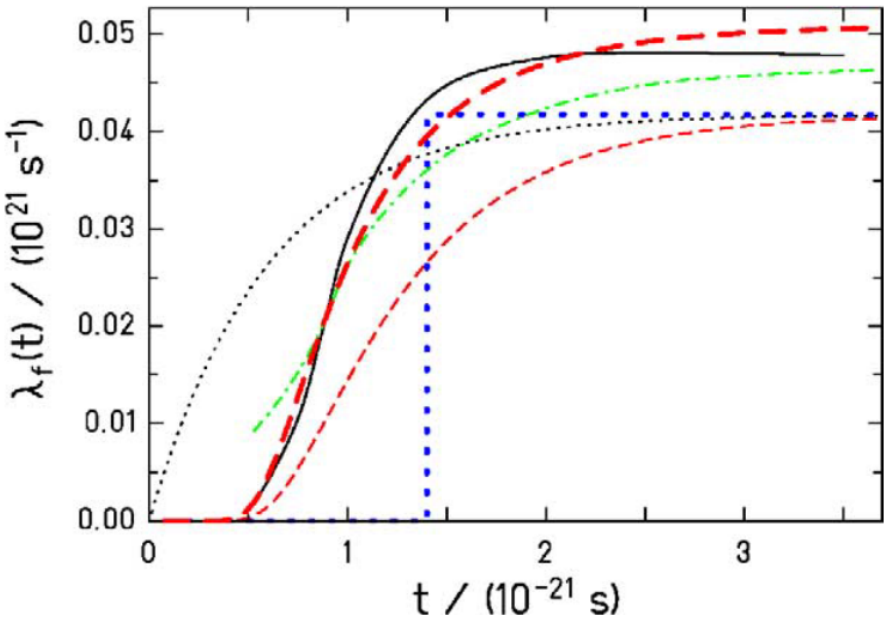

Figure 1.6: *The solution of the Fokker-Planck equation (full line) or the time-dependent escape rate for the case of a fissioning ^{248}Cm nucleus, using the potential introduced in Ref. [42] at temperature $T = 5$ MeV and with a reduced dissipation coefficient $\beta = 5 \cdot 10^{21} s^{-1}$. Different approximations are compared: the step function (thick dotted line), the exponential-like function(thin dotted line), the approximate formulation from Ref. [42]: (dash-dotted line), the approximate formulation from Ref. [43](thin dashed line), and the improved expression proposed from Ref. [44](thick dashed line). Adapted with permission from Ref. [44]. Copyright (2004) by Elsevier B.V.*

Other theories introduce the dynamical aspects of fission by parameterizing the potential energy as a dynamical variable, using microscopic models based on Hartree-Fock [46] and Hartree-Fock-Bogoliubov methods [47, 48]. However, such approaches are limited by the complexity of the many-body calculations and huge computing times.

1.3 Fission yields: a key observable

The yield of a fission fragment is the percentage of that nuclear species produced per fission event. It can be displayed as yields of nuclear charge, neutron number, or nuclear mass. This observable is of great value for nuclear theory, astrophysics, and also for applications in nuclear reactors.

1.3.1 Fision yields in nuclear theory

In the nuclear theory domain, fission yields are very important to develop nuclear structure models, since the produced amount of a nuclear species reveals nuclear configurations that make nuclei more stable and therefore likely to be produced in fission. In this sense, fission yields were decisive in confirming the existence of both neutron and proton magic numbers and introducing the current shell model [25]. Fig. 1.7 shows an overview of the fissioning systems investigated up to 2023 in low-energy fission for different reaction channels.

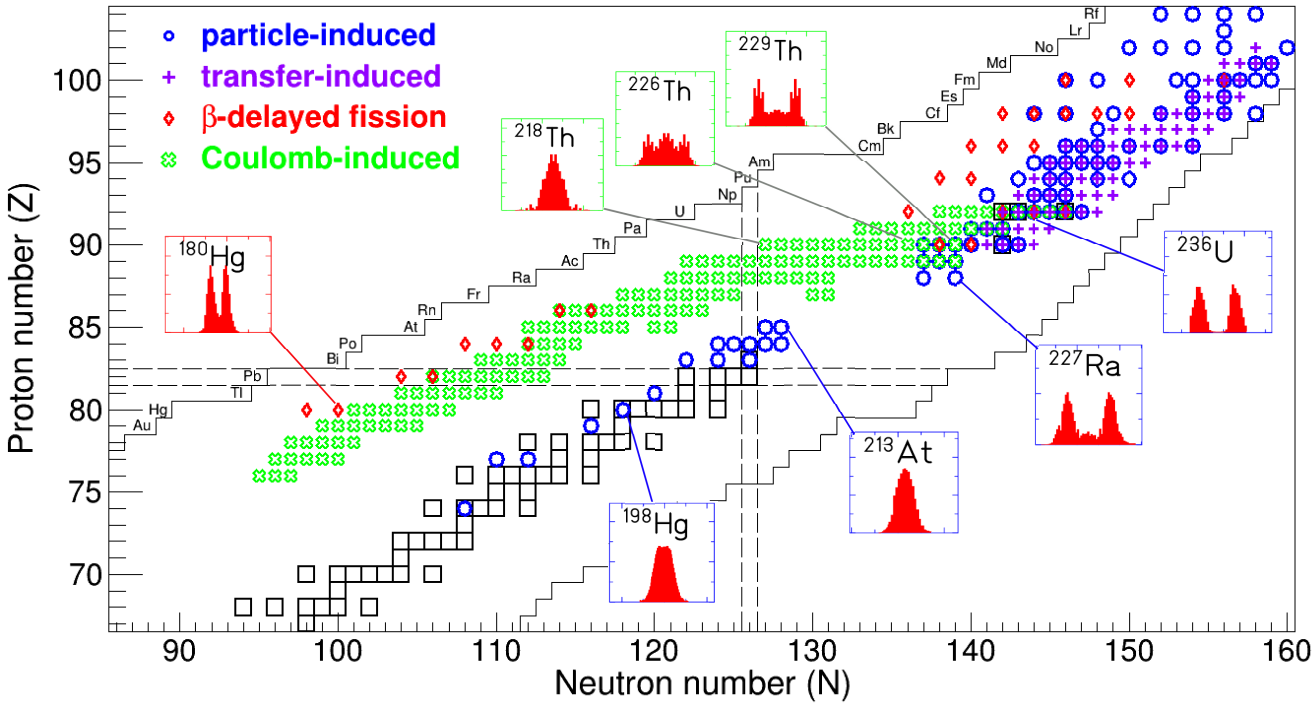

Figure 1.7: *Fissioning systems investigated up to 2023 in low-energy fission with excitation energies up to 15 MeV above the fission barrier. Blue circles: particle-induced and spontaneous fission [49, 50]. Green crosses: Coulomb-induced fission by Schmidt and collaborators in 1996 [51] and in the recent SOFIA/R^3B [52, 53] experiments in inverse kinematics at GSI. Red diamonds: fissioning daughter nuclei studied in β-delayed fission [12, 10]. Plus symbols: transfer-induced fission reactions [54, 22]. The primordial stable isotopes are indicated by black open squares. The limits of known nuclei correspond to AME 2020 [55]. Adapted with permission from Ref. [56]. Copyright (2024) by the Royal Society.*

According to the fission yields and total fragment kinetic energy (TKE), fission was classified into 4 major modes [57]:

- Mass-symmetric super-long (SL): symmetric partition of mass and charge, long elongation at scission, and little shell model influence. The fission fragment neutron distribution on the left side of Fig. 1.8 is a good example of SL with certain contributions of the asymmetric modes.

- Mass-asymmetric Standard I (St1): asymmetric partition, but it is the closest mode to the symmetry of the asymmetric ones. The fissioning system presents a compact shape at scission and quasi-spherical heavy fragment. It is the mode with the highest TKE. The distribution on the right side of Fig. 1.8 is asymmetric and it probably has a major contribution of StI, since the mean neutron number of the heavy fragment is $N_H \approx 82$.

- Mass-asymmetric Standard II (StII): asymmetric partition, very far from symmetry and a deformed heavy fragment with a neutron number typically around $N_H \approx 88$. For low-energy and spontaneous fission of most heavy actinides, yields show an asymmetric partition [58], as seen in Fig. 1.7 evidencing the microscopic effect of the magic numbers.

- Super-asymmetric: the most asymmetric fission case, present in the heavier actinides, such as Cf [59].

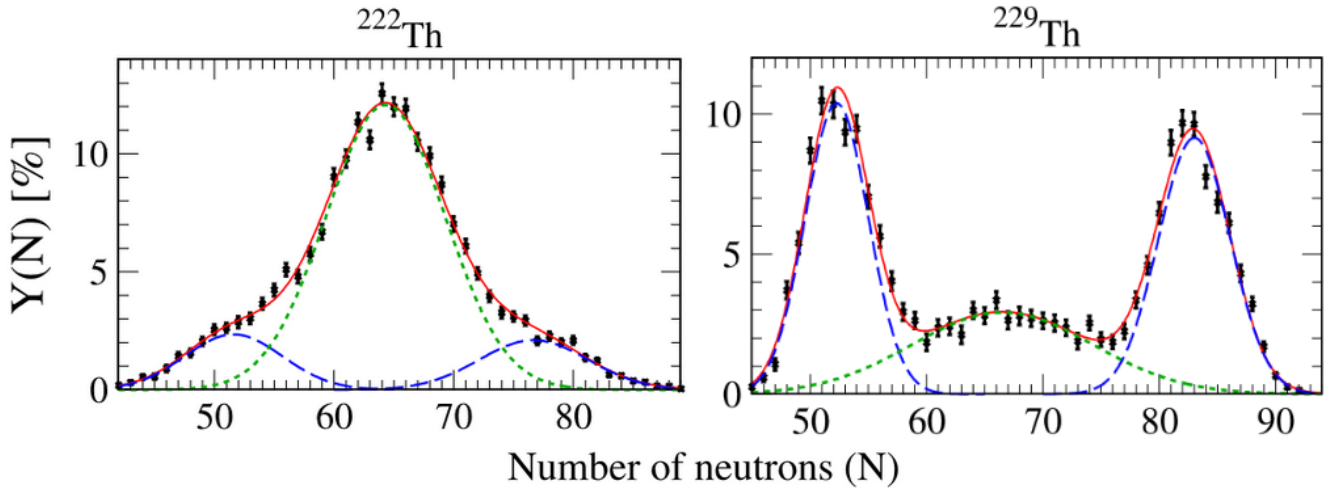

Figure 1.8: *Isotonic yields after prompt-neutron emission for thorium isotopes fitted by a 3-Gaussian function. The total fit (full red lines) is decomposed into one symmetric (dotted green lines) and two asymmetric (dashed blue lines) components. Left: Larger symmetrical contribution. Right: Larger asymmetrical contribution. Adapted with permission from Ref. [54]. Copyright (2022) by the American Physical Society.*

In the majority of actinides, the average mass of the heavier fragment remains nearly constant at A≈140, regardless of the mass of the fissioning nucleus. This indicates that the shell effects of the nascent heavy fragment play a key role in the fission evolution. At the beginning, St1 was associated with the formation of

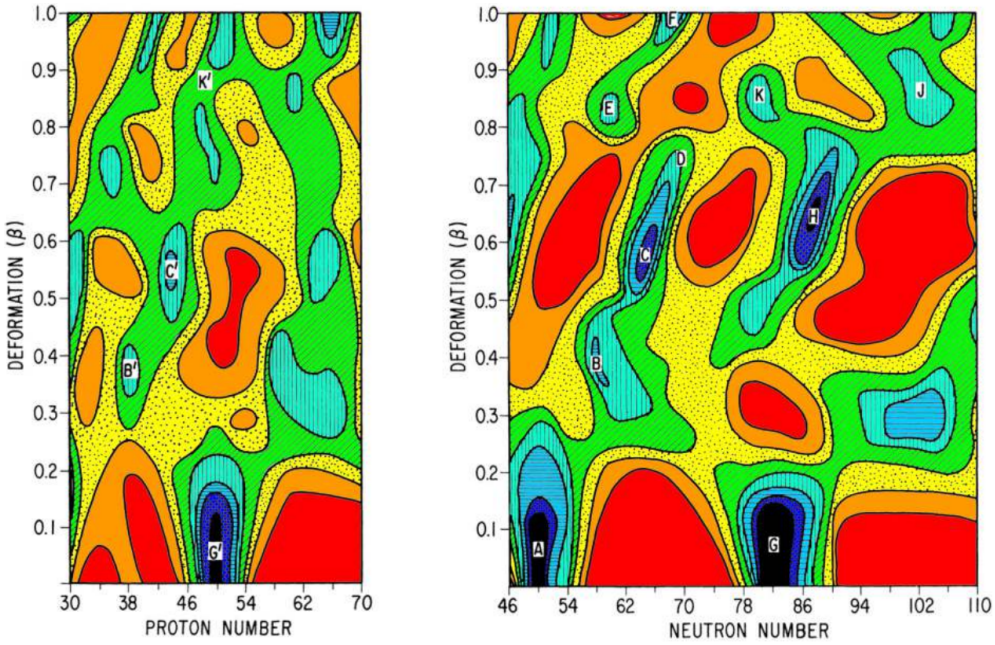

Figure 1.9: *Proton-shell (left) and neutron-shell corrections (right) calculated as a function of deformation (β) and respectively proton and neutron number. The contours are plotted at 1 MeV intervals. Black regions represent the strongest shell corrections containing all values lower than -4 MeV and the inner red region (representing the weakest shell corrections) containing all values greater than +2 MeV. These figures have been modified by adding colour and adapted with permission from Ref. [60]. Copyright (1976) by the American Physical Society.*

the doubly spherical ^{132}Sn heavy fragment, with $Z_H = 50$ and $N_H = 82$, and the StII with the $N_H = 88$ quadrupole deformed shape ($\beta \approx 0.6$), since this points represent the strongest shell corrections, as seen in Fig. 1.9. However, systematic measurements of the proton and neutron number distributions [12, 61] reveal that the neutron number can vary up to 7 units with the compound nucleus mass, as can be seen in Fig. 1.10 bottom pannel. On the contrary, the atomic number remains rather constant at values between Z=52 and Z=56. Recently, it has been suggested [62] that the strong shell effects in ^{132}Sn might not be the only factor affecting, but they could be also associated with some extra stability provided by the octupole-deformed (pear-like shaped) shell gaps at Z=52 and Z=56 [63, 64].

The transition from symmetric to asymmetric fission modes also shows how the microscopic effects introduced by the shell model can be of lower or greater importance over the LDM depending on the excitation energy of the system because fission yields are a mirror of the potential energy. Looking at the potential energy landscape shown in Fig. 1.5, the fissioning systems with low excitation energy would mostly fission through the asymmetric valleys, and with the increasing of the excitation energy, some systems would be able to overcome the higher potential barrier for symmetric fission. Finally, at very

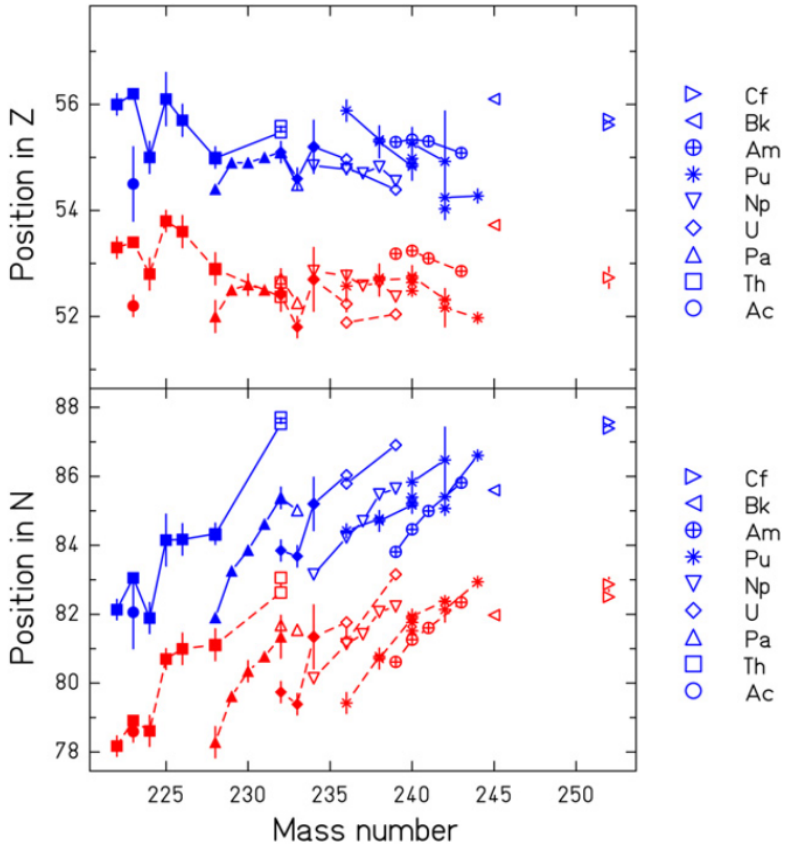

Figure 1.10: *Mean positions of the standard fission channels in atomic number (upper part) and neutron number (lower part) as a function of the fissioning system mass. The values of standard I (standard II) for the isotopes of a given element are connected by dashed (full) lines and marked by red (blue) symbols. Adapted with permission from Ref. [61]. Copyright (2008) by Elsevier B.V.*

high excitation energies, it would not be possible to appreciate the contribution from the asymmetric valleys caused by shell effects, eclipsed by the symmetric contribution. Several studies have been performed in the last years [17, 65, 13, 53] to parameterize the dependence of the yields on the excitation energy. To do so, an effective potential dependent on the excitation energy E and a shape coordinate X ($U_E(X)$) is introduced, as seen in Eq. 1.14, by adding to the macroscopic potential ($U_{macro}(X)$) the microscopic correction ($U_{Shell+pair}(X)$) multiplied by a suppression factor dependent on the energy ($S[E^*(X)]$).

$$U_E(X) = U_{macro}(X) + S[E^*(X)]U_{Shell}(X) + U_{pair}(X) \tag{1.14}$$

This suppression function damps the shell and pairing effects with the increase of excitation energy. Therefore, the value of this function would tend to $S(0) = 1$ for zero excitation energy and would tend to zero for higher excitation energies where microscopic effects vanish. The functional form of the suppression term is usually an inverse exponential of the energy divided by a constant factor that would mark the slope of the function. An example is displayed in Fig. 1.11

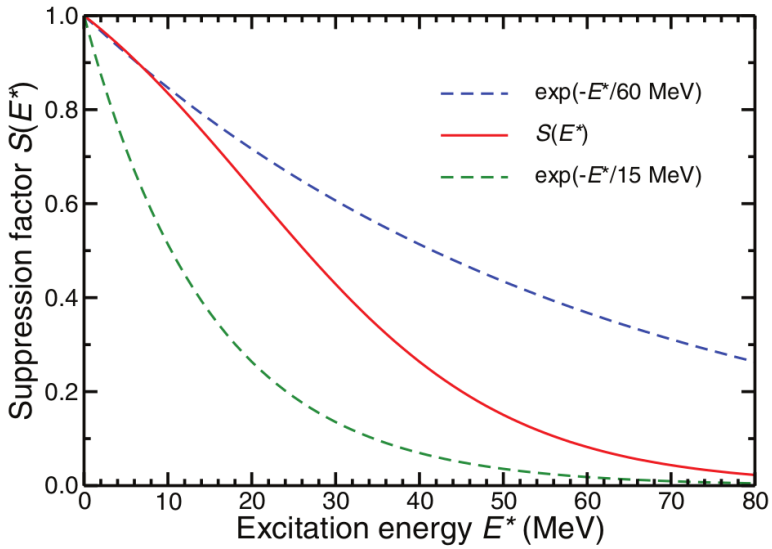

Figure 1.11: *Comparison of suppression functions. The dashed blue and green lines represent respectively $S(E^*) = exp(E^*/60MeV)$ and $S(E^*) = exp(-E^*/15MeV)$, while the solid red line represents the Woods-Saxon function described in Eq.1.15. Adapted with permission from Ref. [17]. Copyright (2013) by the American Physical Society*

for different energy parameters of the exponential and a Woods-Saxon function introduced by [17] and described in Eq. 1.15 with two adjustable parameters to reproduce better the change of slope when changing from the low energy to the high energy range.

$$\mathrm{S(E^*)} = \frac{1 + \mathrm{e}^{-\mathrm{E_1}/\mathrm{E_0}}}{1 + \mathrm{e}^{(\mathrm{E^*}-\mathrm{E_1})/\mathrm{E_0}}} \tag{1.15}$$

1.3.2 Neutron fission yields and energy sorting

Neutron yields were essential to investigate the so-called 'energy-sorting' mechanism [18], which explains the energy transfer between the two nascent fragments right before scission at low excitation energies. Within this theory, the nascent fragments are regarded as mostly independent nuclei that have developed their own shell effects [66] and their own temperatures and are in thermal contact through a neck. It has been demonstrated that for medium-mass nuclei the temperature stays constant with increasing E^* up to 20MeV [67], in a similar way as it happens in nature with first-order phase transitions such as melting or freezing. Therefore, in the asymmetric fission, each fragment would have a different energy-independent temperature. And since the temperature decreases as the surface increases following the formula 1.16 from Ref. [68] (where S are shell and pairing corrections and p_i are parameters for different models), the

lighter fragment should be hotter and the heavier colder.

$$T = \frac{1}{A^{2/3}}(p_1 + p_2 S + p_3 S^2) \tag{1.16}$$

Since the nascent fragments are in thermal contact through the neck, they have a constant and shared excitation energy that can be passed from one to the other through nucleon transfer. Following the premises of constant total energy and constant temperature for each, the compound nucleus could be regarded as a momentarily isolated system that evolves in the direction of increasing entropy, which means maximizing the number of occupied states. Then, energy would flow from the hotter lighter fragment to the colder heavier one, since the light closed-shell nucleus has fewer available states than the heavy or non-closed-shell nucleus [18]. The effect of this energy sorting can be seen in Fig. 1.12, which displays the neutron emission as a function of the mass and has been coined as a 'saw-tooth shape'.

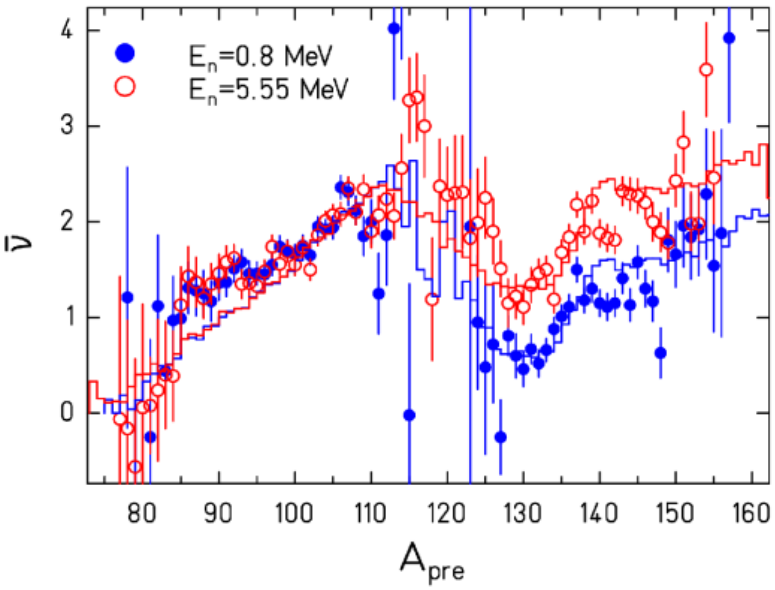

Figure 1.12: *Average number of prompt neutrons as a function of the primary fragment mass for the neutron-induced fission of* ^{237}Np *at two incident neutron energies. Adapted with permission from Ref. [18]. Copyright (2010) by the American Physical Society. Data from [69].*

Prompt neutron emission is an important indicator of the excitation energy since the higher the energy is, the higher should be the emission. After passing the fission barrier the energy in the center of mass reference system (CM) will have only a few MeV's in total kinetic energy (TKE) and the total excitation energy (TXE) is distributed among excitation energy (both collective and intrinsic) and deformation energy, caused by both Coulomb repulsion and shell effects. Right before scission, the lighter fission fragment is more deformed than its partner,

leading to a greater deformation energy, and therefore to a greater neutron emission. It can be seen in Fig. 1.12 for the low energy dataset how most of the lighter fragments show higher neutron emission than their heavier counterparts. The energy sorting mechanism manifests when the projectiles are accelerated to higher kinetic energies, which translates into higher available excitation energy of the compound nucleus. This extra excitation energy only raises the neutron emission on the heavier fragments' side, leaving the complementary lighter one invariant, which is evidence of how the lighter fragment is sending all its energy to the heavier one. In the case of heavy fragments close to reaching the ^{132}Sn shell closures, the shell corrections on T (see Eq. 1.16) would reverse the energy flow direction, transferring the nucleons towards the light fragment so the heavy fragment stays at the doubly magic number. This feature is what would produce the dip around the A = 130 and the peak of its complementary around A = 105, given the plot its characteristic jagged appearance. However, the energy-sorting mechanism cannot explain the insensitivity of the prompt-neutron yield for the light fragments at higher excitation energies [70]. With the increasing excitation energy, the microscopic features, such as shell effects and pairing, vanish. The level density transitions from the superfluid regime to the Fermi regime at the critical energy (supposed between 10 MeV and 20 MeV [68, 71, 67]), and the temperature is not constant with excitation energy anymore, which was the requisite for the energy sorting theory.

1.3.3 Even-odd effect

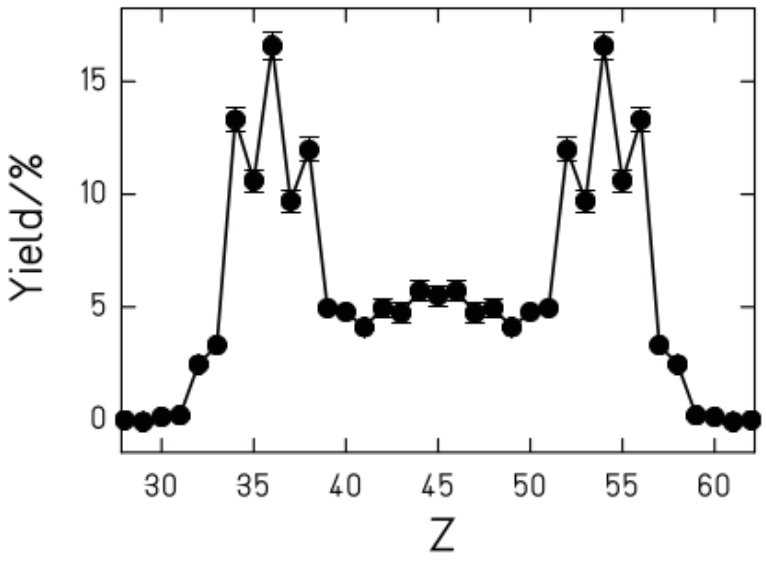

Figure 1.13: *Fission yields observed in the electromagnetic-induced fission of ^{229}Th. Figure from [72] with open access rights.*

Another important piece of information obtained from the study of the fission yields is the amplitudes of the even-odd staggering, an effect extensively observed in low-energy fission [73, 74]. The effect consists of the higher production of even-Z fragments and manifests as a staggering appearance like the one displayed in Fig. 1.13 of the fission atomic yields, showing higher amplitudes for the even-Z fragments and lower for the odd-Z ones. In the case of the even-Z fissioning systems, this feature could be easily understood, since the system would have to spend some energy on breaking proton pairs. However, whereas this effect was expected to fully vanish for odd-Z fissioning systems, an increase in the even yields for the lighter fragment and an increase of the odd yields in the heavy one has been observed instead. This means that the unpaired proton from the odd-Z fissioning systems systematically ends up in the heavy fission fragment. Several studies have been performed in the last few years [75, 76, 77, 78] to explain the nature of this feature, and it has been suggested as a consequence of the energy sorting mechanism in low-energy fission, which leads the unpaired protons to the heavy fragment since it has larger phase space [72].

1.3.4 Fission yields in astrophysics

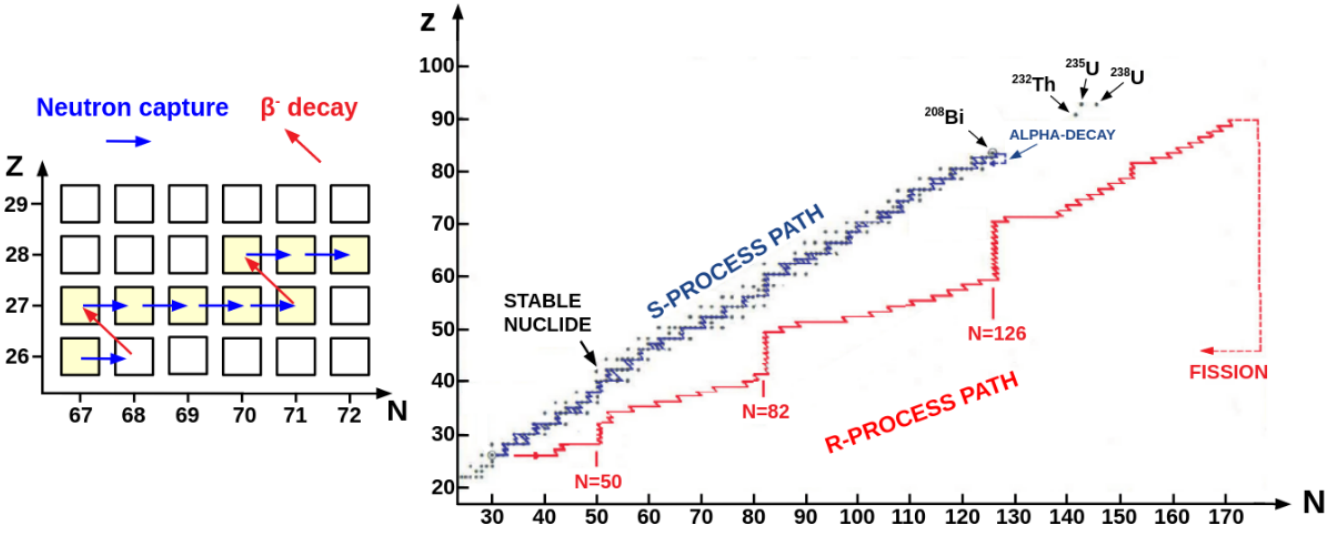

Figure 1.14: *Left: Neutron capture and β^- decay along the chart of nuclide. Right: Difference between s-process and r-process path. Figure from [79] with open access rights.*

Most of the elements heavier than iron present in the Universe are produced by two nucleosynthesis [80] processes: the slow neutron capture process (s-process) and the rapid neutron capture process (r-process). Both processes consist of consecutive neutron captures followed by β^- decays, as can be seen on the left side of Fig. 1.14. This causes the production of nuclei to move diagonally upwards on the nuclei chart. The difference between the two processes is the difference in

the time neutron capture takes, due to the environmental conditions in which it is found. The s-process happens in regular stars, most commonly in asymptotic giant branch (AGB) stars [81], but the r-process happens in violent astrophysical sites with high neutron flux, such as supernova [82], highly magnetized protoneutron star winds [83] or most likely, as it has been strongly suggested after the discovery of the gravitational wave event GW170817 [84], neutron star mergers [85, 86]. Under this high neutron flux, neutrons are captured on timescales faster than the β^- decay timescales. As a result, the r-process follows a less steep diagonal in the nuclide chart, as can be seen on the right side of Fig. 1.14, proceeding further away from the valley of stability than the s-process and producing nuclei much more neutron-rich. The r-process nucleosynthesis keeps moving diagonally

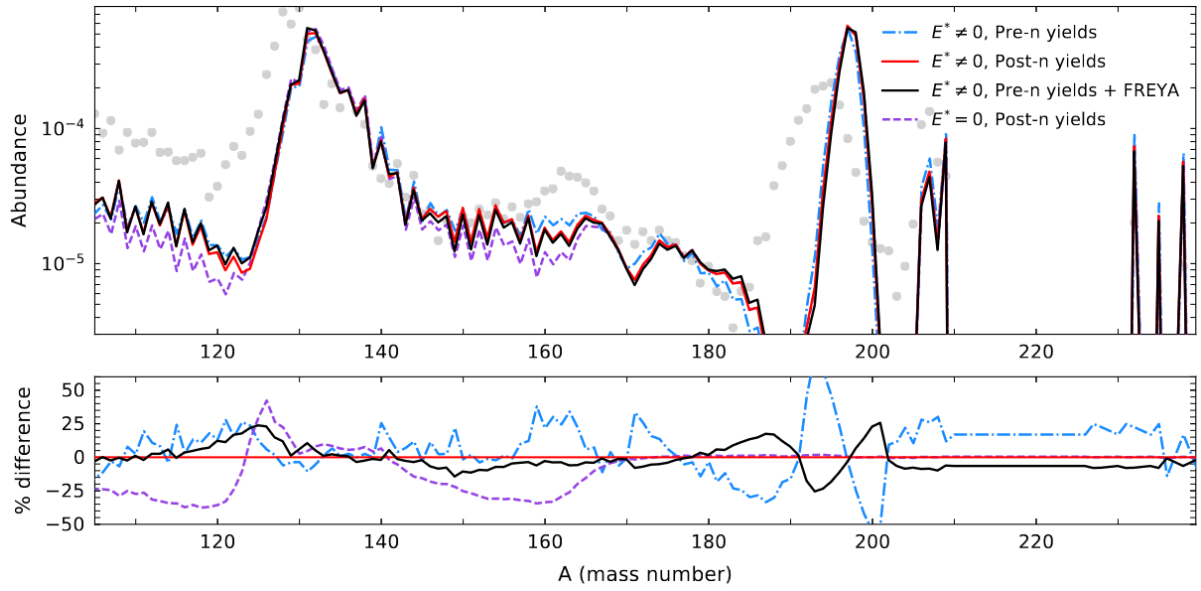

Figure 1.15: *Example of the r-process abundance sensitivity to the excitation energy. Blue, red, and purple lines were calculated with GEF 2016 fragment yields for respectively the cases of pre-neutron emission, post-neutron emission, and no excitation energy. Black lines are from FREYA considering pre-neutron yields. The upper panel shows abundances at 1 Gyr while the lower panel shows the percent of the difference between the different excitation energy considerations. Adapted with permission from Ref. [87]. Copyright (2019) by IOP Publishing Ltd.*

across the chart until the formed nuclei become too heavy and fission occurs. Therefore, fission limits the mass range of the r-process path, directly impacting the nuclide abundance. However, the fission products can be used as seed nuclei to start the r-process again [88]. To constrain theoretical models for the r-process and calculate abundances, accurate measurements of both fission barrier heights and fission yields are required. In addition, it has been recently demonstrated [87] that the effect of the primary fission fragments yield dependence on initial excitation energy should not be neglected since it has a strong influence on the final abundances of heavy elements (up to a 50% difference) as seen in Fig. 1.15.

Chapter 2

Methodology

This chapter will first introduce the experimental methodology, concerning the employed experimental techniques and the setup at GSI facilities. Then, it will give an insight into the software tools used for analyzing the experimental data and the theoretical models used to perform simulations.

2.1 Experimental methodology

In the experiment described in this work, two well-known experimental techniques usually used separately were merged to investigate the fission process: inverse kinematics and proton-induced knockout reactions. A specific reaction channel of interest is the knockout reaction in which a single proton is ripped from the nucleus, known as a quasi-free scattering reaction (p, 2p). The following subsections will review both techniques and the experimental R^3B setup configured to use them together.

2.1.1 The inverse kinematics technique

After the discovery of fission in 1938 and up to the late nineties, the main way to induce fission was through the technique known nowadays as direct kinematics, which consists of bombarding a target made of fissile material with light particles, originally neutrons. During those years, different experimental procedures were used to identify fission fragments. The first attempts consisted of radiochemical methods, where the target was dissolved and the fragments were chemically separated and analyzed using gamma spectroscopy. Among other problems, fission yields could not be accurately measured due to the difficulty of counting the total number of produced fissions [89]. After the sixties, ion beams substituted the conventional ion sources, and fission fragments were detected in-flight using ionization chambers, allowing to measure yields of the fragments before beta decay. During the seventies, several fission experiments were performed at the mass recoil spectrometer Lohengrin at the Institut Laue-Langevin using thermal-neutron induced reactions [90, 91]. The mass recoil spectrometers method

relies on the use of magnetic dipoles to deflect the ions according to their magnetic rigidity, providing a way to identify the ions in mass, according to the relation described in Eq. 2.1.

$$B\rho = \frac{A}{Z \cdot e} u\beta\gamma c \tag{2.1}$$

The variables described in Eq. 2.1 correspond to:
B = Dipole magnetic field [T]
ρ = Curvature radius of the ion inside the magnet [m]
A = Mass number of the ion [A]
Z = Atomic number of the ion [Z]
e = Elementary charge, $1.6021773 \times 10^{-19}$ [C]
u = Atomic mass unit [kg]
β = v/c, ratio of the ion's velocity and the speed of light in vacuum
γ = Relativistic Lorentz factor
c = Speed of light in vacuum, 299792458 [m/s]

Since the atomic number can be obtained from the energy loss in an ionization chamber (because the energy loss is proportional to the square root of the ionic charge of the ion), the bending radius from the tracking, and the velocity from both the time of flight and the path length, the mass identification could be obtained solving Eq. 2.1 for the mass number (A). Nevertheless, performing the experiments in direct kinematics only allowed for identifying the light fission fragments, because the heavy ones had such a small velocity they were decelerated inside the target, reaching the Bragg peak. Therefore, if any energy was deposited in the gas, it did not correlate with the square of the nuclear charge.
Around the nineties, the construction of heavy ion accelerators permitted the development of the inverse kinematics technique, which consists of accelerating the fissile material as a beam instead of using it as a target. Since fission takes place in flight, the two fission fragments are emitted in a narrow cone flying forward at very high velocities. This feature allows to overcome many drawbacks from the previous techniques, like the impossibility of measuring the too-slow heavy ions and the difficulty of detecting both fragments at the same time, since in direct kinematics they are emitted back-to-back in all directions. Also, it expanded the range of suitable isotopes to study fission, since in direct kinematics isotopes are constrained to be long-lived for being used as targets. As it was already mentioned in Sec. 1.1, the use of the inverse kinematics technique in combination with the R^3B setup, allowed for the first time to simultaneously identify both fission fragments in terms of their mass and atomic numbers event by event [7, 8].

2.1.2 Quasi-free (p, 2p) scattering

Quasi-free (p, 2p) scattering reactions were first introduced by Chamberlain and Segrè in 1952 [92]. While performing scattering experiments they observed that when lithium was bombarded with high-energy protons, pairs of protons were emitted in coincidence at approximately 90° to each other. They suggested that light nuclei could be 'transparent' enough to high-energy incident protons to allow observation of an almost free proton-proton scattering within the nucleus, which is why these reactions were coined as 'quasi-free'. What was happening, from a more microscopic point of view, was that the wavelength of the projectile proton is much smaller than the typical distances between nucleons inside the nucleus, and therefore, the reaction is very localized, not affecting the other nucleons. In addition to the two scattered protons, there is the recoiling nucleus, which is the original nucleus with a hole in the energy level previously occupied by the knocked-out proton. If the proton was bound to an energy level below the Fermi surface, the recoil would gain excitation energy corresponding to the energy of this state relative to the Fermi level. The two emitted protons contain information on the kinematics of the reaction, which gives access to the nuclear excitation spectrum of the recoil using the so-called 'missing mass method', which will be explained further down in this section.
The (p, 2p) reactions were widely used in direct kinematics to study the single-nucleon states of light nuclei [93]. Even though heavier nuclei have a larger nuclear density, and therefore the quasi-free cross sections are lower, (p, 2p) reactions have been proven to be a useful tool to study the single-particle structure of heavy nuclei too [94], as well as they have demonstrated effectiveness with light nuclear beams in inverse kinematics [95].

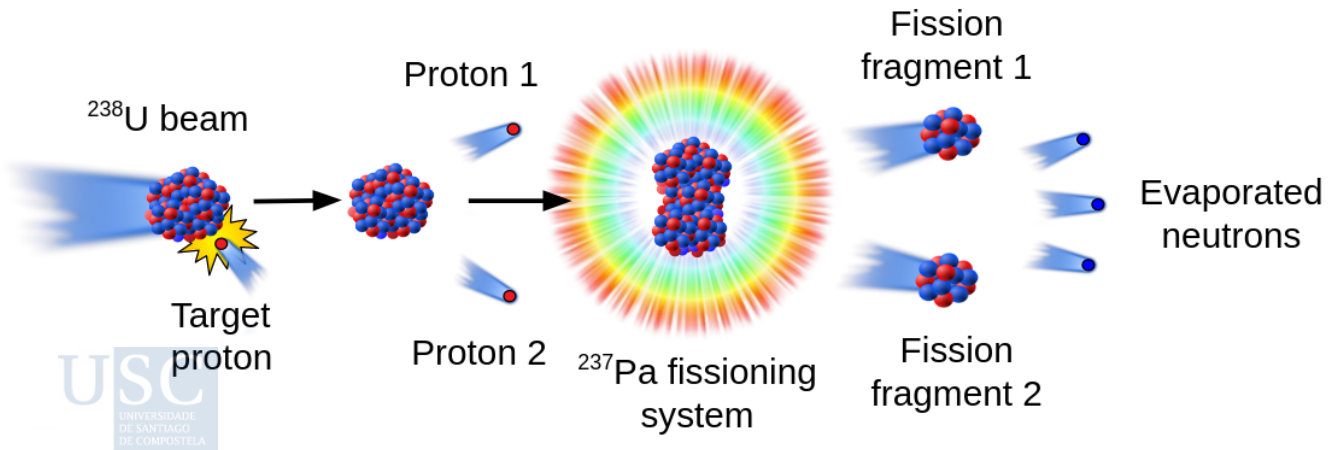

Figure 2.1: *Schematic representation of a quasi-free (p, 2p) reaction in inverse kinematics for a ^{238}U beam impinging onto a LH_2 target.*

The experiment performed in this work was the first of a proposed investigation line that would use (p, 2p) reactions to induce fission in inverse kinematics with radioactive-ion beams. In the experiment, the projectile was ^{238}U and impinged onto a LH_2 target. In quasi-free reactions, a proton is knocked out from the uranium nucleus, producing a heavy recoil nucleus (^{237}Pa) with sufficient excitation energy to eventually undergo fission (see Fig. 2.1). The goal of combining (p, 2p) and inverse kinematics is to achieve an almost complete characterization of the fission process, providing the excitation energy of the fissioning system using missing mass spectroscopy, and providing complete isotopic identification and TKE for the two fission fragments using state-of-the-art detectors of R^{3}B in inverse kinematics.

The missing mass method used to obtain the energy spectrum of the recoil starts by applying the conservation of the momentum in the reaction, as seen in Eq. 2.2. There, the four-momenta described are, from left to right, the one of the heavy-ion projectile (P_A), the one of the target proton (P_p), the momentum of the emitted protons 1 and 2 (P_{p1}, P_{p2}), and the momentum of the recoil nucleus (P_{A-1}).

$$\overrightarrow{P_A} + \overrightarrow{P_p} = \overrightarrow{P_{p1}} + \overrightarrow{P_{p2}} + \overrightarrow{P_{A-1}} \tag{2.2}$$

Since the goal is to obtain the excitation energy of the recoil, Eq. 2.2 is solved for $\overrightarrow{P_{A-1}}$ and the other momenta are expressed in 4-vector formalism, as it can be seen in Eq. 2.3. It has been considered that the projectile moves only in the forward direction (Z) with energy E_A and the proton target is at rest.

$$\begin{aligned}
\overrightarrow{P_{A-1}} &= \overrightarrow{P_A} + \overrightarrow{P_p} - \overrightarrow{P_{p1}} - \overrightarrow{P_{p2}} \\
\overrightarrow{P_{A-1}} &= \begin{pmatrix} E_A \\ 0 \\ 0 \\ P_{ZA}c \end{pmatrix} + \begin{pmatrix} m_pc^2 \\ 0 \\ 0 \\ 0 \end{pmatrix} - \begin{pmatrix} E_{p1} \\ P_{X1}c \\ P_{Y1}c \\ P_{Z1}c \end{pmatrix} - \begin{pmatrix} E_{p2} \\ P_{X2}c \\ P_{Y2}c \\ P_{Z2}c \end{pmatrix}
\end{aligned} \tag{2.3}$$

Calculating the Minkowski norm squared of a 4-vector gives a quantity invariant under Lorentz transformations, which in the case of a 4-momentum is called 'invariant mass', Eq. 2.4.

$$\begin{aligned}
I_{mass} &= \sqrt{\overrightarrow{P_{A-1}} \cdot \overrightarrow{P_{A-1}}} = \sqrt{(E_A + m_pc^2 - E_{p1} - E_{p2})^2 - (P_{X1}c + P_{X2}c)^2} \\
&\overline{-(P_{Y1}c + P_{Y2}c)^2 - (P_{Z1}c + P_{Z2}c - \sqrt{E_0^2 - m_p^2c^4})} = \sqrt{E_{A-1}^2 - P_{A-1}^2c^2}
\end{aligned} \tag{2.4}$$

As seen in Eq. 2.4, the invariant mass is the total energy of the recoil minus the energy from the momentum, leaving only the excitation energy and the rest mass. Therefore, the excitation energy can be obtained by subtracting the mass at rest, Eq. 2.5.

$$E^* = I_{mass} - m_{A-1}c^2 \tag{2.5}$$

Two key observables are needed for Eq. 2.4: the energies and momenta of the two outgoing protons (apart from the beam energy and the masses at rest). It is important to notice that not only quasi-free reactions will occur. After the knock-out, the outgoing protons could interact with the other nucleons inside the nucleus, which is known as re-scattering, and more than one nucleon could be knocked out from the nucleus. Consequently, to select quasi-free reactions, conditions should be applied on the opening angle between the two protons. In a non-relativistic frame, the opening angle between two particles of the same mass is always $\theta = 90°$, and the momentum vector lays in a plane. For a relativistic reaction, the Lorentz-boost shrinks the opening angle to approximately $\theta = 80°$. During the analysis, different conditions on the opening angle will be applied to study the dependence of the data with this observable.

2.1.3 Experimental setup at GSI Facilities

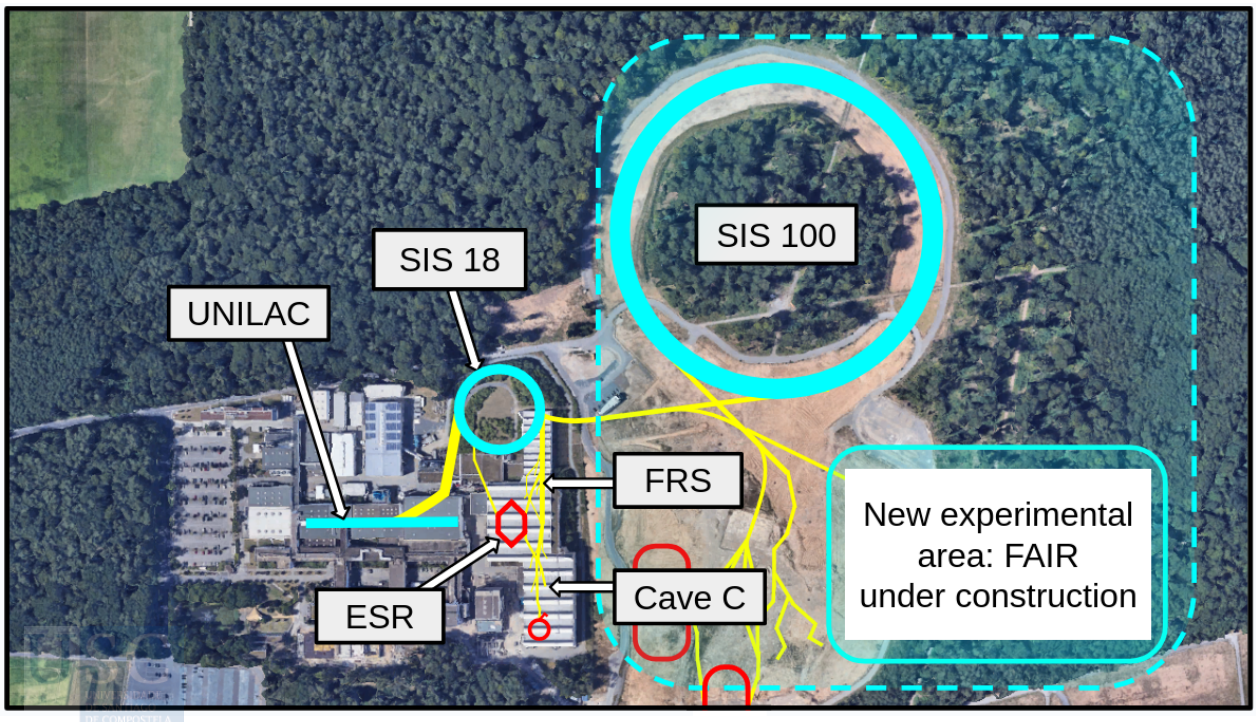

Figure 2.2: *Schematic view of the GSI-FAIR facility. Currently, two acceleration stages exist (UNILAC and SIS-18). Enclosed by the blue square, is the future accelerator (SIS-100) at FAIR.*

The experiment was performed at GSI in March 2021 (experiment ID: s455) using the aforementioned inverse kinematics technique together with the quasi-free (p, 2p) reactions. Primary beams of ^{238}U were delivered by the SIS18 synchrotron and guided to the Cave C experimental area (see Fig. 2.2) to impinge on a LH_2 target at 540 MeV/u to produce (p, 2p) reactions.

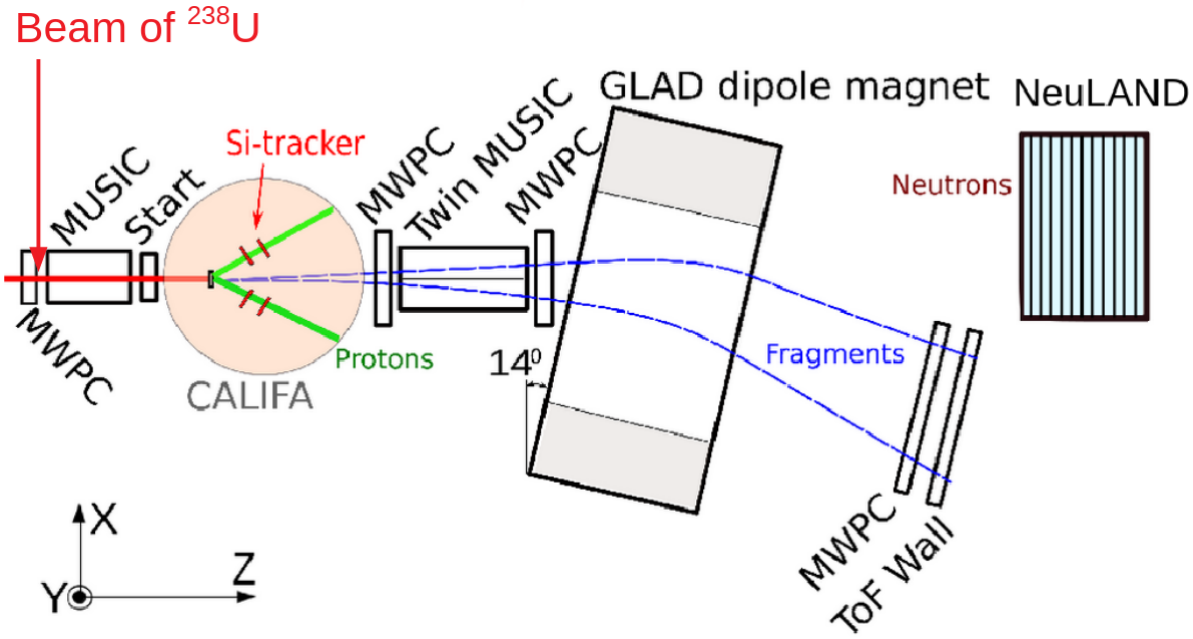

Figure 2.3: *Schematic view of the experimental setup installed at GSI.*

A schematic view of the entire setup is displayed in Fig. 2.3, and pictures of the real setup upstream and downstream of the magnet are displayed in Figs. 2.4 and 2.5, respectively. All the detectors named 'MWPCs' in this scheme are Multi-Wire-Proportional-Chambers that serve to track the trajectories of the particles along the setup. The 'MUSIC' detectors are MUlti-Sampling-Ionization-Chambers, used to obtain the charge of the ions by measuring their energy losses when they pass through the gas filling the chambers. The time of flight is measured by a plastic scintillator detector located before the target named 'Start' and a ToF-Wall composed of 28 plastic scintillators at the end of the setup.

Following the beam path, the first detectors when the beam enters the experimental area are a MWCP and a MUSIC (Triple Music) that serve to measure, respectively, the position and the charge of the primary beam. After the Triple MUSIC, the ^{238}U beam passes through the Start scintillator and enters the vacuum chamber, impinging onto the LH_2 target, where the (p, 2p) reaction takes place. To reconstruct the trajectory of the two protons, a silicon tracker is located

inside the chamber right after the target. The tracker includes two arms, each of them consisting of an array of three AMS-type [1] 0.3 mm thick double-sided silicon-strip detectors. To measure the energy of the protons, the CALIFA calorimeter [2] is placed surrounding the vacuum chamber. CALIFA consists of 1504 CsI(Tl) crystal scintillators covering a polar angular range between 22 and 90 degrees. After fission, the two fission fragments continue moving forward passing through the rest of the setup. The Twin MUSIC ionization chamber is designed with two independent ionization chambers, and those two are divided into two sections, each segmented into 16 anodes. This design allows to measure the atomic number of both fission fragments in coincidence. The two MWPCs, located upstream and downstream from the Twin MUSIC, serve to determine the horizontal angle of the fission fragments inside the Twin. Once inside the GLAD dipole, the fragments follow different trajectories according to their magnetic rigidities. After GLAD, another MWPC measures the final positions of the fragments and the ToF-Wall detector composed of 28 plastic scintillators provides the time of flight with respect to the start signal. Neutrons emitted from the fission fragments are detected in NeuLAND (New Large-Area Neutron Detector) [96], located 15m downstream from the target. Using the measurements of charge, time of flight and trajectory, the mass of the fission fragments can be obtained employing the $\Delta E - B\rho - ToF$ technique, allowing full isotopic identification.

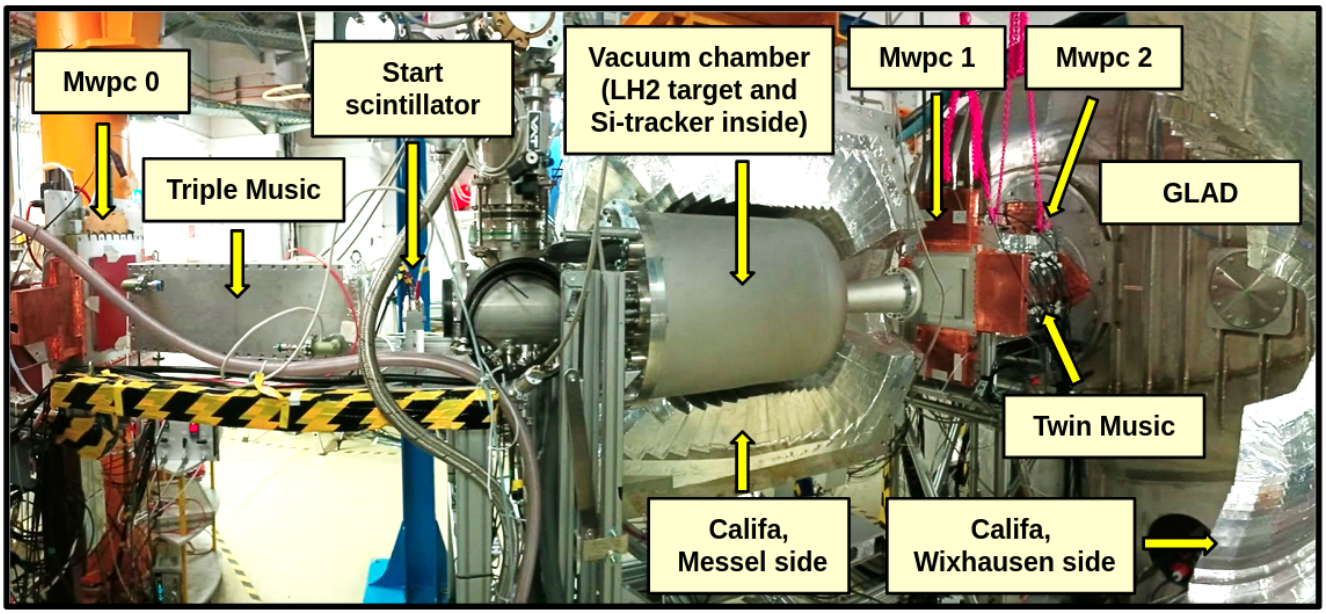

Figure 2.4: *Picture of the setup upstream of the magnet.*

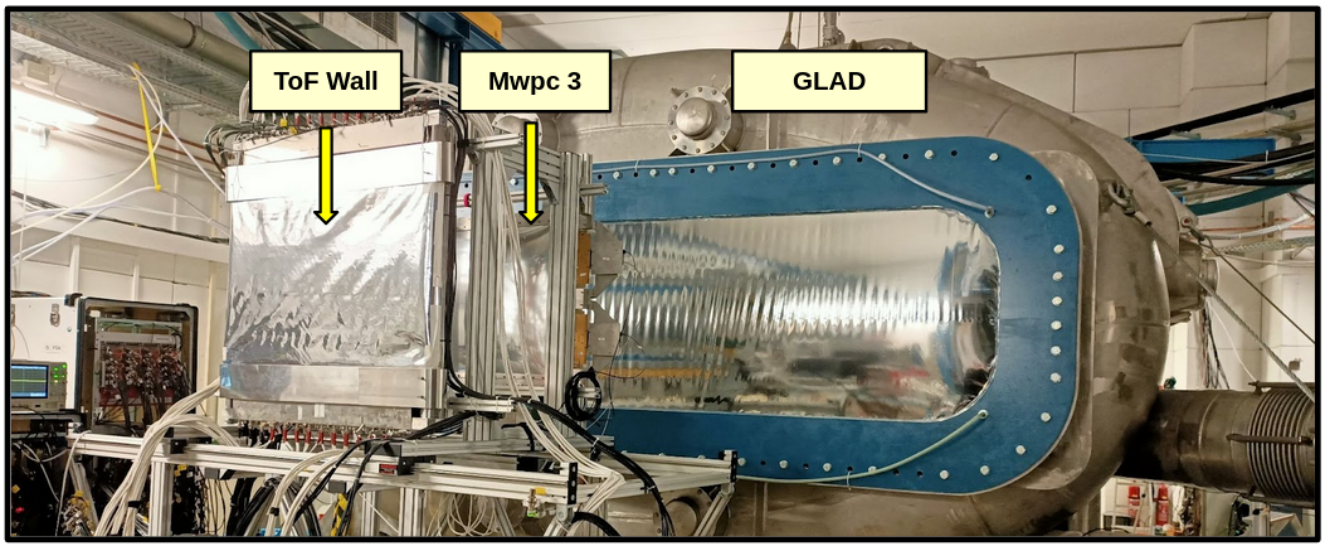

Figure 2.5: *Picture of the setup downstream the magnet.*

2.2 Analysis methodology

2.2.1 Data analysis software: R3BRoot

All the detector calibrations and data analysis explained in the following chapter were performed using the R3BRoot software [97]. The R3BRoot software is based on the FairRoot framework, written in the Root programming language. It has been specifically designed for the data analysis of the R3B (Reactions with Relativistic Radioactive Beams) nuclear physics experiments at the GSI-FAIR research center (Facility for Antiproton and Ion Research). R3BRoot has several classes for each detector in the collaboration designed to convert the raw data of that detector into calibrated data. The detector calibration passes through different stages until it is ready for analysis. Even though some detectors have intermediate levels, there exist 3 main levels of data:

- Pre-stage, the LMD data file: The DAQ stores the data into LMD files. This data must be converted into a root file to be read by the R3BRoot software. This task is not performed by R3BRoot but by the UCESB unpacker [98].
- Raw data: This is the root file produced by the unpacker. The detector's data is not in physical units yet, so the numbers associated with the measured physical magnitudes only indicate the amount of voltage read out by the electronics modules, known as 'channel' units. The R3BRoot class of each detector is designed to compare the obtained values in channels with the corresponding measure of a reference standard.
- Calibrated data: In this root file, the physical magnitudes have been associated with their corresponding physical units. Still, they usually need

an extra step that depends on each detector to be ready for the analysis. This step usually involves developing a final value of the physical magnitude by aligning, adding, or clustering different sectors of the detector

- Hit data: This is the last data level, ready for analysis.

  The detector's calibration explained in the next chapter was performed following this data level scheme. A great part of the work performed in this thesis work consisted of developing, improving, or adapting the existing code for this experiment.

2.2.2 Simulations software

All the simulations performed for this work were done with the Liège Intranuclear Cascade model (INCL) [99], used to simulate reactions of nucleons, pions, and light ions on nuclei, for incident energies ranging from a few tens of MeV to a few GeV. Intranuclear cascade models describe the reaction as a sequence or 'cascade' of independent binary collisions between the hadrons in the nucleus, which follow straight trajectories until they collide with another hadron or escape the nucleus surface. Typically, the INCL simulations are accompanied by another model used to simulate the de-excitation channels of the reaction products. A list of the theoretical models used in this work and their main features are presented:

- ABLA++
  - Fission decay width: described using the time-dependent solution of the Fokker-Planck equations shown in Eq. 1.12.
  - Particle evaporation: described by the Weisskopf-Ewing formalism [35] but modified with an approximation to calculate the distribution of orbital angular momentum during the emission of particles.
  - Level densities: The intrinsic level densities $\rho_{\mathrm{int}}(\mathrm{E})$ are corrected by vibrational $\mathrm{K_{vib}}(\mathrm{E})$ and rotational $\mathrm{K_{rot}}(\mathrm{E})$ factors, as seen in Eq. 2.6, since collective excitations can appear as bands built on the intrinsic single-particle levels.

$$\rho(\mathrm{E}) = \rho_{\mathrm{int}}(\mathrm{E})\mathrm{K_{vib}}(\mathrm{E})\mathrm{K_{rot}}(\mathrm{E}) \tag{2.6}$$

At low energies $\rho_{\mathrm{int}}(\mathrm{E})$ is the constant temperature formula, while for high energies, it is described using the Fermi-gas model [36], which

depends on the excitation energy E* and the angular momentum J as seen in Eq. 2.7

$$\rho_{\mathrm{int}}(\mathrm{E}^*,\mathrm{J}) = \frac{\mathrm{J}+1/2}{\sqrt{2\pi}\sigma^3}\mathrm{e}^{-\frac{\mathrm{J}(\mathrm{J}+1)}{2\sigma^2}}\frac{\sqrt{\pi}}{12}\frac{\mathrm{e}^{\mathrm{S}}}{\widetilde{\mathrm{a}}^{1/4}\mathrm{E}^{*5/4}} \tag{2.7}$$

The term σ^2 is the spin cut-off factor, related to the moment of inertia of the nucleus, S is the entropy and $\widetilde{\mathrm{a}} = \mathrm{E}^*/\mathrm{T}^2$ is the asymptotic level-density parameter in units of MeV^{-1}. It can be parameterized as shown in Eq. 2.8 as a function of the nucleus mass number A.

$$\widetilde{\mathrm{a}} = \alpha_{\mathrm{v}}\mathrm{A} + \alpha_{\mathrm{s}}\mathrm{B_s}\cdot\mathrm{A}^{2/3} \tag{2.8}$$

The parameters α_{v} and α_{s} are the coefficients that correspond respectively to the volume and surface components of the single-particle level densities and were proposed by Ignatyuk [100]. B_s is the ratio between the surface of the deformed and a spherical nucleus [101].

- Multifragmentation treatment: if the temperature of the fissioning system exceeds a mass-dependent threshold suggested in Ref. [102] the multifragmentation is triggered.
- Shell and pairing effects are taken into account in both the level densities calculation and the potential energy description.
- See Ref. [103] for further details about the ABLA model.

- GEMINI ++
  - Fission decay width: for the symmetric fission it is described by the Bohr-Wheeler formula, Eq. 1.10 and for asymmetric fission with the Moretto's formalism [104], which depends on the Z, A of the fission fragments as seen in Eq. 2.9.

$$\Gamma_{\mathrm{ZA}} = \int \frac{\rho_{\mathrm{sad}}}{\rho_{\mathrm{gs}}}\frac{\mathrm{E}^* - \mathrm{B_{ZA}}(\mathrm{J_{gs}}) - \epsilon}{2\pi}\mathrm{d}\epsilon \tag{2.9}$$

  - Particle evaporation: described by Hauser-Feshbach [105] formalism, which strictly conserves angular momentum but requires higher computational time than Weisskopf-Ewing.
  - Energy level densities are described using the Fermi-gas model [36] following the Bethe formula shown in Eq. 2.10, which depends on the excitation energy E* and the angular momentum J. U is the thermal excitation energy, and as shown in Eq. 2.11 it is defined as the

total excitation energy minus the energy component due to angular momentum E_{Yrast} as well as the pairing δP and shell δW corrections.

$$\rho(E^*,J) \approx (2J+1)\exp\left(2\sqrt{a(U(E^*),J)U}\right) \tag{2.10}$$

$$U = E^* - E_{Yrast}(J) - \delta P - \delta W \tag{2.11}$$

$$a(U) \propto \widetilde{a}(U) \tag{2.12}$$

The term $\widetilde{a}(U)$ in Eq. 2.12 is the so-called shell-smoothed level-density parameter. Since the fission decay width is $\Gamma_f \propto \rho_{sd}/\rho_{gs}$, the saddle-point level-density parameter $\widetilde{a}_{sd}$ was scaled by a constant factor to the corresponding ground-state level-density parameter $\widetilde{a}_{sd}$ as shown in Eq. 2.13 to account for the increased surface area of the saddle-point configuration.

$$\widetilde{a}_{sd}/\widetilde{a}_{gs} = 1.036 \tag{2.13}$$

- Multifragmentation treatment: nuclear de-excitation is treated uniquely in terms of binary decays, therefore, multifragmentation is not allowed on a single step. However, it can be produced by sequences of binary breakups .
- Shell and pairing effects are taken into account in the level densities calculation but not in the potential energy description.
- See [106] for further details about the GEMINI ++ model

• SMM

- Fission decay width: described by the Bohr-Wheeler formula, Eq. 1.10.
- Particle evaporation: described by the Weisskopf-Ewing formalism [35].
- Level densities are described using the Fermi-gas model [36] following the Bethe formula shown in Eq. 2.10.
- Multifragmentation treatment: SMM always enters a multifragmentation submodule and then it samples the resulting configuration according to its thermodynamical weight in a given freeze-out volume. This typically results in a multifragmentation threshold several MeVs lower than ABLA, see [107].
- SMM does not take into account shell effects, since this model was developed to describe multifragmentation, which happens at high excitation energies where shell effects are expected to be washed out [108].

Chapter 3

Data Analysis

This chapter will explain the operating principle of each detector in the setup and the steps followed to calibrate them. Calibration is the process of comparing the values obtained by a measuring instrument with the corresponding measurement of a reference standard. The data provided by the detectors is not in physical units as it comes from the electronic modules, so the numbers associated with the measured physical magnitudes only indicate the amount of voltage read out by the electronics, known as 'channel units'. These channel units need to be converted into physical magnitudes as charge, position, or time-of-flight, and each detector requires a different procedure.

This thesis work only concerns the analysis of the detectors involved in the fission fragment identification (MWPCs, ToF Wall, and Twin MUSIC). Therefore, the detectors involved in the (p, 2p) identification (CALIFA and AMS) will be only briefly introduced, further details on their calibration can be consulted in Ref. [109]. The chapter will start with the calibration description of each detector, and then it will go through the procedures followed to obtain the vertex of the reaction, the masses, and the cross sections.

3.1 MWPCs

The Multi Wire Proportional Chambers (MWPCs) are position detectors used to track the trajectories of charged particles. A picture of a MWPC detector without its cover can be seen in Fig. 3.1(left). In this experiment, 4 MWPCs were used in total along the setup, as shown in Fig. 2.3. The $MWPC_0$ is located at the entrance of Cave C to measure the beam position. The MWPCs 1 and 2 are placed, respectively, before and after the Twin MUSIC, since they have their vertical strips segmented in two sections, up and down, improving the position measurement. These two positions allow to calibrate the X position of the fission fragment inside the Twin and obtain the horizontal angle. The $MWPC_3$ is the largest MWPC of them all and is located behind GLAD. It serves to identify the fission fragments' position downstream from GLAD and also to calibrate the Y

position of the ToF Wall which is right behind it.

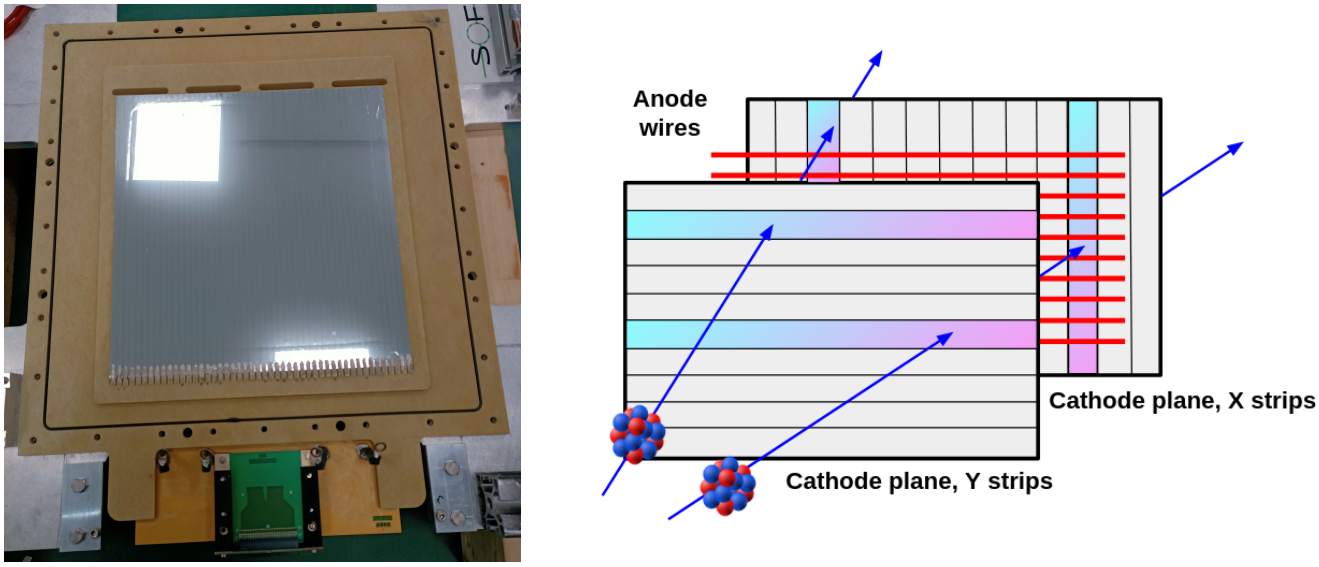

Figure 3.1: *Left: MWPC schematic drawing. Right: MWPC without its cover.*

These detectors are composed of two segmented planes facing each other and enclosing a thin volume of gas. Submerged in this gas, there is a third parallel plane made up of thin equally spaced wires, see Fig. 3.1(right). The inner wires are set to a high voltage, acting as anodes, while the two outer planes are grounded, serving as cathodes. Therefore, an electric field is created inside the active volume, between the planes and the central wires. When a charged particle traverses the detector it ionizes the gas and the produced electrons drift towards the wires, ionizing the counting gas in their path and provoking an avalanche. Finally, electrons are absorbed by the wires, leaving behind an amount of positive ions that induce a charge in the cathodes. These cathode planes are segmented into strips, one vertically and another horizontally, and the closer the avalanche region is to the strip, the higher the charge induced there. Consequently, the position of the strip from the vertical plane with the higher signal will be used to calculate the X coordinate of the fragment's position, and the one with the higher signal in the horizontal plane, the Y. Further technical information on the 4 MWPCs can be found in table 3.1.

3.1.1 Calibration

The calibration of the MWPCs starts by subtracting the average noise level, the so-called 'pedestal', from the data read out by each strip. The pedestals can be seen in Fig. 3.2(left), which shows the correlation of the measured charge (in channels) with the strip number for plane 1 of MWPC1. Each strip of the

MWPCs has a different pedestal due to the different lengths of the cables and the passage of the signal through the electronics.

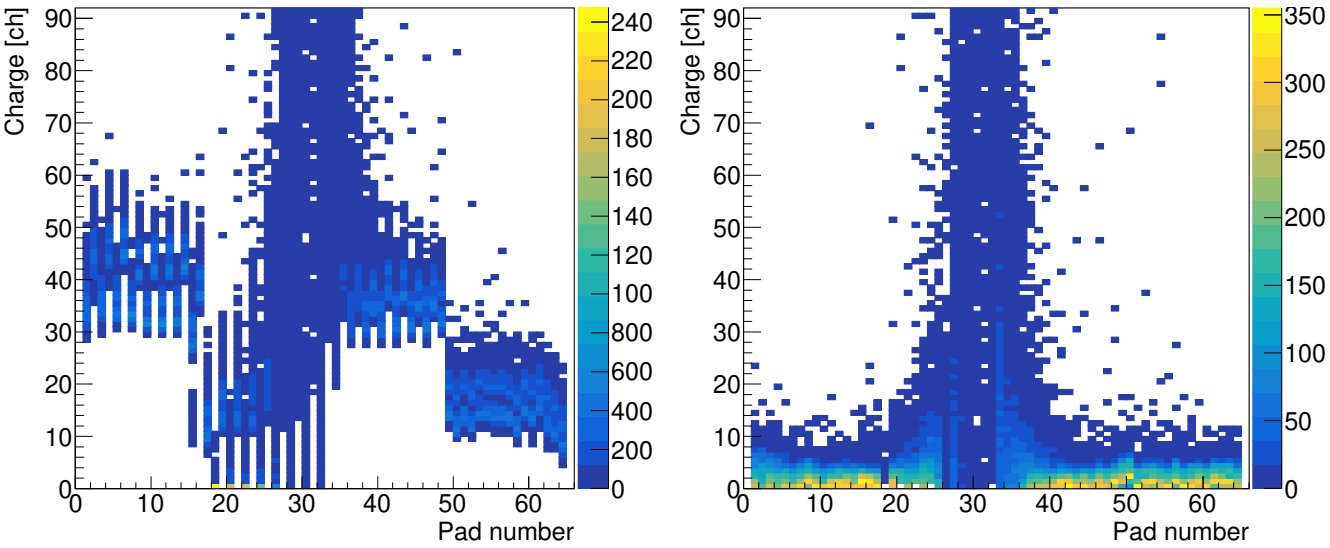

Figure 3.2: *MWPC1 plane 1. Left: Charge in channels per strip number before pedestal subtraction. Right: Charge in channels per strip number after pedestal subtraction.*

This noise signal has a Gaussian-like distribution, so a Gaussian fit can be performed for each strip to obtain the mean value $< \mathrm{Q}_{\mathrm{pedestal}} >$ and the width $\sigma_{\mathrm{pedestal}}$. Then, this pedestal is subtracted from the data as described in Eq. 3.1. In Fig. 3.2(right) the final result can be seen after the pedestals subtraction.

$$\mathrm{Q[ch]} = (\mathrm{Q} - < \mathrm{Q}_{\mathrm{pedestal}} > -3\sigma_{\mathrm{pedestal}})\mathrm{[ch]} \tag{3.1}$$

The fission fragment position calculation starts by calculating the position of the center of the $\mathrm{Pad}_{\mathrm{max}}$ (the strip that measured the maximum charge on its plane) from the center of the detector. This is shown in Eq. 3.2, where $\mathrm{nPad}_{\mathrm{max}}$ corresponds to the number of the strip which measured the maximum charge, 'w' is the width of the strip and 'size' is the length of the whole plane. Fig. 3.3 shows a schematic representation of the variables in the MWPC scheme. Note that in Eq. 3.2 the sign is negative because in the laboratory system of reference (looking downstream), the left side is positive, and the right side is negative.

$$\mathrm{xStrip}_{\mathrm{max}}\mathrm{[mm]} = -\mathrm{nStrip}_{\mathrm{max}}\mathrm{w} - \mathrm{w}/2 + \mathrm{size}/2 \tag{3.2}$$

To obtain the precise position of the fragment, the centroid of the charge distribution is calculated and added to the position of the center of the $\mathrm{Pad}_{\mathrm{max}}$, as it can be seen in Eq. 3.3, where a_2 is the position of the centroid. The most accurate function to represent this charge distribution is the 'hyperbolic squared secant' function, shown in Eq. 3.4, where x is the strip position and a_1 is the

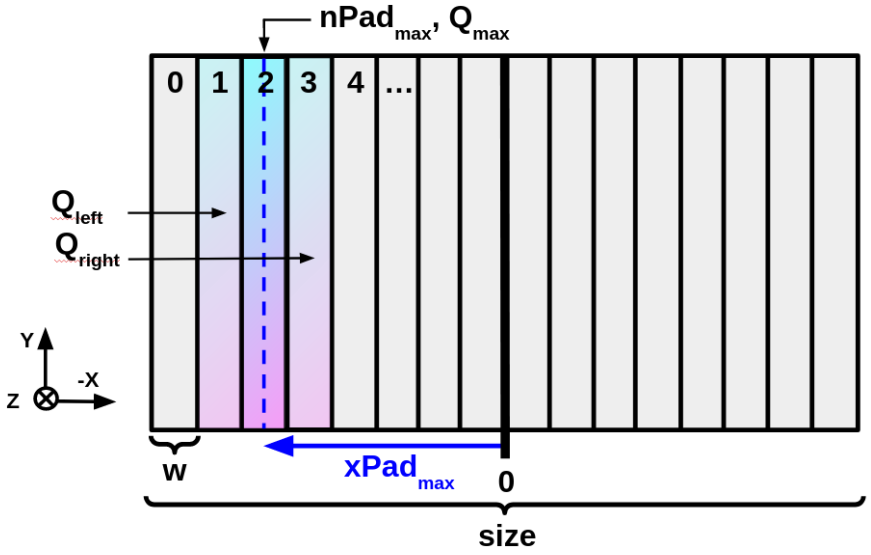

Figure 3.3: *MWPC position reconstruction illustration (note that the number of paddles in the figure is not the real number of paddles).*

amplitude of the distribution. Parameter a_3 stands for the quotient shown in Eq. 3.5, which takes into account the contribution of neighboring strips to the Pad_{max}. In the case of the X plane, these will be those on the right and left, and in the y plane those above and below. Once a_3 is known, the centroid position can be obtained as seen in Eq. 3.6.

$$x[mm] = xStrip_{max} - a_2 \tag{3.3}$$

$$Q(x) = \frac{a_1}{\cosh^2\left(\pi(x - a_2)/a_3\right)} \tag{3.4}$$

$$a_3 = \frac{\pi w}{\cosh^{-1}\left(0.5\left(\sqrt{Q_{max}/Q_{left}} + \sqrt{Q_{max}/Q_{right}}\right)\right)} \tag{3.5}$$

$$a_2 = \frac{a_3}{\pi}\tanh^{-1}\left(\frac{\sqrt{Q_{max}/Q_{left}} - \sqrt{Q_{max}/Q_{right}}}{2\sinh\left(\pi w/a_3\right)}\right) \tag{3.6}$$

Figure 3.4 shows the calibrated Y vs X positions correlation for the $MWPC_1$ in mm. Both MWPCs show a statistics accumulation in the centre due to the beam events, while the $MWPC_3$ has a couple of noisy channels. Another important detail is that the electronic cards of $MWPC_3$ were not well configured in the DAQ (Data Acquisition System) and therefore the distribution ends sharply at -300 and 300 mm.

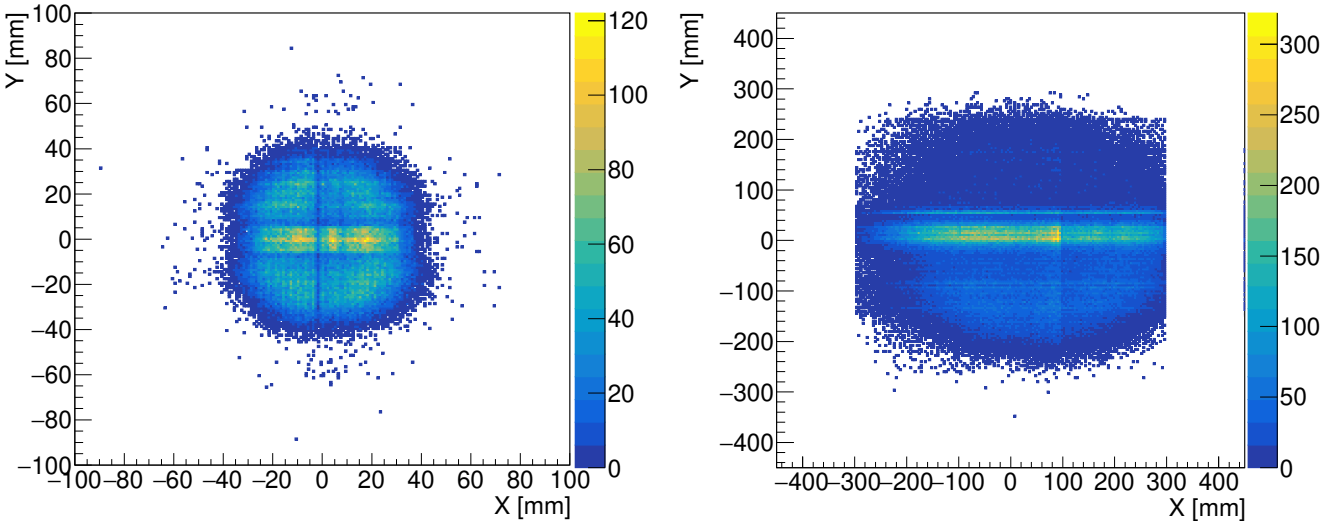

Figure 3.4: *Left: Y[mm] vs X[mm] for $MWPC_1$. Right: Y[mm] vs X[mm] for $MWPC_3$.*

MWPCs	Gas	Dimensions [mm^2]	Number of strips	Horizontal strips width [mm]	Vertical strips width [mm]
$MWPC_0$	Ar [84%] CO_2 [16%]	200x200	64 vertical 64 horizontal	3.125	3.125
$MWPC_1$		200x200	2x64 vertical 40 horizontal	5	3.125
$MWPC_2$		200x200	2x64 vertical 40 horizontal	5	3.125
$MWPC_3$		900x600	288 vertical 120 horizontal	3.125	3.125

Table 3.1: *MWPCs technical information.*

3.2 ToF Wall

The ToF Wall is a time-of-flight measurement detector consisting of 28 plastic scintillators ('paddles') placed vertically next to each other. They are made of a polymer in which a luminescent substance has been dissolved, so when an ionizing particle passes through the luminescent material, it absorbs the ion's energy and de-excites by emitting light. Each paddle has two photomultiplier tubes (PMTs) attached, one at the top and another at the bottom edge, as seen in the schematic drawing of Fig. 3.5(left). When the light emitted by the scintillator reaches the PMTs, electrons are ejected from its photocathode due to the photoelectric effect. The PMT tubes consist of a series of dynodes that accelerate and multiply these primary electrons and induce a significative current pulse in the electronics. The ToF Wall is placed at the end of the setup and works with another 'Start' plastic scintillator at the beginning, so the time difference between them can be measured. A picture of the ToF Wall at the end of the setup is displayed in Fig. 3.5(right).

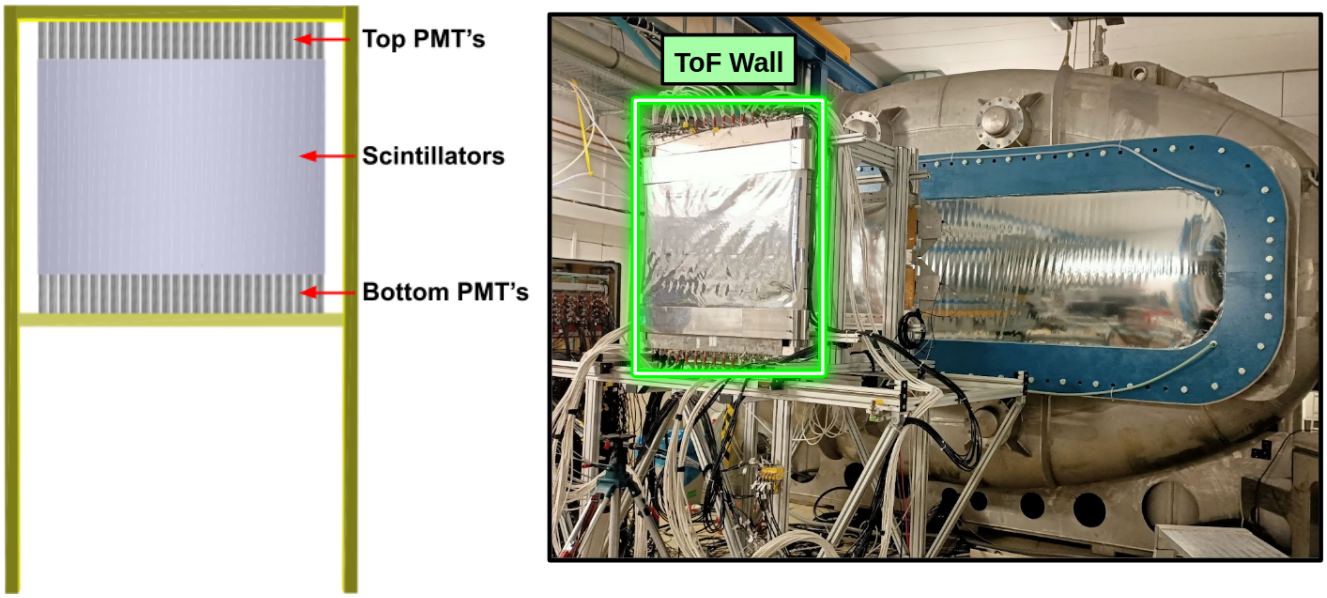

Figure 3.5: *Left: Tof Wall detector scheme. Right: ToF Wall detector in the setup.*

The VFTX modules measure the time of each PMT using an external clock signal as a reference (see Refs. [110, 111] for further details). Then, the raw time-of-flight for each plastic $\mathrm{ToF_{raw}(i)}$ is calculated as shown in Eq. 3.7, calculating the average time of the top and bottom PMTS of the 'ToFWall' and subtracting the average time of the left and right PMTS of the 'Start'.

$$\mathrm{ToF_{raw}(i)} = \frac{\mathrm{t^{ToFWall}_{Top\ Pmt}(i)} + \mathrm{t^{ToFWall}_{Bottom\ Pmt}(i)}}{2} - \frac{\mathrm{t^{Start}_{Left\ Pmt}} + \mathrm{t^{Start}_{Right\ Pmt}}}{2} \tag{3.7}$$

However, the different lengths of the cables used for each plastic and the time it takes signals to pass through the electronics produce delays between signals, causing a misalignment between the plastics. To estimate this offset, 28 sweep runs were performed displacing the ToF Wall, so that the $^{238}_{92}$U primary beam impinged on the center of each plastic and a raw time-of-flight was obtained for each, as seen in Fig. 3.6(left).

The offset for each plastic (the value to have it aligned with the other paddles) must be subtracted from the raw time-of-flight to have all the plastic signals aligned, as shown in Eq. 3.8. Still, this value must be converted into time units. To do so, the expected time-of-flight is obtained from a simulation and added at the end of Eq. 3.8. The final result of the time-of-flight calibration for each plastic is shown in Fig. 3.6(right).

$$\mathrm{ToF(i)} = \mathrm{ToF_{raw}(i)} - \mathrm{offset(i)} + \mathrm{ToF_{Sim}} \tag{3.8}$$

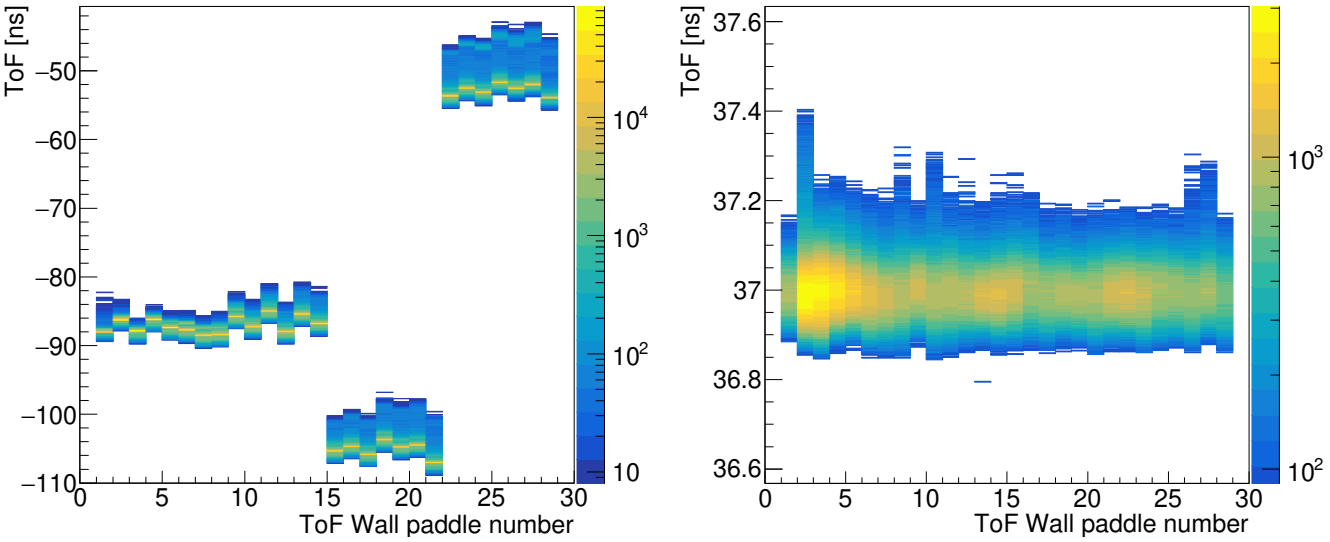

Figure 3.6: *ToF Wall calibration. Left: time-of-flight [ns] vs paddles, misaligned. Right:time-of-flight [ns] vs paddles, aligned.*

Another value derived from the ToF Wall is the vertical position of the fission fragments, since there is a time difference between the 2 signals reaching the PMTs, according to the height at which the plastic was hit. Then, a vertical position can be derived as $Y_{\text{ToF Wall}}\,[\text{ch}] = t_{\text{Top}}^{\text{ToFWall}} - t_{\text{Bottom}}^{\text{ToFWall}}$. This difference is in time units, but it can be converted into mm by correlating it with the Y MWPC_3 position (since it is placed right in front of the ToF Wall) and performing a linear fit, as shown in Fig.3.7(left). The fit is performed within the selected region, to avoid the statistics accumulation a little above Y=0 due to the noise from the paddles where the beam hits. The final result is shown in Fig. 3.7(right), with the Y ToF Wall position in mm.

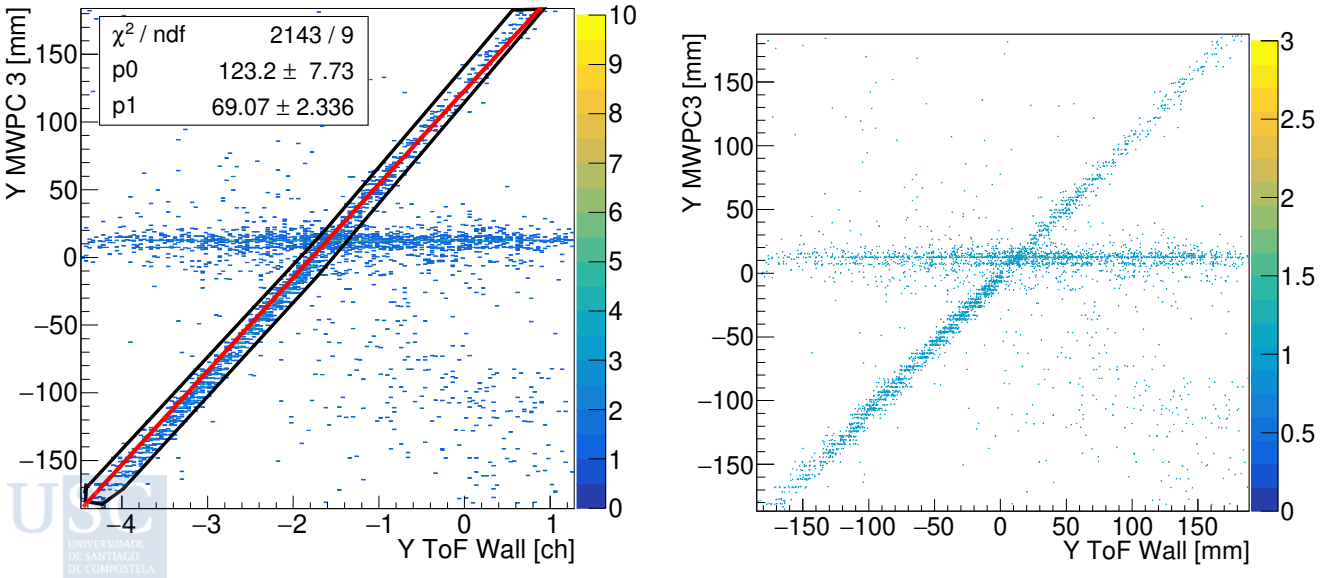

Figure 3.7: *Y MWPC3 and ToF Wall position correlation. Left: before calibration. Right: after calibration.*

In the same way, the X position in $MWPC_3$ must be correlated to the paddle number in Tof Wall, as it can be seen in Fig. 3.8, where the X $MWPC_3$ position distribution per paddle in the ToF Wall is displayed. The distribution covers a range between -300 to 300 mm since the outer $MWPC_3$ electronics cards were not well configured in the DAQ. Therefore, the paddles with data well correlated with $MWPC_3$ range from 7 to 28.

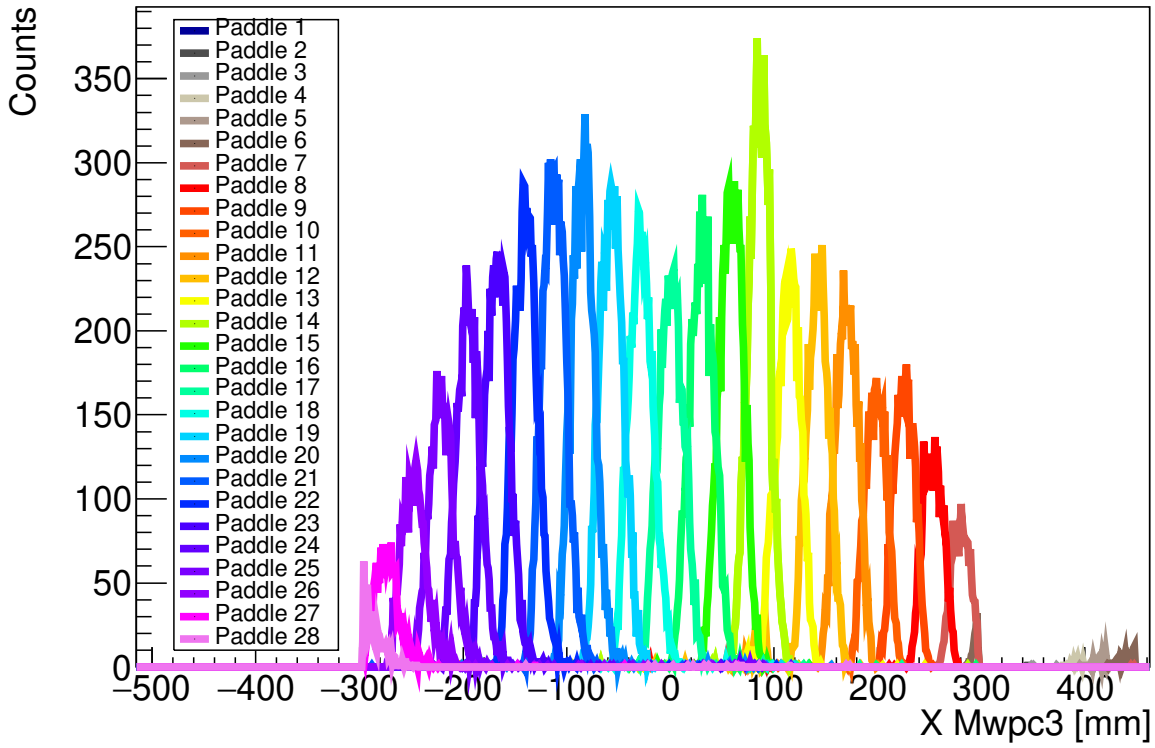

Figure 3.8: *Distribution of X coordinate from $MWPC_3$ per paddle of ToF Wall.*

The last but not least important function of the ToF Wall is to work as a fission trigger provider: when two signals from different plastics are read out by the electronics, it means that two fission fragments were produced. Further specifications of the ToF Wall are presented in Tab. 3.2.

Plastic scintillator type	EJ228
Number of plastic slats	28
Plastics dimensions	(30x600x5) mm^3
Active surface	(5x900x600)mm^3
PMTs	19 pairs of Hamamatsu 6533 in the center 9 pairs of Hamamatsu 10580 at the edges

Table 3.2: *ToF Wall detector technical information.*

3.3 Twin Music

The Twin MUSIC is a specific kind of the standard MUSIC (Multi-Sampling Ionization Chamber) detector used at GSI to measure the charge of ionized particles. A picture of this detector mounted in the setup is shown in Fig. 3.9.

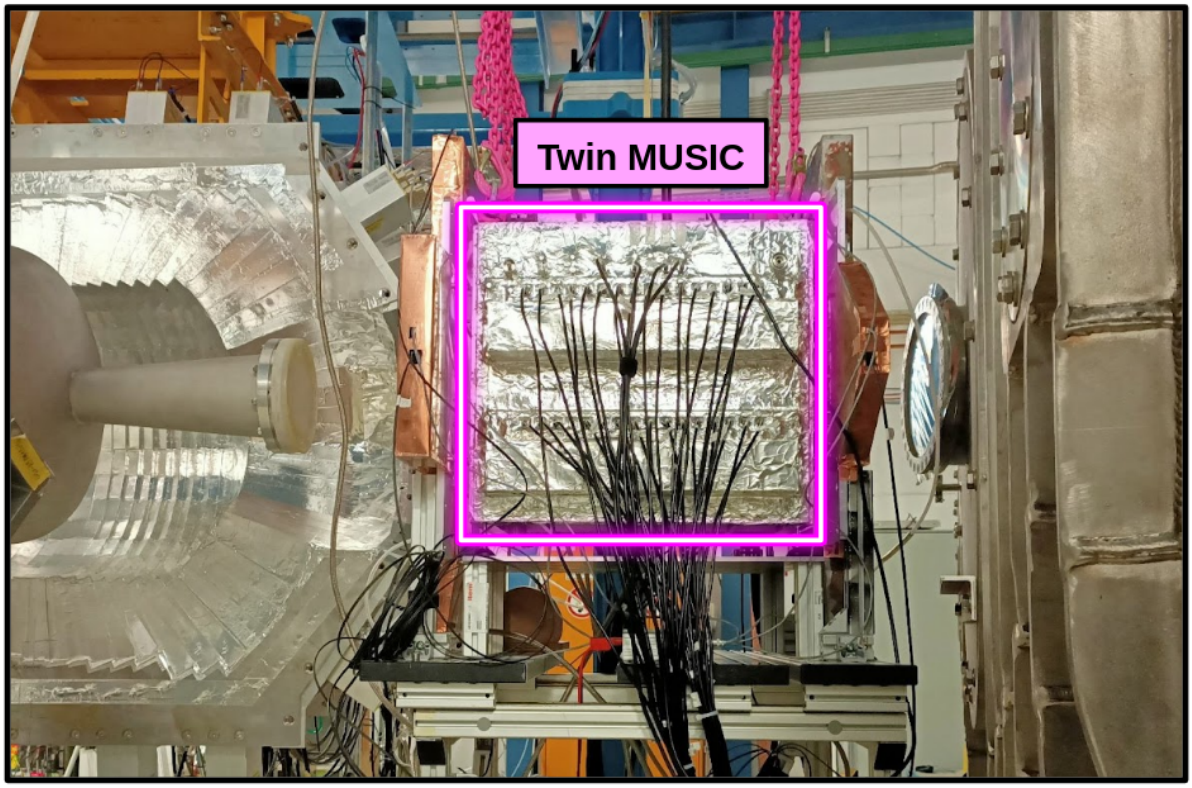

Figure 3.9: *Twin Music detector mounted in the beamline of the fission setup.*

The MUSICs operating principle is based on gas-filled volumes enclosed by parallel planes set to different voltages, one acting as a cathode and the other as an anode. When a charged particle passes through the chamber, the gas in its path is ionized. The electrons are attracted to the anode plane, and therefore they drift towards it. When they reach the anode plane, they induce a signal read out by the electronic modules whose amplitude is proportional to the number of electrons that arrive. Two observables can be extracted from the signals: the energy the ion transferred to the gas and the drift time it took for the electrons to reach the plane from where they were produced. The first one serves to deduce the atomic number of the fission fragments since the energy loss of the ion is proportional to the square root of its ionic charge. The drift time allows for a measurement of the X position of the ion inside the Twin, which can be used afterwards to extract the horizontal angle of the fragment's trajectory. This particular MUSIC, the Twin, differs from the others of its type in that it is a double ionization chamber, meaning that two ionization chambers are put

together sharing a central cathode plane, as it can be seen in Fig. 3.10(left). Therefore, the anode planes are located close to the external right and left edges of the detector and separate each one 113 mm from the central cathode, with a frisch grid placed very close to the anode. The advantage of this configuration is that it allows the measurement of two charged particles independently at the same time, which is exactly what is needed for fission reactions. Due to the kinematics of the fission, the two particles will pass through different sections of the Twin and the charge can be measured for both of them simultaneously but independently.

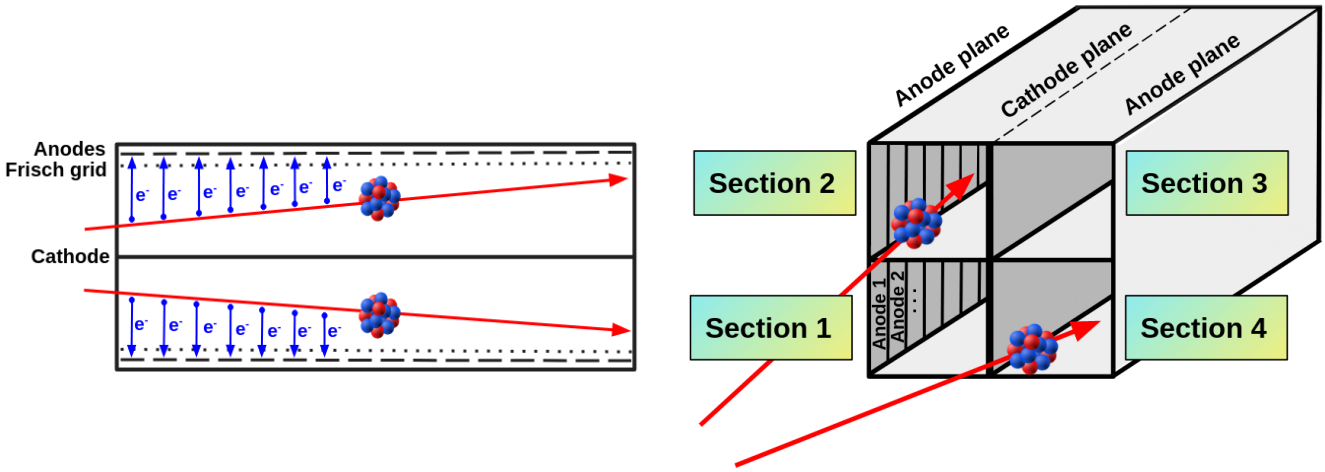

Figure 3.10: *Twin MUSIC schematic representations. Left: Top view. Right: Perspective view.*

Another interesting feature is that each anode plane is also segmented in two parts, up and down relative to the beam line (see Fig. 3.10(right)). Hence, it is as if the Twin MUSIC consisted of four ionization chambers, allowing to better identify the fission fragment. Each part of the anode plane counts with 16 effective anodes to collect the electrons. All the technical information of the detector is provided in table 3.3.

Gas composition	CH_4 [79%], Ar [20%] and CO_2 [1%]
Gas pressure	1 atm
Distance between cathode and frisch grid	110 mm
Distance between anode and frisch grid	3 mm
Active volume	2x(110x220x400) mm^3
Outbox dimension	430x480x550 mm^3

Table 3.3: *Twin MUSIC detector technical information.*

3.3.1 Position calibration

The Twin calibration process starts with the position calibration from channel units to mm. This information is used to reconstruct the horizontal angle of the fission fragment inside the Twin and to correct the dependence of the energy loss in this observable.

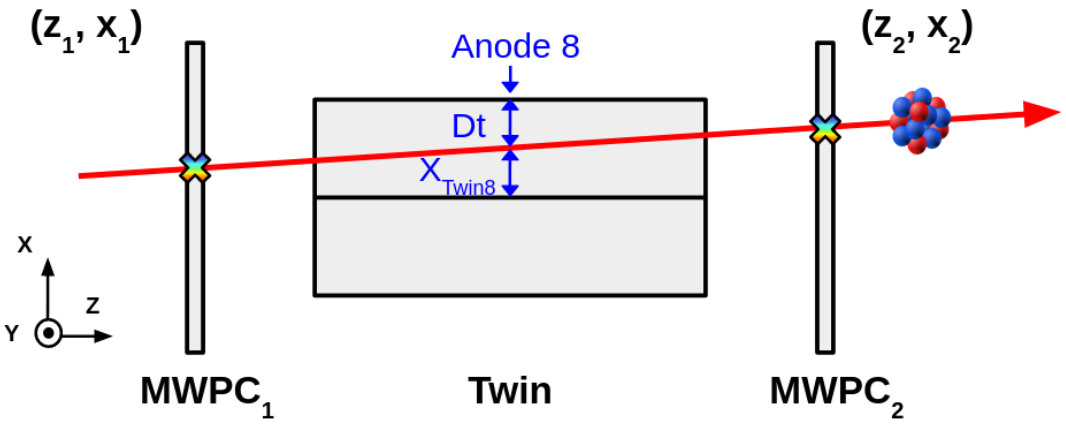

Figure 3.11: *Scheme of the Twin Music and $MWPC_{1,2}$.*

The calibration process can be performed thanks to the MWPCs 1 and 2, which are located right before and after the entrance and exit windows of the Twin Music. In this way, a linear fit between the position of the fission fragment in the $MWPC_1$ (z_1,x_1) and the $MWPC_2$ (z_2,x_2) shown in Fig. 3.11 can be performed to obtain a linear equation for the trajectory of the fragment inside the chamber.

Once the trajectory is known, a first approach for the X position of the fission fragment in the Twin is obtained by evaluating the equation of the trajectory for the Z position of each anode. Fig. 3.12(left) shows the correlation between this X position in mm calculated using the fit from the MWPCs and the drift time from the Twin in channels.

A linear fit is performed in Fig. 3.12(left) to obtain an equation to transform the drift time given by the Twin into mm for each anode. Fit residuals for every anode in each section are aligned and centered at zero, as shown in Fig. 3.12(right). Results for the X positions of the fragments inside the Twin for the anode 8 of each section are portrayed in Fig. 3.13(left). The distribution extends approximately from -60 to 80 mm. It is slightly shifted to the left side (negative side) since the unreacted beam was hitting the left side.

Finally, once the X positions inside the Twin are known, the horizontal angle can be calculated as shown in Eq. 3.9, where Z_{target} is the position in Z of the target in the setup.

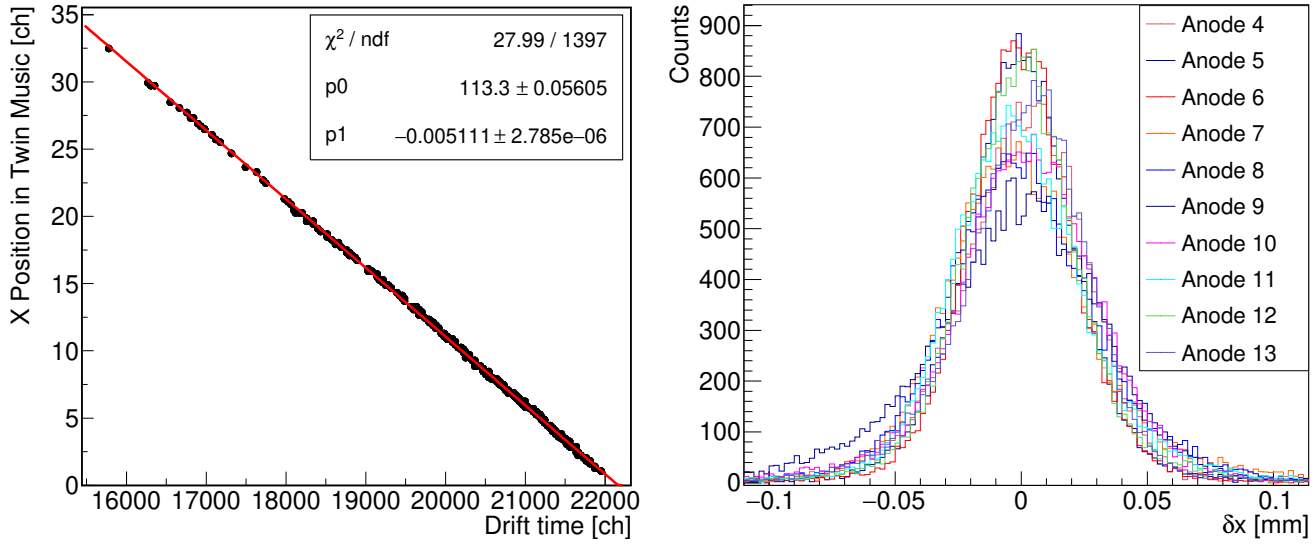

Figure 3.12: *Drift time calibration. Left: Correlation between X position in mm from fit and drift time, Section 1, anode 8. Right: Fit residuals for all section 1 anodes.*

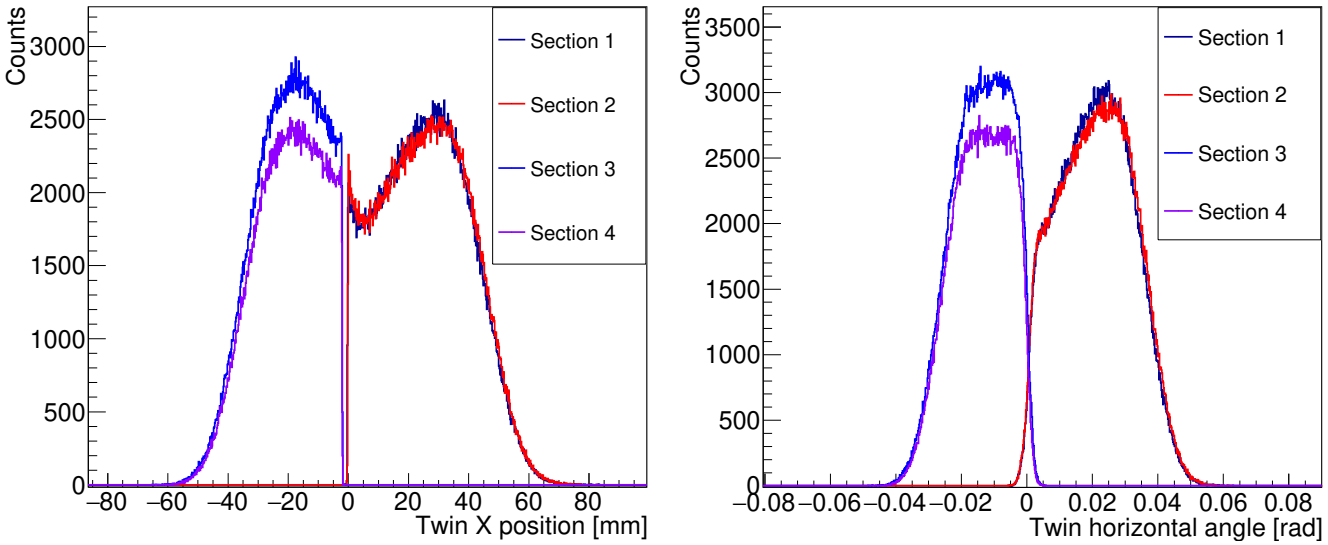

Figure 3.13: *Left:Twin Music X position distribution for the anode 8 of each section. Right: Twin Music horizontal angle distribution for the anode 8 of each section.*

$$\theta_{\text{Twin}} = \text{arctg}\left(\frac{\text{X}_{\text{Twin}}}{\text{Z}_{\text{target}}}\right) \tag{3.9}$$

The distribution of the horizontal angle measured by the Twin can be seen in Fig. 3.13(right), extending from approximately -40 to 50 mrad and peaking around ± 5 mrad, slightly shifted to the left because of the beam position.

3.3.2 Atomic number calibration

The atomic number calibration process of the Twin MUSIC has been divided into 4 steps within this section. The first corresponds to the alignment of the energy signals of the anodes for each Twin section, to have all the anodes at the same energy level. The second corresponds to the fission fragments sorting, where the fission fragments measured downstream from the magnet are identified with those upstream. The following step consists of correcting dependencies of the Twin energy loss on two variables (ToF and drift time). The last step corresponds to the final atomic charge identification.

Anodes charge alignment

Since the Twin pre-amplifiers have different gains to convert the number of electrons into voltage, the amplitude of the signals obtained for each are not absolute values. To have absolute values, the calibration starts with the anode signal alignment. This is accomplished by correlating the energy spectra of each anode with a reference anode on its section and performing a linear fit, as shown in Fig. 3.14. In this analysis, the anodes number 8 of each section were chosen as reference, since they are located in the middle of the section and thus free of edge effects. For the same reason, the three first and last anodes of each section were discarded from the analysis.

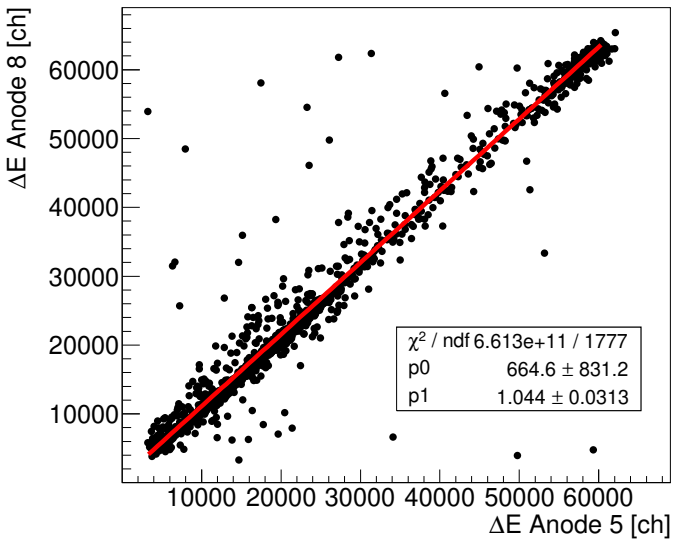

Figure 3.14: *Energy loss correlation of the anodes 8 and 5.*

Using the linear fit from Fig. 3.14 the energy signal of each anode is aligned to the energy signal of the reference anode. The results of the alignment process are displayed in Fig. 3.15. In this example, it can be seen in Fig. 3.15 (left) how before the energy alignment the anode 6 peaked at a different energy than the

rest of the anodes. In 3.15 (right) all energies are well-aligned. This alignment procedure and also the following corrections have been applied independently on the 4 different sections of the Twin Music.

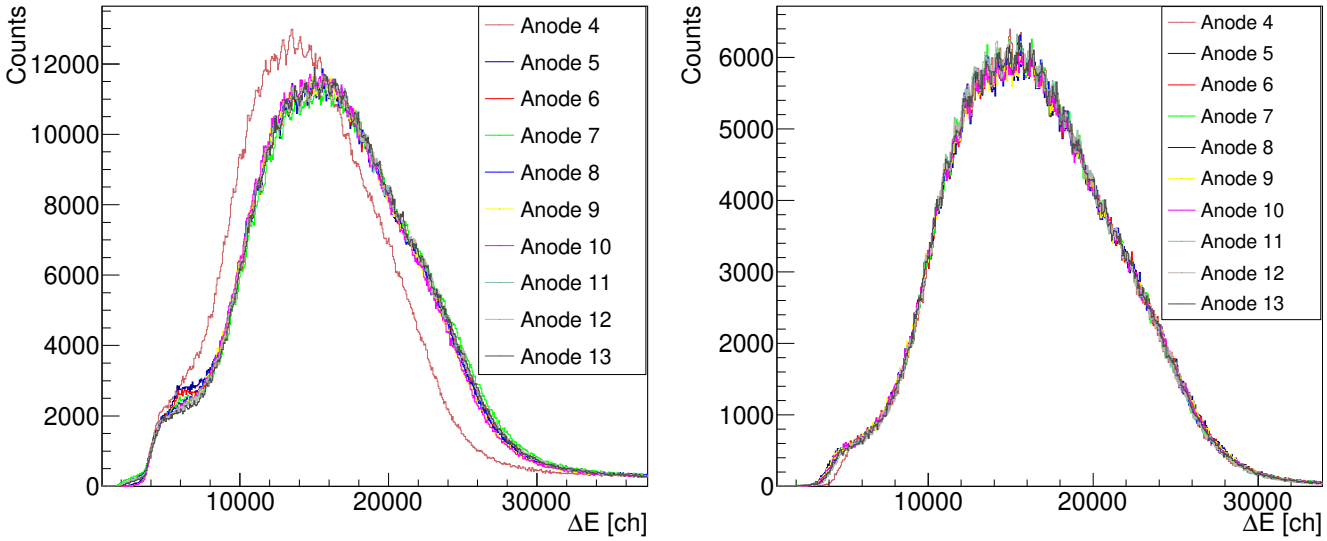

Figure 3.15: *Energy loss distributions for each anode in section 3 of the Twin Music, before (left) and after (right) the energy alignment.*

Once all anodes are aligned, the total energy loss of each fission fragment in a Twin section is computed as the sum of all the energy losses measured in each anode that provides a signal and divided by the number of those anodes. This is shown in Eq. 3.10, where ΔE_j is the energy loss measured per anode j, n is the number of anodes with signal and ΔE_i is the total energy of section i.

$$\Delta E_i = \frac{\sum_{j=1}^{n} \Delta E_j}{n} \tag{3.10}$$

Fig 3.16 shows the energy correlation for the fission fragments inside the Twin. It shows 4 different accumulations of statistics marked in the figure. The events enclosed in the red triangle correspond to the fission fragments, therefore this triangle will be selected for studying the fission. The events on the diagonal enclosed with a green rectangle correspond to events where the beam went through two sections up and down on the same side of the Twin. While studying beam events, the Twin MUSIC must be calibrated differently, calculating the ΔE_i for 2 sides of the Twin instead of 4 sections (adding the energy of the anodes up and down). The events enclosed within violet rectangles correspond to beam events mixed with fission fragments or fragmentation products (pile-up events). Finally, the orange circle corresponds to beam events passing through the two sides of the Twin MUSIC. To perform the

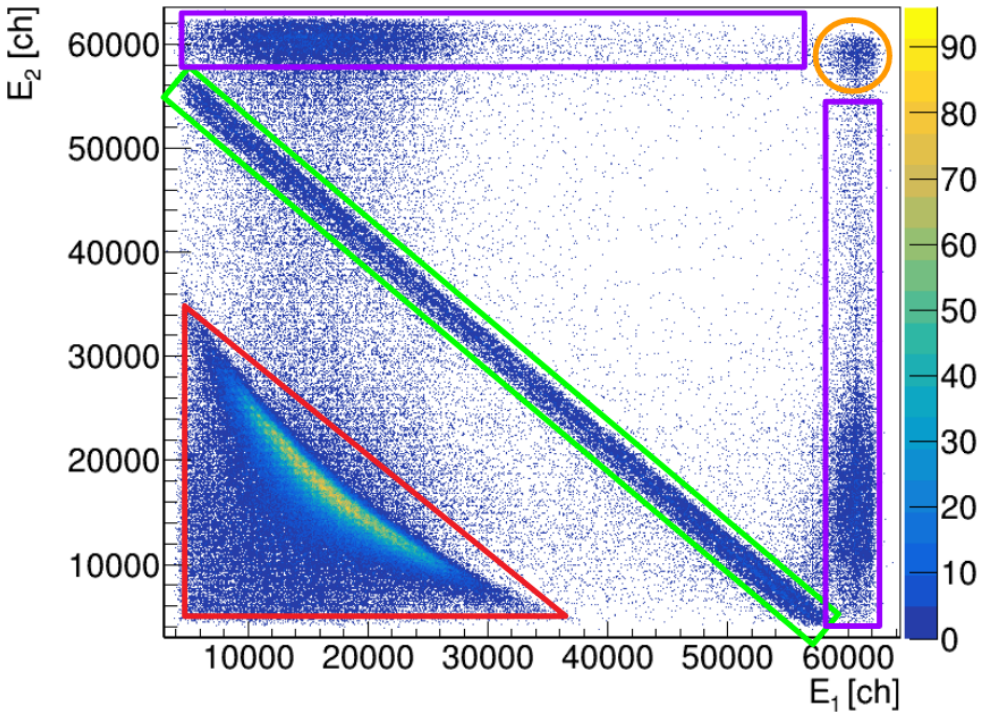

Figure 3.16: *Energy loss correlation for two fission fragments in the Twin MUSIC.*

following calibration steps, only the events within the red triangle will be selected.

Fission fragments sorting

A crucial part of the analysis is to correctly assign the downstream variables (time-of-flight from Tof Wall and the (X, Y) positions from $MWPC_3$) to each fission fragment detected upstream in the Twin MUSIC. The fission fragments sorting is also needed to obtain the masses later since for applying Eq. 2.1 the tracking of each fission fragment along the setup is required. The assignment of the downstream variables will be done differently depending on which was the situation upstream in the Twin MUSIC, distinguishing between the 6 possible cases displayed in Fig. 3.17.

Because of the kinematics of the reaction, 2 fission fragments will not pass through the same Twin section, therefore that case is not considered. What could happen though, is that an ion traverses two sections of the Twin during its trajectory along the detector (more likely up and down rather than left and right since those are separated by the cathode). This case must be treated when selecting beam events, but not when selecting fission fragments, since they are difficult to differentiate from events where two uranium ions reacted in the target and produced pile-up. Therefore, those cases are discarded, and only the 6 cases previously mentioned will be analyzed. The assignment will be as follows:

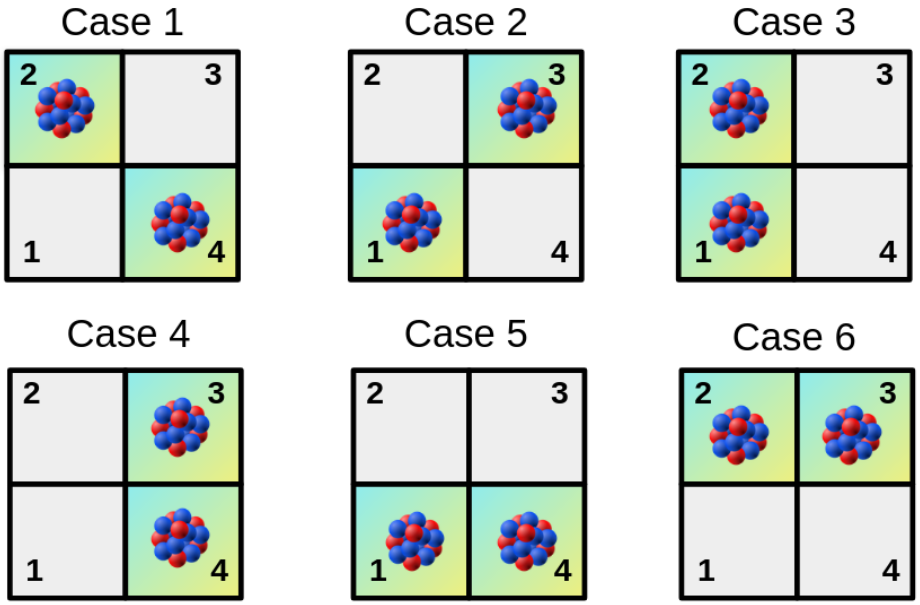

Figure 3.17: *Schematic representation of the front view of the Twin MUSIC, displaying the 6 possible cases for fission fragments distribution between the 4 sections.*

- Cases 1,2,3 and 4: the assignment of the downstream variables to the upstream fragments will be done depending on the Y coordinate. This is the ideal situation since ions are deflected inside the magnet in the XZ plane.
  - Fragments that were in the lower sections of the Twin will be assigned to those that were lower downstream.
  - Fragments that were in the upper sections of the Twin will be assigned to those that were higher downstream.
- Cases 5 and 6: here it is not possible to assignate according to Y position, since both fragments are up or down. Therefore, the assignment is done depending on the X coordinate.
  - Fragments that were in the left sections of the Twin will be assigned to those that were more to the left downstream.
  - Fragments that were in the right sections of the Twin will be assigned to those that were more to the right downstream.

Despite all of the 6 displayed cases being considered, cases 1 and 2 are the most likely. Cases 3 and 4 represent 18% of the fission events and cases 5 and 6 only a 6%. Fig. 3.18 shows 6 reconstruction examples, one for each possible combination.

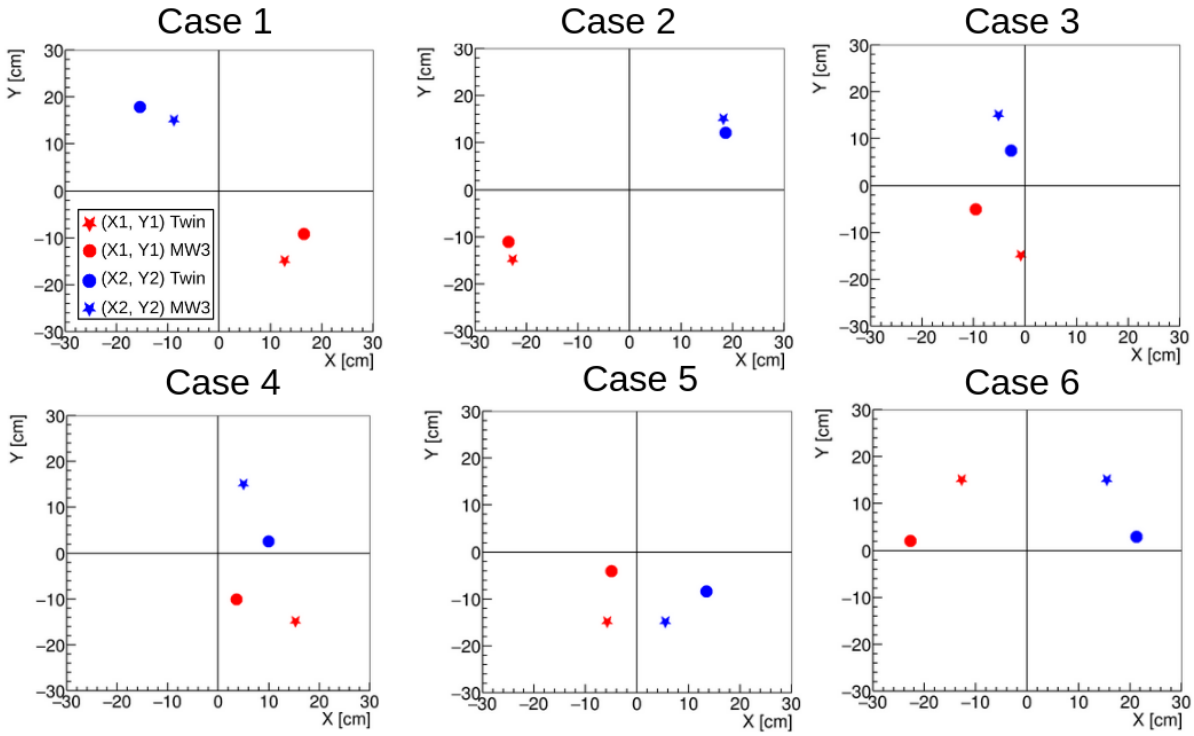

Figure 3.18: *Assignation example for each case. Since Twin MUSIC does not measure the Y position, it has been located at -15cm for lower sections and at 15cm for upper sections only for this illustration.*

Energy loss corrections

The energy must be corrected by its dependence on the velocity of the fission fragments and the drift time of the electrons to achieve the best possible resolution.

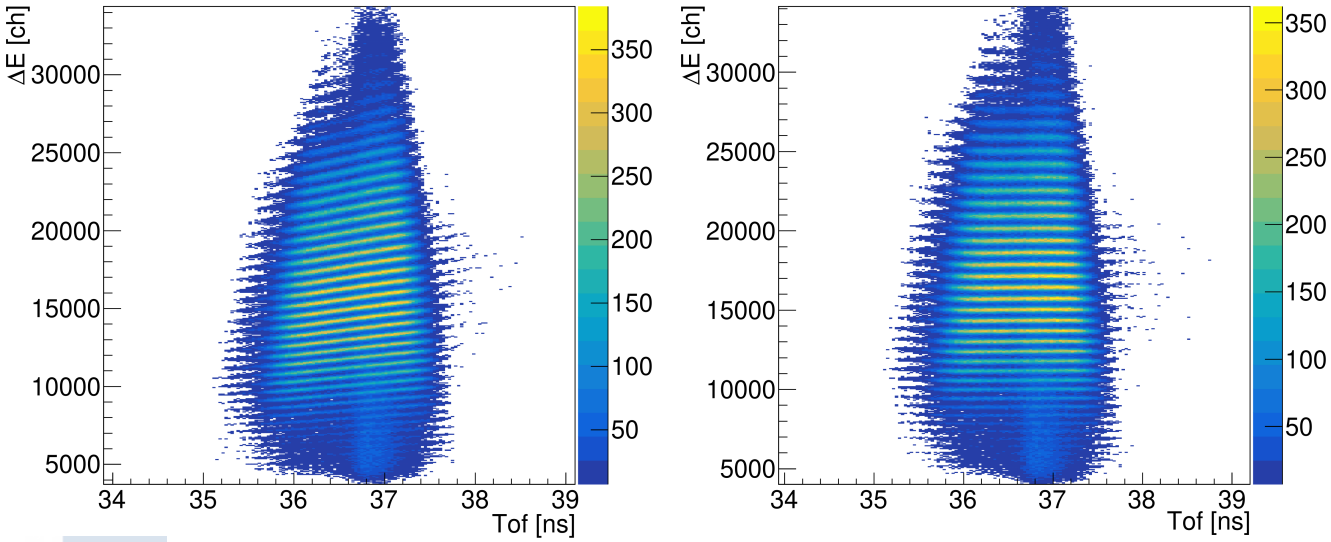

Figure 3.19: *Energy loss in section 1 of the Twin Music vs. the time-of-flight of the fission fragments, before (left) and after (right) the dependency correction.*

The amount of energy an ion deposits in a certain material has a strong

quadratic inverse dependence on its velocity, as seen in the Bethe-Bloch formula. Thus, the higher the velocity of the ion, the lower the energy deposition in the Twin gas. This effect is revealed when correlating the energy loss in the Twin with the ion's velocity. However, the calculation of the velocity requires the reconstruction of the length of the trajectory of the fission fragment and this will be done later in the analysis. Therefore, the correction is done by correlating the energy loss with the time-of-flight, as shown in Fig. 3.19(left).

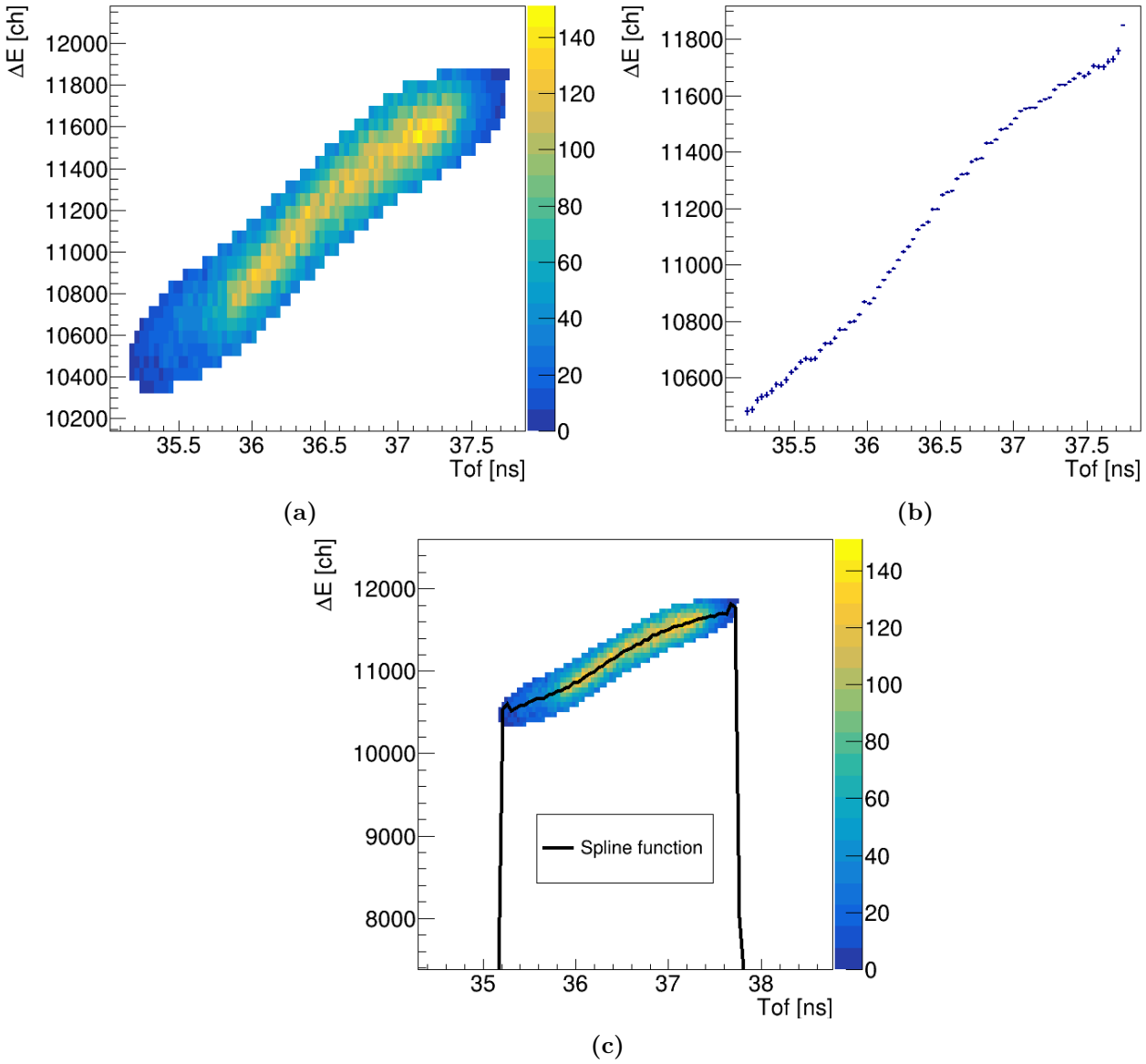

Figure 3.20: *Stages of the ToF dependency correction. (a) Cut selecting a charge. (b) Profile in x for the selected cut. (c) Spline function evaluated in the data within the cut.*

Each of the horizontal lines in Fig. 3.19(left) corresponds to a different fission fragment atomic number, and it can be seen for each line how energy increases with the increase in time-of-flight: the higher the time-of-flight, the lower the velocity, and thus, the higher the amount of energy deposited by the ion. To

correct this dependence, polynomials of a higher order than a straight line are required to reproduce the behaviour better. In this analysis, another kind of function has been used to correct these dependencies: a spline function. A spline is a piecewise-defined function, where each piece is defined by a polynomial. At the joints (usually referred to as 'knots') the functions must have the same value of the first and second derivatives, which can only be achieved if the polynomials are of third order or higher.

The first step to start correcting is to define a cut in Fig. 3.19(left) for one of the charges, see Fig. 3.20(a). Then, a profile in x is performed within the cut. The profile function calculates the mean value of the y variable (charge in channels) for each bin in x (ToF), as displayed in Fig. 3.20(b). This profile function is used as input to calculate the spline, which is shown in Fig. 3.20(c). Then, the data is corrected using Eq. 3.11, where ΔE_{mean} is the average deposited energy for the selected charge, and Spline(ToF) is the evaluation of the spline function for the ToF values within the cut. The result of the correction can be seen in Fig. 3.19 (right).

$$\Delta E_{corr} = \Delta E_{mean} \frac{\Delta E}{\text{Spline(ToF)}} \tag{3.11}$$

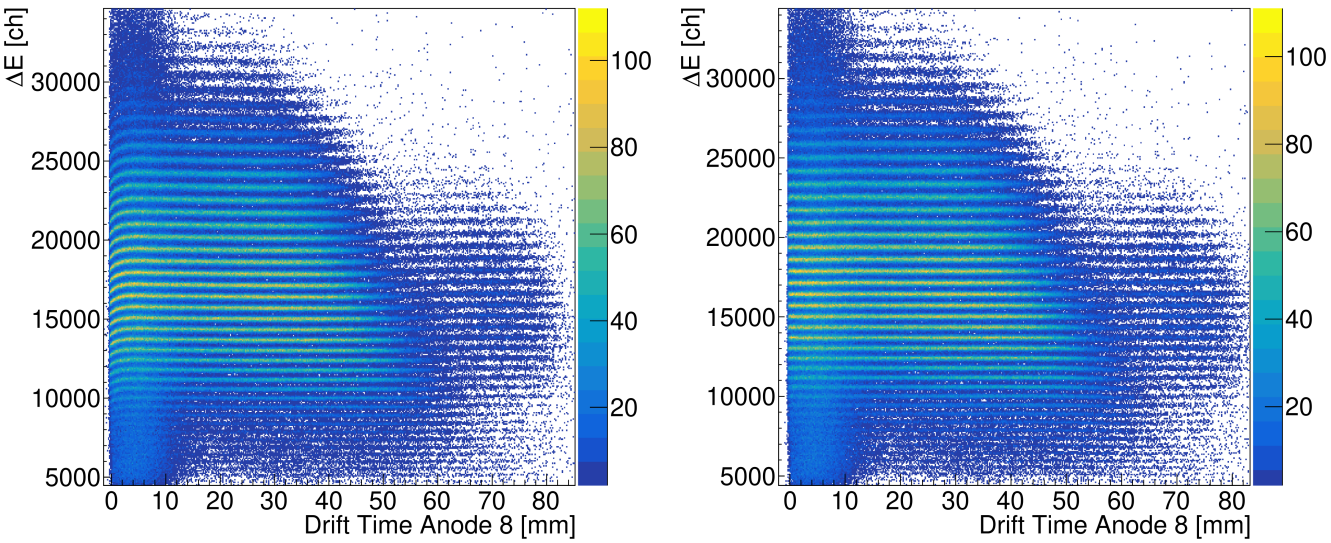

Figure 3.21: *Energy loss in section 1 of the Twin Music vs. the drift time of the electrons, before (left) and after (right) the dependency correction.*

The energy loss also has a dependence on the drift time of the electrons towards the anodes. When a fission fragment passes close to the central cathode of the Twin, some of the produced ionization electrons might be absorbed by the cathode or traverse it to the opposite section. Since these electrons do not arrive at their correspondent anodes in the section they were generated, the anodes

measure a smaller amount of electrons. The result is a drop in the measured energy close to the position of the central cathode, X=0, as can be seen in Fig. 3.21(left). This dependence has been corrected following the same procedure used for the ToF with the spline function. The corrected correlation is shown in Fig. 3.21(right), where all the lines look straight at X=0.

Atomic number identification

Once all the dependences of the energy loss have been corrected, the atomic number of the fission fragments can be deduced, as the ionic charge is proportional to the square root of the energy loss. However, the energy is given in channel units by the electronics, and a calibration must be performed to pass from the arbitrary units to the physical magnitude. The calibration carried out in this analysis consists of two main steps. The first step starts by identifying the peaks of the charge spectra, as shown in Fig. 3.22(left). Then, the mean values of the peaks are correlated with consecutive integer numbers, since the atomic numbers of the ions have to be integers. Performing a polynomial fit like the one displayed in Fig. 3.22(right) gives the method to convert from arbitrary units to atomic number units. Nevertheless, as the integers have been randomly assigned, the actual values of the atomic number are yet unknown, which leads to the discussion of the second step of the calibration.

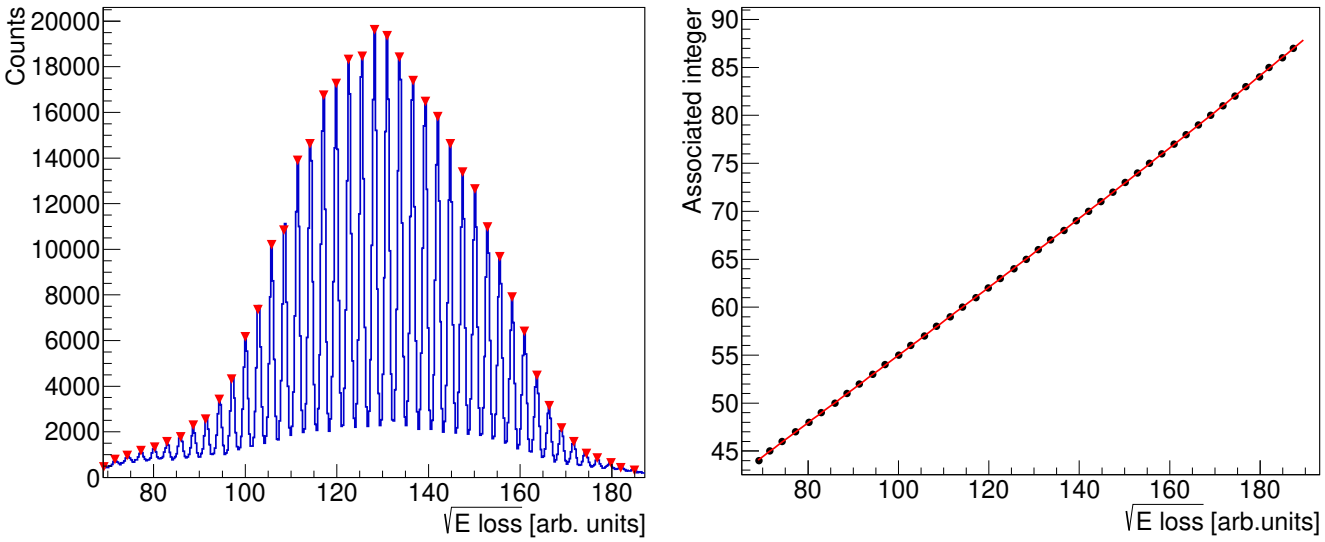

Figure 3.22: *Charge spectrum in arbitrary units (left) and its correlation with an integer index and posterior polynomial fit (right).*

The second step of the calibration begins with an alignment because it is likely that the resulting spectra of the different Twin sections are misaligned, as seen in figure 3.23. The four spectra are plotted together and they are aligned by adding or subtracting integer numbers so they have the same mean value and reach the

maximum possible overlap, see in figure 3.23. The final resolution achieved is $\Delta Z = 0.38$ FWHM in charge units [Z] for the central charges. For the lightest distinguishable peaks is about $\Delta Z = 0.6$ FWHM and about $\Delta Z = 0.8$ FWHM for the heaviest ones.

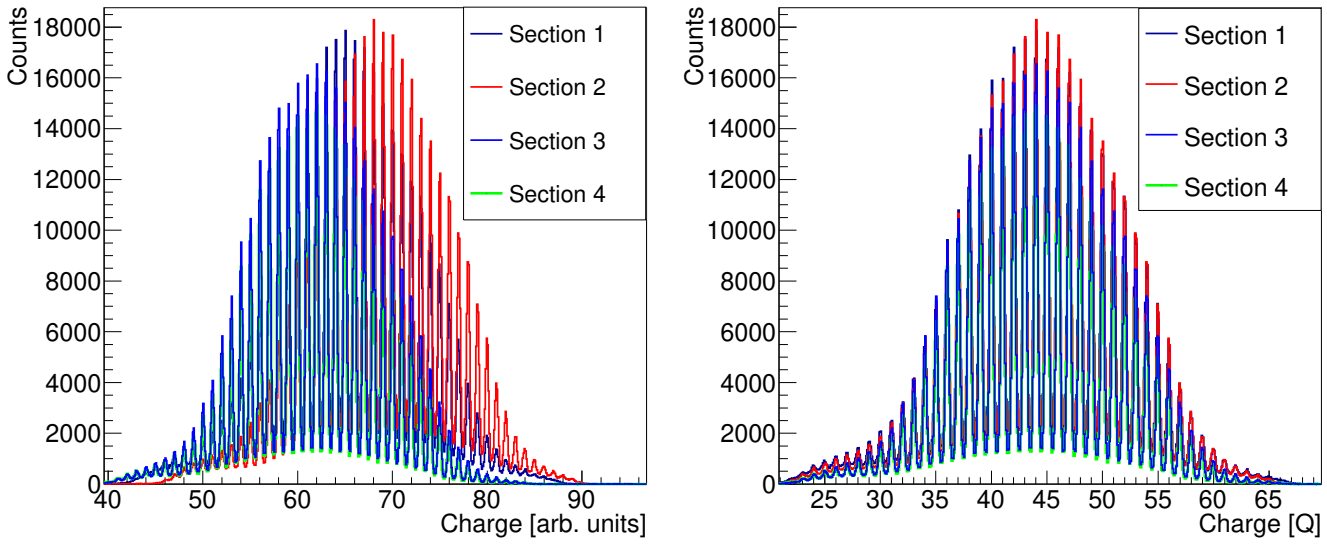

Figure 3.23: *Comparison of the charge spectra of the four sections of the Twin Music, misaligned (left) and aligned (right).*

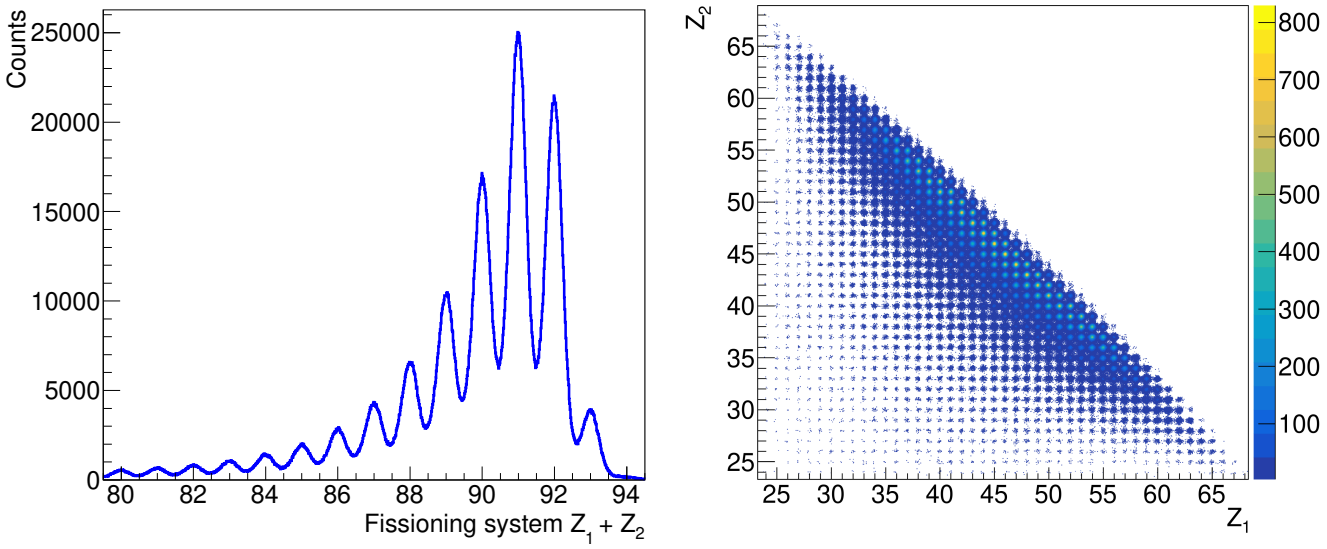

Figure 3.24: *Fission fragments charge identification results. Left: Fissioning system spectrum. Right: Fission fragments charge correlation.*

The fissioning system charge spectra must be computed to deduce the atomic number of the fission fragments. The atomic number of the fissioning system that gave rise to the fission fragments is obtained by simply adding the atomic numbers of both fragments. Hence, the charge of the different Twin sections is added pair by pair over the 6 possible combinations for the two fission fragment's trajectories

inside the Twin. However, due to the kinematics of the fission reaction, most of the fission fragments will go through opposite sections of the Twin. Finally, the way to know if the alignment works, is to check that the peak with the highest statistics in the spectrum is the one with the highest expected cross section for the reaction. In this work, this is the case for $Z_1 + Z_2 = 91$, corresponding to Pa. The resulting fissioning system spectrum is displayed on Fig. 3.24(left). Since the beam is $^{238}_{92}$U, when the desired quasi-free (p,2p) reaction takes place the produced nucleus is an excited $^{237}_{91}$Pa. However, it is important to notice that this peak for $Z_1 + Z_2 = 91$ will not have only $^{237}_{91}$Pa systems, it will have the contribution for other lighter $_{91}$Pa isotopes as well, since the $^{237}_{91}$Pa can also de-excite via neutron emission and undergo fission after. It is also possible to obtain different excited $_{91}$Pa isotopes when the reaction is not quasi-free. A selection in the opening angle between the protons serves to select the quasi-free reactions in which there is no evaporation of neutrons before fission. The 92 charge peak contributions come from reactions in which one or more neutrons were removed from the projectile but none of its protons interacted. For the following peak, the charge 93 can occur due to charge exchange reactions with the target. Such reaction would involve that a proton from the target turned into a neutron by emitting a π^+, and that a neutron from the projectile picked it up converting it into a proton.

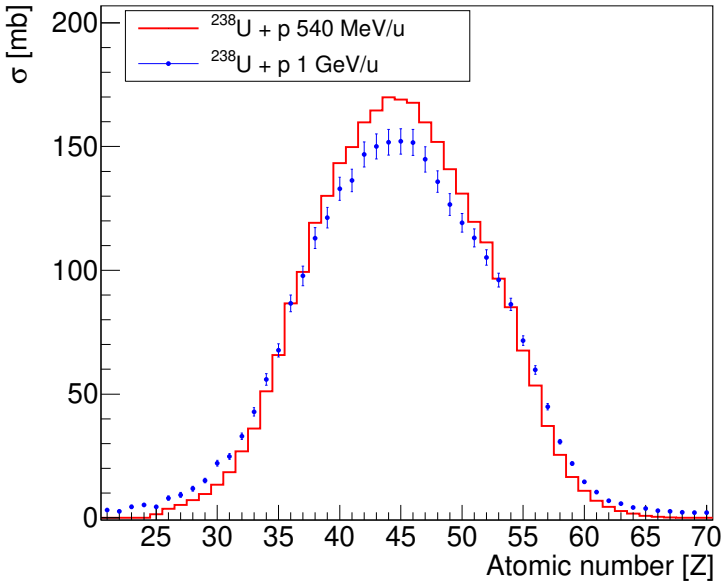

Figure 3.25: *Atomic charge distribution from this experiment compared with previous data from Ref. [112].*

The correlation of the derived charge for both fission fragments Z_1 and Z_2 is shown in Fig. 3.24(right) in a two-dimensional cluster plot. Each diagonal of clusters in this Fig. corresponds to a different fissioning system produced in the reaction, and each cluster on the diagonal corresponds to a different pair of

resulting fission fragments.

Finally, the obtained atomic charge distribution from this work is compared in Fig. 3.25 with previous data of ^{238}U impinging on a ^{238}U target but at 1 GeV from Bernas et al. [112]. The two distributions overlap rather well, serving as a validation for the calibration result. To compare it with Bernas, the total fission cross-section was calculated to normalize the spectrum. The calculation of the fission cross-section was not introduced yet, but it is discussed in Sec. 3.8.

3.3.3 Vertex reconstruction

The knowledge of the positions of the fission fragments inside the Twin MUSIC ($x_{\text{Twin 1}}, x_{\text{Twin 2}}$) together with the horizontal angles (θ_1, θ_2) allows to reconstruct the fission fragments trajectories in Eq. 3.12 and find their intersection point as shown in Eq. 3.13, which is where fission took place.

$$x = x_{\text{Twin 1}} + \tan(\theta_1)z, \quad x = x_{\text{Twin 2}} + \tan(\theta_2)z \tag{3.12}$$

$$z_{\text{vertex}} = \frac{x_{\text{Twin 1}} - x_{\text{Twin 2}}}{\tan(\theta_2) - \tan(\theta_1)}, \quad x_{\text{vertex}} = x_{\text{Twin 1}} + \tan(\theta_1)z_{\text{vertex}} \tag{3.13}$$

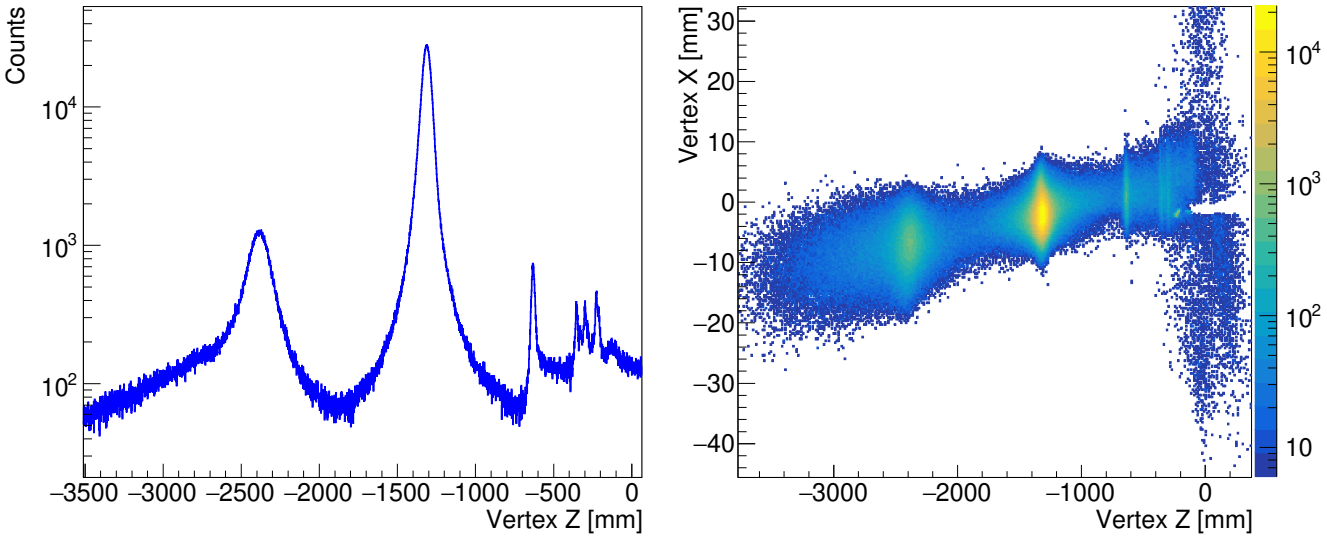

Figure 3.26: *Reconstructed fission vertex position. Left: Vertex Z position [mm]. Right: Vertex (Z, X) position [mm].*

The vertex position along the Z axis is displayed in Fig. 3.26(left), where the peak with the highest statistics in the plot corresponds to the fissions inside the LH_2 target. The other peaks correspond to fission reactions with other material along the beam line along the setup, like the start scintillator before the target or the exit window of the vacuum chamber, after the target. This represents very

valuable information because it enables to select the fission events that occured in the target and to discard the others. In Fig. 3.26(right) the correlation of the (Z,X) vertex positions is presented. As it can be seen, the beam entered with a certain angle, which is why the beam events appear always on the right side of the Twin and MWPCs. Still, most of the beam events hitting the target are centered around -2mm with a dispersion of $\Delta X = 2$mm.

3.4 Neuland

NeuLAND, the New Large Area Neutron Detector, is a neutron detector composed of several planes of plastic scintillator bars with a thickness of 5 cm and a length of 2.7 m. It currently consists of 12 double planes, each containing 100 bars, 50 in vertical and 50 in horizontal orientation, creating a surface of 2.5x2.5 m. At the ends of each bar, photomultipliers are attached to detect the light created in the scintillator. Counting with several planes increases the likelihood of interaction. Once the neutron interacts with a nucleus, it can scatter a proton, an alfa particle, or other light ions which are detected by the scintillators. By reconstructing the tracks of the charged particles the neutron multiplicity can be calculated. The GLAD magnet deflects the charged particles

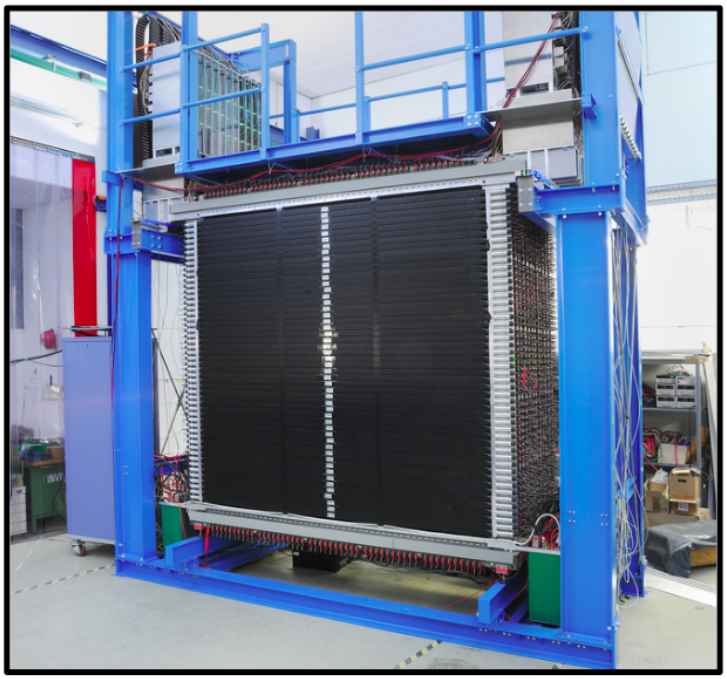

Figure 3.27: *NeuLAND detector in the setup.*

from the original beam path to identify them by their magnetic rigidity. However, neutrons are unaffected by the magnetic field and can be detected by NeuLAND located downstream at zero degrees with respect to the beam path. A picture

of NeuLAND in the setup can be seen in Fig.3.27. Neuland data was calibrated for this experiment, but due to the high neutron multiplicities produced in fission (around 10), and the lack of algorithms to reconstruct more than 4 neutrons, it was not used for the work.

3.5 Califa

CALIFA (CALorimeter for the In Flight detection of γ rays and light charged pAr-ticles) is a highly segmented scintillator calorimeter designed to surround the R^3B target area. It works as a high-resolution $\gamma-$ray spectrometer and high-energy charged particles calorimeter, since it has been specifically designed to study quasi-free scattering reactions, such as (p,2p) or (p,pn). For that channel, both highly energetic light-charged particles (protons about 300 MeV) and γ ray from the de-excitation of the residual fragment must be detected.

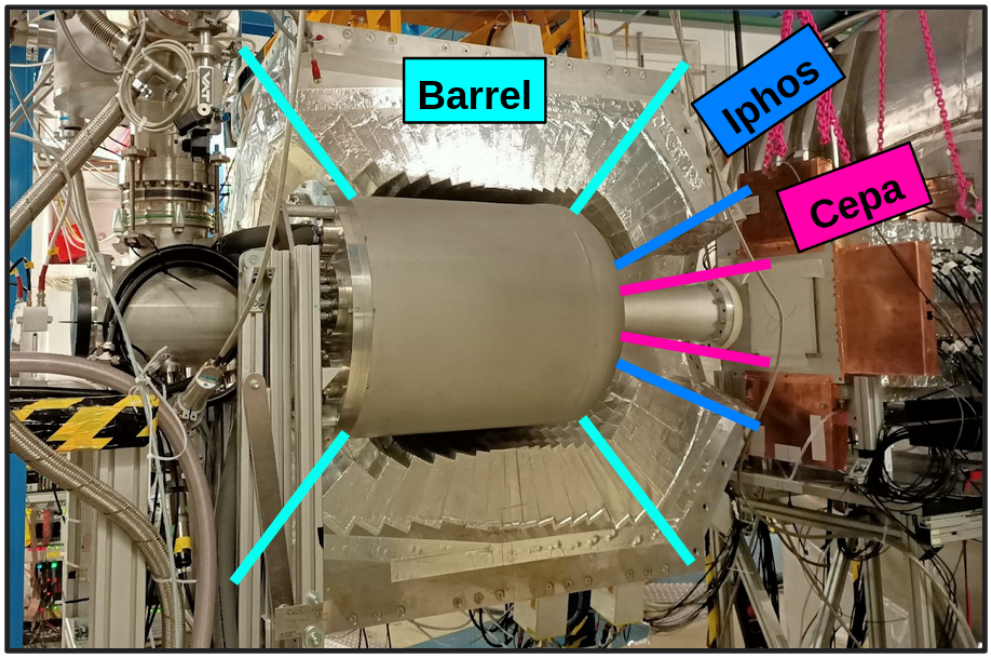

Figure 3.28: *Califa detector picture, Messel side.*

The detector design is composed of 2560 scintillator crystals, most of them CsI(Tl). The Califa's crystals operation mode is similar to that of any other scintillator: when a gamma or a charged particle passes through the crystal, the material absorbs the energy and de-excites emitting light. This light is collected at the end of the crystal by an APD (Avalanche PhotoDiode), the semiconductor equivalence of a PMT. The crystals are disposed surrounding the target area, and the detector is divided into two halves, named Messel and Wixhausen. Each one of the halves is composed of 2 parts: the barrel and the Endcap, and can be seen

in Fig. 3.28. The Endcap is composed of two parts, Iphos and Cepa (this last one was still not mounnted at the moment of the experiment). To see further specifications of each section of Califa, see Tab. 3.4.

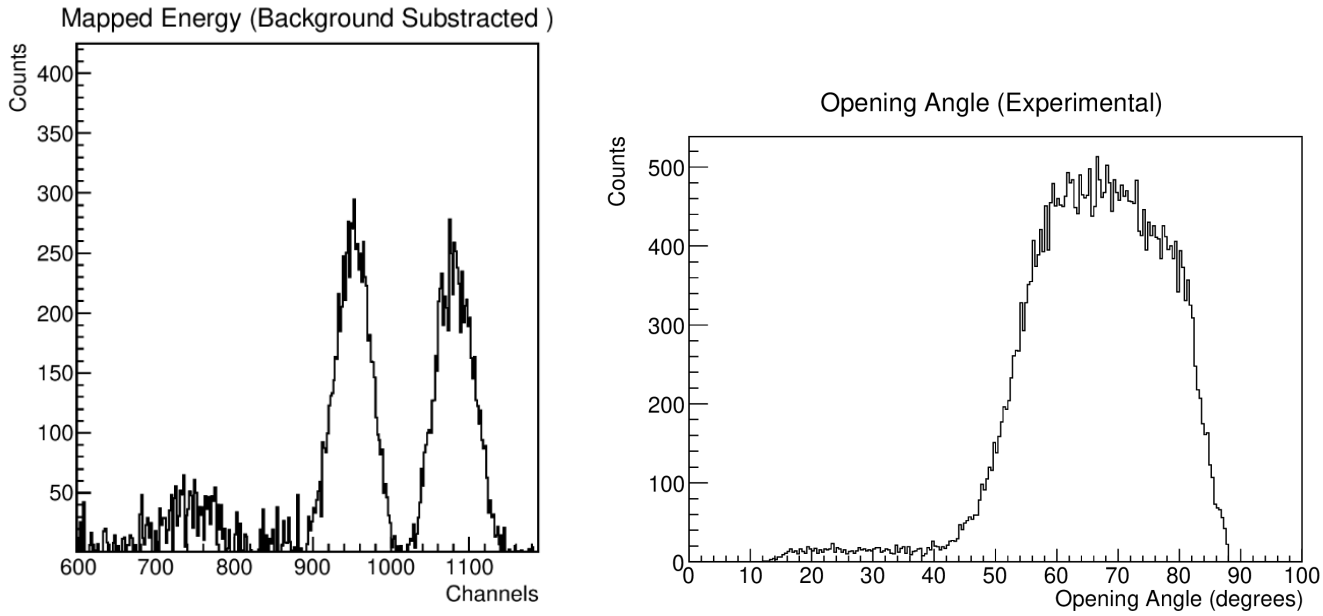

Figure 3.29: *Left: γ ray spectrum of a ^{60}Co source measured with Califa. Right: Opening angle between two protons emitted in a knockout reaction. Figures from Ref. [109].*

The calibration of this detector has been done by the other Ph.D. student analyzing this experiment, Gabriel García Jiménez [109]. To calibrate the detector, a ^{60}Co source has been used, which undergoes β^- decay, resulting in ^{60}Ni which de-excites by emitting two characteristic γ rays with energies of 1.17 and 1.33 MeV and can be seen in Fig. 3.29(left). These peaks are used to convert the electronic channel units into energy units. Fig. 3.29(right) shows the resulting opening angle distribution, which is around 80^o for the pure quasi-free (p, 2p) but in the distribution it is mixed with events where the protons suffered re-scattering with the other nucleons in the projectile.

3.6 Si-tracker and LH_2 target

The Si-tracker is a detector developed for tracking (in x and y) protons and heavy ions produced in high-energy reactions. In this experiment, it is used to track the trajectories of the two protons emitted in the (p, 2p) reaction. Together with the protons energy measurement performed by Califa, the momenta can be reconstructed and used to calculate the excitation energy of the recoiling nucleus.

Specifically, the Si-tracker used for this experiment is a double-sided Si microstrip detector (μDSSD) developed to track high-energy cosmic rays at the

Section	Crystal number	Crystal type and size	Coverage angle	γ-ray Energy resolution for 1 MeV γ rays	Energy range for protons in Lab system and energy resolution
Barrel	1952	CsI(Tl), 22cm	(43.2-140.3)^o	<6 % ΔE/E	320 MeV 1% ΔE/E
Endcap Iphos	512	CsI(Tl), 22cm	(19-43.2)^o	<6 % ΔE/E	700 MeV 1% ΔE/E
Endcap Cepa	96	Phoswhich: $LaBr_3$, 7cm $LaCl_3$, 8cm	<19^o	<6 % ΔE/E	700 MeV 1% ΔE/E

Table 3.4: *Califa detector technical information from Ref. [113].*

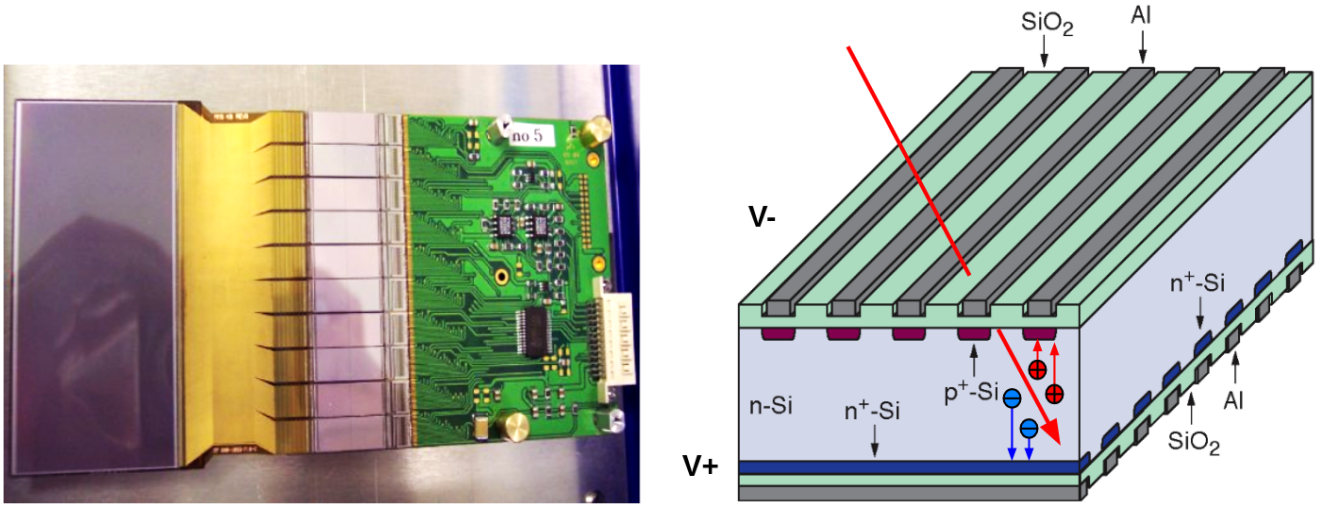

Figure 3.30: *Left: Picture of an AMS detector. From the left to the right the components are: the sensor, the capton cable, the coupling capacitors, the VA chips and the front-end electronics board. Right: Operating principle of a Double-sided microstrip detector.*

Alpha Magnet Spectrometer (AMS) at the International Space Station (ISS). A picture of one of the 6 Si-trackers employed in this experiment can be seen in Fig. 3.30(left).

The basic principle of operation of these detectors is the same as that of any other n-type semiconductor detector, but with the two sides segmented in perpendicular directions to track in both x and y coordinates. Fig 3.30(right) shows a scheme of the operating principle. The junction side (called S-side or p-side) of the detector is composed of strips of Si material doped positively (p^+ Si) and connected to a negative voltage. The bulk or depletion area is negatively doped (n Si), and the ohmic side (K- or n- side) is more negatively doped (n^+ Si) than the bulk and segmented in strips connected to a positive voltage. When a charged ion passes through the depletion area, the electrons in the material

are excited and pass from the valence to the conduction band, creating pairs of electrons and holes. The electrons drift toward the p^+ Si strips and the holes toward the n^+ Si strips, inducing a signal that is read by the front-end electronics. Further technical specifications are shown in table 3.5.

Dimensions	72 mm x 40 mm x 0.3 mm
Number of strips	640 strips in P side 384 strips in N side
Bias voltage	75 V
Front end electronics and read out	VA_hdr9a from IDEAS SIlicon Strip DEtector REadout Module (SIDEREM)

Table 3.5: *AMS detectors technical information.*

In the experiment 6 AMS detectors were used to track the protons coming out from the target. The disposition of the sensors surrounding the LH_2 target can be seen in Fig. 3.31(left), with the P-side of the sensors pointing towards the target. Each AMS detector had a 10 μm thin gold layer in front of it to stop the delta electrons produced in the reaction. Fig. 3.31(right) shows a better view of the LH_2 target, which is 15 cm thick and has a diameter of 42mm. The target cell is made of Mylar and composed of an entrance window and an exit window of respectively 120 μm and 180μm. During the experiment, the target was further wrapped in 10 insulation foils 5 μm thick to reduce heat flux via radiation. The hydrogen is liquefied in a cryostat and kept at a temperature of 20K.

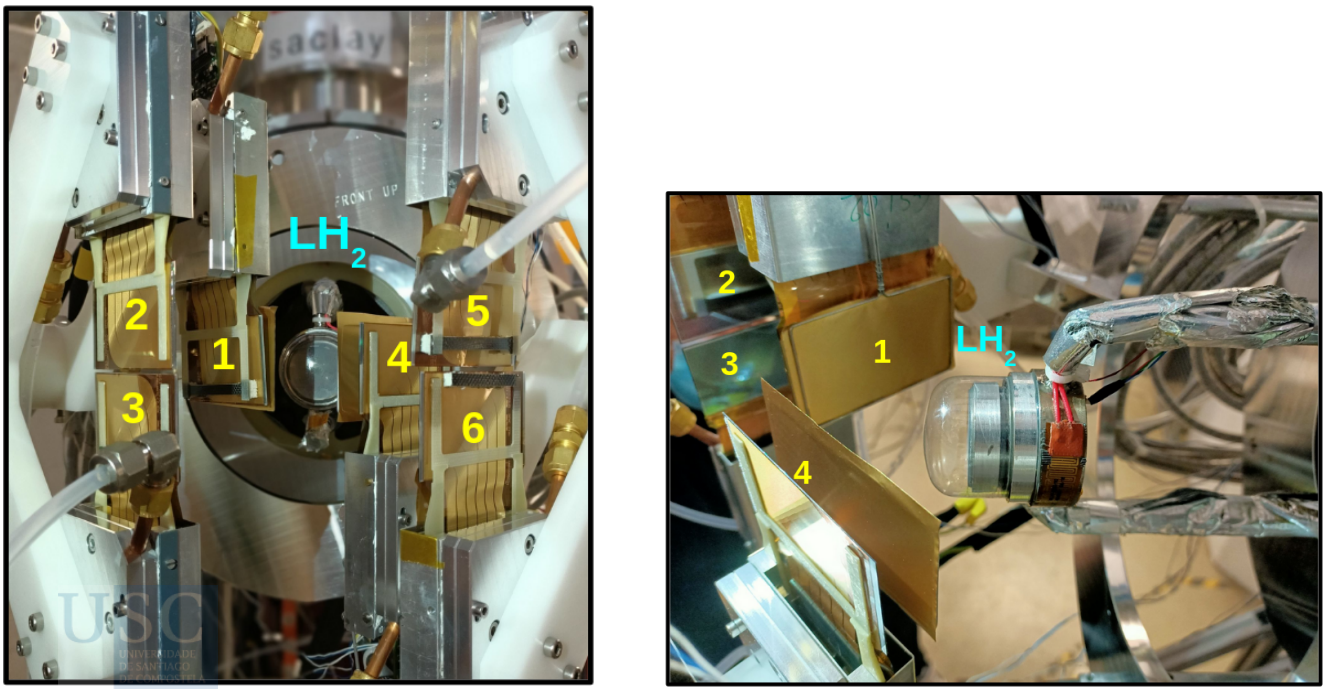

Figure 3.31: *Pictures of the 6 AMS detectors surrounding the LH_2 target.*

3.7 Mass reconstruction

To obtain mass identification of the fission fragments, 4 observables are needed: the atomic number, the trajectory length, the time-of-flight, and the magnetic rigidity (Bp) of the ion inside the dipole. At this point of the analysis, both atomic number and time-of-flight are known. The trajectory length can be reconstructed using the position information from the MWPCs and following fully geometrical methods, which have been employed for many experiments that used the previous magnet ALADIN, see Ref. [114]. However, this approach is based on the assumption that the dipole is a perfect dipole and the field is perfectly homogeneous in only one direction. This approximation might work not so well for GLAD since the dipole is considerably larger. To obtain the best possible resolution, another method based on a simulation has been used to reconstruct the masses.

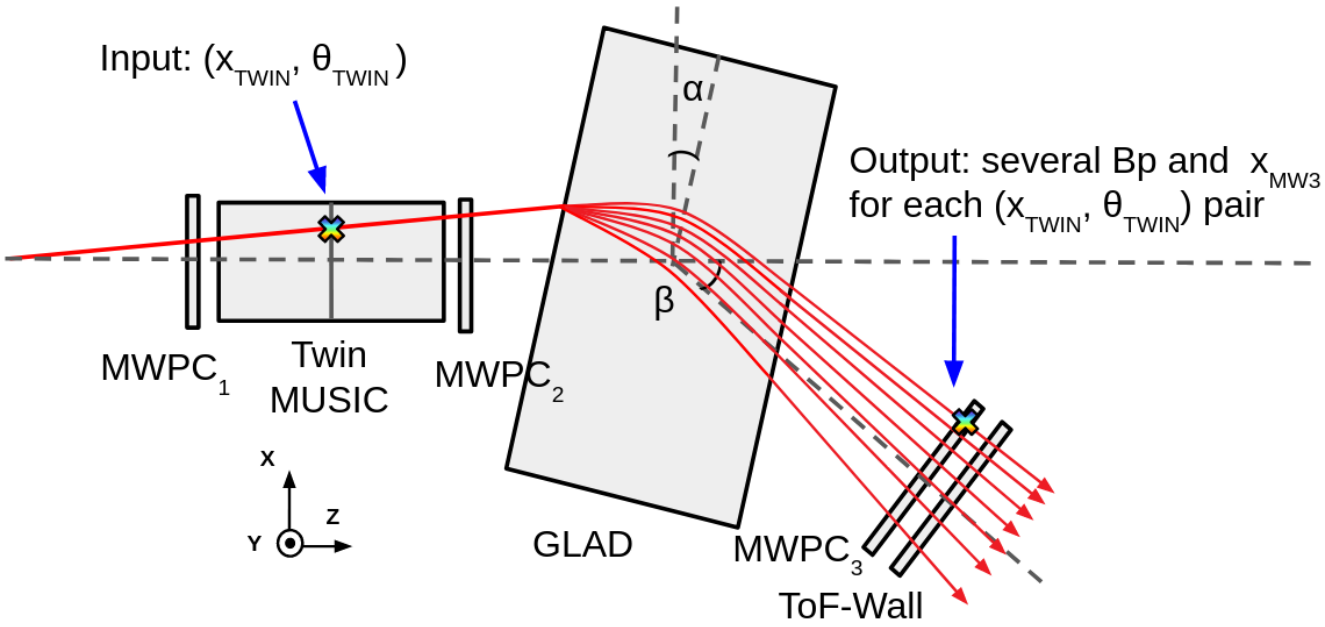

Figure 3.32: *Schematic representation of the simulation method to reconstruct the masses.*

The method uses as input an experimental data file. For each one of the events in the file, which follows a trajectory determined by θ_{Twin} and $\mathrm{X}_{\mathrm{Twin}}$, several trajectories will be simulated inside the magnet, typically around 15. An initial Bρ value is given for the first trajectory and then the value is increased in steps of 0.2 Tm for each trajectory. The method is illustrated in Fig. 3.32. For each Bρ value, the momentum of the ion is calculated as shown in Eq. 3.14, and the values projected onto the ZX plane coordinates as shown in Eq. 3.15 using the information on the angle by the Twin MUSIC.

$$p = \frac{B\rho Z}{3.3356} \tag{3.14}$$

$$p_X = p_1 \sin(\theta_{Twin}), \quad p_Z = p_1 \cos(\theta_{Twin}) \tag{3.15}$$

The simulation needs several things as inputs: the initial momenta (defined in Eq. 3.15), the (Z, X) coordinates of the reconstructed reaction vertex, the magnet current, GLAD's magnetic field map and the positions information from all detectors. The simulation propagates the initial trajectories from the reaction vertex to the ToF Wall.

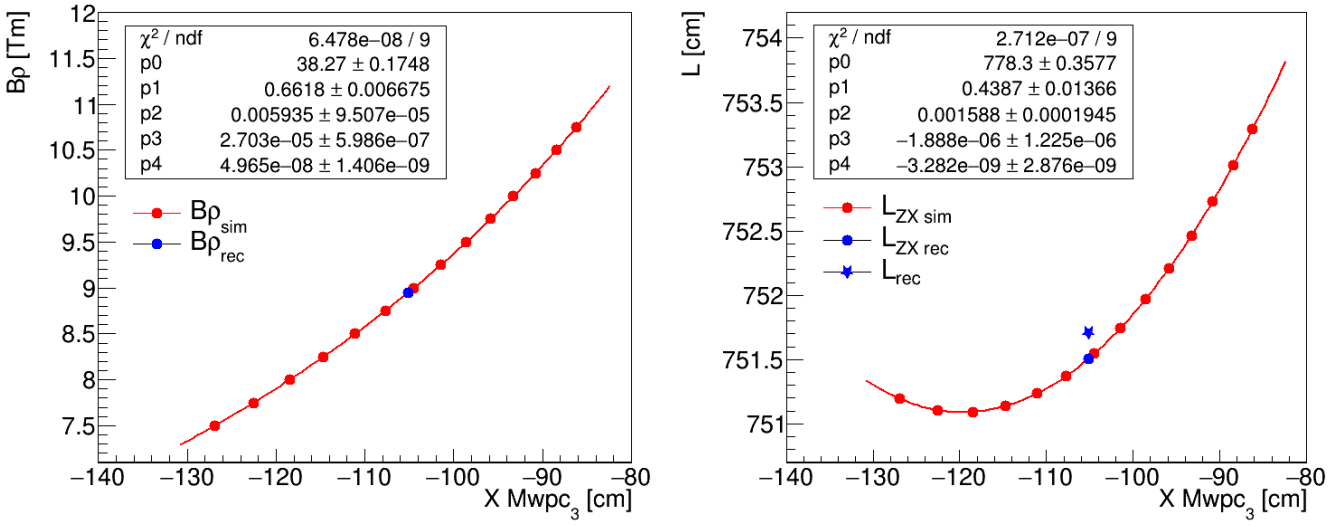

Figure 3.33: *Left: Bρ correlation with the X position in MWPC$_3$ The red points correspond to the simulated Bρ and the blue point the reconstructed Bρ using the fit. Right: Length correlation with the X position in MWPC$_3$. The red points correspond to the simulated length in the ZX plane and the blue point to the reconstructed length in the ZX plane using the fit. The blue star corresponds to the total reconstructed length.*

For each event in the input file, the output has a collection of several simulated Bρ with their respective simulated X positions in the MWPC$_3$ and the fragment path length in the ZX plane. Then, event by event, the simulated Bρ can be correlated with the X of the MWPC$_3$, as shown in Fig. 3.33 (left) and a polynomial fit like the one shown in Eq. 3.16 can be performed. This fit is used to calculate the experimental Bρ from the measured X position in the MWPC$_3$. The same can be done for the path length in ZX, as shown in Fig. 3.33 (right) and Eq. 3.17. However, this length has been calculated in the ZX plane without taking into account the Y coordinate. To obtain the whole length of the trajectory, the Y coordinate measured in the ToF Wall is added quadratically to the reconstructed length in the ZX plane, as shown in Eq. 3.18.

$$B\rho = B\rho_0 + B\rho_1 X_{Mwpc3} + B\rho_2 X^2_{Mwpc3} + B\rho_3 X^3_{Mwpc3} + B\rho_4 X^4_{Mwpc3} \tag{3.16}$$

$$L_{ZX} = L_{ZX0} + L_{ZX1}X_{Mwpc3} + L_{ZX2}X^2_{Mwpc3} + L_{ZX3}L^3_{Mwpc3} + L_{ZX4}X^4_{Mwpc3} \quad (3.17)$$

$$L = \sqrt{L^2_{ZX} + Y^2} \quad (3.18)$$

Once the Bρ and the total length of the fission fragment path are reconstructed, the mass number of the fragment can be calculated using Eq. 3.19, already presented in the previous chapter.

$$A = \frac{B\rho \cdot Ze}{u\beta\gamma c} \quad (3.19)$$

The mass reconstruction method was validated using simulated data as input, as seen in Appendix R.8. The simulation was performed using the expected resolution of the detectors, which means $\Delta T = 40$ ps FWHM for the ToF Wall, $\Delta X = 300$ μm FWHM for the MW_3 and $\Delta X = 70$ μm for the Twin MUSIC. However, for the real data the ToF resolution could be larger than 100 ps FWHM as seen in Sec. A.2, which is larger than the $\Delta T = 40$ ps FWHM used in the simulation and results in worse mass resolution too. Since the mass resolution worsens with the increase of the fission fragment charge, it was only possible to differentiate masses for fission fragments with atomic number Z=36 and 37. The origin of the ToF resolution issue is still under debate, but a likely option could be the closeness of the ToF Wall to GLAD since its magnetic field could affect the signals from the PMTs.

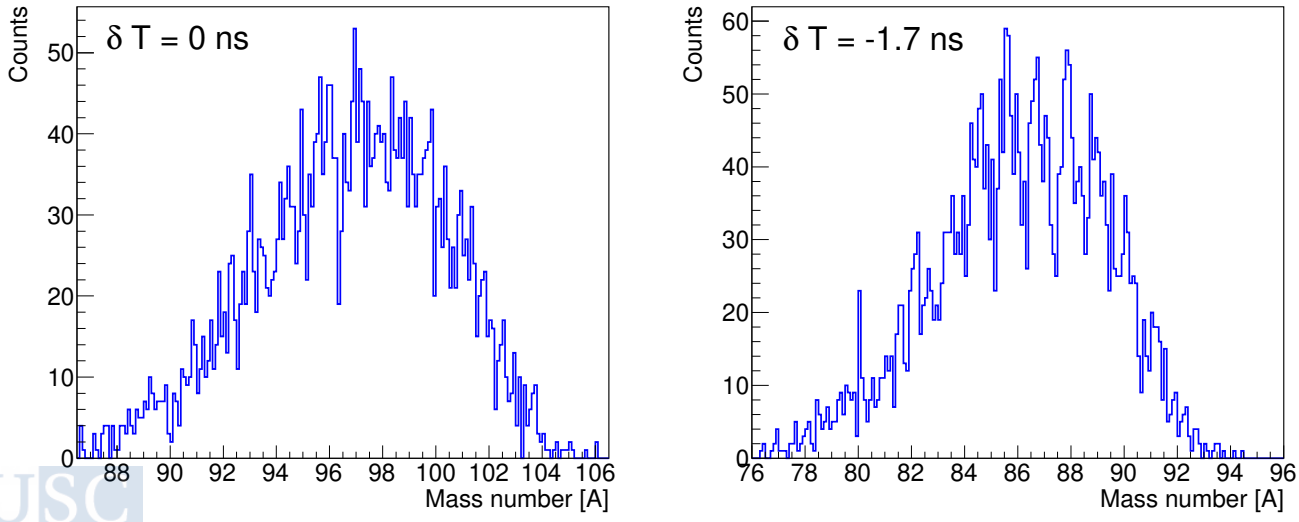

Figure 3.34: *Left: Mass number distribution of the fission fragments with atomic charge Z = 36 and ToF Wall paddle number 22. Right: Same as left but displacing the time-of-flight original distribution an offset of δT= -1.7ns.*

However, it has been found that some scintillator paddles have a considerably better mass resolution when adding a certain time offset to their time-of-flight. An example is shown in Fig. 3.34 for the paddle number 22. The left plot shows the mass distribution without adding any offset to the time-of-flight, and the mass peaks are barely distinguishable. The right plot shows the resulting mass distribution for the same plastic when adding a time offset of δT = -1.7 ns to the time-of-flight. It can be seen how the central masses peaks are much better resolved in comparison with the previous case.

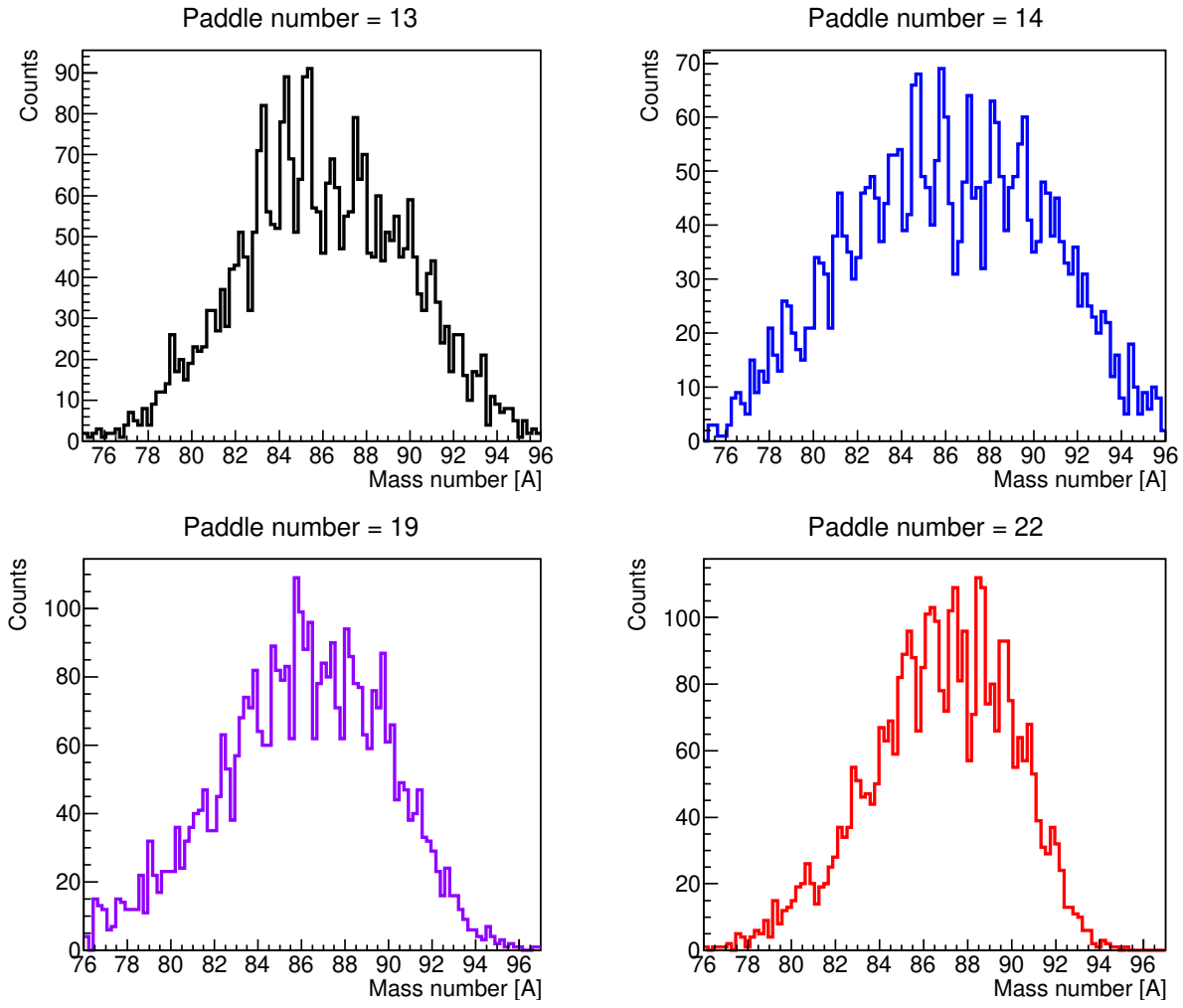

Figure 3.35: *Mass distribution for 4 different Tof Wall paddles.*

However, this approach does not work for all paddles, and for the ones that do, there is no clear any tendency, that is, each paddle needs a different time offset unrelated to the others. This was not expected in principle, since an alignment was performed using the sweep runs, as described in Sec. 3.2. However, the sweep runs were performed at the beginning of the experiment, and conditions could have changed since those runs. The best mass resolution results were found for paddles numbers 13,14,19 and 22, as shown in Fig. 3.35, with a resolution

around $\Delta A = 0.8$ FWHM for the central peaks of the distributions.

After applying the necessary offsets in time for each paddle to obtain a better mass resolution, the mass distributions become displaced from their original values and misaligned between paddles. This can be seen in Fig. 3.36 (left), where the resulting mass number distribution is plotted against the paddle number. The red dots correspond to the original mean values of the mass distributions when the mass was calculated without any offset in the time-of-flight.

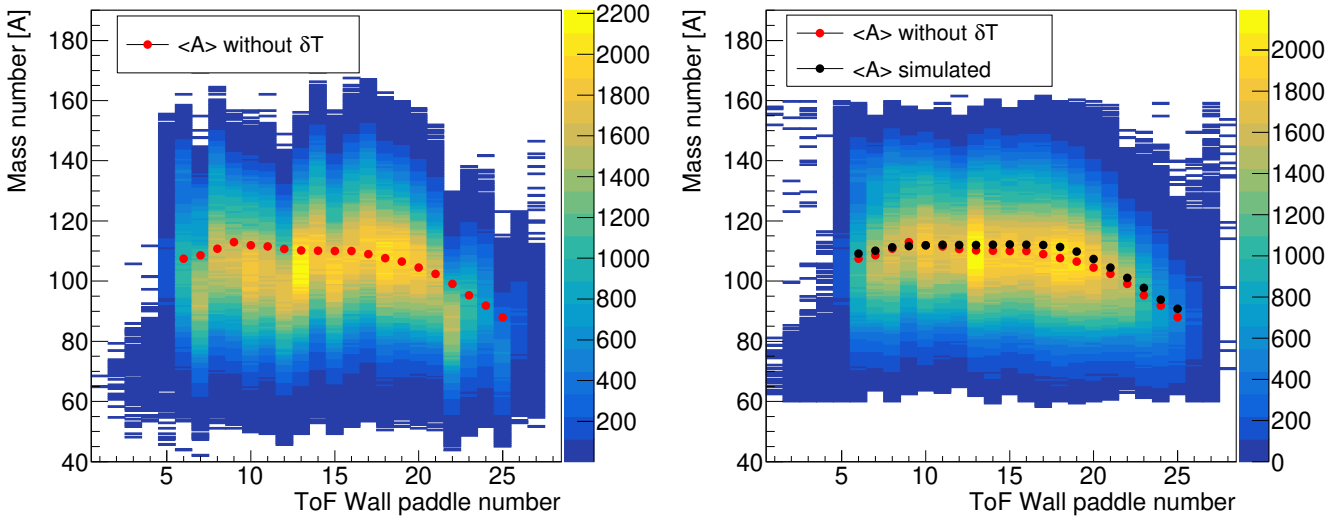

Figure 3.36: *Left: Mass distribution calculated with the time offset against the Tof Wall paddle number. Right: Same as left, but after adding an offset to displace the mass distributions to their original values.*

To correct this misalignment, a mass offset δ_A is calculated as seen in Eq. 3.20 by subtracting the mean value of the mass distribution calculated with the time offset $< A_{\delta T} >$ from the mean of the original distribution $< A >$. The resulting offset is added to the mass calculated with the time offset to get the final mass value. It can be seen in Fig. 3.36 (right), how after applying this offset the masses are aligned with the original values and also follow the same tendency of the simulated mean masses, represented by the black dots.

$$\delta_A = < A > - < A_{\delta T} > \rightarrow A = A_{\delta T} + \delta_A \tag{3.20}$$

The next step to improve the resolution would be correcting the mass dependence on the vertical position, as it was done for the simulated input data. However, no well-defined lines were observed when plotting the mass against the Y position, as seen in Fig. 3.37. Therefore, the Y dependence was not corrected for the experimental data.

The total mass resolution is calibrated using previous experimental data for the same reaction of ^{238}U impinging on a hydrogen target but at 1 GeV from Bernas

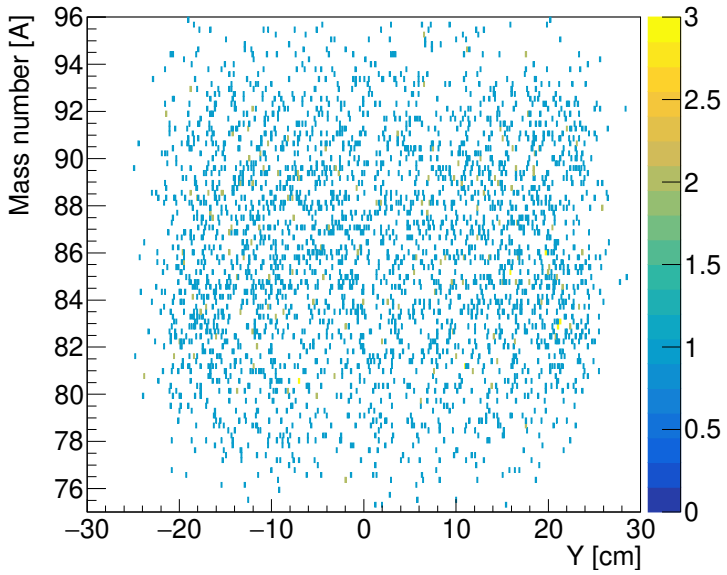

Figure 3.37: *Mass dependence on the Y coordinate measured by the Tof Wall.*

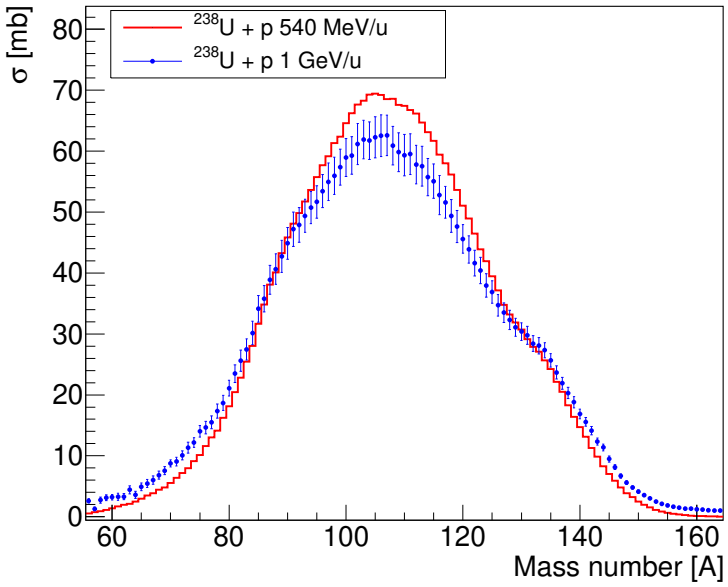

Figure 3.38: *Mass distribution from this experiment compared with previous data from [112].*

et al. [112], as seen in Fig. 3.38. The mass distribution presents a characteristic shape defined by a dominating peak in the center, originating from the symmetric fission, and two peaks at the sides from asymmetric fission. However, due to neutron evaporation of the fission fragments from the symmetric peak, the central peak is shifted to the left, eclipsing the light asymmetric peak. The criteria to align the mass spectrum was to center the heavy asymmetric peak with the data from Ref. [112]. The mass distribution was also compared with the ^{238}U data induced via Coulex from Pellereau et al. [8]. To do so, $Z_1 + Z_2 = 92$ was selected and the isobaric yields were systematically compared with the Coulex yields for different mass addition conditions looking for the lowest residue. The mass addition cut

with the lowest residue was found to be $A_1 + A_2 = 236$, which is displayed in Fig. 3.39 and is in good agreement with the Coulex yields. The Results section will provide more details about the selection in mass addition as an indicator of the excitation energy.

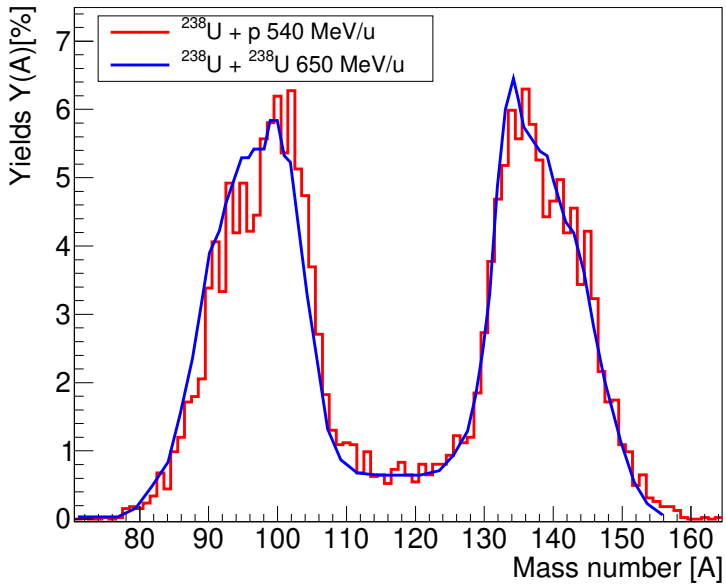

Figure 3.39: *Comparison of the isobaric yields normalized to 200% from the experiment of this work and Pellereau et al. [8].*

3.8 Total and partial fission cross-section

A cross-section is a measure of the effective surface area seen by a beam impinging on a target and therefore it is measured in units of an area, usually mb. Since this effective area is proportional to the probability that an interaction between the projectile and the target takes place, cross-sections are the typical experimental observable to measure reaction probabilities. The cross-section can be extracted using the attenuation law displayed in Eq. 3.21, which describes how an initial amount of beam particles N_{intial} decreases exponentially to N_{final} when it passes through a layer of material of thickness x.

$$N_{final} = N_{initial} e^{-\frac{1}{x}\sigma} \tag{3.21}$$

Solving this equation for σ and substituting the number of final particles by the number of particles that reacted ($N_{reaction} = N_{initial}$ - N_{final}), the total reaction cross section can be calculated as shown in Eq. 3.22.

$$\sigma_{reaction} = -x \ln\left(1 - \frac{N_{reaction}}{N_{initial}}\right) \tag{3.22}$$

For the calculation of the cross-section of a specific reaction channel, such as fission, the number of particles that reacted in the formula must be substituted by the number of particles that reacted in that specific channel. To calculate the total fission cross-section for the ^{238}U beam in the LH_2 target, the final expression can be seen in Eq. 3.23. There, $N_{\text{U arrived at target}}$ corresponds to the number of uranium particles that reached the target and $N_{\text{U fissions in target}}$ the number of those which underwent fission.

$$\sigma_{\text{fission}} = -x \ln\left(1 - \frac{N_{\text{U fissions in target}}}{N_{\text{U arrived at target}}}\right) \tag{3.23}$$

Once the total fission cross-section is obtained, the partial fission cross-sections can be calculated, which correspond to the fission probability for the different possible fissioning systems, the ones displayed in Fig. 3.24 (left). These can be calculated as shown in Eq. 3.24, multiplying the total fission cross-section by the production yield of each fissioning system. The production yield is the fraction of every fissioning system produced in the reaction over the total number of fission events. It is calculated by integrating the number of counts under each fissioning system peak (N_j) in Fig. 3.24 (left) and dividing it by the integral of the whole spectrum ($\sum_{i=1}^{94} N_i$). The number of counts per fissioning system is corrected by a factor (F_j) based on a simulation which takes into account the counts that were lost because of the interaction of the fission fragments with matter.

$$\sigma_{\text{fission j}} = \sigma_{\text{fission}} \frac{N_j F_j}{\sum_{i=1}^{94} N_i} \tag{3.24}$$

To calculate the number of uranium nuclei that reached the target and the ones that also fissioned, to be used in Eq. 3.23, a combination of the information given by the data acquisition system (DAQ) and the detector information will be done. The following subsection will briefly introduce how the DAQ stores the data to understand the DAQ-related correction factors applied to the fission cross-section calculation. The last subsection will explain the correction factor associated with the detectors and the final formula.

3.8.1 DAQ Trigger system: How to count events

The DAQ is the software that controls the read-out of the electronic modules that digitize the data measured by the detectors. It is the system in charge of synchronizing the signals coming from different detectors and deciding which ones are saved for later analysis. Since not every event in the experiment is of interest for the studied physics case, the DAQ works with something called 'triggers' to

reduce the amount of recorded data. A trigger is a logical signal that commands the DAQ to store the data of an event only if a specific detector or group of detectors that measure the reaction channel of interest has provided a signal. The trigger information for each event is stored as a 16-digit number called a TPat bit-mask or simply 'mask'. Each one of the digits in the mask is named one logic 'bit', and they are turned on (turn from 0 to 1) if the condition of having a signal in the desired detector/s is fulfilled. An index number named 'TPat' is given to every condition in the detectors that activates one bit in the mask. An example of a mask can be seen in Eq. 3.25 for the $TPat_1$ and $TPat_2$.

$$\begin{aligned} &0000000000000001 \rightarrow TPat_1 : \text{Start} \\ &0000000000000011 \rightarrow TPat_1 \text{ and } TPat_2 : \text{Start and fission} \end{aligned} \tag{3.25}$$

$TPat_1$ corresponds to events where the start scintillator at the entrance of the setup has given a signal (meaning that the beam has arrived at the beginning of the setup), and it activates only the rightmost bit in the mask. The $TPat_2$ activates the second bit in the mask (starting from the right), and it happens when both the start and the 'fission' condition are fulfilled. The fission condition is that at least 2 different paddles in the ToF Wall must have provided a signal since that implies that most likely two fission fragments have arrived at the end of the setup. The whole list of TPats used in this experiment is listed in Table 3.6. The first 12 TPats correspond to on-spill trigger patterns, which means that they were recorded when the beam was going through the setup. The last two TPats correspond to the off-spill (no beam) trigger and serve to collect cosmics data to calibrate either Califa (13th TPat) or Neuland (14th TPat). Among the on-spill, there were 2 different blocks of TPats. The first block (first six TPats) corresponds to events where the AMS detectors were available to record data, which was useful for the (p, 2p) reaction channel. The second block has the same trigger conditions as the first, but they were recording data while AMS was busy, meaning that they will not contain AMS data.

To calculate cross-sections, the number of events in the TPat of interest for the reaction channel should be counted over the number of total events. For example, in the case of a fission cross-section, one should count how many times a fission TPat happened over the times an incoming beam TPat happened, as described at the beginning of the section. In an ideal situation, this could be done just by replacing the number of counts from $TPat_2$ as $N_{\text{U fissions in target}}$ and the number of counts from $TPat_1$ as $N_{\text{U arrived at target}}$ in Eq. 3.22. However, those counts

TPat number	On-spill or Off-spill	AMS free or busy	Condition	DS	DT
1	On	Free	Start	1024	0.999
2	On	Free	Start and fission	128	0.999
3	On	Free	Start and Califa 2 halves	32	0.99
4	On	Free	Start, fission, and Califa 2 halves	1	0.96
5	On	Free	Start and Califa 1 half	128	0.99
6	On	Free	Start, fission, and Califa 1 half	32	0.99
7	On	Busy	Start	1024	0.44
8	On	Busy	Start and fission	32	0.49
9	On	Busy	Start and Califa 2 halves	16	0.53
10	On	Busy	Start, fission, and Califa 2 halves	1	0.65
11	On	Busy	Start and Califa 1 half	32	0.51
12	On	Busy	Start, fission, and Califa 1 half	8	0.53
13	Off		Califa 1 half		
14	Off		Neuland		

Table 3.6: *TPats matrix. The downscaling (DS) and dead time (DT) factors are given as an example from an arbitrary run. Note that these numbers change for different runs in the experiment.*

should be corrected for several factors such as dead times, efficiencies, secondary reactions, etc. The first corrections that ought to be applied originates from the proper DAQ modules: the dead time and the downscaling corrections. The dead time is the time during which the DAQ cannot accept new TPat requests because it is busy recording the previous one. This dead time is different for every TPat since it also depends on the dead time of the slowest detector used to create the TPat. The dead time factor for each TPat can be defined as shown in Eq. 3.26. Note that even though it is given the name of 'dead time' factor, the calculation corresponds to the fraction of accepted events because the DAQ was 'alive' (not in dead time).

$$\mathrm{DT}_{\mathrm{factor}} = \frac{\mathrm{N}_{\text{ Accepted events}}}{\mathrm{N}_{\text{ Requested events}}} \tag{3.26}$$

In this experiment, a special correction factor must be introduced due to the existence of two symmetric blocks with only the difference of whether AMS was free or not to take data. As an example, every time an event with a Start and Fission signal was recorded, the DAQ should decide if sending it to the AMS busy or AMS free block. Since the number of events sent to each block can vary with the TPat, this effect is also corrected by the factor defined in Eq. 3.27.

$$\mathrm{AMS}_{\mathrm{factor}} = \frac{\mathrm{N}_{\text{ Event AMS busy block}}}{\mathrm{N}_{\text{ Event AMS busy block}} + \mathrm{N}_{\text{ Event AMS free block}}} \tag{3.27}$$

The last DAQ correction that should be applied comes from the so-called downscaling factors. Usually, some TPats are less important than others for the physic case, and then, a downscaling factor can be applied for those to reduce the amount of recorded data. For example, the biggest downscaling factor in this experiment is applied to $TPat_1$, because it only corresponds to Start events. This factor is 1024, meaning that only 1 out of 1024 events from this TPat will be recorded. The downscaling factor for each TPat can be defined as shown in Eq. 3.28. It is important to point out that the downscaling factors are chosen by the user for each TPat depending on its physical interest.

$$DS_{factor} = \frac{N_{\text{ Accepted events}}}{N_{\text{ Stored events}}} \tag{3.28}$$

The 3 aforementioned corrections should be applied for the final number of counts of each TPat, resulting in a final correction factor as shown in Eq. 3.29. The fission cross-section will be calculated using only $TPat_1$ and $TPat_2$ for the sake of simplicity, even though it would be also possible to calculate it using other combinations of fission TPats.

$$N_{TPat}\text{corrected} = N_{TPat}\,\frac{DS_{factor}}{DT_{factor}(1 - AMS_{factor})} \tag{3.29}$$

Up to here the discussion focused on corrections regarding how the data is stored in the TPats. In the following subsection, the counts coming from each TPat will be rearranged and corrected according to the information gathered from the detector's analysis.

3.8.2 Detector corrections

Most of the detector corrections that have to be applied to the fission cross-section calculation come from the Twin MUSIC. This is because, even though the ToF Wall is used as the fission trigger, it will be the Twin which takes the final decision of whether the event is fission or not. This is because it is needed for both the charge identification and the vertex reconstruction, ensuring that the two measured particles are fission fragments and that they originate at the target and not from other material in the setup. Despite being the best detector in the setup to identify fission, the Twin cannot be used as a fission trigger, since as a gaseous detector it will always be much slower than a scintillator-detector as the ToF Wall. Therefore, events from both $TPat_1$ and $TPat_2$ will be considered as fission if they are identified as fission by the Twin, which means that they show at least 2 signals in different sections of the Twin with an energy correlation enclosed by the graphical cut represented in Fig. 3.40 by a red triangle. This area coincides

with the one displayed in Fig. 3.24 (right), which is the same figure but calibrated.

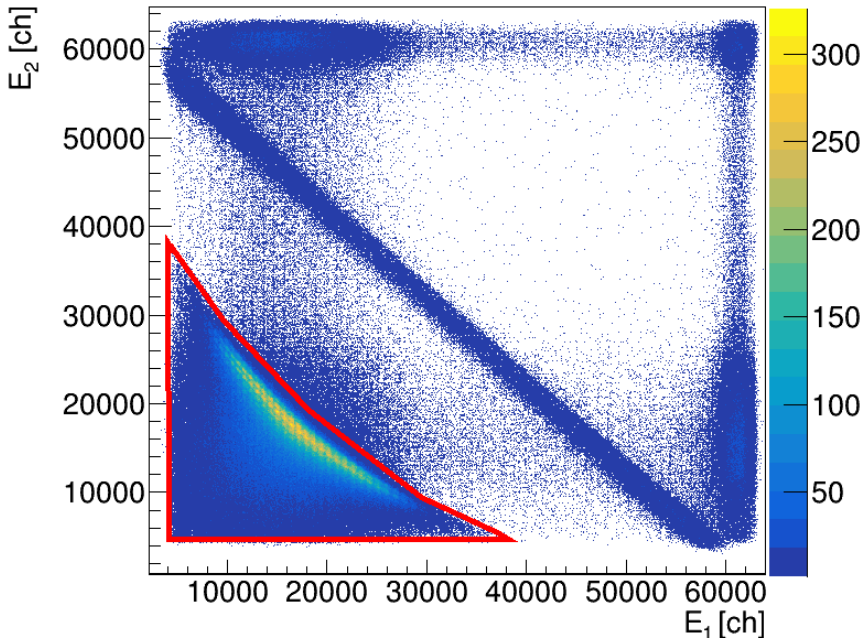

Figure 3.40: *Energy loss correlation for two fission fragments in the Twin MUSIC. The red triangle encloses the fission fragments area. This graphical cut is used to identify if the event measured in the Twin MUSIC is fission or not.*

Something to take into account is that when looking at $TPat_1$ data some fission events are identified with the Twin, even though $TPat_1$ does not include a fission trigger. The fission events that were recorded in $TPat_1$ can be of 2 kinds:

- Fission events that had $TPat_1$ and $TPat_2$ bits active in the mask and suffered from DS in $TPat_2$. These fission events are already taken into account when $TPat_2$ counts are corrected by its DS_{factor}.
- Fission events that had $TPat_1$ bit active in the mask but did not have $TPat_2$ because ToF Wall did not have 2 signals from different paddles due to a lack of efficiency. The way to distinguish these fissions in $TPat_1$ from the previous kind is to select the fissions that left less than 2 paddles signal at the ToF Wall. These fissions should be added to the fissions calculated from $TPat_2$.

To calculate the fission cross-section, not all the fission events can be counted: only those that originated in the target. Therefore, the vertex position plot is used to select fission events from the target peak, which corresponds to the events enclosed between the two red vertical dashed lines in Fig. 3.41. However, this selection does not take into account the background generated by the surrounding peaks. To deal with this, a Breit Wigner fit is performed for the scintillator and target peaks to estimate the fraction of each one contributing to the other

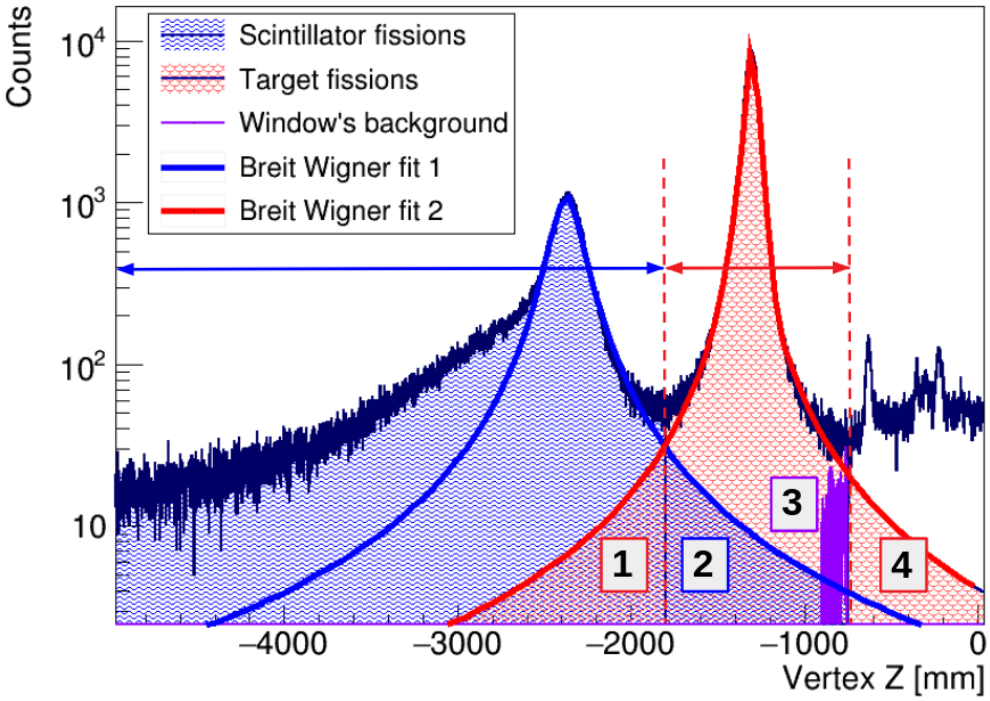

Figure 3.41: *Fission vertex Z position reconstruction. The numbers in the figure mark where the tails of the Breit Wigner from a peak contribute to the background of the adjacent regions. 1: Target background in the scintillator counts. 2: Scintillator background in the target counts. 3: Steel Window background in the target counts (obtained by subtracting the target's Breit Wigner fit to the spectrum). 4: Target background in the steel window region.*

peak. Another factor to take into account is that not all fission events from the target peak have been produced by uranium ions impinging on the target. There is a percentage that may originate from those uranium nuclei that suffered from spallation in the scintillator (or another material before the target) and the spallation residual undergoes fission in the target. The same can happen inside the target, for example, the uranium ions can suffer a spallation reaction in the first half of the target and that spallation can result in fission in the second half. All these reactions that do not correspond to fission of uranium in the target are referred to as 'secondary reactions'. For this analysis, the cross-section has been calculated following 2 different methods, which are very similar but differ in the way secondary reactions before the target are corrected. Method 1 uses the number of fission events that took place at the scintillator by selecting the scintillator peak in Fig. 3.41 to estimate the number of events lost in secondary reactions, while method 2 estimates the secondary reactions by multiplying the number of incomings by the estimated reaction rates.

3.8.3 Method 1

The fission cross section is calculated using Eq. 3.30, where the number of uranium nuclei that fissioned in the target is calculated by Eq. 3.31 and the number of uranium ions that reached the target by Eq. 3.33. Both equations are corrected by different fractions of N_{Fsci}, which is defined in Eq. 3.32 and corresponds to the number of fission events from the first peak in Fig. 3.41. Most of these fission events originate at the scintillator. Still, a small fraction might come from other materials, such as the thin steel entrance window to the vacuum chamber, or other materials before the scintillator (see the list for materials before the target in table A.1). These materials before the target cause the left side of the scintillator peak in Fig. 3.41 to have a slower drop than the ones on the right, since after the vacuum chamber window there are no layers of matter until the target.

$$\sigma_{\text{fission}} = -\text{x} \ln\left(1 - \frac{\text{N U fissions in target}}{\text{N U arrived at target}}\right) \tag{3.30}$$

$$\text{N U fissions in target} = \left(\frac{N_{2Ftgt} DS_2}{DT_2(1-AMS_2)Eff_{Twin2}} + \frac{N_{1Ftgt<2} DS_1}{DT_1(1-AMS_1)Eff_{Twin1}}\right) F_{tgt} - N_{Fsci} F_{sci} \frac{\sigma_{Ssci}}{\sigma_{Fsci}} P_{Rtgt} P_{Ftgt} \tag{3.31}$$

$$N_{Fsci} = \left(\frac{N_{2Fsci} DS_2}{DT_2(1-AMS_2)Eff_{Twin2}} + \frac{N_{1Fsci<2} DS_1}{DT_1(1-AMS_1)Eff_{Twin1}}\right) \tag{3.32}$$

$$\text{N U arrived at target} = \frac{N_1 DS_1}{DT_1(1-AMS_1)} - N_{Fsci} F_{sci}\left(1 + \frac{\sigma_{Ssci}}{\sigma_{Fsci}}\right) \tag{3.33}$$

All the variables and factors used in the equations above will be described in the following list to understand how the corrections are applied (except the downscaling (DS), dead-time (DT) and AMS factors, which were already defined in the 3.8.1 section). The numerical values for each factor can be consulted in table A.3.

Description of the variables used in Eq. 3.31:

- N_{2Ftgt} : Number of counts from $TPat_2$ that were identified as fission using the Twin graphical cut from Fig.3.40 and with a vertex position at the target using the limits from Fig.3.41
- $N_{1Ftgt<2}$: Number of counts from $TPat_1$ that were identified as fission using the Twin graphical cut from Fig.3.40 and with a vertex position at the target using the limits from Fig.3.41 and had less than 2 paddles firing at ToF Wall. These fissions were not recorded in $TPat_2$ due to a lack of efficiency of the ToF Wall, but they must be counted as valid fission events too.
- $Eff_{Twin2} = \frac{N_{2Twin>8anodes}}{N_{2Sci}}$: Twin efficiency for $TPat_2$, calculated as the ratio of events measured by the Twin (with at least 8 anodes) and the events measured by the Start scintillator.
- $Eff_{Twin1} = \frac{N_{1Twin>8anodes}}{N_{1Sci}}$: Twin efficiency for $TPat_1$.
- $F_{tgt} = 1 + I_1/I_{tgt} + I_4/I_{tgt} - I_2/I_{tgt} - I_3/I_{tgt} - P_{R\frac{1}{2}tgt}P_{Stgt}P_{R\frac{1}{2}tgt}P_{Ftgt} - P_{Rwdw}P_{Fwdw}$: Factor to correct the number of fission events coming from the target. The I_i/I_{tgt} ratios correspond to the integral of the counts for each background contribution marked with a number in Fig.3.41. The other factors correspond to the reaction probabilities needed to estimate the counts lost in secondary reactions inside the target and the mylar and aluminum window wrapping the target:
  - $P_{R\frac{1}{2}tgt}$: Probability that a uranium projectile reacts in the first half of the target.
  - P_{Stgt} : Probability that the uranium reaction in the first half of the target was spallation.
  - $P_{R\frac{1}{2}tgt}$: Probability that the spallation residue reacts in the second half of the target.
  - P_{Ftgt} : Probability that the spallation residue reaction was a fission event.
  - P_{Rwdw} : Probability that a uranium projectile reacts in the mylar and aluminum wrapping of the target.
  - P_{Fwdw} : Probability that the uranium reaction in the mylar and aluminum wrapping of the target was fission.
- N_{Fsci} : Number of fissions that happened in the scintillator or the previous materials.
- $F_{sci} = 1 - I_1/I_{sci} + I_2/I_{sci}$: Factor to correct the number of fission events from the scintillator. The I_i/I_{sci} ratios correspond to the integral of the counts for each background contribution marked with a number in Fig.3.41

- Ratio $\frac{\sigma_{\mathrm{Ssci}}}{\sigma_{\mathrm{Fsci}}}$: this ratio is a proportionality factor between fission and spallation events, and it is used to convert the obtained number of fissions coming from the scintillator ($N_{\mathrm{Fsci}}F_{\mathrm{sci}}$) into the expected number of spallation events. Due to the lack of data on the reactions, the ratio has been estimated using the data for the reaction and fission cross sections from Ref. [115] for C and H, because the scintillator is composed of both (Scintillator BC 400: H[10]C[9]). Since the steel window of the vacuum chamber was located right in front of the scintillator, there must be a little contribution coming from there too. Therefore, this conversion factor has been calculated as a weighted arithmetic mean between the ratio $\frac{\sigma_{\mathrm{SH[10]C[9]}}}{\sigma_{\mathrm{FH[10]C[9]}}}$ and the ratio $\frac{\sigma_{\mathrm{SCu}}}{\sigma_{\mathrm{FCu}}}$, where the weights were the thickness of each material in the cave. Due to the lack of data on Fe, the cross sections have been taken from Ref. [115] for Cu as an approximation. However, since the thickness of the scintillator was much larger than the iron, the result of the weighted arithmetic mean is closer to the one of the plastic.

- P_{Rtgt} : Probability that a uranium spallation residue reacts in the target.

- P_{Rtgt} : Probability that a spallation residue undergoes fission.

Description of the variables used in Eq. 3.32:

- N_{2Fsci} : Number of counts from TPat_2 that were identified as fission using the Twin graphical cut from Fig.3.40 and with a vertex position at the scintillator using the limits from Fig.3.41.

- $N_{\mathrm{1Fsci<2}}$: Number of counts from TPat_1 that were identified as fission using the Twin graphical cut from Fig.3.40 and with vertex position at the scintillator using the limits from Fig.3.41 if less than 2 paddles of the ToF Wall fired.

Description of the variables used in Eq. 3.33:

- N_1: Number of events in TPat_1. This counter, multiplied by its correction factors, represents the total number of events that passed through the scintillator.

- Factor $(1 + \frac{\sigma_{\mathrm{Ssci}}}{\sigma_{\mathrm{Fsci}}})$: This factor multiplied by N_{Fsci} corresponds to the number of fissions plus the spallations produced in the materials before the target.

3.8.4 Method 2

The fission cross section is calculated using Eq. 3.34, where the number of uranium nuclei that fissioned in the target is calculated with Eq. 3.35 and the

number of uranium ions that reached the target by Eq. 3.37. In this case, the information from Fig. 3.41 for the fissions before the target is not used. The secondary reactions are estimated using only the number of incoming projectiles $\left(\frac{N_1 DS_1}{DT_1(1-AMS_1)}\right)$ and the reaction probabilities in the layers of matter before the target (see table A.1).

$$\sigma_{\text{fission}} = -\text{x} \ln\left(1 - \frac{\text{N U fissions in target}}{\text{N U arrived at target}}\right) \tag{3.34}$$

$$\text{N U fissions in target} = \left(\frac{N_{2Ftgt} DS_2}{DT_2(1-AMS_2)Eff_{Twin2}} + \frac{N_{1Ftgt<2} DS_1}{DT_1(1-AMS_1)Eff_{Twin1}}\right) F_{tgt} - N_{Ssci} P_{Rtgt} P_{Ftgt} \tag{3.35}$$

$$N_{Ssci} = \frac{N_1 DS_1 P_{Rbtgt} P_{Sbtgt}}{DT_1(1-AMS_1)} \tag{3.36}$$

$$\text{N U arrived at target} = \left(\frac{N_1 DS_1}{DT_1(1-AMS_1)}\right)(1 - P_{Rbtgt}) \tag{3.37}$$

Since Method 1 and Method 2 have a lot in common except for the secondary reactions correction, most of the variables were already defined in the previous sections. Therefore, only the new variables will be explained in the following list.

Description of the variables used in Eq. 3.35:

- N_{Ssci} Number of spallation events that occured in the scintillator or in matter upstream from it.
- P_{Rtgt} : Probability that the spallation residue reacts in the target.
- P_{Ftgt} : Probability that the spallation residue reaction was a fission events.
- P_{Rbtgt} : Probability that a uranium projectile reacts before the target. It has been calculated using the entire list of materials between the entrance of the cave and the target.
- P_{Sbtgt} : Probability that the uranium reaction was spallation.

Description of the variables used in Eq. 3.37:

- P_{Rbtgt} : Probability that a uranium projectile reacts before the target. It has been calculated using the entire list of layers of matter between the entrance of the cave and the target. This factor is used to correct the number of incoming ions for all events lost in reactions before the target.

Chapter 4

Results

In this chapter, the main results obtained in the thesis are presented in two different sections. The first section is dedicated to the pre-saddle dynamics, that is, the evolution of the fissioning system from the moment of the reaction to the saddle point, and the second to post-saddle dynamics, that is, the evolution from the saddle to the final fission fragments. Since spallation reactions cover a wide range of excitation energies, fission can be studied both at low and high excitation energies, selecting a specific reaction channel. Therefore, the pre-saddle dynamics section will study observables sensitive to the dissipative and transient effects that manifest at high excitation energies before the saddle point, such as the partial fission yields and the widths of the charge distributions. The post-saddle dynamics section will focus on the observables sensitive to the physics between the saddle and the scission configuration, like the fission yields and the total kinetic energy. Special attention will be paid to the evolution of these observables with excitation energy to understand phenomena related to energy sorting that manifest themselves at low excitation energies, such as neutron excess or the even-odd effect.

4.1 Pre-saddle dynamics

In this section, the total fission cross-section for the $^{238}\mathrm{U} + \mathrm{p}$ reaction at 540Mev/u is presented and compared with previous experimental data. The partial fission cross sections and the widths of the charge distributions are obtained for different fissioning systems and compared with previous experimental data and simulations. To do so, the INCL simulation software was combined with different de-excitation models such as ABLA, GEMINI, or SMM. In this way, the importance of taking into account features such as dissipation, transient time, or shell effects can be tested, as well as the different formalisms the models use to calculate level densities.

4.1.1 Total fission cross section

Methods 1 and 2 described in sections 3.8.3 and 3.8.4 have been used to calculate the fission cross-section from 5 different runs of the experiment. To have an average value for each run, the fission cross section and the twin efficiencies were calculated for each group of 12 spills (about 3000 counts for each group). The measurement of this average value has two types of uncertainty associated. One is the type A uncertainty, associated with the statistical analysis, and the other is a type B uncertainty due to the lack of precise knowledge of the different parameters used during the corrections [116]. Both the mean values and the uncertainties for the different correction parameters can be consulted in table A.3. For each group of 12 spills, a random value within the estimated variation range was assigned to every correction factor. By doing so, the uncertainty of the mean of the fission cross section for each run corresponds to the combined uncertainty of type A and type B. Finally, the mean value of the 5 runs is calculated using a weighted mean (weighted by the statistics of each run) and the uncertainty corresponds to the variance of the weighted mean corrected for over- or under-dispersion [117]. The results for each run and the final average and uncertainties are displayed in table 4.1. A more detailed description of the averages and uncertainties treatment can be found in Sec. A.5.

Run	Fission cross-section [mb] Method 1	Fission cross-section [mb] Method 2
209	1540 ±10 (101)	1542 ±10 (103)
216	1513 ±14 (53)	1519 ±14 (52)
217	1516 ±7 (46)	1523 ±7 (46)
221	1494 ±5 (46)	1500 ±5 (47)
223	1478 ±8 (59)	1485 ±8 (60)
Average	1511 ±13	1516 ±12

Table 4.1: *Fission cross-section results for 5 experimental runs. The uncertainties of each run correspond to the uncertainty of the mean, and the value in parenthesis corresponds to the standard deviation of the distribution.*

Both methods result in a very similar value, which is expected because they have much in common. Still, the fact that they are so close serves to prove that the corrections by secondary reactions were well evaluated. The final result for method 1 is displayed in Fig. 4.1. As can be seen, there is a good agreement with previous experimental results from Ref. [118] in inverse kinematics and Ref. [119] in direct kinematics. It also agrees with the theoretical calculations from INCL+ABLA within the corresponding experimental uncertainties (this can be better seen in Fig. 4.1 inset).

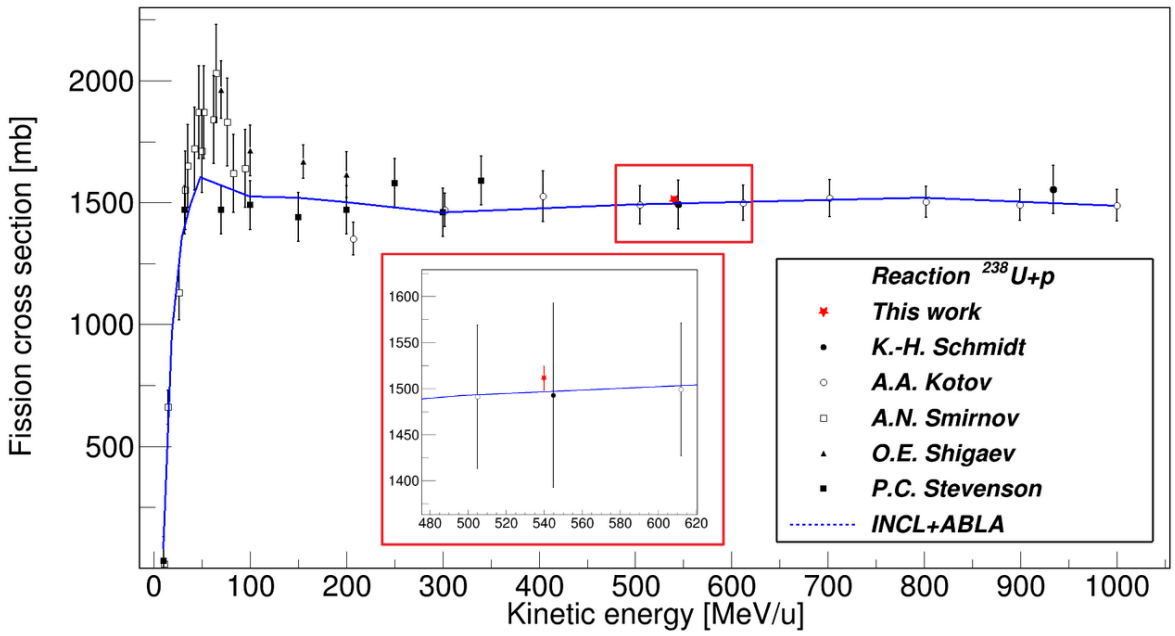

Figure 4.1: *Fission cross-section dependence on the projectile's kinetic energy. Experimental data from previous works taken from Ref. [120].*

4.1.2 Partial fission cross sections

The partial fission cross-sections are the cross-sections for the different fissioning systems that can be produced in the reaction. The fissioning systems are selected by adding $Z_1 + Z_2$ of the fission fragments since the proton evaporation probabilities are very low. Then, the partial cross sections were calculated using Eq. 3.24. To obtain the number of events for each fissioning system, an integral was performed over the fissioning systems charge distribution plots displayed in Fig. 4.2. The distributions displayed in Fig. 4.2 range between $Z_1 + Z_2 = 80$ and 93, and have a resolution of $\Delta Z < 0.4$ FWHM for the central charges in all fissioning systems. It can be seen how the lighter fissioning systems show a more Gaussian-like shape, while the heavier ones become wider and more flat at the top. This is the effect of changing from a high to low energy reaction channel when moving from more to fewer nucleons removed from the projectile, as seen in Fig. 4.3, which shows the excitation energy evolution with the fissioning system charge.

The lighter fissioning systems were generated in more violent reactions where many nucleons were removed from the projectile and the recoil was left with high excitation energy. For high-energetic fissioning systems, the symmetric channel dominates over the asymmetric, and therefore the atomic number distributions show a Gaussian-like shape as the ones from $Z_1 + Z_2 = 80$ to 90. However, heavier fissioning systems were produced in reactions closer to single proton knockout, where fewer nucleons were removed and the recoil had less excitation energy.

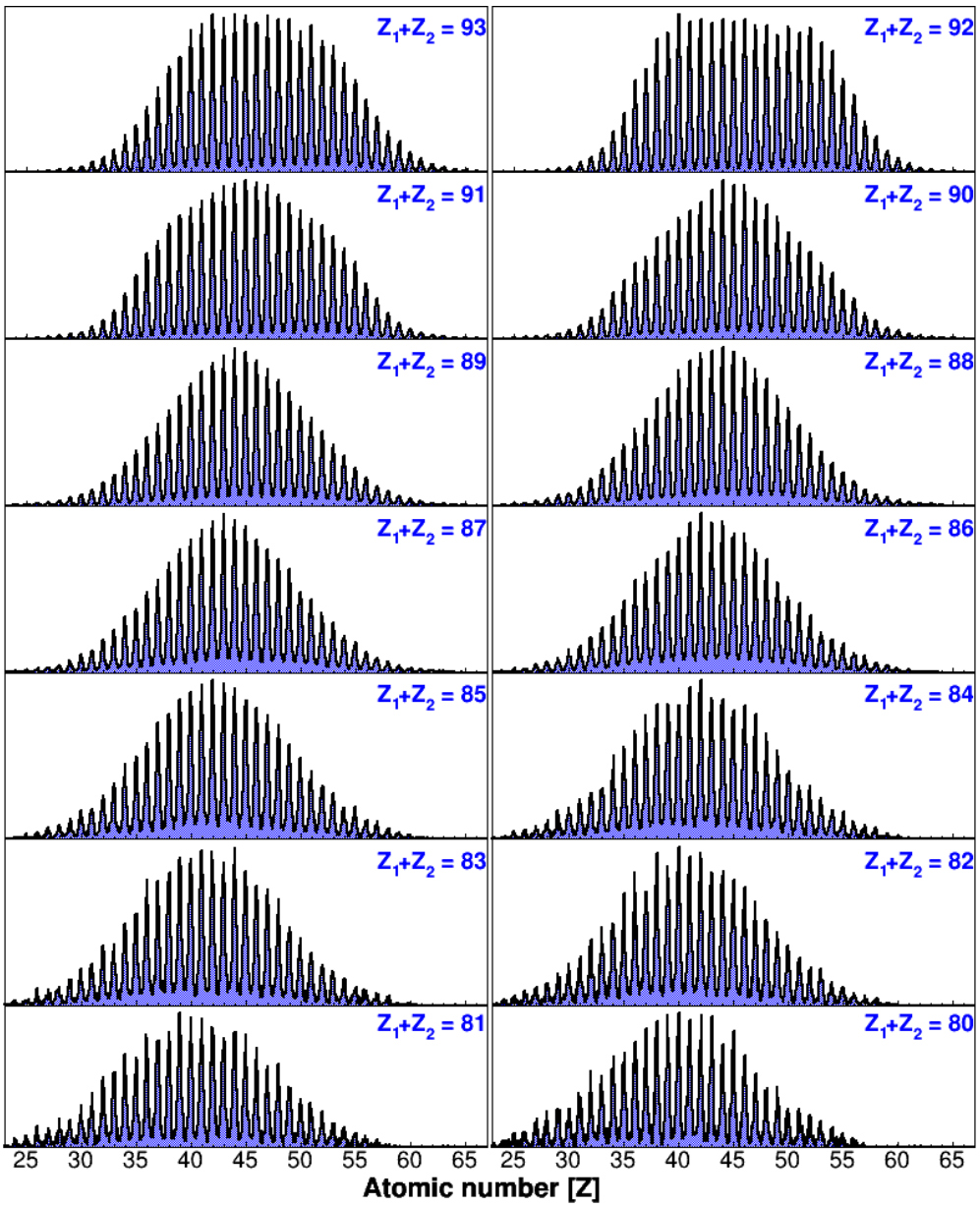

Figure 4.2: *Atomic charge distribution for each fissioning system produced in the reaction* $^{238}\mathrm{U} + \mathrm{p}$ *at 540 MeV/u.*

These systems mostly fission through the asymmetric valleys. In these graphs, since no selection for (p, 2p) was applied, asymmetric charge distributions will not be directly seen, because there is still a lot of contribution from (p, 2pXn) reactions. Still, the flattening at the top of the distribution is a hint of the two asymmetric peaks.

Fig. 4.4 shows the resulting partial fission cross for each distribution displayed in Fig. 4.2 in comparison with previous experimental data and simulations. The partial fission cross-section for both reactions on carbon (black dots) and proton (red triangles) targets presents a maximum for $Z_1 + Z_2 = 91$. This

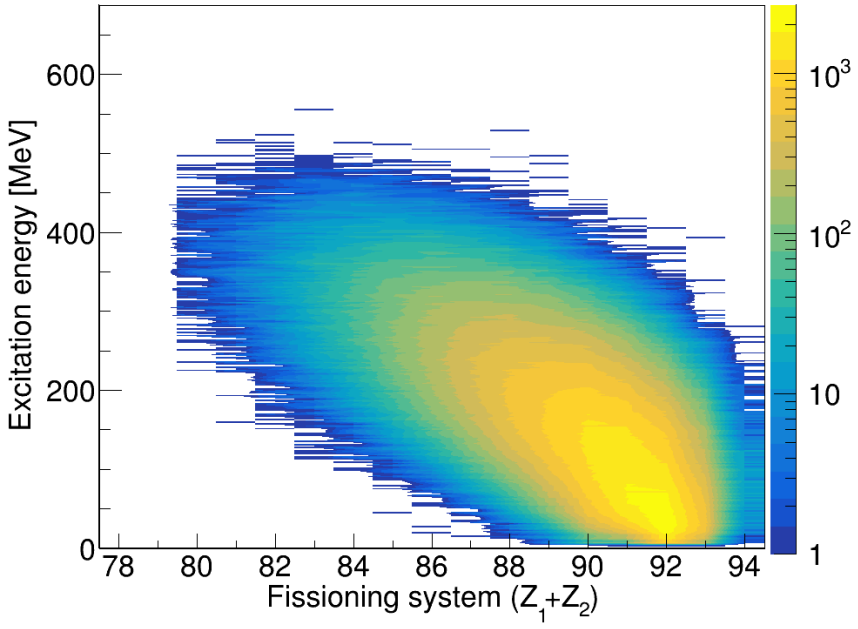

Figure 4.3: *Excitation energy dependence on the fissioning system charge. This graph has been obtained from data simulated with INCL+ABLA [103].*

corresponds to the Pa fissioning systems, which originated when only a proton was removed from the projectile. The second largest cross-section corresponds to the fission of uranium when the projectile passes through the target without reacting or only having neutrons removed. For heavier systems produced in charge exchange reactions, the fission cross-section drops quickly. For all the fissioning systems, the fission cross-section is greater in the carbon target, since the reaction cross-section increases with the mass of the target nucleus. This difference increases when moving towards lighter systems because in the carbon target fragmentation reaction occurs, where the probability of removing more nucleons is higher.

The results are compared with several theoretical calculations based on INCL simulations and different de-excitation models. All de-excitation models reproduce the data rather well for the heaviest fissioning systems, that is, the low-energy reaction channels. It is for the lighter fissioning systems, or, high-energy reaction channels, where some models overestimate or underestimate the fission-cross section. The ABLA - Bohr Wheeler model (pink short-dashed line) does not take into account dissipation or transient times, while the ABLA - Kramers model (violet long-dashed line) takes into account dissipation but no transient times. As expected, both models overestimate the fission cross sections for the lighter systems, because at high excitation energies, the transient time effect becomes more noticeable and causes a reduction of the fission probability

which is not taken into account in these statistical models. The models in better agreement with the experimental data are the ones for ABLA when including a dissipation coefficient ($\beta = 4.5 \times 10^{21} s^{-1}$, from Refs. [121, 122, 15]) and Fokker-Planck time-dependent fission decay widths as the one in Eq. 1.12 (dark-blue solid line) and GEMINI (blue long-dashed-dotted line). GEMINI does not take dissipation or transient times into account and still reproduces the data. This is because the fission probability depends on the ratio between the level density at the saddle and at the ground state, and as shown in Eq. 2.13, GEMINI has a parametrization of this ratio dependent on the excitation energy adjusted with experimental data (while the one used for ABLA was independent of the excitation energy). The SMM calculation (green short-dashed-dotted line) does not include dissipation or transient effects, which in principle would overestimate the fission cross-sections. Instead, SMM underestimates the fission cross-sections. The reason could be an overestimation of the multifragmentation reactions over the other channels, since it has been observed in previous studies [107] that SMM has lower multifragmentation thresholds which lead to higher multifragmentation cross sections than ABLA and GEMINI and deviations from experimental data. In conclusion, either taking into account dissipation and transient time effects as ABLA or parametrizing energy level densities with experimental data like GEMINI, would correctly reproduce the fission cross sections for high excitation energies.

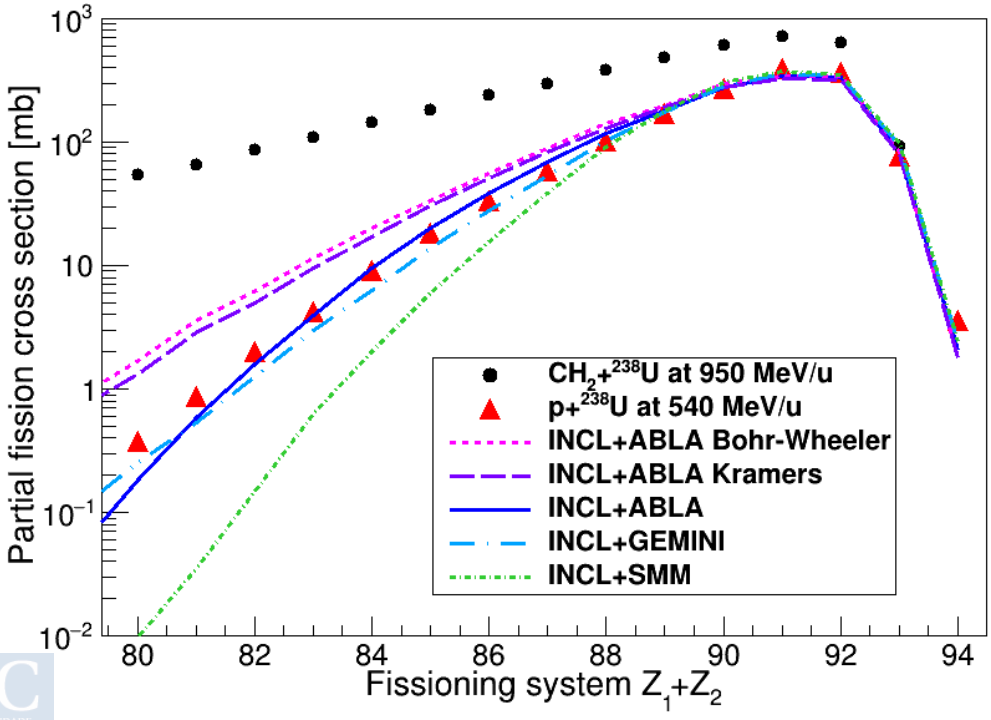

Figure 4.4: *Partial fission cross sections for the fissioning systems produced in the $p + ^{238}U$ at 540 MeV/u reaction. Data for the reaction $CH_2 + ^{238}U$ at 950 MeV/u taken from Ref. [123].*

4.1.3 Widths of the fission fragment charge distributions

Another important observable derived from the atomic charge distributions of the fission fragments in Fig. 4.2 are the widths of the distributions for each fissioning system. These are calculated as the width of the Gaussian fit performed over the charge distributions, as shown in Fig. 4.5 (binning has been changed with respect to Fig. 4.2).

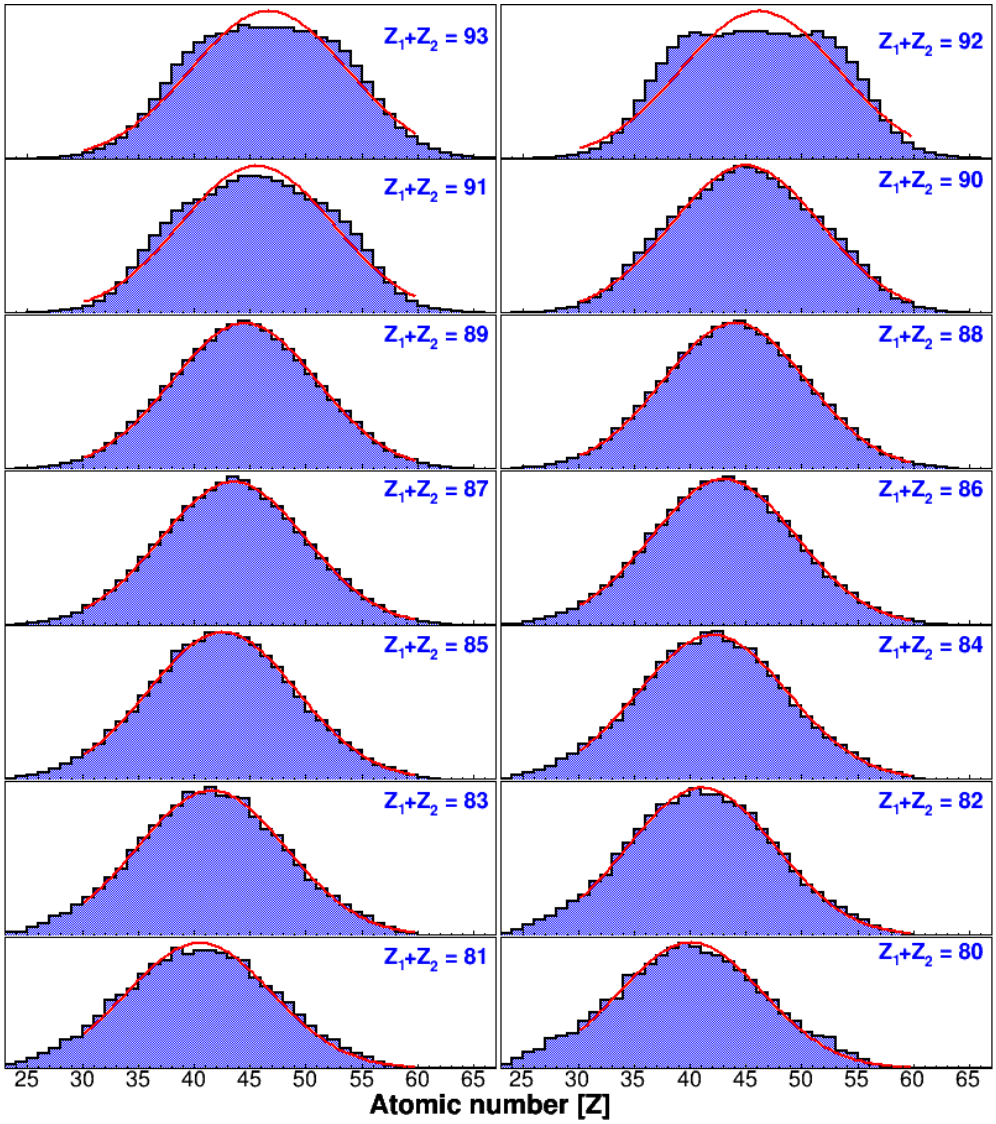

Figure 4.5: *Atomic charge distribution for each fissioning system produced in the reaction* $^{238}\mathrm{U} + \mathrm{p}$ *at 540 MeV/u. Gaussian fits are performed for each fissioning system.*

The results for the widths of the charge distributions of the fission fragments from this experiment are presented in Fig. 4.6 for each fissioning system, and compared with previous experimental data and simulations. In previous studies using ^{208}Pb projectiles, it had been concluded that the width of the charge distribution was independent of the target choice [122, 15, 124]. However, the

widths from this experiment show a clear difference from those obtained for the same reaction but heavier targets, such as CH_2 and Al from Refs. [123, 125]. This can be explained by the dependence of the width of the distribution on two observables: the temperature at the saddle and the curvature of the potential. The width of the atomic charge distributions was demonstrated to be sensitive to

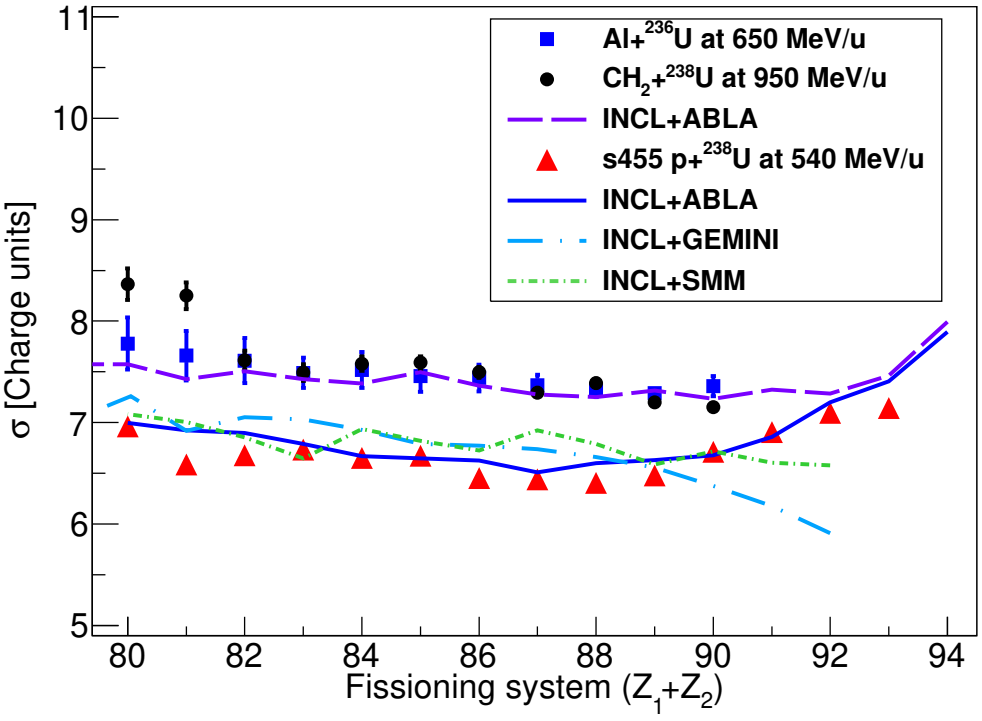

Figure 4.6: *Widths of the charge distribution for the fissioning systems produced in $p+^{238}U$ at 540 MeV/u. Data for the reactions with CH_2 and Al taken from Refs. [123, 125] respectively.*

the temperature at the saddle point, as shown in Eq. 4.1 [126], where A is the mass number of the fissioning system, T_{saddle} the temperature at the saddle and $\frac{dV^2}{d\eta^2}$ the second derivative of the potential with respect to η, the mass-asymmetry deformation parameter. The deformation parameter η indicates the degree of mass asymmetry of the fissioning system, and it is defined in Eq. 4.1 too, where M_{ff} is the mass of the fission fragment.

$$\sigma^2 = \frac{A^2 T_{saddle}}{16\frac{dV^2}{d\eta^2}}, \quad \eta = \frac{4/A}{M_{ff} - A/2} \tag{4.1}$$

Since the temperature at the saddle point directly relates to the excitation energy, and this to the number of nucleons removed, the widths of the charge distribution increase for the lighter fissioning systems, as seen in Fig. 4.7 (left) for all the reactions. The second derivative $\frac{dV^2}{d\eta^2}$ is usually referred to as 'curvature' or 'stiffness', and represents the curvature of the macroscopic potential. Large curvatures in the macroscopic potential translate into narrower symmetric modes

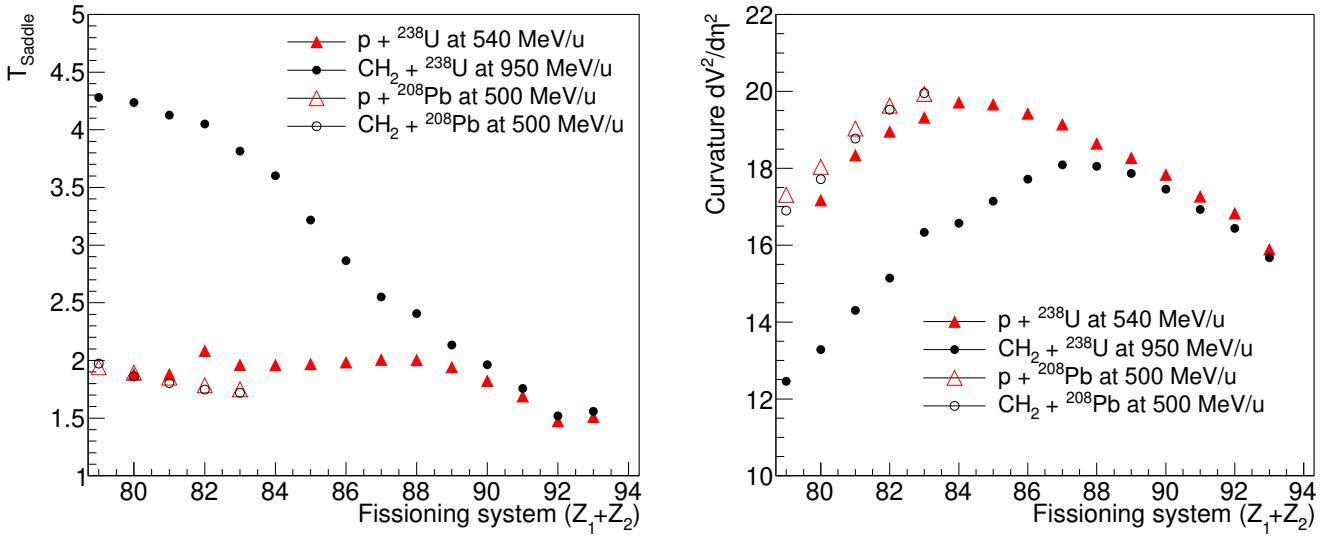

Figure 4.7: *Temperature (left) and curvature (right) at the saddle point for the different fissioning systems produced in the reactions presented in the legend. Both figures are based on simulations using INCL+ABLA. ABLA calculates the curvature using the parameterization from Ref. [127].*

in the yields, and therefore smaller widths of the charge distribution. The evolution of the curvature as a function of the fissioning systems exhibits a maximum for a certain fissioning system, as seen in Fig. 4.7 (right).

Therefore, the difference in the width of the charge distribution between spallation and fragmentation reactions presented in Fig. 4.6 can be explained because the fragmentation reaction reaches higher temperatures at the saddle point and presents lower curvatures, as seen in Fig. 4.7 for $CH_2 + ^{238}U$, both factors contributing to the increase in the width. For both reactions, it can be seen that the width increases from $Z_1 + Z_2 \approx 85$ towards the lighter systems, since the temperature increases and the curvature drops. In previous experiments with Pb [122, 15, 124], the width could have remained constant when changing the target because the temperature at the saddle and the curvature have very similar values, as shown in Fig 4.7. Concerning simulations, the violet long-dashed line is the INCL+ABLA calculation for the fragmentation reaction and reproduces the data rather well except for the two lightest systems. For the reaction of this work, calculations were done with INCL+ABLA (dark blue solid line), INCL+GEMINI (blue long-dashed-dotted line) and INCL+SMM (green short-dashed-dotted line). The ABLA calculation is the one that better reproduces the data, especially for the heaviest fissioning systems, since for $Z_1 + Z_2 > 89$, GEMINI and SMM fail to reproduce the data tendency. This might happen due to GEMINI and SMM not taking into account shell effects in the potential energy description, which become more noticeable for these low-energy channels and contribute to the broadening of the fission widths.

4.2 Post-saddle dynamics

In this section, the dependence of several post-saddle observables on the excitation energy will be analyzed. The section will start with a study on the observables that are sensitive to the excitation energy of the fissioning system since as it will be further explained within the section, it was not possible to directly reconstruct the excitation energy using the Si-tracker. Therefore, other observables will be evaluated as an indicator of the excitation energy and calibrated to energy units by comparing them with previous experimental data. Afterward, several suppression functions will be tested for the fission yields of this experiment at different excitation energy conditions. Then the even-odd staggering, neutron excess and total kinetic energy will be studied for different excitation energy conditions.

4.2.1 Fission yields evolution with the excitation energy

One of the main goals of this experiment was to study the evolution of the fission yields with the excitation energy of the fissioning system. The excitation energy reconstruction was thought to be made using the missing energy method, which requires the momenta reconstruction of the knocked-out protons from the (p, 2p) reaction. The momenta would be reconstructed using Califa's energy loss measurement and the AMS tracking. However, AMS was exposed to high rates of delta electrons from secondary ionizations along the setup and it was not possible to reconstruct the proton's trajectories using this detector. To see a further detailed explanation of the AMS issue, see Ref. [109]. Therefore, other observables that were sensitive to the excitation energy of the fissioning system had to be used: the opening angle between the two knocked-out protons and the mass of the final fission fragments. The opening angle for the quasi-free (p, 2p) should be centered at 80º as commented in 2.1.2 due to the Lorentz Boost shrinking the angle.

Fig. 4.8 shows the evolution of both elemental (left) and isobaric (right) fission yields for the Z=91 fissioning system with the opening angle. The blue line is a thin cut around 80º, which should have a considerable contribution of quasi-free (p, 2p) reactions. Since these reactions lead to a fissioning system with low excitation energies, shell effects become noticeable by the appearance of two asymmetry peaks. The asymmetry decreases with decreasing opening angle, as seen in the last cut, which is mostly symmetric. In the isobaric yields, the peak of the lighter fragments for the asymmetric fission has higher yields than the heavier and it is partially eclipsed. This is due to the neutron evaporation from the symmetric fission fragments, which shifts the distribution to the left.

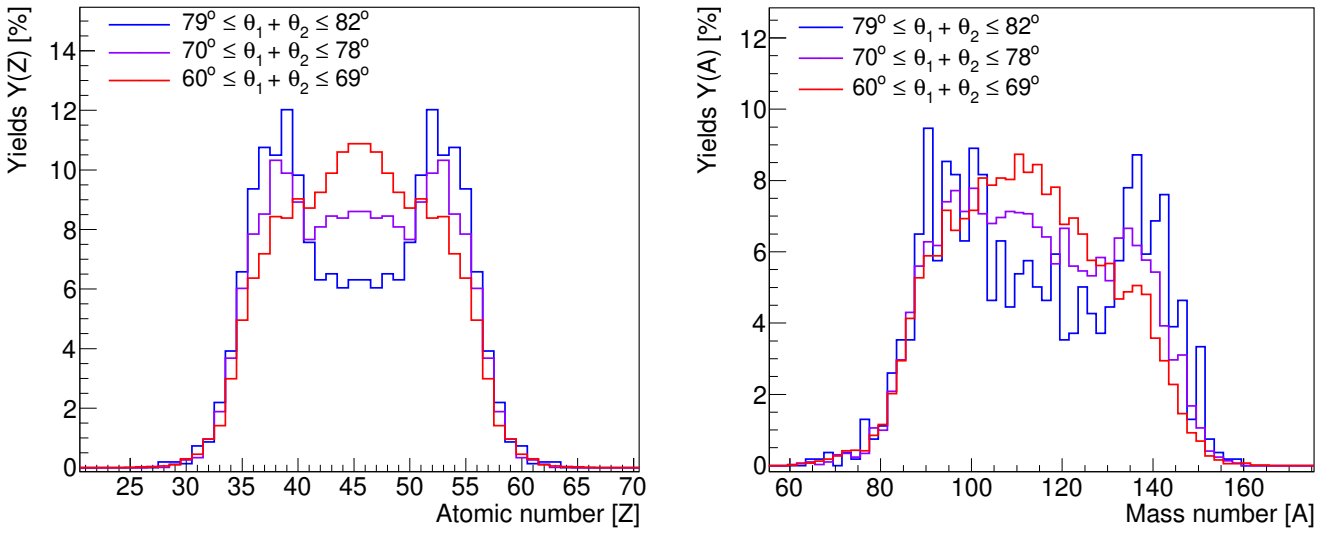

Figure 4.8: *Evolution of the fission yields normalized to 200% for Z=91 fissioning systems at different opening angle conditions. Left: Elemental fission yields. Right: Isobaric fission yields (2 masses per bin).*

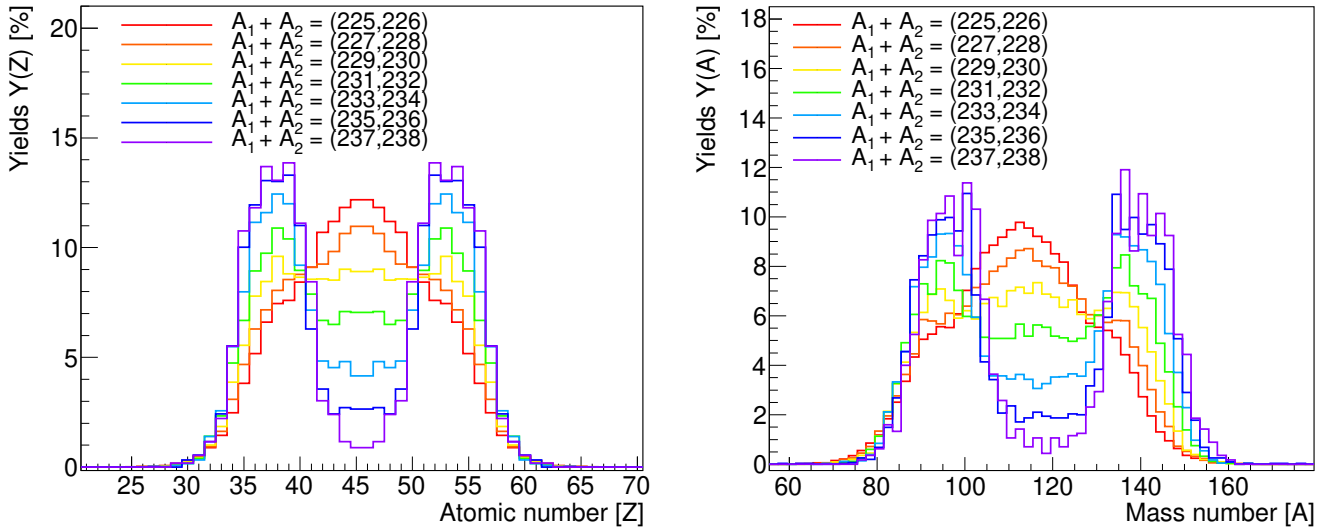

Figure 4.9: *Evolution of the fission yields normalized to 200% for Z=91 fissioning system at different cuts in mass addition. Left: Elemental fission yields. Right: Isobaric fission yields (2 masses per bin). The fission yields with their statistical error can be consulted in the tables A.5-A.11 for Y(Z) and in tables A.5-A.11 for Y(A).*

Another observable that is very sensitive to the excitation energy is the mass of the fissioning system, because the higher the excitation energy of the system, the more neutrons it will evaporate, and the lighter the system will become. This observable can be approximated by adding the mass of the two complementary fission fragments. It is important to notice that this is just an approximation because the fission fragments can evaporate several neutrons after the scission, which is not taken into account just by adding the final mass of the fission fragments. Therefore, from now on, this observable will be referred to as 'mass addition'. By performing cuts on the mass addition, the evolution of the yields

with the energy can be inferred. The evolution is shown in Fig. 4.9 for both elemental (left) and isobaric (right) fission yields for the fissioning system Z=91. Each line corresponds to a cut of 2 consecutive masses, and it can be seen in both plots how the yields evolve from symmetric to asymmetric with increasing mass addition. This observable seems to be more sensitive to the excitation energy than the opening angle since it allows to reach an almost fully asymmetric distribution for the last cut in $A_1 + A_2 = (237,238)$.

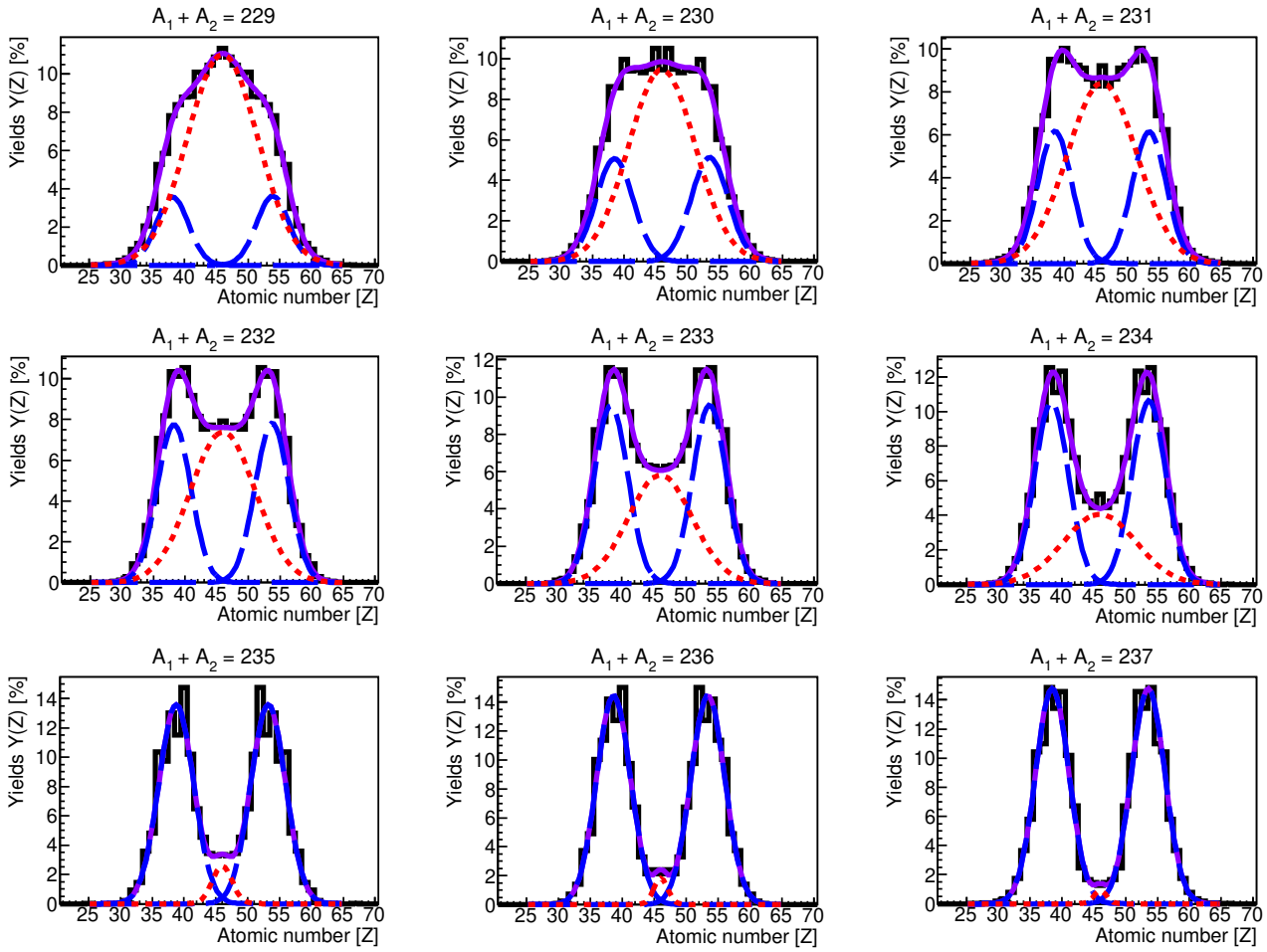

Figure 4.10: *Elemental fission yields normalized to 200% for Z=92 fissioning system. Each cut corresponds to a different mass addition cut. Within each graph, the black full line represents the experimental data, the blue long-dashed lines are the asymmetric Gaussian fits, the short-dashed red line is the symmetric Gaussian fit, and the full violet line is the 3 Gaussian fit. The fission yields data with the errors are listed in tables A.26-A.34.*

In this work, a calibration was performed to infer the excitation energy from the mass addition of the fission fragments. To do so, the peak-to-valley ratio was calculated for different fissioning systems as written in Eq. 4.2, where Y_{Lasym}, Y_{Hasym} and Y_{sym} are, respectively, the amplitudes of the light-asymmetric, heavy-asymmetric and symmetric peaks. To obtain the amplitude of each peak, a 3-Gaussian fit was performed for each fissioning system, as seen in Fig. 4.10.

$$\text{Peak} - \text{to} - \text{valley ratio} = \frac{(\text{Y}_{\text{Lasym}} + \text{Y}_{\text{Hasym}})/2}{\text{Y}_{\text{sym}}} \tag{4.2}$$

Fig. 4.11(left) shows the correlation between the mass addition and the peak-to-valley for this experiment. Fig 4.11(right) shows the correlation between the excitation energy and the peak-to-valley ratio for a reaction in direct kinematics with neutrons from Zöller et al. [128] and the Coulex reaction from Pellereau et al. [8]. Regarding the Zöller et al. data, the excitation energy was calculated using INCL+ABLA for each incident neutron energy. It can be seen how both plots (left and right) show a similar decreasing exponential tendency, and the peak-to-valley from Pellereau et al. coincides with the one for this reaction at $A_1 + A_2 = 236$, as seen in Fig. 3.39. Therefore, an exponential fit is performed over the Zöller et al. and Pellereau et al. data to obtain an equation that enables the conversion from peak-to-valley ratio to excitation energy, which can be seen in Eq. 4.3. The fit parameters and their uncertainties are displayed in the plot.

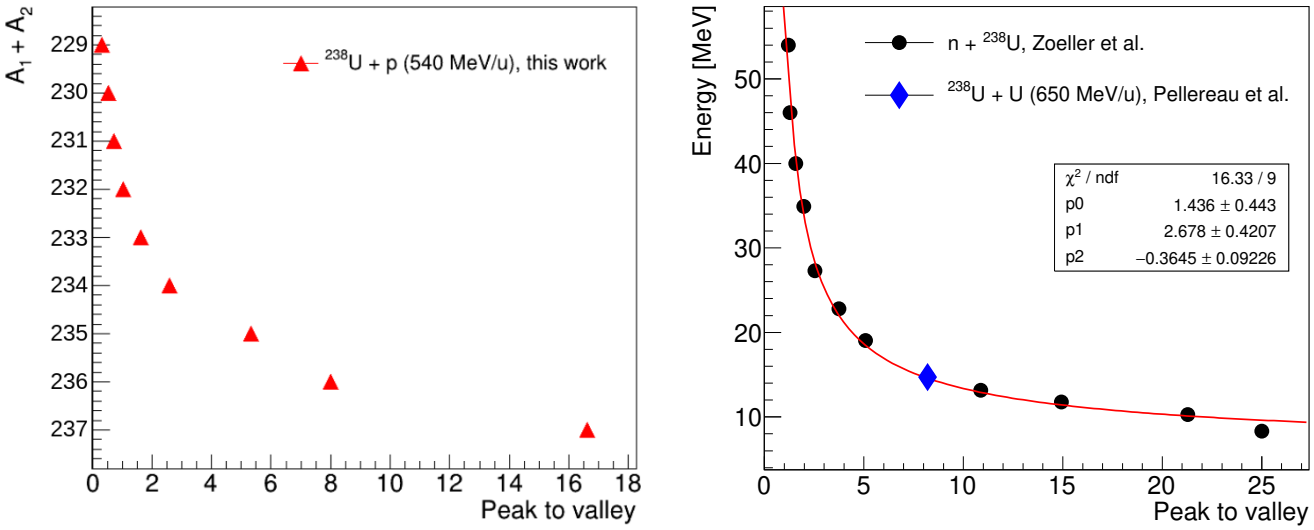

Figure 4.11: *Left: Correlation between mass addition of the fission fragments and the peak-to-valley ratio. Right: Correlation between excitation energy and the peak to-valley-ratio from Zöller et al [128] and Pellereau et al. [8].*

$$\text{E[MeV]} = \exp(\text{p0} + \text{p1}(\text{Peak} - \text{to} - \text{valleyratio})^{\text{p2}}) \tag{4.3}$$

Fig. 4.12 shows the peak-to-valley ratio correlation with the excitation energy for several data sets. The red triangles correspond to calibrated excitation energies from this work, based on Eq. 4.3. The data follows a behaviour consistent with data at lower excitation energies from Vives et al. [129] and Ramos et al. [130],

and the calibration point at a mass addition of 236 is also in good agreement with Koning et al. [131]. The horizontal error bars in the figure are not uncertainties, they correspond to the range in excitation energy associated with 1 unit in mass addition. As can be seen, this range increases with excitation energy, which means that for lower mass addition cuts, the range covered in excitation energy is wider.

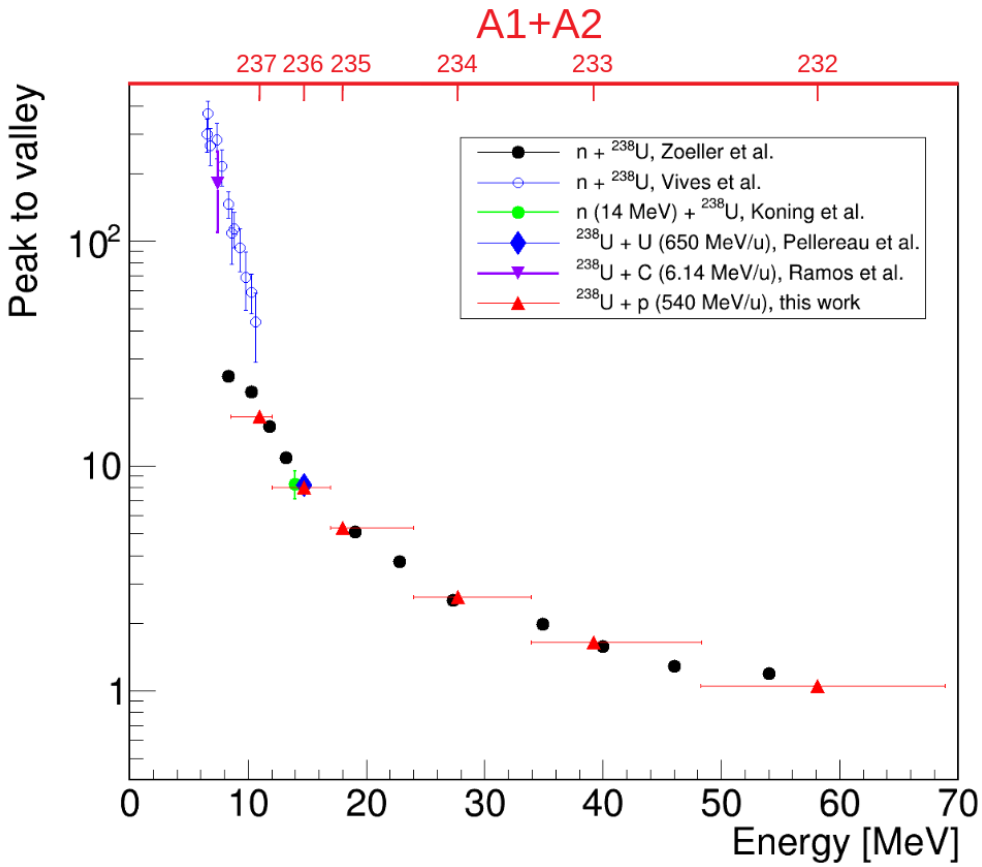

Figure 4.12: *Evolution of the peak-to-valley ratio as a function of both the excitation energy of the fissioning system and the mass addition. The fissioning system Z=92 has been selected for the red triangles corresponding to the data from this work. The horizontal error bars in the figure are not uncertainties, they correspond to the range in excitation energy associated with the range selected in mass addition. The data from previous experiments was taken from Zöller et al. [128], Vives et al. [129], Koning et al. [131], Pellereau et al. [8] and Ramos et al. [130].*

In addition, a simulation was performed with INCL+ABLA to test the correspondence between the mass addition and the excitation energy. Fig. 4.13 (left) shows the energy distribution corresponding to each one of the mass addition cuts between 231 and 237. As can be seen, even though the mean value of the excitation energy increases with the decrease in mass addition, there is a lot of contamination in every cut from all the others. This is due to all the possible combinations of nucleon knock-out and neutron evaporation that could lead to that mass addition of the final fission fragments. Fig. 4.13 (right) shows the mean value of the Excitation energy corresponding to each one of the mass addition cuts. The first 4 points starting from the right in this plot (237,236,235 and 234)

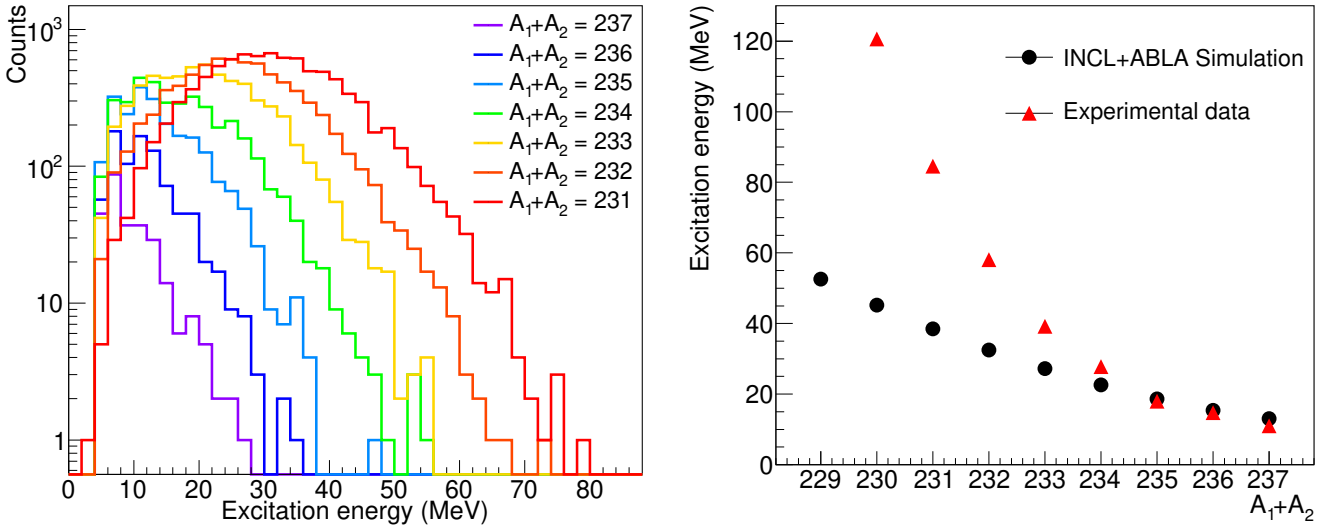

Figure 4.13: *Left: Simulated excitation energy distribution per mass addition. Right: Correlation of the excitation energy with the mass addition for both experimental calibrated data and simulation.*

are in fair agreement with the simulated data, coinciding also with the points with a reasonable energy range in Fig. 4.12. Below mass addition 234, there is no agreement anymore between the simulation and the calibration with experimental data. As a conclusion, one can trust the calibration for these 4 mass addition cuts above 233, but taking into account that each one covers a certain range in excitation energy and that they will have contamination from other energies.

4.2.2 Damping of shell effects with the excitation energy

In this section, different suppression functions are compared to check how well they reproduce the damping of the shell effects with the excitation energy for the fission yields of this experiment. To do so, the reaction is simulated with INCL+ABLA for different suppression functions and compared with the experimental data for several mass addition cuts. These cuts range from almost complete symmetry at A=229, to almost complete asymmetry at A=237, which corresponds to around 11 MeV based on the calibration. The employed functions are the Woods-Saxon function described in Eq. 1.15 proposed by Randrup in Ref. [17] and the purely exponential form $S(E^*) = \exp(-E^*/E_0)$. The functions were tested varying the parameters over a wide range and minimizing the residue with respect to the difference to the experimental data.

In Fig. 4.14 the fission yields for $Z_1 + Z_2 = 92$ and the different mass addition cuts are displayed together with the results for the different suppression functions for comparison. The blue line corresponds to the Woods-Saxon function proposed by Randrup [17], taking the same parameters $E_0 = 15$MeV and $E_1 = 20$MeV used in the article. The green and orange lines correspond, respectively, to the

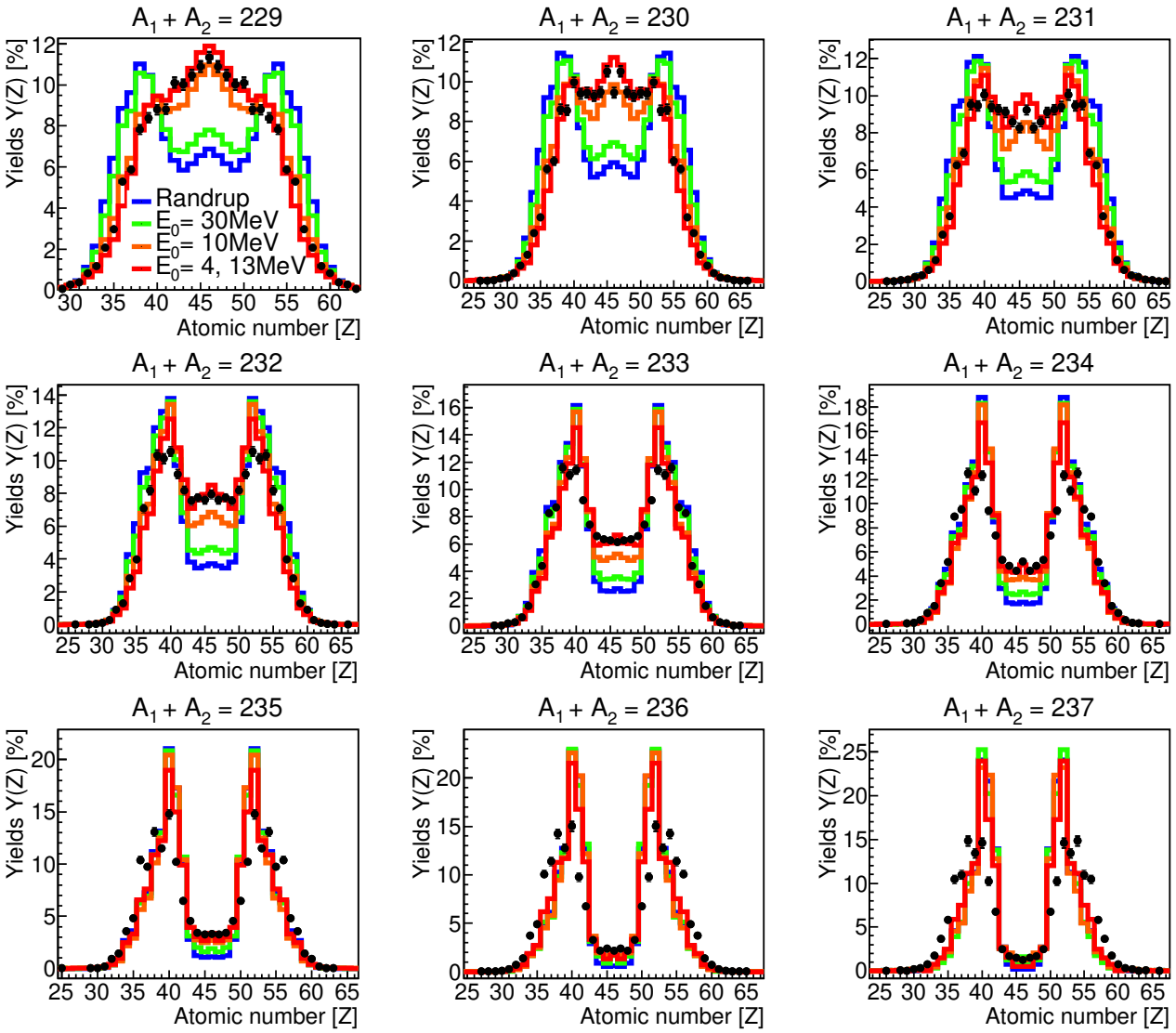

Figure 4.14: *Atomic fission yields normalized to 200% for Z=92 fissioning systems and different cuts in mass addition. The experimental data is represented by black dots and the INCL+ABLA simulation with solid lines. The blue line corresponds to the Woods-Saxon function proposed by Randrup [17] with* $E_0 = 15$ *MeV and* $E_1 = 20$ *MeV. The other lines correspond to the exponential* $S(E^*) = exp(-E^*/E_0)$*, with* $E_0 = 30$ *MeV for the green line and* $E_0 = 10$ *MeV for the orange line. The red line is a combination of* $E_0 = 4$ *MeV for excitation energies lower than 20 MeV and* $E_0 = 13$ *MeV for higher excitation energies.*

exponential functions $S(E^*) = \exp(-E^*/30MeV)$ and $S(E^*) = \exp(-E^*/10MeV)$. It was found that the Woods-Saxon function works better for the low energy range, up to 20MeV. It can be seen in the figure how for the default values E_0 and E_1 from Randrup's publication, the function remains rather asymmetric at $A_1 + A_2 = 229$, while the experimental data is mostly symmetric. This also did not change substantially for other combinations of the E_0, E_1 parameters. In the case of the exponentials, lower E_0 values performed rather well, as observed in the plot for the orange line compared to the green line. However, they could not

fully reproduce the experimental data. In conclusion, even though some of the chosen parameters for both the exponential and Woods-Saxon functions fitted rather well for certain energy ranges, none of them reproduced the asymmetry along the whole range in mass addition. It was finally found that the option that minimized the residue was a combination of two exponentials, $E_0 = 4MeV$ for the excitation energies below 20MeV and $E_0 = 13MeV$ for excitation energies above 20MeV, represented with a red line in the figure. A figure of the residues can be found in Fig. A.8. This fact can be understood in terms of the transition between the superfluid and gas phases, as pointed out by Egidy et al. [68], in which the critical energy is found around 15-20 MeV.

4.2.3 Fission modes

In this section, the fission modes Super-Long (SL), Standard I (StI), and Standard II (StII) were evaluated for both the atomic number and neutron fission yields for the fissioning system $Z_1 + Z_2 = 92$ along different cuts in mass addition. Fig 4.15 shows the fission modes fit of the atomic charge yields, and Fig. 4.16 shows the fit of the neutron yields. The fits displayed in these figures were performed using a single Gaussian for the SL mode and two Gaussians for each asymmetric mode, as shown in Eq. 4.4 for the fit of the atomic yields. The fit for the neutron yields is the same, but substituting Z for N and Z_{sum} for $A_{sum} - Z_{sum}$.

$$\begin{aligned} \mathrm{Fit(Z)} = \mathrm{A_{SL}} \cdot \exp\left[\frac{1}{2}\left(\frac{\mathrm{Z} - <\mathrm{Z_{SL}}>}{\sigma_{\mathrm{SL}}}\right)^2\right] + \\ \mathrm{A_{StI}} \cdot \exp\left[\frac{1}{2}\left(\frac{\mathrm{Z} - <\mathrm{Z_{StI}}>}{\sigma_{\mathrm{StI}}}\right)^2\right] + \mathrm{A_{StI}} \cdot \exp\left[\frac{1}{2}\left(\frac{\mathrm{Z_{sum}} - \mathrm{Z} - <\mathrm{Z_{StI}}>}{\sigma_{\mathrm{StI}}}\right)^2\right] + \\ \mathrm{A_{StII}} \cdot \exp\left[\frac{1}{2}\left(\frac{\mathrm{Z} - <\mathrm{Z_{StII}}>}{\sigma_{\mathrm{StII}}}\right)^2\right] + \mathrm{A_{StII}} \cdot \exp\left[\frac{1}{2}\left(\frac{\mathrm{Z_{sum}} - \mathrm{Z} - <\mathrm{Z_{StII}}>}{\sigma_{\mathrm{StII}}}\right)^2\right] \end{aligned} \tag{4.4}$$

As it has been done in previous studies for the fit of the neutron yields [54], a fit for a single Gaussian for the SL mode and a single Gaussian too for the asymmetric contribution (see Eq. 4.5) was performed and is displayed in Fig. 4.17.

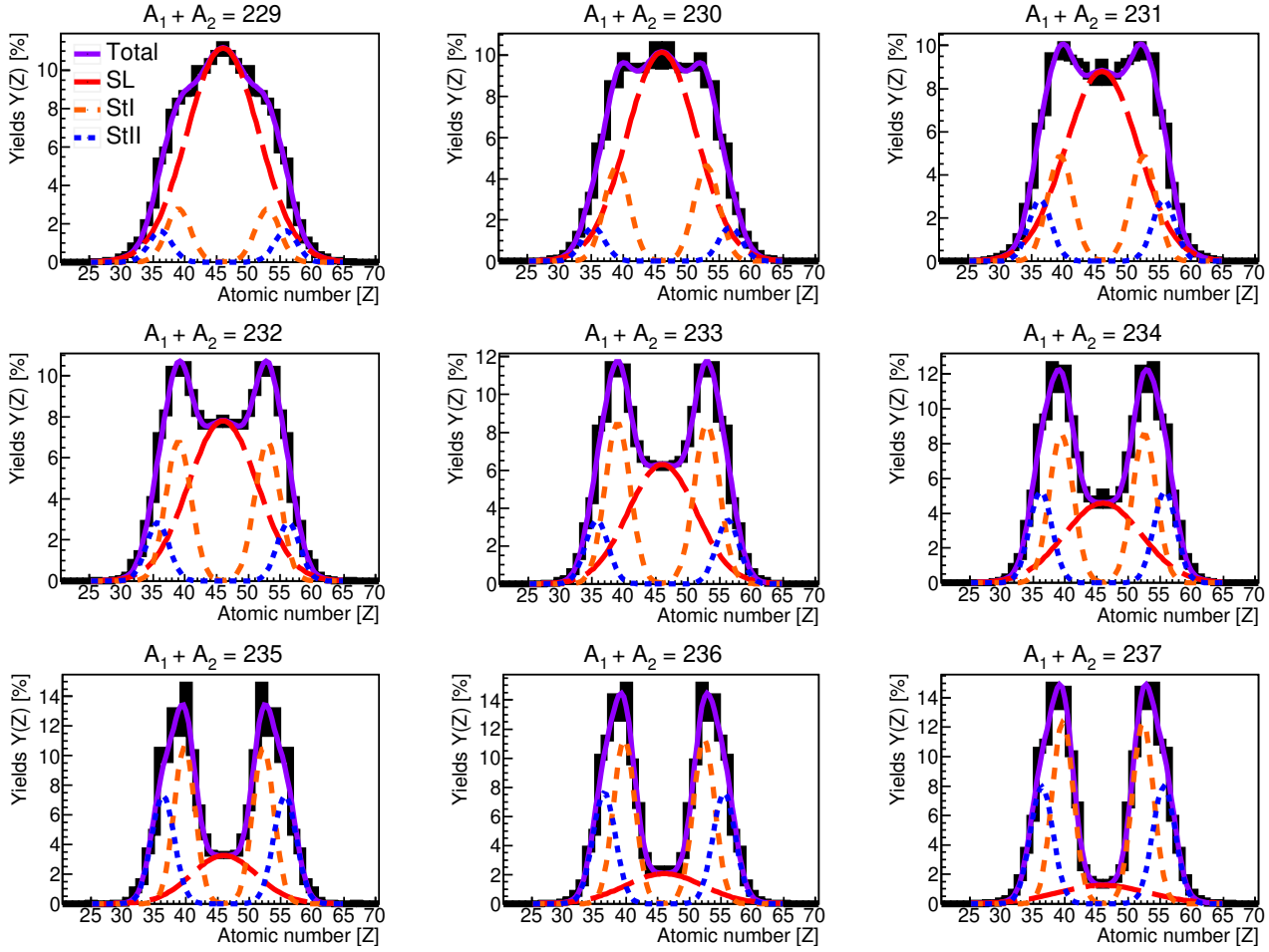

Figure 4.15: *Atomic number fission yields normalized to 200% for Z=92 fissioning system and different cuts in mass addition. The experimental data is represented by a black solid line. The data is fitted for different fission modes: Super Long (red long-dashed line), Standard I (orange short-dashed line), and Standard II (blue dotted line).*

$$\mathrm{Fit(N)} = \mathrm{A_{SL}} \cdot \exp\left[\frac{1}{2}\left(\frac{\mathrm{N} - <\mathrm{N_{SL}}>}{\sigma_{\mathrm{SL}}}\right)^2\right] + \mathrm{A_{Asym}} \cdot \exp\left[\frac{1}{2}\left(\frac{\mathrm{N} - <\mathrm{N_{Asym}}>}{\sigma_{\mathrm{Asym}}}\right)^2\right] + \mathrm{A_{Asym}} \cdot \exp\left[\frac{1}{2}\left(\frac{\mathrm{A_{sum}} - \mathrm{Z_{sum}} - \mathrm{N} - <\mathrm{N_{Asym}}>}{\sigma_{\mathrm{Asym}}}\right)^2\right] \tag{4.5}$$

In all the fits shown within this section, the parameters were not fixed except for $<\mathrm{Z}>$=46 for SL for the atomic charge yields. For the rest, the parameters were free to vary within their expected ranges. Fig. 4.18 shows the parameters derived from the fission modes fit (the amplitudes, widths, and mean positions of the peaks) for the atomic number yields (left side) and neutron yields (right side).

Figs. 4.15 and 4.16 show a clear evolution from the SL dominating at low mass additions to a dominance of the asymmetric modes for mass additions larger

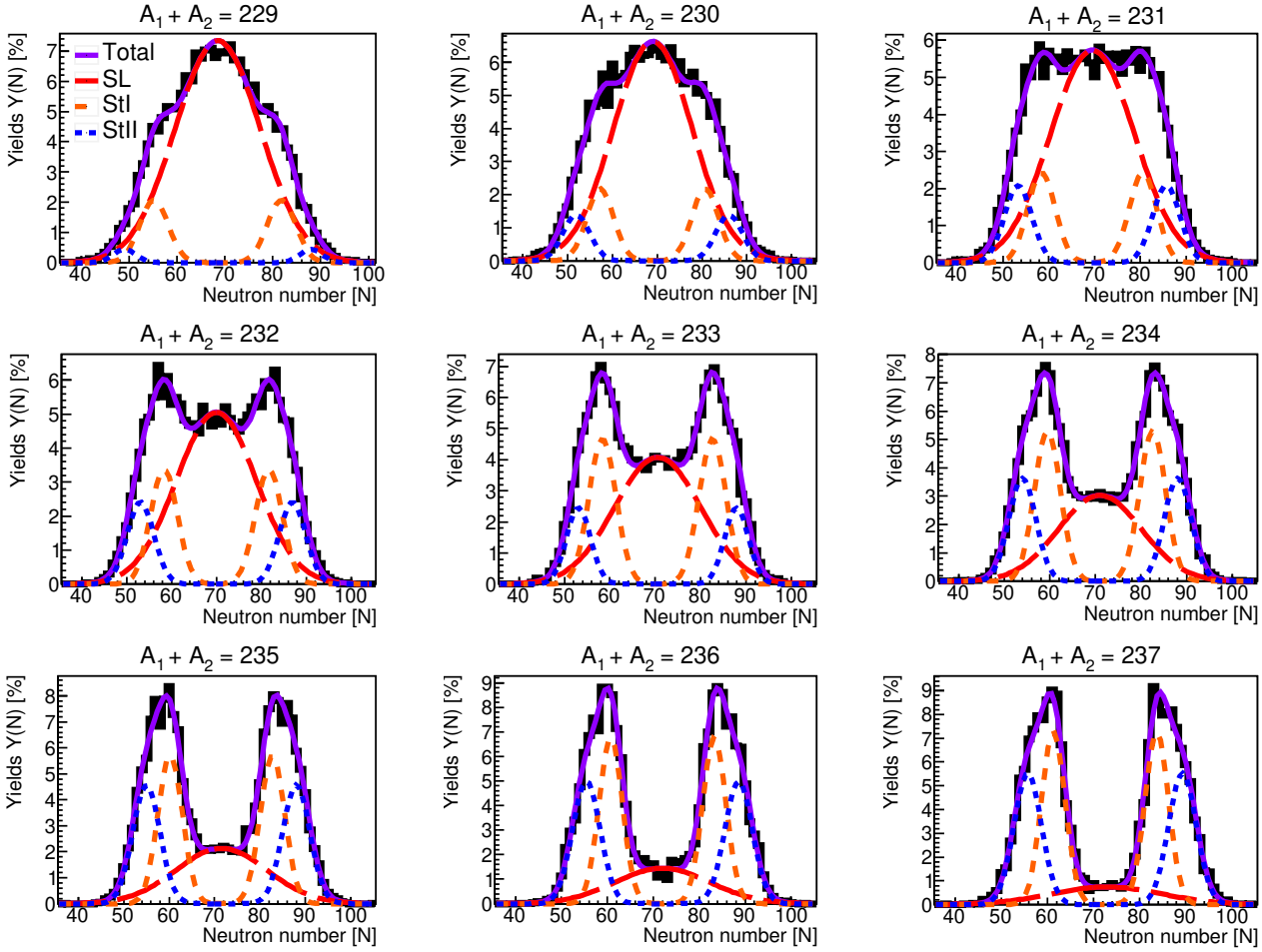

Figure 4.16: *Neutron fission yields normalized to 200% for Z=92 fissioning system and different cuts in mass addition. The experimental data is represented by a black solid line. The data is fitted for different fission modes: Super Long (red long-dashed line), Standard I (orange short-dashed line), and Standard II (blue dotted line).*

than $\approx A_1 + A_2 = 233$. This can also be seen in the top panel of Fig. 4.18 that compares the amplitude of the peaks. The amplitude decreases for SL and increases for StI and StII with the mass addition. In general, a dominance of the StI mode over the StII is observed. The central panel of Fig 4.18 shows the correlation between the mean position of the two asymmetric modes in atomic charge with the mass addition. For the atomic charge yield fit, the mean values remain rather constant along the whole range. For the heavy fragment, the position of the StI remains at $< Z_H > = 53$ and the StII at $< Z_H > = 56$. This is in good agreement with previous measurements for the ^{238}U [132] and could be due to the enhanced stability provided by the octupole-deformed shell gaps at Z=52 and Z=56 [63, 64]. However, the mean peak positions for the neutron number yields show a slightly increasing tendency with the mass addition, ranging from $< N_H >= 81$ to 84 in StI and from $< N_H >= 87$ to 89 for StII. This increase in the mean position is due to the neutron evaporation. For the lower mass

addition cuts, that is, higher excitation energies, the systems evaporate more neutrons, shifting the distribution to the left. The heavier fissioning systems were produced at lower energies and therefore evaporated fewer neutrons. It has been observed that the asymmetric modes drop faster with the mass addition for the light partner (about $\Delta N = 8$ neutrons difference between 229 and 237) than for the heavy one ($\Delta N \approx 2$). However, the fit for the single asymmetric contribution (black open dots in the figure), shows the same slope for the light and heavy fragments ($\Delta N \approx 4$) and is in fair agreement with the data from Coulex induced fission of ^{234,235}U from Ref. [54]. Fig. 4.18 lower panel shows the correlation

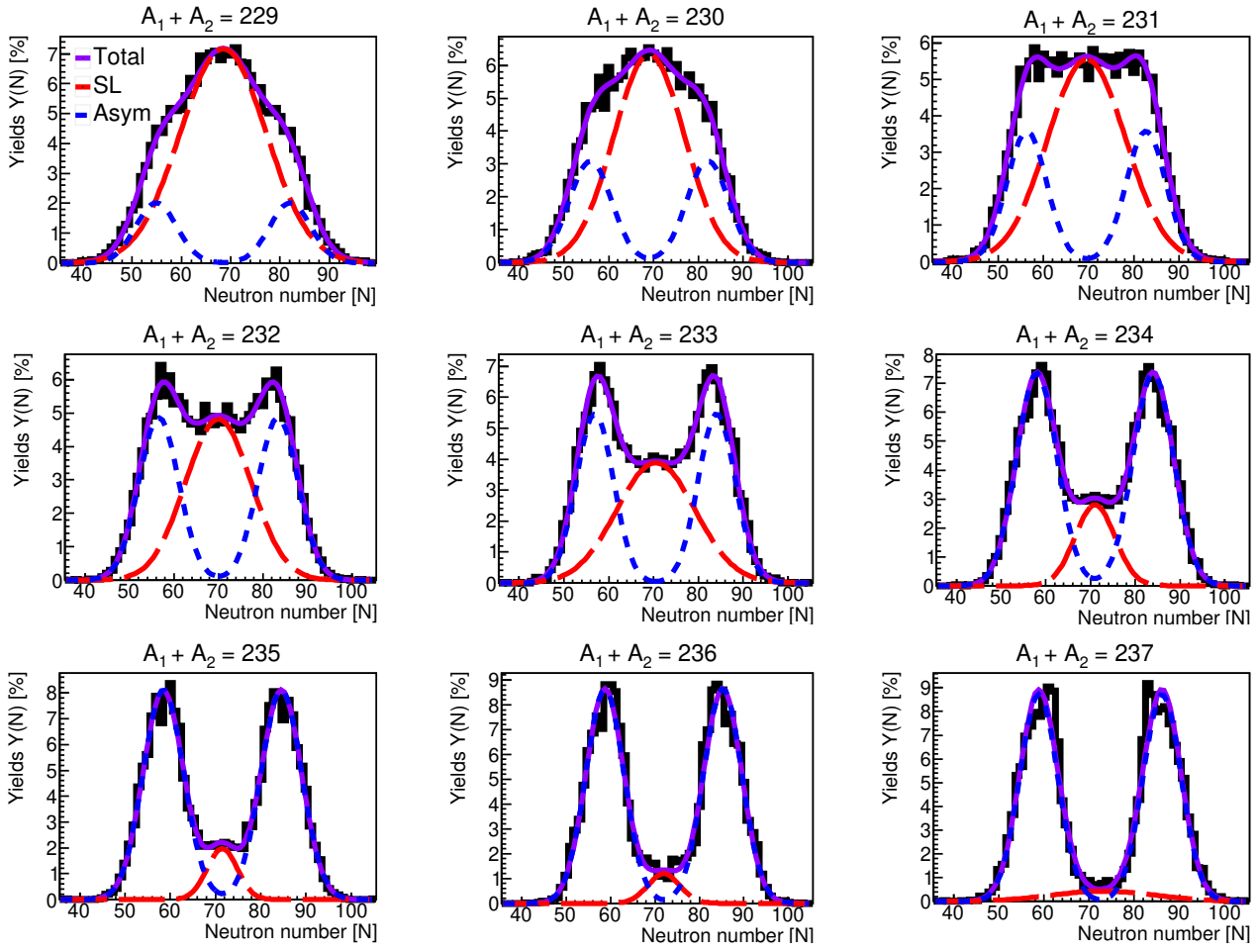

Figure 4.17: *Neutron number fission yields normalized to 200% for Z=92 fissioning system and different cuts in mass addition. The experimental data is represented by a black solid line. The data is fitted for different fission modes: Super Long (red long-dashed line) and one asymmetric mode (blue short-dashed line).*

between the width of the fission modes and the mass addition. For both the atomic and neutron yields, the StI and StII modes remain rather constant during the whole mass addition range. The SL mode shows the largest widths. This width increases with the mass addition at the same time as this component reduces its amplitude.

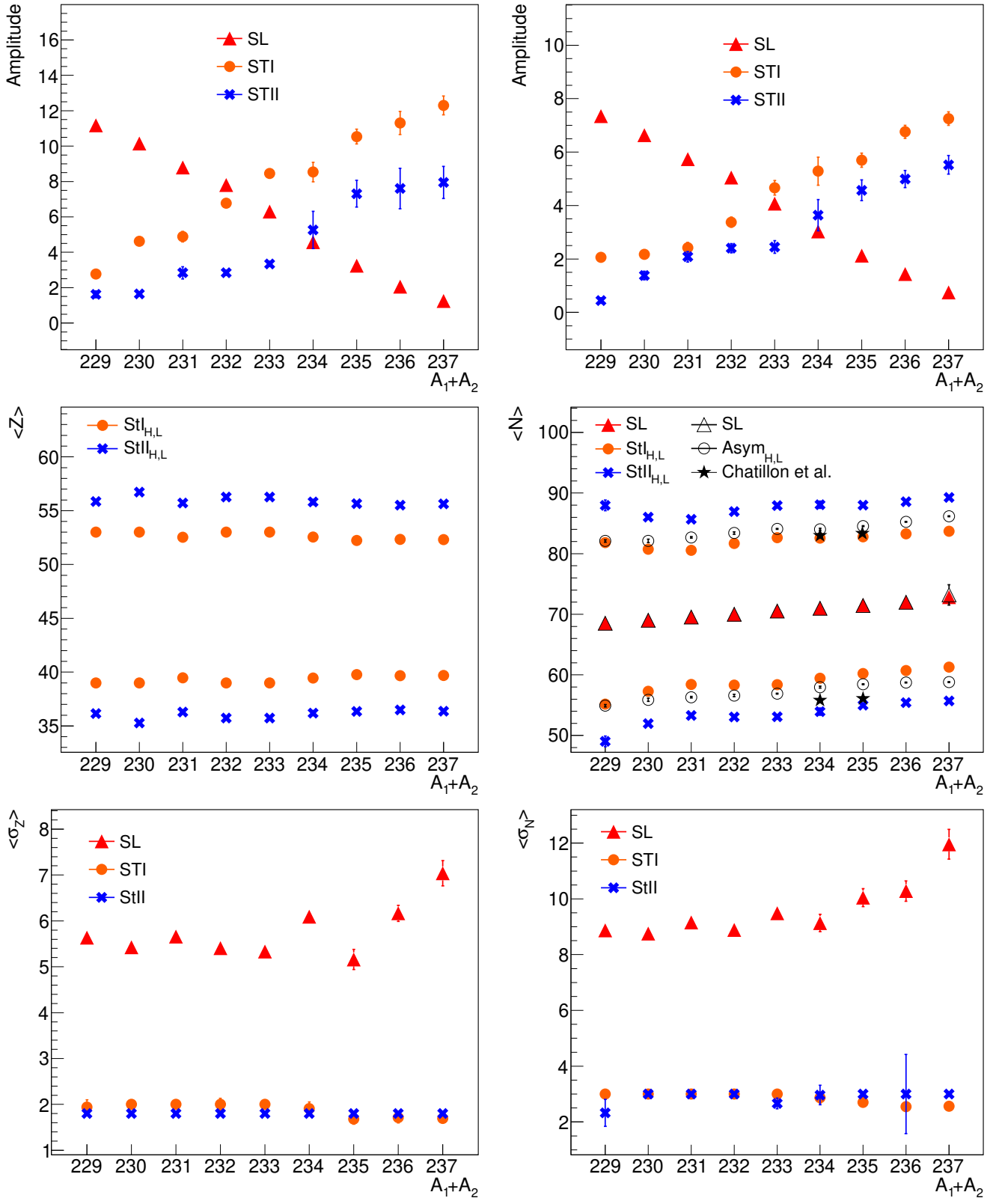

Figure 4.18: *In this figure, the amplitudes, mean positions, and widths of the different fission modes are represented for the atomic and neutron yields against the mass addition. Left side: fission mode parameters obtained for the atomic number yields. Right side: fission mode parameters obtained for the neutron number yields. Top pannels: amplitudes. Middle panels: mean position of each peak. Data marked with black stars is taken from Ref. [54]. Bottom panels: widths.*

4.2.4 Even-odd staggering

The even-odd effect has been studied for the fissioning systems Z=92 and 91 using different mass addition cuts that range from almost complete symmetry at A=229 to almost complete asymmetry at A=237 (around 11 MeV). The even-odd effect can be evaluated using 4.6 from [73], which describes the local deviation from a Gaussian-like distribution.

$$\delta(\mathrm{Z}+1.5) = \frac{(-1)^{\mathrm{Z}}}{8}\left(\ln\mathrm{Y}(\mathrm{Z}) - \ln\mathrm{Y}(\mathrm{Z}+3) + 3[\ln\mathrm{Y}(\mathrm{Z}+2) - \ln\mathrm{Y}(\mathrm{Z}+1)]\right) \quad (4.6)$$

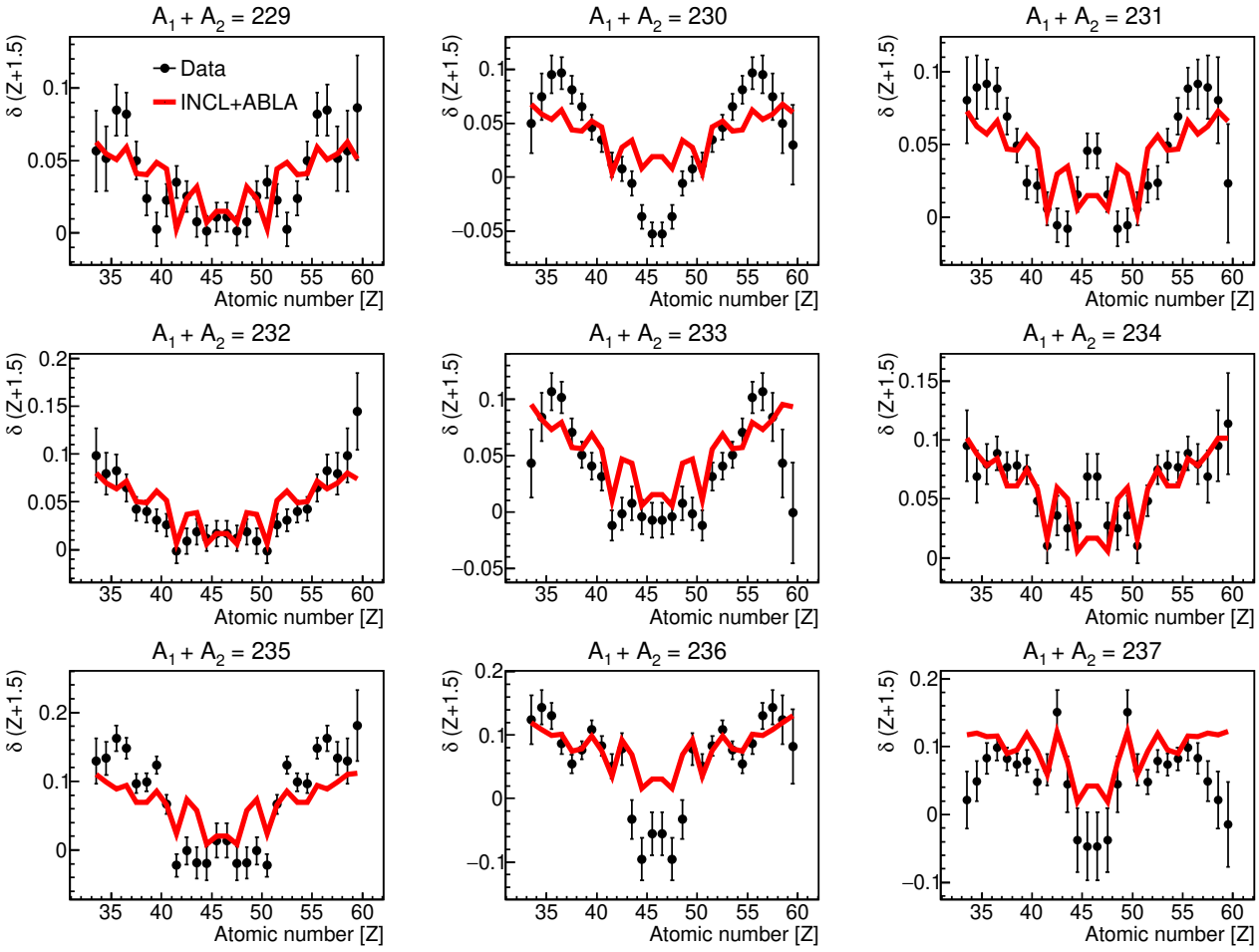

Figure 4.19: *Local even-odd effect for the fissioning system $Z_1 + Z_2$ =92 as a function of the fission fragment atomic number and comparison with simulations from INCL+ABLA.*

In Fig. 4.19 the local even-odd effect is displayed for the fissioning system Z=92. Since this is an even fissioning system, the plots show a characteristic parabola-like shape, due to the enhanced production of even fission fragments for the asymmetric fissions (giving positive even-odd local amplitudes) and the vanishing of the effect for the symmetric fission. The comparison with simulations

is pretty reasonable for the asymmetric regions but does not reproduce the results very well for the symmetric region or the edges in several cases, probably most noticeable for the case of $A_1 + A_2 = 230$. The cases 236 and 237 show a strong negative even-odd amplitude for the symmetric region, but conclusions are not easy to obtain from here since they correspond with a very low statistics region and could be affected by statistical fluctuations.

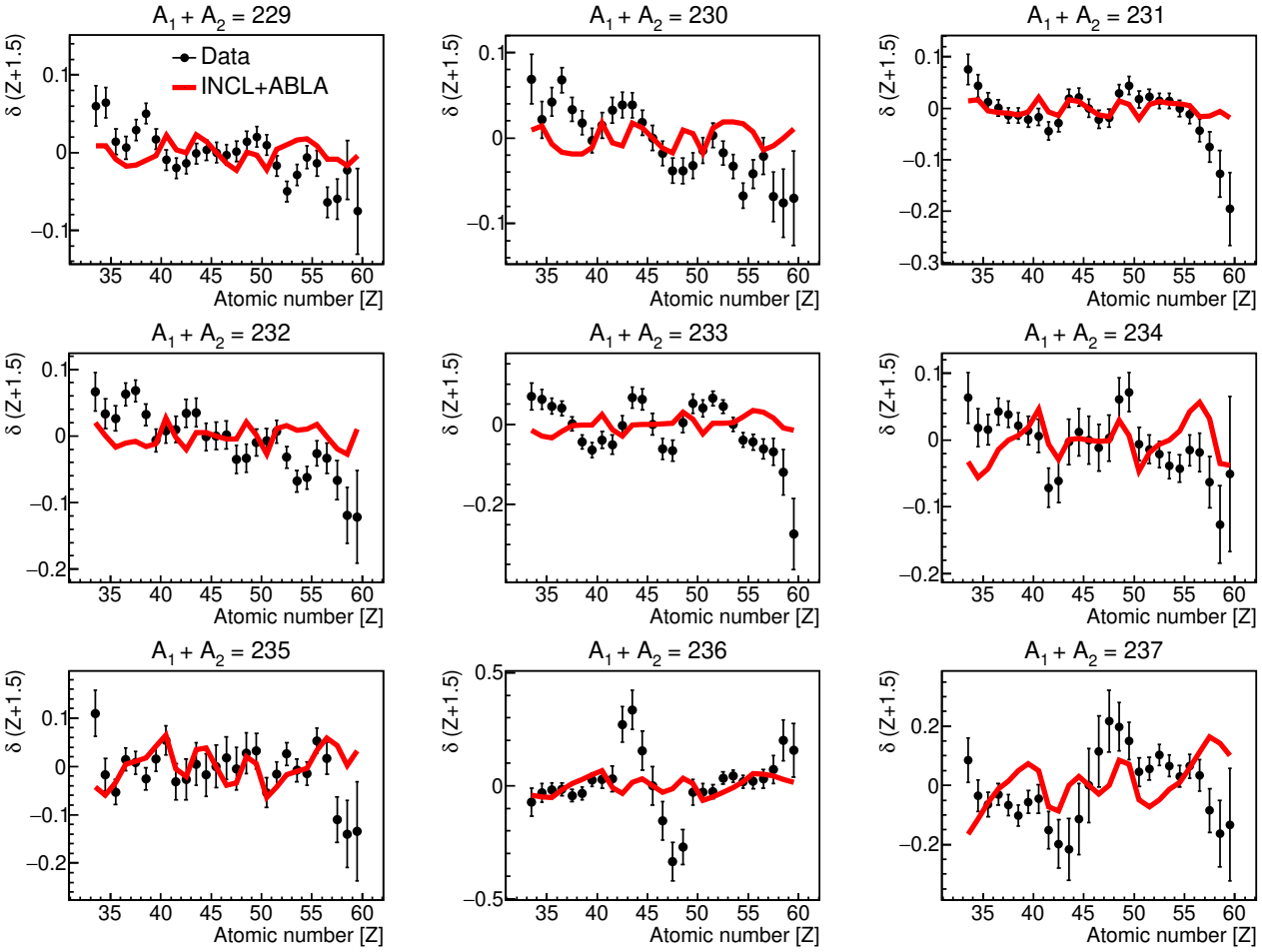

Figure 4.20: *Local even-odd effect for the fissioning system $Z_1 + Z_2$ =91 as a function of the fission fragment atomic number and comparison with simulations from INCL+ABLA.*

In Fig. 4.20 the local even-odd effect is displayed for the fissioning system Z=91. In this case, the fissioning system is odd, and then there is always at least 1 unpaired proton to relocate in one of the fission fragments. As discussed in section 1.3.3, it has been experimentally observed that the unpaired proton tends to end in the heavy fragment due to the energy sorting mechanism [72]. This can be seen in the figure, since for most of the mass addition cuts the even-odd effect shows a positive amplitude for the light fragment and a negative for the heavy one.

Eq. 4.7 was used to study the global even-odd effect evolution with energy. This equation evaluates the difference between the even and odd fission yields

averaged by the whole production.

$$\delta = \frac{\sum_{\text{Zeven}} \text{Y(Z)} - \sum_{\text{Zodd}} \text{(Z)}}{\sum_{\text{Z}} \text{Y(Z)}} \tag{4.7}$$

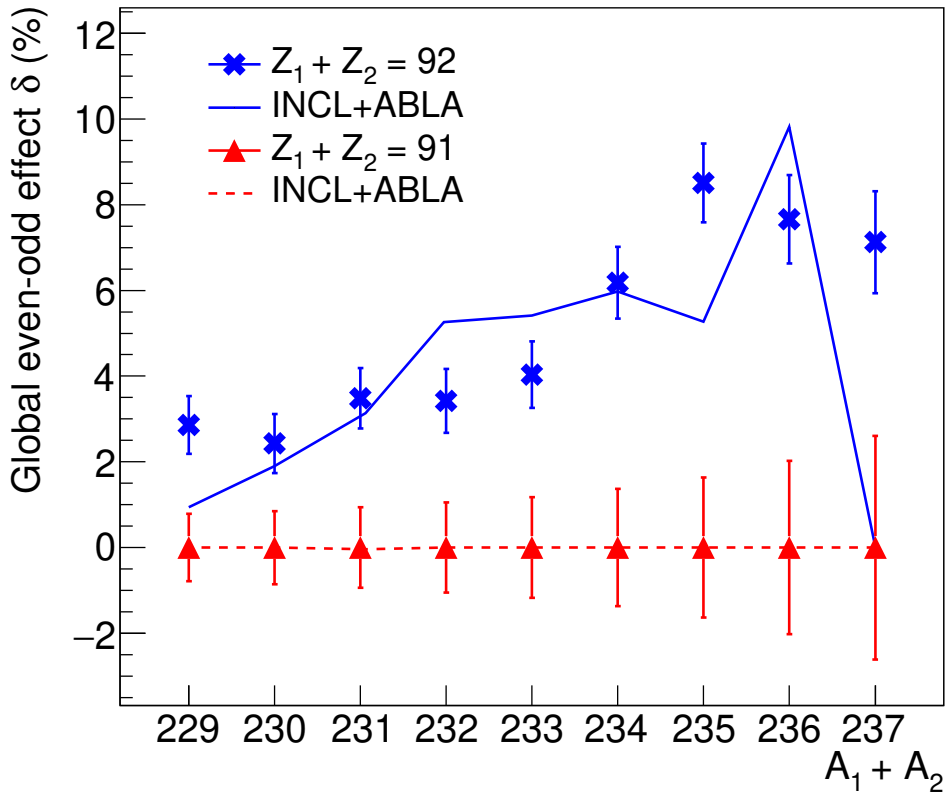

Figure 4.21: *Global even-Odd effect for the fissioning systems $Z_1 + Z_2$ =91 and 92 as a function of the mass addition.*

The results for the global even-odd effect are displayed in Fig. 4.21. For the fissioning system Z=92 the effect shows a general increasing trend with the mass addition or, which is the same, with the decrease in excitation energy of the fissioning system. This behaviour is expected, since the higher the excitation energy, the higher the energy available to break proton pairs, and therefore the even-odd effect vanishes. Despite the general increasing trend, the effect seems to decrease for the last two points (236,237) for both fissioning systems. This was already observed for the local even-odd effect since the symmetric region shows negative values. For Z=91, the positive amplitudes from the light region counterbalance the negative amplitudes from the heavy region, leading to a value of zero for the global even-odd effect, as predicted by the simulation.

4.2.5 Neutron excess

The neutron excess of the fission fragments is defined as the ratio between the average number of neutrons and protons. It is a useful variable to study the energy sharing between the nascent fission fragments since the excitation energy is transferred from one to the other by passing nucleons through the neck. Fig. 4.22 (left) shows the total neutron excess of this experiment (without any selection condition) in comparison with the experimental data of ^{238}U impinging on hydrogen [112] and deuterium [133] targets at 1 GeV/u. The results from this experiment show higher neutron excess than the others because the beam was less energetic, leading to lower excitation energies and consequently less neutron evaporation. Since the deuterons have more nucleons, the maximum excitation energy a deuteron can induce is higher, showing the lowest neutron excess. All the data sets show an increase in the neutron excess with the atomic number, which is known as 'charge polarization'. This happens because the nucleus needs to keep more neutrons to counterbalance the Coulomb repulsion increasing with Z^2.

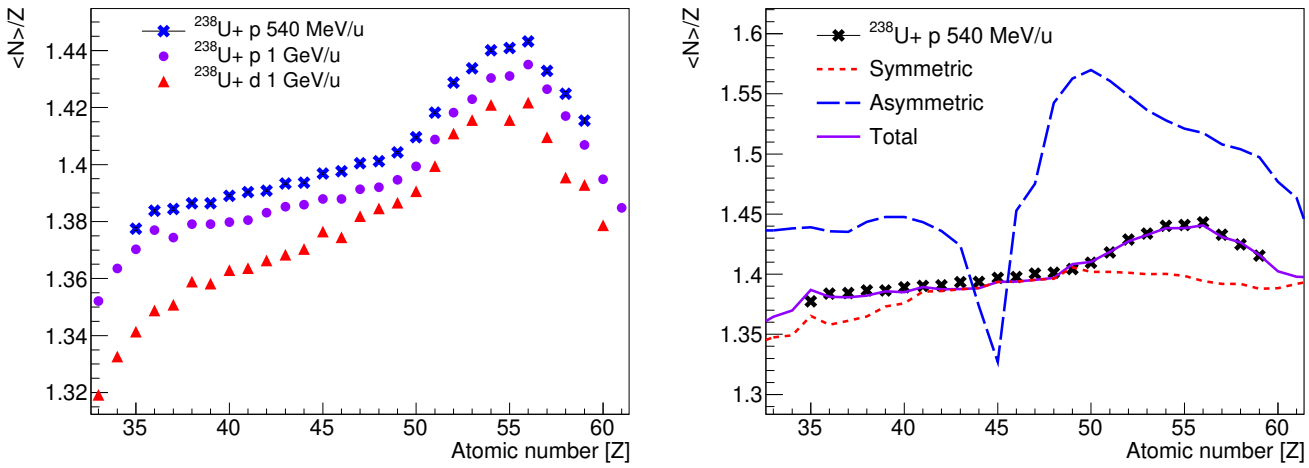

Figure 4.22: *Left: Neutron excess of the fission fragments as a function of the atomic number. The data for the violet dots and red triangles was taken respectively from Refs. [112] and [133]. Right: The experimental neutron excess (black crosses) is compared with simulated data with INCL+ABLA for 3 different cases: asymmetric fission modes (blue long-dashed line), symmetric fission modes (red short-dashed fission modes) and the total distribution (violet solid line).*

However, a peak is observed around Z=55 above the smooth tendency. To better illustrate this point, Fig. 4.22(right) shows the experimental neutron excess compared to an INCL+ABLA calculation for the neutron excess of the different fission modes. The peak in Z=55 is the result of the convolution of the symmetric modes (the blue long-dashed) with high fission yields at Z=46 (see Fig. 4.9(left), red line), and the asymmetric modes (red short-dashed) with high statistics at Z=52-56 (see Fig. 4.9(left), violet line). As seen in the figure, the resulting violet

line reproduces the experimental data rather well.

To study the evolution of the neutron excess with excitation energy, a selection is made for atomic number addition Z=92 and different cuts in mass addition, as seen in Fig. 4.23. The neutron excess for the lowest cuts in mass addition (or higher excitation energies) from the red triangles to the blue stars shows a regular increase with the atomic charge, as expected to counterbalance the Coulomb repulsion. However, the two last cuts show a characteristic bump around Z=50 and a dip on its complementary fission fragment Z=42. This is especially noticeable for the last mass addition cut (237, 238) which using the calibration from Fig. 4.12 should correspond to excitation energies below 10MeV. This is due to shell effects becoming noticeable at these low excitation energies, such as the proton magic number at Z=50 and the neutron magic number at N=82. When the fissioning system evolves from the saddle towards the scission, a heavy nascent fragment with Z=50 and a high neutron number will show enhanced stability when getting close to N=82. Therefore, the neutrons would pass from the light fragment to the heavy fragment through the neck until the heavy one reaches N=82 or close. That is also why its complement fragment in Z=42 shows the lowest ratio: it passed its neutrons to the heavy partner.

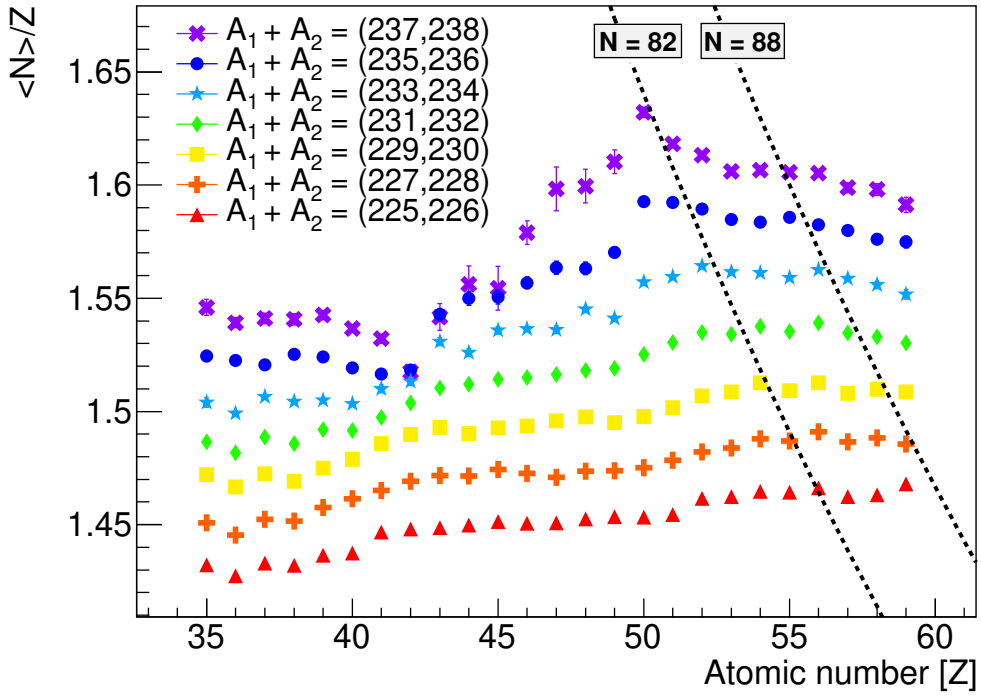

Figure 4.23: *Neutron excess as a function of their atomic number for Z=92 and different cuts in mass addition.*

In Fig. 4.24 the neutron excess evolution with the mass addition is displayed for (p, 2p) reactions. To select the (p, 2p) channel, Z=91 fissioning systems and an opening angle of 80^o between the knocked-out protons are chosen. Since this

selection is more restrictive, the mass additions were gathered in groups of 4 to reunite more statistics. The error bars are larger in this plot for the smaller masses addition since the data file was taken under downscaling conditions that favoured the storage of (p, 2p) data over other events. In this case, the dip of the fission fragment complementary to the Z=50 is in Z=41, since the fissioning system is Z=91. It can be seen that the dependence is similar to that presented in Fig. 4.23, just more dispersed due to lower statistics.

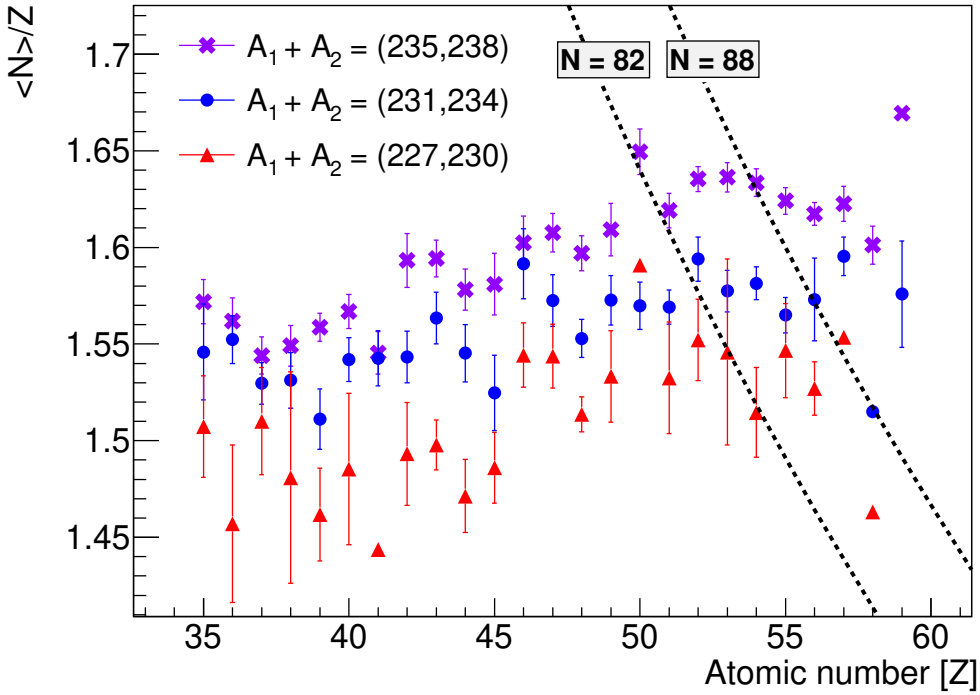

Figure 4.24: *Neutron excess as a function of their atomic number for Z=91 and opening angle 80º at different cuts in mass addition.*

4.2.6 Neutron multiplicities

In this section, the number of evaporated neutrons through the fission process is reconstructed. The number of neutrons emitted by the fissioning system between the saddle and scission points is known as 'pre-scission' neutron multiplicity (ν_{pre}), and the number of those emitted by the fission fragments as 'post-scission' (ν_{post}). The total multiplicity (ν_{total}) is calculated by subtracting the number of neutrons in the fission fragments from the projectile's neutron number, as shown in Eq. 4.8, where A_{proj} and Z_{proj} are respectively the mass and atomic number of the projectile, and A_i, Z_i (i=1,2) the ones of the two fission fragments.

$$\nu_{Total} = A_{proj} - Z_{proj} - (A_1 - Z_1 - A_2 - Z_2) \tag{4.8}$$

The post-scission neutron multiplicity can be estimated using the Unchanged Charge Distribution (UCD) approach, which assumes that the mass-charge relation of the fissioning system at the saddle point is the same for the fission fragments at the scission point. Therefore, the mass of the fission fragment at scission ($A_{i,sci}$) can be calculated as shown in Eq. 4.9, where A_{sad} and Z_{sad} are respectively the mass and charge at the saddle. Since the proton evaporation probabilities are very low, it is assumed that the atomic number of the fission fragments at the scission is the same as for the final fragments. In the same way, the atomic number of the fissioning system at the saddle is obtained by adding the atomic number of the final fission fragments. Due to the impossibility of measuring the A_{sad}, a mean value was estimated for each Z_{sad} using simulations with INCL+ABLA.

$$A_{i,sci} = Z_{i,sci}\frac{A_{sad}}{Z_{sad}} \tag{4.9}$$

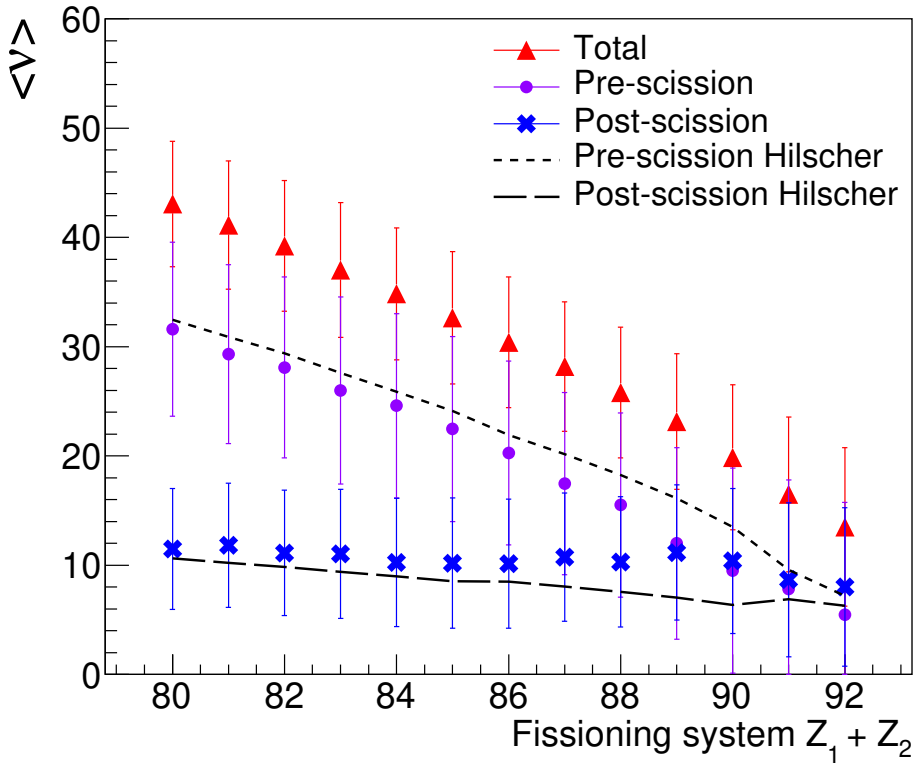

Figure 4.25: *Average neutron total, pre- and post-scission multiplicities compared with the systematics proposed by [134]. The error bars do not correspond to the uncertainty of the average but to the width of each multiplicity distribution.*

The post-scission neutron multiplicity for each fission fragment is estimated as shown in Eq. 4.10, subtracting the final mass of the fission fragment from the mass at the scission. Then, the pre-scission neutron multiplicity is obtained by subtracting the post-scission multiplicities of both fragments from the total, see

Eq. 4.11.

$$\nu_{\mathrm{i,post}} = \mathrm{A_{i,sci}} - \mathrm{A_i} \tag{4.10}$$

$$\nu_{\mathrm{pre}} = \nu_{\mathrm{total}} - \nu_{\mathrm{1,post}} - \nu_{\mathrm{2,post}} \tag{4.11}$$

The results of these estimations are presented in Fig. 4.25 and compared with the parameterization proposed by Hilscher and Rossner [134] based on systematics measurements of neutron multiplicities in fusion-fission reactions of different nuclei. It can be seen that the neutron multiplicities estimated assuming UCD are in fair agreement with the empirical parameterization within the error bars. The parameterizations of Hilscher are shown in Eqs. 4.12 and 4.13 for the pre- and post-multiplicities respectively, where it can be seen that 80% of the ν_{total} corresponds to the neutrons evaporated before scission and only 20% occurs afterwards.

$$\nu_{\mathrm{pre}} = 0.8(\nu_{\mathrm{total}} - \nu_0) \tag{4.12}$$

$$\nu_{\mathrm{post}} = \nu_0 + 0.2(\nu_{\mathrm{total}} - \nu_0) \tag{4.13}$$

The term ν_0 is an offset that takes the fissility of the fissioning system into account, since for higher fissilities the fission probability becomes stronger than the neutron evaporation and the pre-scission multiplicity decreases. This parameter depends on the fissioning system atomic number and ranges from 2.5 neutrons for $\mathrm{Z_{sad}} < 86$, to 3 neutrons for $86 \leq \mathrm{Z_{sad}} \leq 90$ and 4.5 for $\mathrm{Z_{sad}} > 90$.

Another way to estimate the neutron multiplicity is by using the neutron excess shown in Fig. 4.23. To do so, the highest mass addition cut ($\mathrm{A_1} + \mathrm{A_2} = 237{,}238$) is taken as a reference, and using the difference presented in Eq. 4.14 an average neutron emission multiplicity can be obtained for each mass addition cut relative to the lowest energy cut.

$$\nu_{\mathrm{A_1+A_2}} = \mathrm{Z}\left[\left(\frac{<\mathrm{N}>}{\mathrm{Z}}\right)_{237,238} - \left(\frac{<\mathrm{N}>}{\mathrm{Z}}\right)_{\mathrm{A_1+A_2}}\right] \tag{4.14}$$

The results are displayed in Fig. 4.26, providing a clearer view of the energy sorting mechanism similar to the saw-tooth shape [18], which states that the energy would flow from the hot light fragment to the cold heavy one via neutron transfer since it has a bigger availability of states. Fig. 4.26 shows that for the lighter atomic numbers, the relative neutron multiplicity varies around 3 units between the blue dots and the red triangles. However, for the heavier atomic

numbers, the multiplicity varies around 7 neutrons, meaning that when the excitation energy increases, this energy is driven towards the heavy partner, since it evaporates more neutrons.

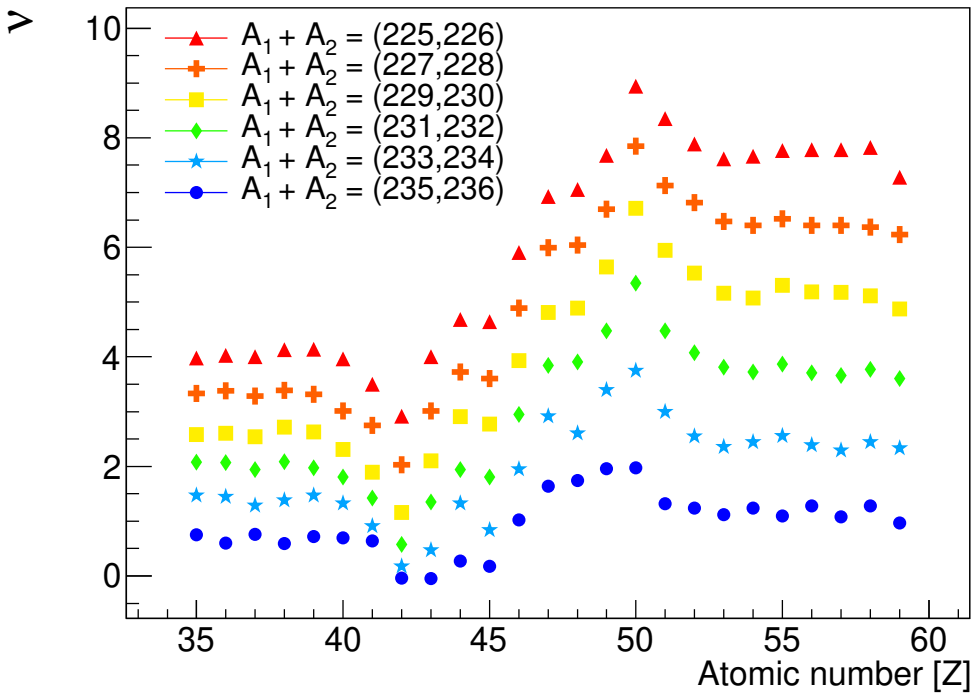

Figure 4.26: *Average neutron multiplicity relative to the mass addition cut* $A_1 + A_2 = 237{,}238$.

4.2.7 Total Kinetic Energy at scission

The total kinetic energy gained by the fission fragments at scission is mostly due to the Coulomb repulsion between them in addition to a small contribution of pre-scission velocity. Assuming that the kinetic energy is caused entirely by the Coulomb repulsion, it can be expressed as seen in Eq. 4.15, where D would be the center of mass distance of the two fragments [60]. The LDM model parameterizes this distance D as a function of the masses of the fragments at the scission, their deformation (β_1 and β_2), and the separation d between the tips of the spheroids. Therefore, this observable will be affected by structural effects at scission when selecting high excitation energies.

$$< \mathrm{TKE} >= 1.44\frac{Z_1 Z_2}{D} = \frac{1.44 Z_1 Z_2}{r_0[A_{1,sci}^{1/3}(1+\frac{2}{3}\beta_1) + A_{2,sci}^{1/3}(1+\frac{2}{3}\beta_2)] + d} \tag{4.15}$$

Since the masses at scission estimated with the UCD approximation brought reasonable results for the neutron multiplicities, they are used to calculate the total kinetic energy of the fission fragments, as presented in Eq. 4.16. The

Lorentz's factors for the two fission fragments (γ_1, γ_1) are calculated using the velocities in the center of mass reference system. The details of the velocities calculation can be consulted in A.7.

$$< \text{TKE} >= \text{A}_{1,\text{sci}}(\gamma_1 - 1) + \text{A}_{2,\text{sci}}(\gamma_2 - 1) \tag{4.16}$$

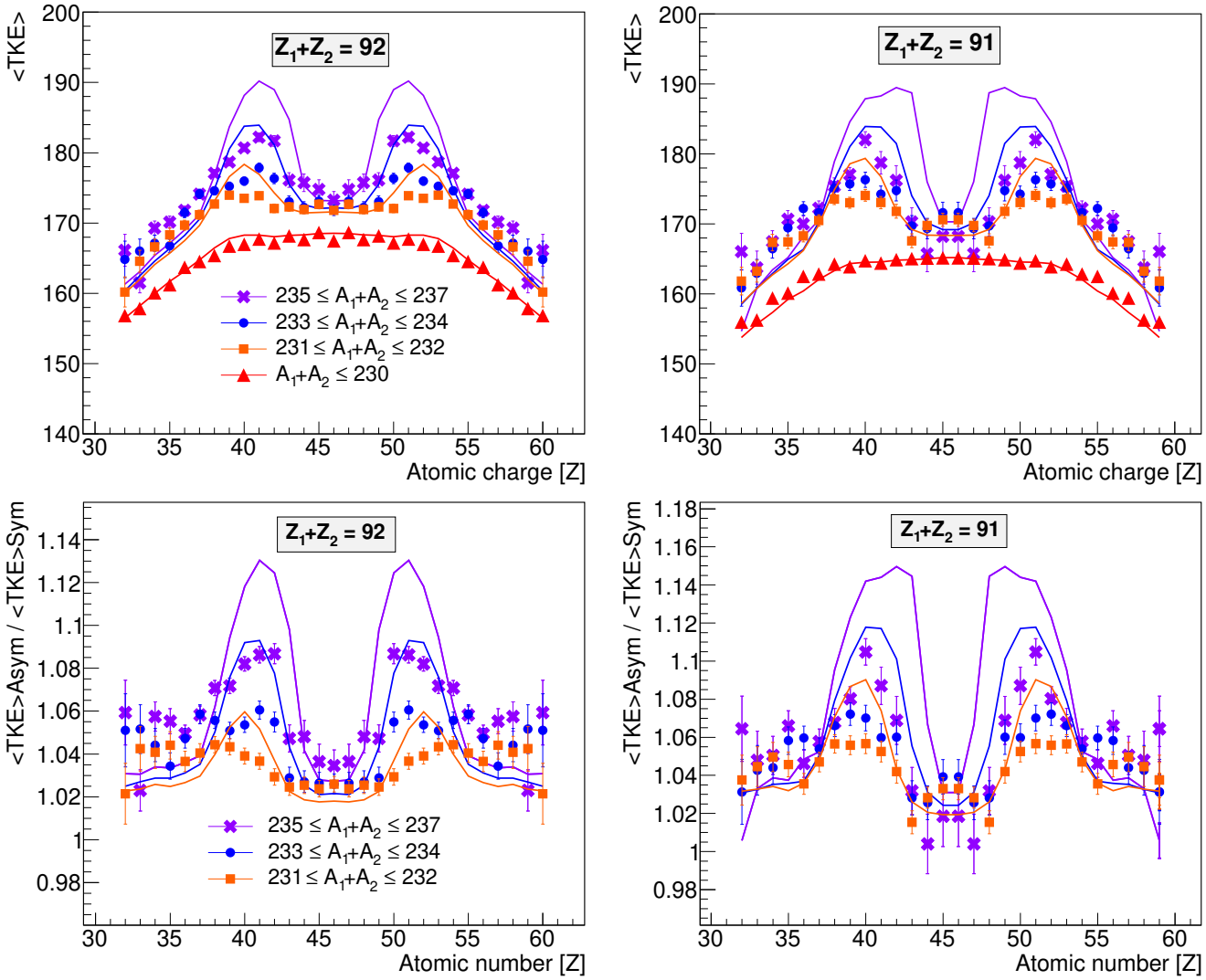

Figure 4.27: *Upper panel: Average total kinetic energy for the fissioning systems Z=92 (left) and Z=91 (right) as a function of the fission fragment charge for different cuts in mass addition. The markers represent the experimental data while the lines of the same colour represent the simulated data for each mass addition cut. Lower panel: TKE ratios described in Eq. 4.17 for the fissioning systems Z=92 (left) and Z=91 (right) as a function of the fission fragment charge for different mass addition cuts.*

The average total kinetic energies for each fission fragment are presented in the upper panels of Fig. 4.27 for the fissioning system Z=92(left) and Z=91(right), and compared with simulated data from INCL+ABLA. The evolution of the kinetic energy with the excitation energy is visible since the mass cut for the lowest mass addition cut is mostly flat in the central region, while two humps emerge for the asymmetric channels when increasing the mass addition. When

the asymmetry increases, the separation d between the surfaces of the fragments and the deformation decreases [132], producing an increase in the TKE and leading to the observed humps. It can be seen that the cut for the lower masses $A_1 + A_2 < 230$ presents the best agreement with the simulation, implying that some of the deformations in ABLA might need to be adjusted. In the lower panels of the same figure, the ratio of the TKE for the asymmetric cuts over the TKE of the symmetric one (the red triangles cut in the upper panel) is presented. As seen in Eq. 4.17, this ratio only depends on the relation of the deformation and distance parameters and indicates the effective change in deformation. For the highest mass addition cut, an effective change of 9% can be observed for Z=92 and of 11% for Z=91.

$$\frac{< \mathrm{TKE} >_{\mathrm{Asymmetric}}}{< \mathrm{TKE} >_{\mathrm{Symmetric}}} = \frac{\mathrm{D}_{\mathrm{Asymmetric}}}{\mathrm{D}_{\mathrm{Symmetric}}} \tag{4.17}$$

Chapter 5

Conclusions

This chapter will provide a review of the main results extracted from the analysis and evaluate the achievement of the objectives proposed at the beginning of the work. Simultaneously and based on the results obtained, it will be evaluated what changes could be introduced in the future to improve this type of measurement.

In this research work, the fission of ^{238}U was investigated using proton-induced knockout collisions at 540 MeV/u in inverse kinematics. The use of the R^{3}B setup allowed for the full identification of both fission fragments in atomic and mass number event by event. The atomic number was obtained from the energy loss measurements in a double ionization chamber (the Twin MUSIC) with an average resolution of $\Delta Z = 0.38$ FWHM for the central charges. The mass number of the fragments was reconstructed employing the well-known $\Delta E - B\rho - ToF$ technique, based on the different magnetic rigidities of the fragment inside the GLAD dipole. The mass resolution was around $\Delta A = 0.8$ FWHM for the central masses of the ToF Wall plastics with distinguishable peaks. The wide range of excitation energies produced in the proton knockout together with the full isotopic identification allowed for the study of observables sensitive to pre- and post-saddle fission dynamics.

One of the main goals of this experiment was to prove the suitability of the (p, 2p) induced fission in combination with the SOFIA (Studies Of FIssion with Aladin) setup to give access to the complete characterization of the fissioning system and the fission fragments. The fissioning system would be characterized thanks to the integration of the CALIFA calorimeter [2] and the AMS Silicon tracker [1] developed by the R^{3}B collaboration, which would allow the reconstruction of the excitation energy using the missing energy method. However, the large delta-electron multiplicities produced in secondary ionizations along the setup make it impossible to reconstruct the trajectories of the protons using this detector. Still, other observables were evaluated as an indicator of the excitation energy, and the mass addition of the fission fragments proved

very sensitive. Therefore, the evolution of different observables with the mass addition was studied, and it was calibrated to excitation energy using previous experimental data to estimate the energy range covered by each mass addition cut. In conclusion, the method allowed to perform only a modest characterization of the fissioning system due to technical issues that should be tackled in the future. The most appropriate solution to deal with the large delta-electron multiplicity would be replacing the AMS Silicon tracker with a new technology based on ultra-thin silicon-based Monolithic Active Pixels Sensors (MAPS), called ALPIDE sensors [135], developed by the ALICE Collaboration. A pixel detector would provide enough angular resolution to reconstruct the vertex of the reaction and differentiate the outgoing protons from the delta electrons. Regarding the fission fragments characterization part, the atomic number resolution was more than satisfactory, while the mass resolution was less than expected. This experiment was the first to use GLAD, the new R^3B magnet that replaced ALADIN. GLAD has a better acceptance and allows for a higher magnetic rigidity, but its magnetic field is not Gaussian. This should not be a problem for the reconstruction of the trajectories inside the magnet, since the mass reconstruction method used the real GLAD field map and the results were very positive. However, the GLAD magnetic field is larger now than with ALADIN, and the ToF Wall was placed very close ($\sim$1.5m) to the magnet to maximize the geometrical acceptance. Therefore, the PMTs could be affected by the residual field of the magnet. To improve the mass resolution in the future, it would be convenient to test the performance of the ToF-Wall when placed that close to the magnet and evaluate different possible shieldings.

The experimental technique was useful for studying fission at both low and high excitation energy ranges by properly selecting the reaction channel. For the pre-saddle stage, the partial fission yields and fission widths were analyzed as a function of the atomic number addition of the fission fragments. It was observed how the fission cross-section dropped quickly towards the lighter fissioning systems, which is a signature of the dissipation phenomena manifesting at high excitation energies and favouring neutron evaporation over fission. Several de-excitation models were coupled to the INCL reaction model and benchmarked with the experimental data. It was an interesting finding that both ABLA and GEMINI described rather well the fission cross-section for the whole fissioning systems range, despite having a very different parameterization. ABLA includes a Fokker-Planck time-dependent fission decay width, while GEMINI does not take into account dissipation or transient times, but its energy level densities are parameterized using experimental data. Regarding the study of the fission

widths, it was observed that the selection of the target has a non-negligible impact on the results. Specifically, the results of this experiment were compared with a fragmentation reaction of ^{238}U on a CH_2 target. Spallation and fragmentation reactions lead to fissioning system distributions of different fissility ranges. Since the stiffness of the potential greatly depends on the fissility, the fission widths are directly affected. The comparison of the models for the fission widths showed that in this case, ABLA is the one that better reproduces the data, since GEMINI does not include the shell effects visible for the heaviest fissioning systems.

For the post-saddle stage, the evolution with the excitation energy of several observables sensitive to the energy sorting and shell effects was studied. Since it was proven that the mass addition ($A_1 + A_2$) is very sensitive to the excitation energy, this observable was calibrated to have an estimation of the energy ranges. By performing several cuts in the mass addition, different suppression functions were evaluated in the transition from the symmetric to the asymmetric fission. It was observed that the Woods-Saxon function proposed by Randrup et al. [17] works rather well for low excitation energies, but it is not enough to describe the damping at excitation energies higher than ∼15MeV. The suppression function in best agreement with the experimental data was found for a combination of two exponentials, $S(E^*) = \exp(-E^*/4MeV)$ for the excitation energies below 20MeV and $S(E^*) = \exp(-E^*/13MeV)$ for excitation energies above 20MeV.

The fission modes were evaluated for different mass addition cuts for both the atomic and the neutron yields. A general predominance of the StI mode was observed over the StII. For the heavy fragment, the position of the StI mode remains constant through the different mass addition cuts at $< Z_H >= 53$, and the StII at $< Z_H >= 56$, which is in fair agreement with the predicted enhanced stability of the octupole-deformed shell gaps at Z=52 and Z=56 [63, 64]. The mean positions for the neutron in the fission modes show a slightly increasing tendency with the mass addition (due to the decreasing of the neutron evaporation), varying between $< N_H >= 81 - 84$ for the StI and between $< N_H >= 87 - 89$ for the StII.

The global and local even-odd staggering amplitudes were calculated for different conditions in mass addition. A general increase in the global amplitude was observed when increasing the mass addition, or in other words, decreasing the excitation energy. An interesting decrease was observed for the two heaviest systems, $A_1 + A_2 = 236,237$ but due to the limited mass resolution it is not possible to distinguish if this is just a feature introduced by the contamination of lower fissioning systems. The local even-odd amplitude showed a positive

parabolic shape for $Z_1 + Z_2 = 92$, as expected for an even fissioning system, and for $Z_1 + Z_2 = 91$ a positive amplitude in the light fragments and negative in the heavy ones. This is also expected for an odd fissioning system since the unpaired proton tends to drift to the heavy fragment due to the energy sorting mechanism [78]. For both cases, it was observed that the change of a single mass addition unit in the condition, resulted in very different appearances of the even-odd amplitudes, demonstrating the big dependence of this observable on the excitation energy. The simulation performed with INCL+ABLA reproduced the local even-odd amplitude for the asymmetric fragments in $Z_1 + Z_2 = 92$, but failed to reproduce the data for $Z_1 + Z_2 = 91$.

The neutron excess was studied for different mass addition cuts. This observable showed a clear evolution from the polarization effect at the high excitation energy cuts to revealing shell effects for the low excitation energy cuts. The shell effects were observed for the lowest energy cuts, where the neutron excess peaked at Z=50, reaching the neutron magic number N=82. The dip on the complementary fragment of Z=50 for both $Z_1 + Z_2 = 92$ and 91 fissioning systems was also observed.
The neutron pre- and post-scission multiplicities were estimated using the UCD approximation to calculate the masses at the scission point, and the results are in good agreement with the parametrization proposed by Hilscher. The TKE was calculated using the same approximation for the masses, and several cuts in mass addition were performed. The TKE is also very sensitive to the excitation energy, which was visible for the lower energy cuts, showing two humps for the asymmetric atomic numbers. The simulation performed with INCL+ABLA showed a good agreement for the high-energy mas addition cuts and the symmetric region of the low-energy cuts but overestimated the height of the asymmetric humps, indicating the necessity to adjust the deformation parameters in ABLA.

Resumo

R.1 Introducción

Esta tese trata sobre o análise do experimento de fisión realizado nas instalacións do GSI (Alemania) en marzo de 2021 pola colaboración internacional R^3B (Reactions with Relativistic Radioactive beams), que realiza estudos con feixes exóticos relativistas (entre centos de MeV e 1GeV).

Na última década realizáronse experimentos de fisión sen precedentes nas instalacións do GSI utilizando a técnica de cinemática inversa en combinación con detectores de última xeración desenrolados pola colaboración R^3B . Por primeira vez na historia da fisión, foi posible medir e identificar simultáneamente ambos fragmentos de fisión en termos do seu número atómico e másico [7, 8] e de extraer correlacións entre observables sensibles á dinámica do proceso de fisión [9] e a estructura nuclear no punto de escisión [10, 11].

Este experimento en particular, está deseñado para combinar as técnicas de fisión por cinemática inversa e as reaccións de espalación e knockout. Se ben hai numerosos estudios realizados usando estas dúas técnicas por separado, este é o primeiro experimento que combina ambas, polo que se trata dunha proba de concepto. A nova técnica experimental proporcionará medicións cinemáticas completas mediante a obtención da enerxía de excitación do sistema fisionante e a identificación en número másico, numero atómico e enerxía cinética dos dous fragmentos de fisión evento a evento. Ditas medidas poden realizarse usando a configuración experimental de SOFIA (Studies Of FIssion with Aladin) cun medidor de posición de silicio baseado en detectores tipo AMS [1] e o calorímetro CALIFA (CALorimeter for In-Flight detection of γ rays and high energy charged pArticles) [2] desenrolados pola colaboración R^3B. Dado que as reaccións de knockout e espalación producen sistemas fisionantes nun amplio rango de enerxías de excitación, este mecanismo pode utilizarse para estudiar a fisión a altas e baixas enerxías seleccionando correctamente o canal de reacción.

R.2 Obxectivos

Os principais obxectivos desta tese son os seguintes:

- Comprobar a capacidade desta técnica experimental para obter medidas da cinemática completa, así como probar a súa versatilidade para realizar estudos de fisión a altas e baixas enerxías de excitación, tendo accceso a observables sensibles a dinámica previa e posterior ao punto de sela da fisión.
- Estudar a evolución co sistema fisionante de observables previos ao punto de sela sensibles aos efectos de disipación, tales como as seccións eficaces parciais e as anchuras de fisión.
- Estudar a evolución dos rendementos de fisión coa enerxía de excitación e obter unha parametrización dunha función de supresión que concorde cos resultados experimentais.
- Estudar a dependencia coa enerxía de excitación de diferentes observables posteriores ao punto de sela, tales como o exceso de neutróns, o efecto par-impar e as enerxías cinéticas totales dos fragmentos.

R.3 Introducción a fisión

R.3.1 Marco teórico

A fisión é unha reacción nuclear que consiste na división dun núcleo pesado en dous núcleos máis lixeiros, ademais doutras partículas maís pequenas como neutróns, protóns e partículas α. É unha reacción exotérmica que libera grandes cantidades de enerxía en forma de raios gamma e de partículas aceleradas a altas velocidades. A fisión foi descuberta en 1939 por Lise Meitner e Otto Hahn [6] cando bombardeaban núcleos de Uranio con neutróns na búsqueda de producir elementos transuránicos. Non obstante, no canto de producir elementos máis pesados ca o uranio, nas súas mostras atoparon Bario, o que signficaba que a reacción estaba producindo fragmentos máis lixeiros: o núcleo se estaba rompendo.

Este proceso de ruptura pódese dividir en dúas etapas, que en términos macroscópicos están definidas polo balance das enerxías de superficie e de repulsión culombiana no sistema fisionante. A primeira etapa vai dende o momento da reacción ata o definido como 'punto de sela', a partir do cal o proceso de fisión é irreversible. Durante esta etapa, a enerxía de superficie

incrementa coa deformación máis rápido do que a repulsión coulombiana decrece ao afastarse as cargas. Isto xera unha barreira de potencial que o sistema debe de superar para poder fisionar, agás no caso de fisión espontánea por efecto túnel. Se o sistema ten suficiente enerxía de excitación como para sobrepasar esta barreira, o sistema pasa á segunda etapa da fisión, que vai entre o punto de sela e o punto de escisión. Nesta etapa, a enerxía coulombiana decrece máis rápido que o incremento da enerxía de superficie, resultando nunha caída de potencial, polo que o sistema evoluciona a estados cada vez máis deformados ata rematar coa ruptura do sitema en dous fragmentos. Tras a escisión, a repulsión culombiana entre os dous fragmentos actúa afastándoos e dotándoos de altas enerxías cinéticas.

Aínda que a fisión foi descuberta hai 85 anos, aínda carece dunha descripción completa e satisfactoria debido a súa complexidade. En 1939, os científicos Niels Bohr e John Archibald Wheeler [19] parametrizaron o proceso en base ao modelo da gota líquida (LDM), que trata o núcleo de forma puramente macroscópica. En 1948 M.G. Mayer suxeriu que certos número de neutróns ou protóns no núcleo formaban configuracións particularmente estables [25], os denominados 'números máxicos', que tiñan a súa orixe nun fenómeno cuántico, o acoplamento espín órbita dos nucleóns. Isto deu comezo ao actual modelo de capas do núcleo, e fixo evidente a necesidade de parametrizar a fisión tendo en conta tamén os efectos microscópicos coma as capas nucleares ou os efectos de emparexamento de nucleóns. En 1966, V.M. Strutinski desenvolveu o chamado método macroscópico-microscópico [31] que consistía en corrixir o potencial macroscópico polas contribucións microscópicas.

Ademáis da influencia dos efectos microscópicos no potencial, tamén se comprobou que a fisión precisa dunha descripción dinámica. En 1940 Kramers introduciu que a evolución do sistema fisionante ata o punto de sela estaba suxeito a forzas disipativas, e que debería de ser parametrizado en base a ecuacións de teoría de transporte coma as de Fokker-Planck (FPE) [37]. A introducción deste parámetro de disipación suxería que a fisión estaba sometida ao acoplamento dos modos de enerxía colectivos e intrínsecos, un fenómeno que se manifestaba sobre todo a altas enerxías de excitación reducindo as probabilidades de fisión e favorecendo outros canais de desexcitación coma a evaporación de neutróns. Posteriormente, Weidenmüller [40], Grangé [41] e Bhatt [42] atoparon que o sistema precisaba dun certo tempo de tránsito para deformarse ata alcanzar o estado estacionario definido por Kramers, e fixeron un enfoque dependente do tempo utilizando modelos de transporte baseados no Langevin ou FPE.

R.3.2 Observable clave nos estudos de fisión nuclear: os rendementos

Un observable clave no estudio da fisión nuclear son os coñecidos como 'rendementos de fisión', que é a porcentaxe que se produce de cada especie nuclear na fisión. Este observable é de gran valor para a teoría nuclear, para aplicacións en reactores nucleares e para determinar a abundancia dos elementos pesados no universo debido á relevancia da fisión no 'proceso r' de nucleosíntesis estelar [87].

En canto a teoría nuclear, os rendementos de fisión foron determinantes para confirmar a existencia de números máxicos de neutróns e protóns, xa que os diferentes modos de fisión puñan en evidencia a preferencia dos sistemas por fisionar dando lugar a determinadas configuracións de neutróns e protóns. Os modos de fisión clasifícanse en dous grandes grupos, o simétrico, nos cales os dous fragmentos teñen similar carga e masa, e os modos asimétricos, nos cales un dous fragmentos é sustancialmente más grande cao outro. Os modos asimétricos aparecen como consecuencia dos efectos microscópicos como as capas, que favorecen a producción dun núcleo máis pesado se este está preto de conseguir unha configuración nuclear máis estable Ao principio, o modo de fisión asimétrico coñecido como 'St1' estaba asociado coa formación do fragmento pesado dobremente máxico de ^{132}Sn, con Z=50 e N=82, e o modo 'StII' coa deformación cuadrupolar asociada a N=88. Porén, medicións sistemáticas das distribucións do número de protóns e neutróns [12, 61] revelan que o número de neutróns pode variar ata 7 unidades coa masa do núcleo composto, mentres que o número atómico permanece bastante constante en valores comprendidos entre Z=52 e 56. Suxeriuse polo tanto [60] que podería existir unha estabilidade adicional proporcionada por os ocos de capa con deformación octupolar en Z=52 e Z=56 [63, 64].

Os modos de fisión tamén dependen da enerxía de excitación do sistema fisionante, outro observable clave no proceso de fisión. A altas enerxías os modos de fisión son predominantemente simétricos, debido a que a contribución dos efectos microscópicos é pequena en comparación cos macroscópicos. Non obstante, ao baixar a enerxías de excitación máis próximas a barreira, o modo simétrico vai minguando e os asimétricos, eclipsados a altas enerxías, comezan a ser visibles. Nos últimos realizáronse numerosos estudios [17, 65, 13, 53] para parametrizar a dependencia dos rendementos de fisión coa enerxía de excitación Para facelo, buscase unha función de supresión dependente da enerxía de excitación que atenúe o efecto da corrección microscópica sobre o potencial

macroscópico co crecemento da enerxía de excitación.

Os rendementos de fisión do número de neutrones foron moi importantes para comprender a repartición de enerxía que ten lugar entre o fragmento lixeiro e o pesado na evolución do sistema fisionante dende o punto de sela ata o de escisión. Segundo esta teoría, o fragmento pequeno e altamente excitado transfire a enerxía cara o fragmento pesado e de baixa enerxía, xa que este ten unha maior dispoñibilidade de estados [18]. Este mecanismo tamén se propón como o responsable do efecto par-impar observado nos rendementos, caracterizado por unha maior producción dos núcleos con números pares de protóns, e na transferencia do protón desapareado ao núcleo pesado [72].

R.4 Metodoloxía

Neste estudo combínanse as técnicas de cinemática inversa e de reaccións de knockout inducidas por protóns, que procederanse a describir a continuación.

A técnica da cinemática inversa consiste en acelerar aos núcleos pesados para facelos reaccionar contra un branco, ao revés do que se fai nos estudos en cinemática directa, no cal o núcleo pesado actúa como branco e as partículas lixeiras como proxectil. A introducción desta técnica supuxo un gran avance para os estudos de fisión, xa que deste modo os dous fragmentos de fisión saen cara adiante a altas enerxías cinéticas, posibilitando a detección dos dous fragmentos e a identificación en carga e masa. Ademáis, os estudos en cinemática directa estaban suxeitos á utilizar como brancos núcleos estables, mentres que en cinemática inversa pódense facer estudios de núcleos exóticos.

As reaccións de knockout inducidas por protóns arrincan nucleóns das capas internas dos núcleos, deixando ao remanente da reacción cunha enerxía de excitación proporcional á da capa que foi arrincado. O caso particular das reaccións de knockout nas que un sólo protón é arrincado do núcleo coñécese como reacción case-libres (p, 2p). Chámanse 'case-libres', porque á interacción limítase aos dous protóns involucrados, sen afectar aos demais nucleóns. Neste tipo de reaccións é posible reconstruír a enerxía de excitación do remanente coñecendo o momento dos dous protóns saíntes da reacción e empregando o 'método da masa perdida', que se basa en aplicar a conservación do momento.

R.5 Dispositivo experimental

O experimento realizouse no acelerador de partículas GSI en marzo de 2021, utilizando a técnica de cinemática inversa con reaccións de knockout inducidas por protóns. Os feixes primarios de ^{238}U foron producidos polo sincrotrón SIS18 e guiados ata o área experimental para impactar nun branco de hidróxeno líquido a 540MeV/u. A disposición dos detectores pode verse na Fig. R.1.

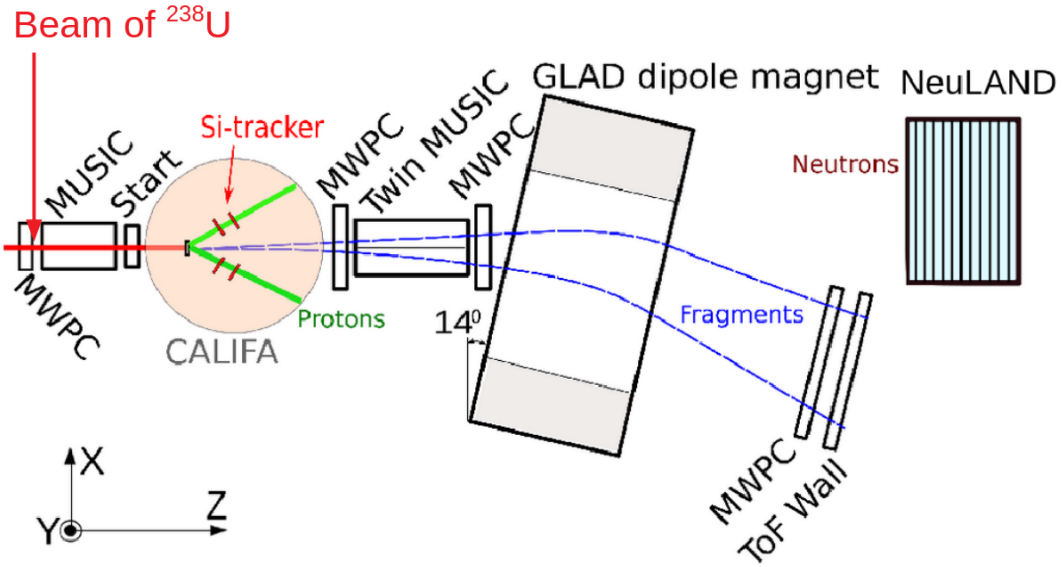

Figure R.1: *Montaxe experimental no GSI*

Para a caracterización do sistema de fisión, o dispositivo conta co detector CALIFA para medir as enerxías dos protóns resultantes do knockout, e os detectores AMS para reconstruír a traxectoria dos mesmos. Para a caracterización dos fragmentos de fisión, o dispositivo experimental conta con varios detectores medidores de posición ao largo do setup coñecidos como MWCPs, un medidor de tempo de voo (o ToFWall) e unha cámara de ionización a Twin MUSIC. A Twin MUSIC conta con 4 cámaras de ionización para poder medir simultánemente o número atómico dos dous fragmentos de fisión a través da pérdida de enerxía destes dentro do gas. Tamén conta con NeuLAND, un detector de neutróns para reconstruír as multiplicidades de neutróns evaporados durante o proceso. A masa dos fragmentos pódese reconstruír grazas ao método $\Delta E - B\rho - ToF$, que se basa nas diferentes rixideces magnéticas dos ións de diferente masa ao pasar polo campo magnético dun dipolo, GLAD. Desta forma, coñecendo o número atómico do fragmento (Z), a súa velocidade (β, γ), o radio de curvatura dentro do imán (ρ) e o campo magnético, o número másico pode calcularse usando a Eq. R.1.

$$B\rho = \frac{A}{Z \cdot e} u\beta\gamma c \tag{R.1}$$

R.6 Análise de datos

O análise de datos comprende a calibración de detectores. A calibración é o proceso de comparación valores obtidos por un instrumento coa medida correspondente dun estándar de referencia. Os datos proporcionados polos detectores non están en unidades físicas senón en unidades de electrónica. Estas unidades de electrónica deben converterse en magnitudes físicas como carga, posición ou tempo de voo, e cada detector ten un procedemento diferente. Ademáis, cada unha debe correxirse polas diferentes ganacias das unidades de medida ou de dependencias con outras variables. Os procesos máis sinalados da calibración comprenden:

- Sustracción dos pedestais nas MWPCs. As unidades de medida das MWPC, chamados 'strips', teñen diferentes valores de ruído causados pola electrónica, chamados 'pedestais' que deben sustraerse dos datos.
- Aliñamento de ToF-Wall. As unidades de medida do ToF-Wall, chamadas 'paddles' deben de estar centrados no mesmo valor de tempo de voo.
- Calibración da Twin MUSIC. A enerxía dos ánodos da Twin MUSIC debe de estar aliñada. Do mesmo modo, débese de correxir a dependencia da pérdida de enerxía no gas pola tempo de voo dos fragmentos e polo tempo de deriva dos elctróns na cámara.

Unha vez calibrados os instrumentos, pódese proceder ao cálculo dos rendementos de fisión, o cal consiste en calcular o porcentaxe producido dunha determinada especie con respecto á producción total. Ademáis das calibracións, o análise de datos tamén require do cálculo de certas magnitudes de importancia. Cabe destacar:

- Cálculo do vértice de reacción. Coñecendo a posición e o ángulo horizontal dos dous fragmentos de fisión dentro da Twin, é posible calcular a intersección da traxectoria dos dous fragmentos. Deste modo, pódense seleccionar os eventos que veñan sólo do branco e non de reaccións con outros elementos do montaxe
- Reconstrucción do Bρ dentro do imán e da lonxitude total da traxectoria. Para reconstruír estas dúas magnitudes, empregouse un método basado en simulación, usando as posicións reais dos detectores no montaxe e o mapa do campo magnético de GLAD. Para cada evento real, xéranse mediante simulación 10 ións cada un cun momento diferente. Cada ión seguirá unha traxectoria diferente dentro do imán e medirase nunha posición x diferente

da MWPC3 que está situada despois do dipolo. Usando estes 10 puntos, faise un axuste polonómico de Bρ coa posición x da MWPC3 e da lonxitude coa posición x da MWPC3. Coñecendo esta ecuación e o valor da posición x na MWPC3, pódese obter os valores de rixidez magnética e lonxitude. Unha vez obtido isto, o valor da masa pode calcularse usando a Eq. R.1.

R.7 Resultados

Os resultados presentáse en dúas partes, a primeira parte adicada aos resultados relacionados coa dinámica de fisión anterior ao punto de sela e a segunda parte adicado á dinámica posterior ao punto de sela.

R.7.1 Dinámica previa ao punto de sela

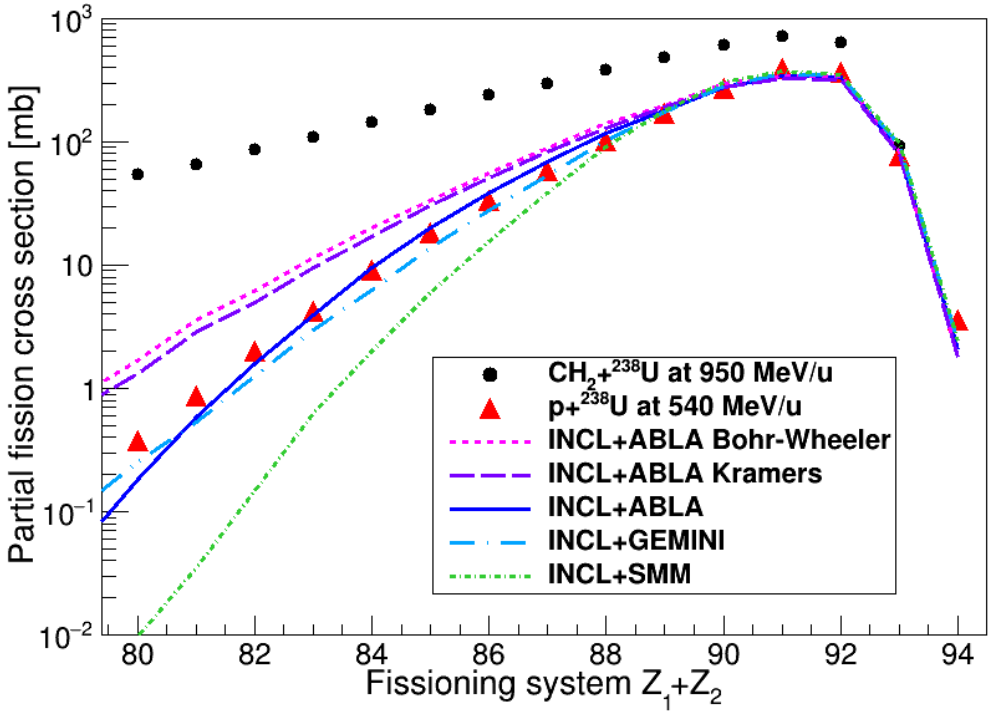

Figure R.2: *Seccóns eficaces parciais para os sistemas fisionantes producidos na reacción $p + ^{238}U$ a 540 MeV/u. Datos para a reacción $CH_2 + ^{238}U$ a 950 MeV/u obtidos de [123]*

.

Observouse como a seccións eficaces parciais de fisión caen rápidamente para os sistemas de fisión máis lixeiros, como pode comprobarse na Fig. R.2, o que é indicativo da aparición de fenómenos de disipación que se manifestan a altas enerxías de excitación. Varios modelos de desexcitación foron acoplados ao modelo de reacción INCL e compáraronse cos datos experimentais. Foi un descubrimento interesante que tanto ABLA como GEMINI describen bastante

ben as seccións transversais de fisión para os diferentes sistemas de fisión estudados, a pesar de ter unha parametrización moi diferente. Mentres que ABLA consiste nunha descrición dependente do tempo utilizando as ecuacións de Fokker-Planck tendo en conta a disipación, GEMINI non ten en conta a disipación nin o tempo de tránsito senón que ten unha parametrización de densidade de nivel baseada en datos reais.

En canto ao estudio das anchuras de fisión, atopuse que a elección do branco ten un impacto importante nos resultados. Isto é debido a que anchura depende da fisilidade, e diferentes brancos dan lugar a diferentes distribucións de sistemas fisionantes que cubren rangos de fisilidade distintos. Tamén se observou que neste observable, o modelo ABLA reproduce mellor os datos, xa que ten en conta os efectos de capa que producen o ensanchamento das anchuras de fisión para os sistemas fisionantes de menor enerxía de excitación.

R.7.2 Dinámica posterior ao punto de sela

Para esta etapa do proceso de fisión, estudouse a evolución de diferentes observables coa enerxía de excitación do sistema fisionante. Non obstante, non foi posible reconstruír a enerxía de excitación usando os AMS. Isto debeuse a producción de numerosos electróns delta provintes de reaccións secundarias ao longo do dispositivo, que imposibilitaron distinguir os electróns dos protóns no detector. Polo tanto, estudiouse qué outros observables eran sensibles a enerxía de excitación, e atopouse que a suma de masas dos fragamentos de fisión era moi sensible. Isto débese a que unha maior enerxía de excitación do sistema fisionante

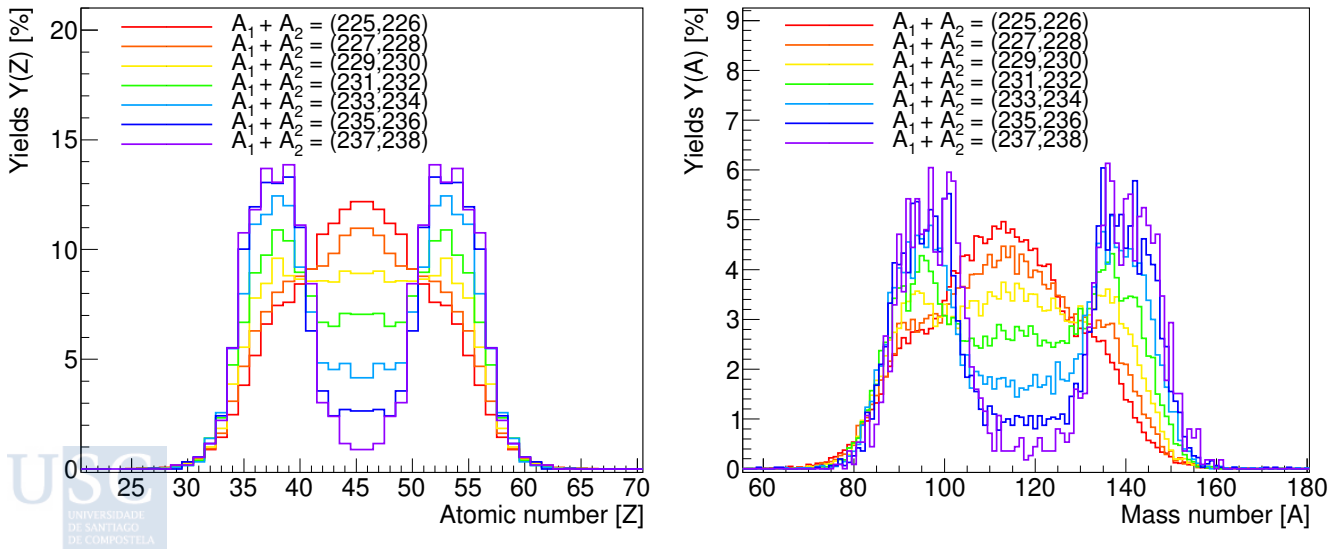

Figure R.3: *Evolution of the fission yields normalized to 200% for Z=91 fissioning system at different cuts in mass addition. Left: Elemental fission yields. Right: Isobaric fission yields.*

evaporará un maior número de neutróns, o que da lugar a dous fragmentos de fisión con menor masa. Polo tanto, a suma de masas está inversamente coa enerxía de excitación. Na Fig. R.3 poden observarse os rendementos de fisión en número atómico (esquerda) e másico (dereita) para diferentes condicións en suma de masas. Pode apreciarse cómo os rendementos para as sumas de masas baixas amosan modos de fisión simétricos asociados as alta enerxía de excitación, mentres que as sumas de masas altas amosan os modos simétricos característicos das altas enerxías de excitación. Polo tanto, a suma de masas calibrouse para pasala a unidades de enerxía e empregouse este observable como indicador da enerxía de excitación.

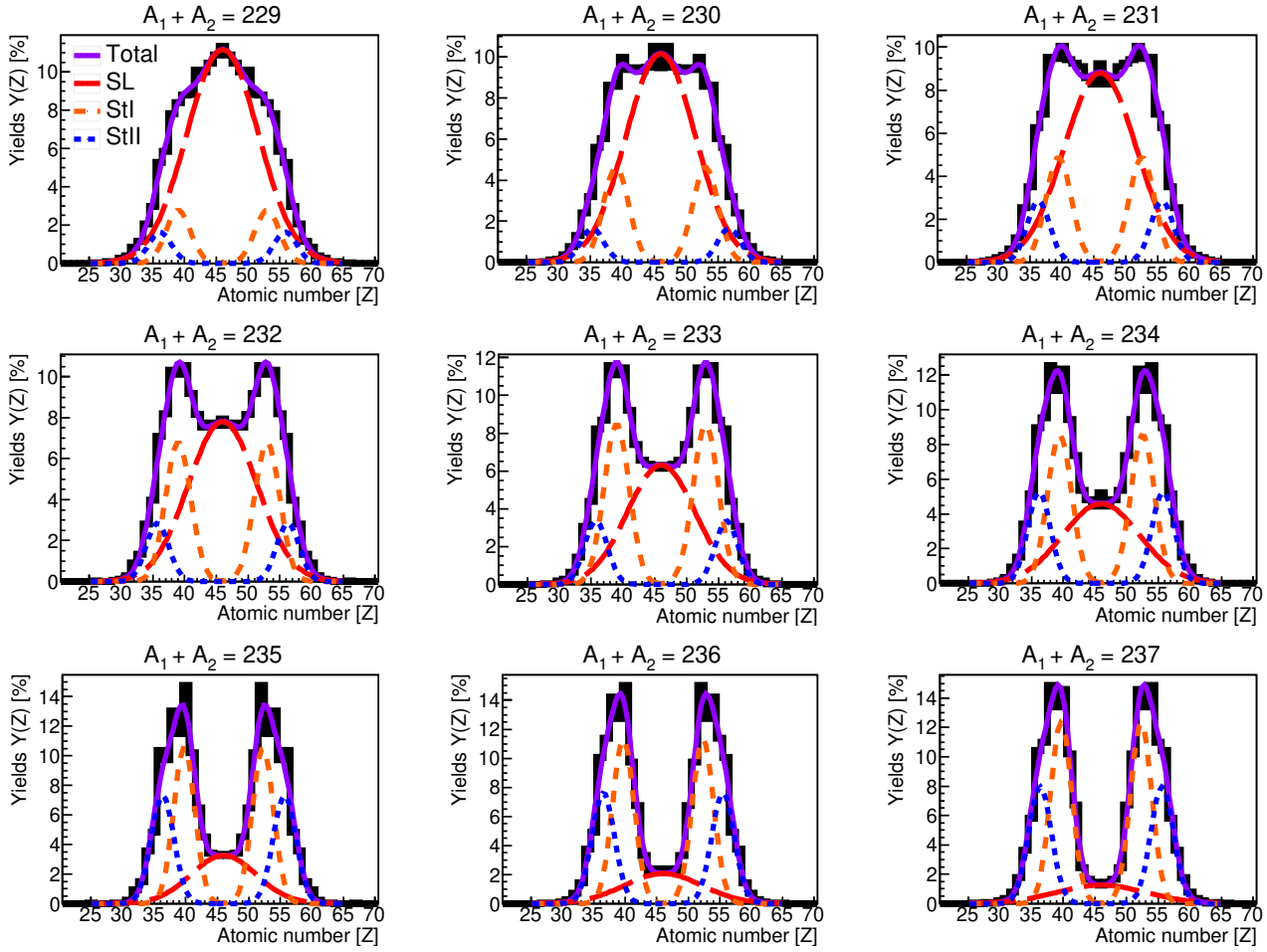

Figure R.4: *Rendementos de fisión normalizados ao 200% para o sistema fisionante Z=92 e para diferentes cortes en suma de masas. A liña negra representa os datos experimentais, e axústanse 3 modos de fisión diferentes: o súper longo (liña vermella de trazos longos), Standard I (liña laranxa de trazos curtos) e Standard II (liña azul punteada).*

Os rendementos de fissión baixo as diferentes condicións en suma de masas foron empregados para evaluar para diferentes funcións de supresión. Observouse que a función Woods-Saxon proposta por Randrup [17] funciona razoablemente

ben para baixas enerxías de excitación, pero non é suficiente para describir o amortecemento dos rendementos de fisión a enerxías de excitación superiores a 15 MeV. A función de supresión en mellor acordo cos datos experimentais atopouse para unha combinación de dous exponenciais, $S(E^*) = \exp(-E^*/4MeV)$ para as enerxías de excitación inferiores a 20MeV e $S(E^*) = \exp(-E^*/13MeV)$ para enerxías de excitación superiores a 20MeV.

Os modos de fisión foron estudados para diferentes cortes en suma de masas, tanto para os rendementos de fisión atómicos coma os de neutróns. Na Fig. R.4 pódense ver os rendementos atómicos axustados polos modos de fisión SL (súper longo) para as fisións simétricas, e os modos StI e StII para as fisións asimétricas. Os valores medios do número de protóns resultaron en $< Z_H >= 53$ para o StI e $< Z_H >= 56$ para o StII, en boa concordancia coa predición da estabilidade para os modos deformados octupolares en Z=52,56 [63, 64]. Para o número de neutróns, obsérvase in incremento do número de neutróns coa suma de masas, dando lugar a valores entre $< N_H >= 81 - 84$ para o StI e $< N_H >= 87 - 89$ para o StII.

As amplitudes do efecto par-impar foron calculadas, tanto para o efecto global coma para o local, e foron estudadas para diferentes condicións en suma de masas. Atopouse un aumento da amplitude global do efecto ao disminuír a enerxía de excitación, excepto por os dous puntos de baixas enerxías. A amplitude local do efecto par-impar mostra a forma dunha parábola con valores positivos para os sistemas fisionantes de número atómico 92, como se pode apreciar na Fig.R.5 , o esperado para un sistema fisionante par. Os resultados están en boa concordancia coa simulación de INCL+ABLA nas rexións de fisión asimétrica. Para os sistemas fisionantes con número atómico 91, atópase unha amplitude positiva nos fragmentos lixeiros e negativa nos pesados. Isto tamén coincide co esperado, xa que nos sitemas de fisión impares o protón desemparexado tende a rematar no fragmento pesado debido ao mecanismo de repartición de enerxía [72].

O exceso de neutróns foi estudado para diferentes condicións de suma de masas. Como pode observarse na Fig. R.6, para as sumas máis baixas (ou enerxías de excitación máis altas), o exceso de neutróns amosa un crecemento uniforme coa carga do fragmento de fisión, o cal é o esperado, posto que ao aumentar o número de protóns o de neutróns tamén aumenta para contrarrestar a repulsión culombiana, fenómeno coñecido como polarización. Non obstante, para as sumas de masa máis altas (enerxías de excitación máis baixas) os efectos de capas comezáronse a facer visibles, xa que o exceso de neutróns mostraba un

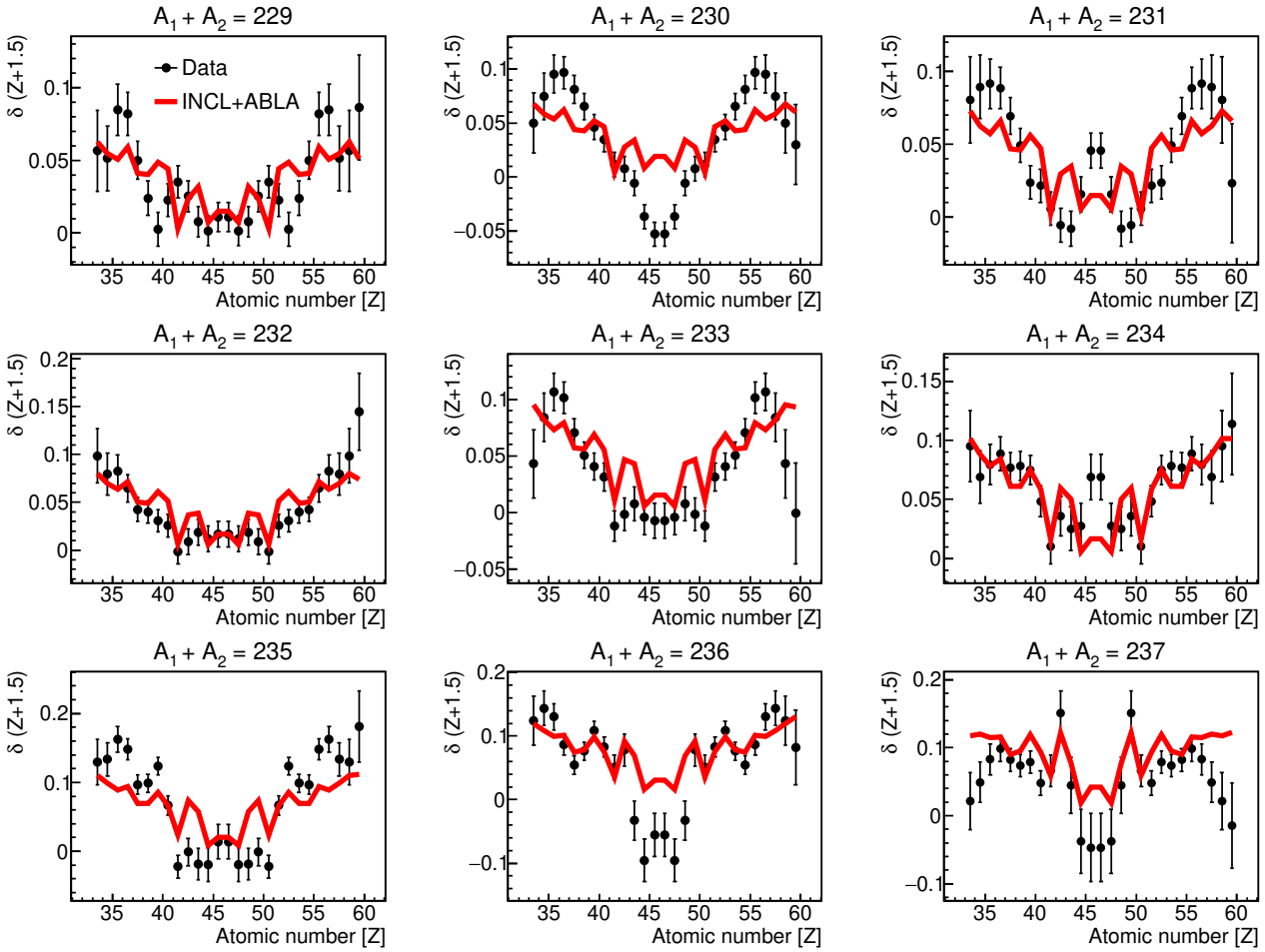

Figure R.5: *Amplitude do efecto par-impar local para o sistema fisionante $Z_1 + Z_2$ =92 en función do número atómico do fragmento de fisión.*

pico para Z=50 correspondéndose con N=82, ámbolos dous números máxicos.

Estimáronse as multiplicidades de neutróns antes e despois da escisión mediante a aproximación de UCD para calcular as masas no punto de escisión, e os resultados son de acordo coa parametrización proposta por Hilscher [134] . A enerxía cinética total foi calculada a partir das masas dos fragmentos no punto de escisión e as velocidades. De novo, este observable tamén foi estudado para diferentes condicións en suma de masas. Observouse cómo os datos para as sumas de masas máis baixas (maiores enerxías de excitación) amosaban enerxías cinéticas máis altas, debido a que as deformacións e as distancias de separacións entre os dous fragmentos son menores nos modos de fisión asimétricos. Así mesmo, as enerxías cinéticas amosaban unha concordancia razoable coa simulación de INCL+ABLA.

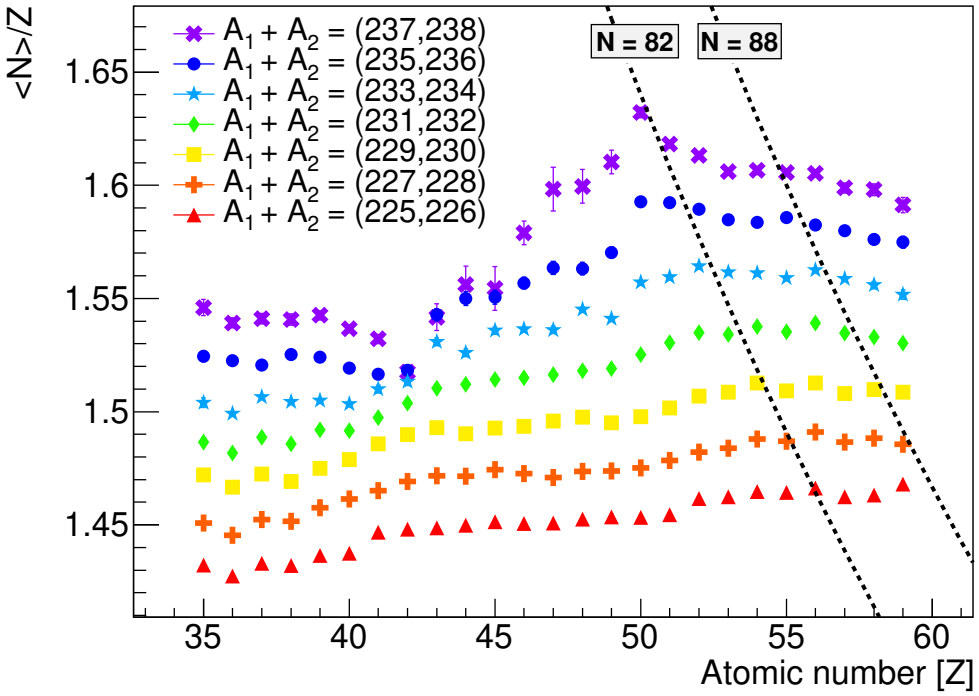

Figure R.6: *Número medio de neutróns por número atómico en función do número atómico do fragmento de fisión para* $Z_1 + Z_2 = 92$ *e diferentes condicións en suma de masas.*

R.8 Conclusións

En base aos resultados obtidos, pode sacarse en conclusión que esta nova técnica experimental apunta ser válida para a obtención de medidas da cinemática completas. Non obstante, precisa dalgunhas modificacións no setup, como substituír os AMS por detectores de píxeles, tales coma os ALPIDE, dado que a alta multiplicidade de electróns delta impediu a obtención da enerxía de excitatión con AMS. Non obstante, outros observables sensibles a enerxía de excitación foron empregados, tales coma o ángulo de apertura entre os protóns e a suma de masas dos fragmntos de fisión. Da mesma forma, probou a súa utilidade como mecanismo para estudiar a fisión a altas e baixas enerxías de excitación, estudando fenmenos da dinámica de fisión tanto antes como despois do punto de sela. As seccións eficaces de fisión e as anchuras foron obtidas e comparadas con calculos teóricos. Estudouse a evolucións dos rendementos de fisión coa enerxía de excitación e atopouse unha parametrización para a función de supresión que describise os datos experimentais. Diferentes observables sensibles ao mecanismo de repartición da enerxía, tales como o exceso de neutróns e o efecto par-impar foron estudados para diferentes enerxías de excitación. Calculando as masas no punto de escisión coa aproximación UCD, as multiplicidades de neutróns e as enerxías cinéticas totales foron reconstruídas, dando resultados en concordancia coas parametrizacións e modelos teóricos.

Appendix

A.1 Mass reconstruction using simulated data as input

In order to test the performance of the masses reconstruction method, data has been simulated using the real geometry of the setup in the cave and giving the expected resolution of the detectors, which means $\Delta T = 40$ ps FWHM for the Tof Wall, $\Delta X = 300$ μm FWHM for the MW_3 and $\Delta X = 70$ μm for the Twin MUSIC. The mass distribution result is displayed in Fig. A.1(left) as an example for the fission fragments of atomic charge Z=40. The distribution shows alternating high and low peaks, which come from the odd-even effect, enhancing the production of fragments with even atomic numbers.

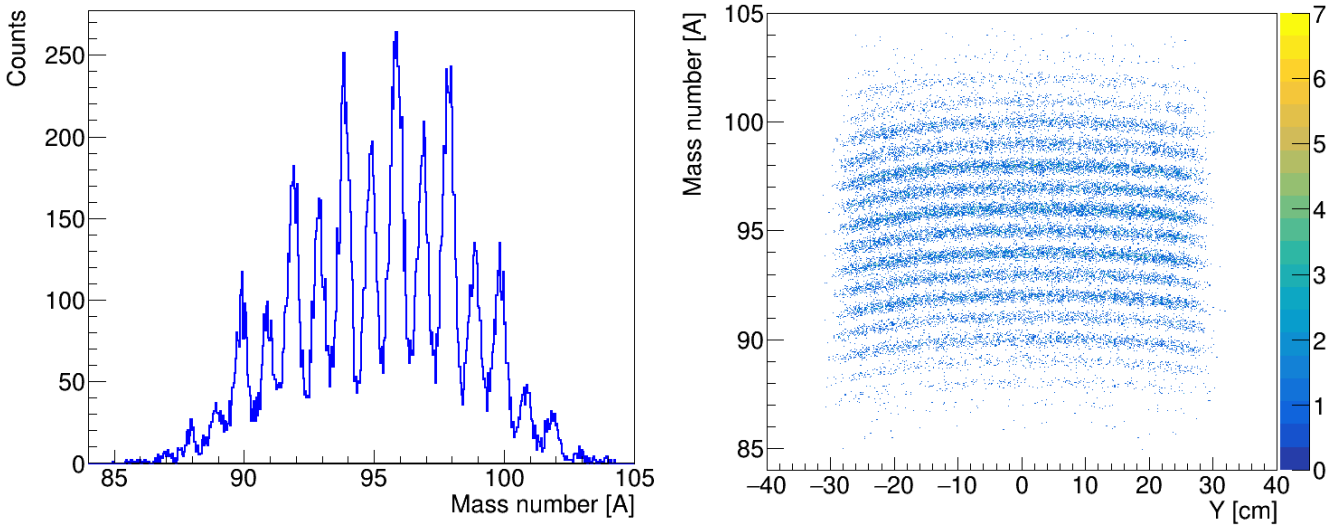

Figure A.1: *Left: Mass number of the fission fragment distribution. Right: Mass number dependency on the Y position of the fission fragment in the ToF Wall.*

The mass number has a dependency on the Y position of the fission fragment, as can be seen in Fig. A.1(right). The origin of this dependence has to do with the fact that the method only gives as input for the simulation an initial value of momenta in the ZX plane, as shown in Eq. 3.15, but not in Y. However, in reality, the momenta are distributed homogeneously in X and Y, since the fission fragments are emitted in the forward direction in a narrow cone because of the Lorentz boost, as can be seen in Fig. A.2 while plotting the position of the position in Y in the ToF Wall against the paddle number. Therefore,

fission fragments measured in the plastics further away from the center will have a smaller dependency on Y, because the fragments were emitted closer to the ZX plane, while the ones in the center of the ToF Wall will have a bigger dependency. The dependency has an arch shape, resulting in slightly smaller masses for the fragments further from the ZX plane. This is because those fragments that had more momenta in Y were given total momentum lower than the real one, which would be the addition of the momenta in the 3-axis. The reason why initial values of momenta were only given in the ZX plane is the lack of data in the Y position of the fission fragments in the MWPCs because of inefficiency. This should not be a problem if the mass resolution is good enough to distinguish masses since the dependency can be easily corrected.

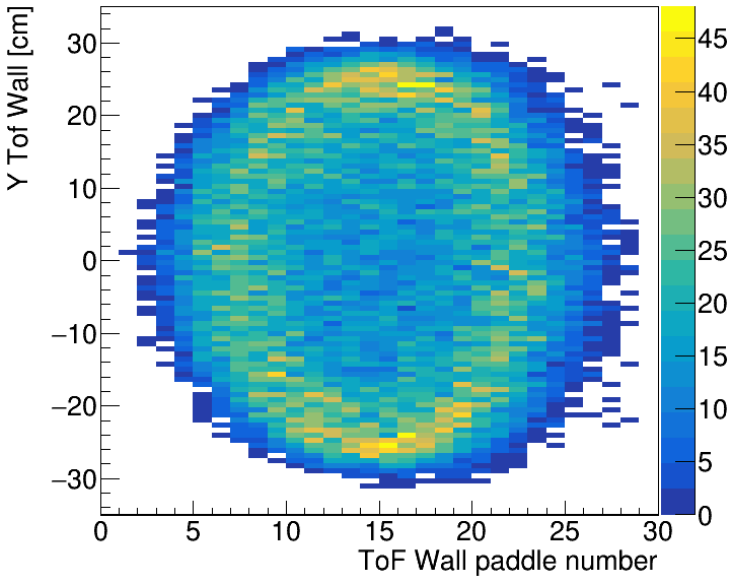

Figure A.2: *Y vs paddle*

The dependency of the mass number on the Y position has been corrected following the same procedure used for the ToF and drift time in the Twin calibration, further detail can be consulted in Sec. 3.3.2. The corrected correlation is shown in Fig. A.3(left), where now all the lines look straight. Having done this, it can be seen in Fig. A.3(right) how the mass distribution peaks are better defined. Specifically, the mass resolution has changed from $\Delta A = 0.75$ FWHM in mass number units [A] for the central charges in Fig. A.1(left) to $\Delta A = 0.43$ FWHM in Fig. A.3(right), demonstrating the importance of this correction to achieve a good mass resolution.

Fig. A.4 shows the mass distribution for all the fission fragments. Even though the symmetric fission peak in the center dominates the distribution, the asymmetric peaks are noticeable towards the edges, around A=90 for the light fragments and around 130 for the heavy fragments. The peak of the heavy

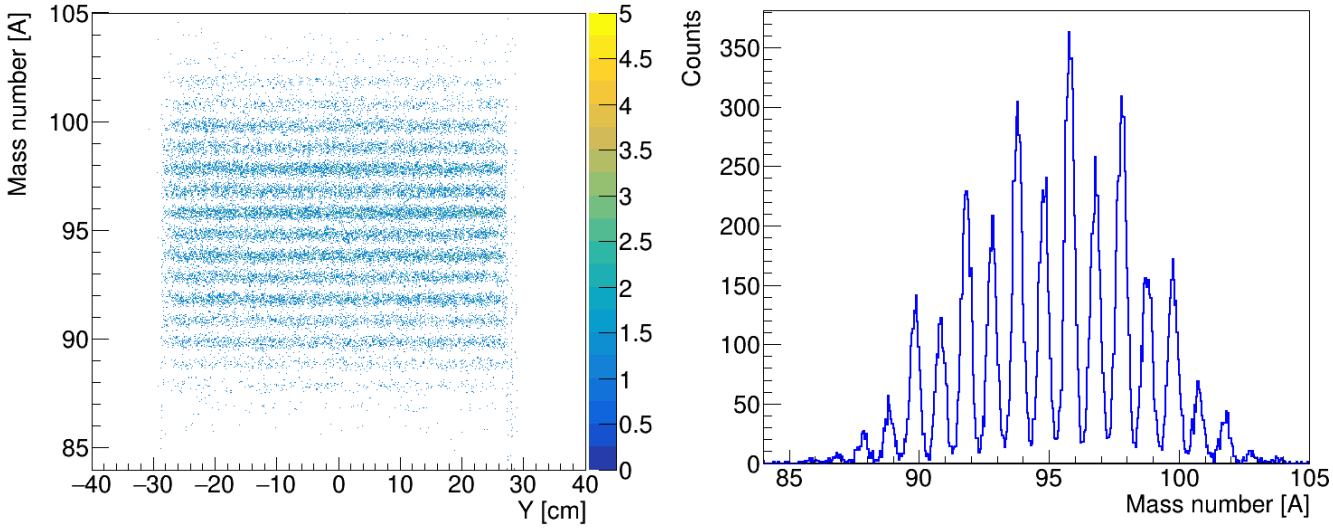

Figure A.3: *Left: Mass number correlation with Y position of the fission fragment in the ToF Wall after the correction. Right: Mass number of the fission fragment distribution corrected by Y dependence.*

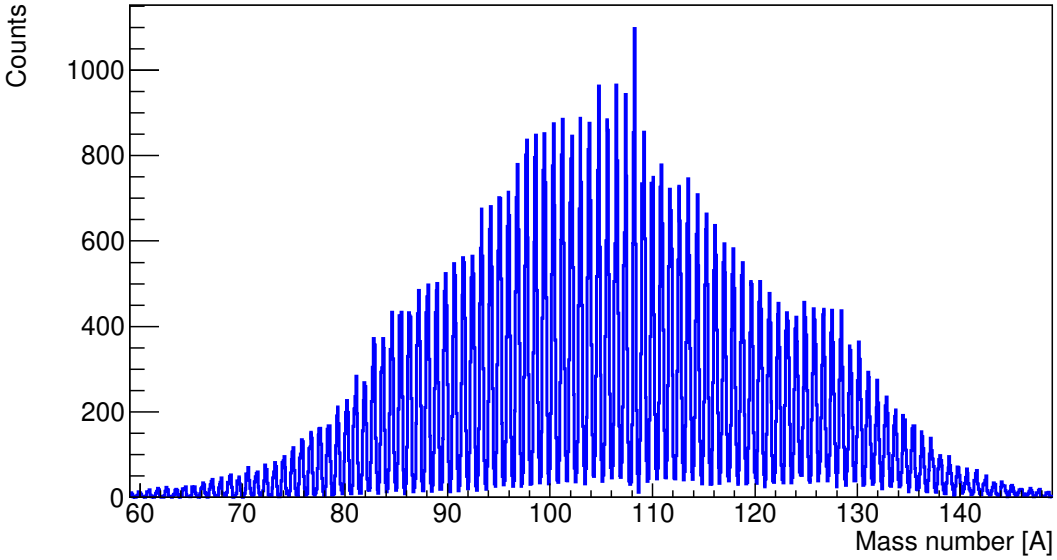

Figure A.4: *Mass number distribution for all the fission fragments*

fragments is much more noticeable than the peak of the light ones. This is due to the neutron evaporation of the fragments from the symmetric peak, which reduces the mass of the fragments, shifting the symmetric peak towards the left. In this way, the symmetric peak eclipses the light-asymmetric peak and leaves the heavy-asymmetric peak more unveiled.

A.2 Time-of-flight resolution

In order to obtain the time-of-flight resolution, only beam events are selected, for which a sweep run is chosen. The atomic number identification in the Twin MUSIC for these heavy ions is done following the same procedure conducted with the fission fragments. Still, the charge collected by the anodes is added differently. For the fission fragments, the charge of all the anodes within a section was added to obtain the average energy loss in each of the 4 sections. For the beam events, the Twin will be treated as if it had 2 sections: left and right. To do so, the charge of the anode with the highest charge deposition of the sections up and down will be added for each side of the Twin (left and right). The reason to proceed this way is that the beam hits the Twin MUSIC very close to its center (in general a little shifted to the left), causing the beam to pass through both sections up and down more often. Fig. A.5 shows the Twin identification of the beam events.

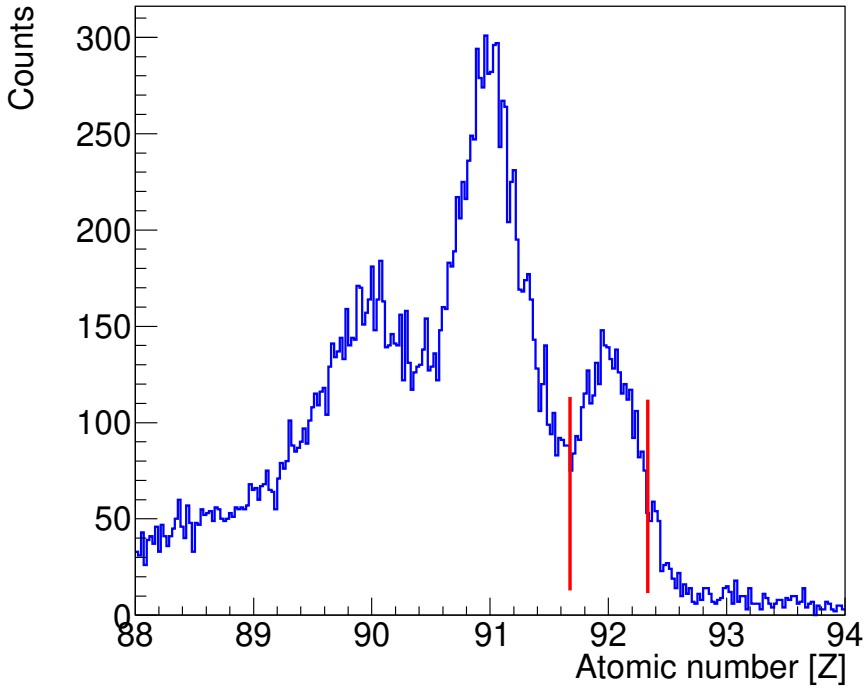

Figure A.5: *Atomic number identification for heavy ions in the Twin MUSIC. The peak within the red bars corresponds to the U fully stripped.*

The beam coming from the synchrotron is fully stripped (the ion does not have any electron), however, since the beam and spallation events have a much higher Z than the fission fragments, there is a certain probability that they pick up electrons along their passage through the setup. In Fig. A.5, the peak with the highest atomic number (within the red bars) corresponds to fully stripped U events, while the other peaks to the left might have a contribution from the charge states of the heavier ones. The peak corresponding to Z=91 would have

the contribution from Pa fully stripped and U that picked up 1 electron. To obtain the ToF resolution, only the events from the Z=92 peak will be selected. Also, only one paddle is selected (paddle 15, since it has the highest contribution to Z=92).

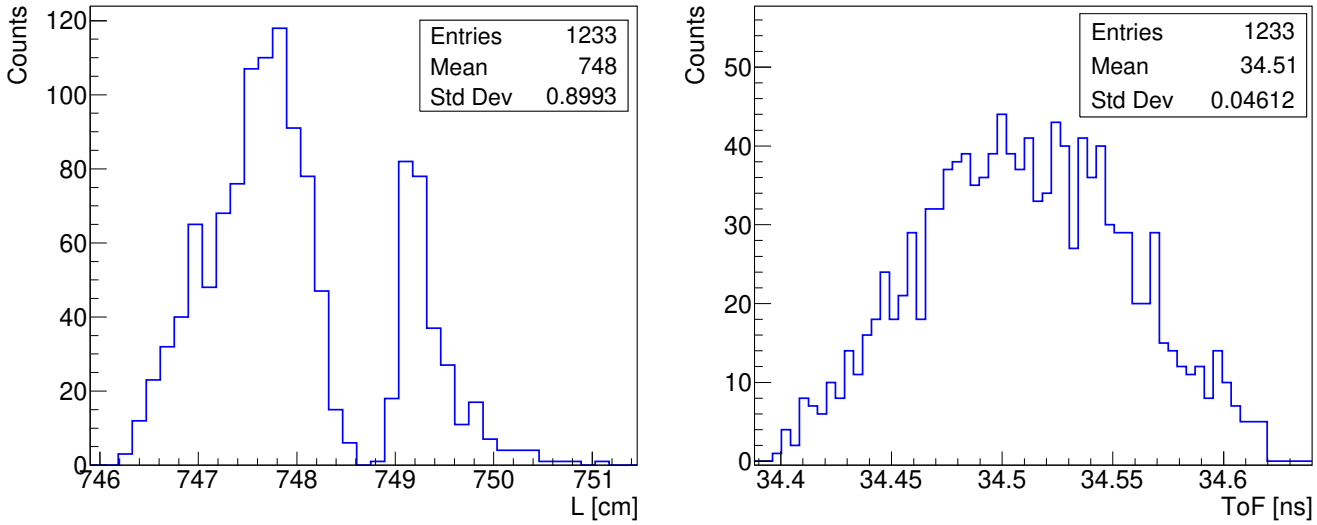

Figure A.6: *Reconstructed length distribution (left) and ToF distribution (right) for Z=92 in Twin and paddle 15 in the ToF Wall. The gap located around 748 cm in the reconstructed length corresponds to the events lost in the Twin MUSIC cathode.*

The resolution of the ToF has a contribution from the trajectory spread caused by the magnet. This can be evaluated by calculating the standard deviation of the reconstructed length ($\sigma = 0.9$ cm, as seen in Fig. A.6 (left)) and dividing it by the average velocity. This results in a contribution to the time-of-flight of 0.042 ns, while the intrinsic resolution of the time-of-flight is $\sigma = 0.046$ ns, as seen in Fig. A.6 (right). Calculating the quadratic sum of both, the final resolution of the beam events is ΔToF = 146 ps FWHM.

A.3 Atima List of Materials

Name	Matter	ρ (g/cm^3)	Thick. (mg/cm^2)	Thick. (cm)
Window	Fe	7,874	79,29	0,0101
Air	Air	0,001205	18,07	15
$MWPC_0$ Window	Mylar	1,38	1,67	0,0012
$MWPC_0$ Gas	$ArCO_2$	0,00171	0,34	0,2
$MWPC_0$ Pads	Mylar	1,38	1,67	0,0012
$MWPC_0$ Gas	$ArCO_2$	0,00171	0,86	0,5
$MWPC_0$ Central Cathode	Ar	0,001662	2,01E-3	0,0012
$MWPC_0$ Gas	$ArCO_2$	0,00171	0,86	0,5
$MWPC_0$ Window	Mylar	1,38	1,67	0,0012
Air	Air	0,001205	11,75	9,75
TRIM Window	Mylar	1,38	3,46	0,0025
TRIM Field Cage	Mylar	1,38	3,46	0,0025
TRIM CO_2	CO_2	0,001842	1,29	0,7
TRIM CH_4	CH_4	0,0006	16,8	28
TRIM CF4	CF4	0,00372	14,14	3,8
TRIM Ar	Ar	0,001662	55,51	33,4
TRIM Field Cage	Mylar	1,38	3,46	0,0025
TRIM Stripper	Nb	8,57	60,68	0,0071
TRIM Field Cage	Mylar	1,38	3,46	0,0025
TRIM Field Cage	Mylar	1,38	3,46	0,0025
TRIM Stripper	Nb	8,57	60,68	0,0071
TRIM Field Cage	Mylar	1,38	3,46	0,0025
TRIM Field Cage	Mylar	1,38	3,46	0,0025
TRIM Window	Mylar	1,38	3,46	0,0025
Air	Air	0,001205	15,06	12,5
Sci Window	Mylar	1,38	6,92	0,005
Sci 1st Half	BC400	1,032	154,5	0,075
Sci 2nd Half	BC400	1,032	154,5	0,075
Sci Window	Mylar	1,38	6,92	0,005
Air	Air	0,001205	68,69	57
Vacuum Chamber Window	Steel	8	40,64	0,0051
LH_2 Window	Mylar	1,38	17,26	0,0125

Table A.1: *Table of materials between the entrance of the cave and the target window.*

Name	**Matter**	ρ **(g/cm^3)**	**Thick. (mg/cm^2)**	**Thick. (cm)**
LH_2 Target	LH_2	0,0708	106,2	1,5
LH_2 Window	Mylar	1,38	24,85	0,018
Target Isolation	Mylar	1,38	6,91	0,005
Vacuum Chamber	Air	1E-10	1,13E-5	113
Vacuum Chamber Window	Steel	8	40,64	0,0051
Air	Air	0,0012	33,74	28
$MWPC_1$ Window	Mylar	1,38	1,66	0,0012
$MWPC_1$ Gas	$ArCO_2$	0,00171	0,34	0,2
$MWPC_1$ Strips	Mylar	1,38	1,66	0,0012
$MWPC_1$ Gas	$ArCO_2$	0,00171	0,86	0,5
$MWPC_1$ Strips	Mylar	1,38	1,66	0,0012
$MWPC_1$ Gas	$ArCO_2$	0,00171	0,51	0,3
$MWPC_1$ Window	Mylar	1,38	1,66	0,0012
Air	Air	0,0012	5,42	4,5
TWIM Window	Mylar	1,38	3,46	0,0025
TWIM gas	CH_4	0.0006	25.12	41.87
TWIM gas	Ar	0.00166201	17.62	10.6
TWIM gas	Co_2	0.001842	0.98	0.53
TWIM Window	Mylar	1,38	3,46	0,0025
Air	Air	0.001205	4.52	3.75
$MWPC_2$ Window	Mylar	1,38	1,66	0,0012
$MWPC_2$ Gas	$ArCO_2$	0,00171	0,34	0,2
$MWPC_2$ Strips	Mylar	1,38	1,66	0,0012
$MWPC_2$ Gas	CO_2	0.001842	0.92	0,5
$MWPC_2$ Strips	Mylar	1,38	1,66	0,0012
$MWPC_2$ Gas	$ArCO_2$	0.00171	0,51	0,3
$MWPC_2$ Window	Mylar	1,38	1,66	0,0012
Air	Air	0.001205	14.76	12.25
GLAD window	Mylar	1.38	6.92	0.005
GLAD window	Steel	8	160	0.02
GLAD gas	He	0.000166322	68.19	410
GLAD window	Mylar	1.38	23.47	0.017
Air	Air	0.001205	92.46	76.7296
$MWPC_3$ Window	Mylar	1,38	1,66	0,0012
$MWPC_3$ Gas	$ArCO_2$	0,00171	0,34	0,2
$MWPC_3$ Strips	Mylar	1,38	1,66	0,0012
$MWPC_3$ Gas	CO_2	0.001842	0.92	0,5
$MWPC_3$ Strips	Mylar	1,38	1,66	0,0012
$MWPC_3$ Gas	$ArCO_2$	0.00171	0,51	0,3
$MWPC_3$ Window	Mylar	1,38	1,66	0,0012
Air	Air	0.001205	91.58	76
ToF Wall window	Mylar	1.38	1.66	0.0012
ToF Wall plastics	BC 400	1.032	526.42	0.5101

Table A.2: *Table of materials between the target and the end of the seetup.*

A.4 Fission cross-section correction factors

Factor	Value	Comments
$\mathrm{Eff_{Twin2}}$	0.83 ± 0.01	The Twin efficiency is calculated spill-to-spill for each file in the experiment. The value shown here corresponds to the mean value for a file.
$\mathrm{Eff_{Twin1}}$	0.77 ± 0.01	Same as for $\mathrm{Eff_{Twin2}}$, but for $\mathrm{TPat_1}$
$\mathrm{I_1/I_{tgt} + I_4/I_{tgt} - I_2/I_{tgt} - I_3/I_{tgt}}$	0.0061 ± 0.0025	The uncertainty was estimated by varying the Breit Weigner limits for the fit.
$\mathrm{P_{R\frac{1}{2}tgt}}$	0.03 ± 0.009	Reaction rate for half of the target (7.5 mm), obtained with Atima (uncertainties set to 3%)
$\mathrm{P_{Ftgt}}$	0.74 ± 0.16	Average fission probability for a ^{238}U spallation residue impinging on a proton target. Calculated using simulation with INCL.
$\mathrm{P_{Stgt}}$	0.26 ± 0.16	Approximated as 1- $\mathrm{P_{Ftgt}}$
$\mathrm{P_{Rwdw}}$ (Mylar)	(26 ± 7.8)·10^5	Reaction rate for 230μm of Mylar (target wrapping), obtained with Atima (uncertainties set to 3%)
$\mathrm{P_{Fwdw}}$ (Al)	(6.0 ± 1.8)·10^5	Reaction rate for 2μm of Aluminum (target wrapping), obtained with Atima (uncertainties set to 3%)
$\mathrm{P_{Fwdw}}$	0.74 ± 0.16	Due to the lack of data on fission in these materials, the probability for a ^{238}U spallation residue impinging on a proton target has been used as an approximation.
$\mathrm{F_{tgt}}$	1.0058 ± 0.0025	Total factor to correct target's fissions: $\mathrm{F_{tgt} = 1 + I_1/I_{tgt} + I_4/I_{tgt} - I_2/I_{tgt} - I_3/I_{tgt} - P_{R\frac{1}{2}tgt}P_{Stgt}P_{R\frac{1}{2}tgt}P_{Ftgt} - P_{Rwdw}P_{Fwdw}}$
$\mathrm{F_{sci}}$	1.0000 ± 0.0041	Factor to correct scintillator's fissions: $\mathrm{1 - I_1/I_{sci} + I_2/I_{sci}}$. The uncertainty was estimated by varying the Breit Weigner limits for the fit.
$\frac{\sigma_{\mathrm{Ssci}}}{\sigma_{\mathrm{Fsci}}}$	0.888±0.064	$\frac{\sigma_{\mathrm{Ssci}}}{\sigma_{\mathrm{Fsci}}} = \frac{\frac{\sigma_{\mathrm{SH[10]C[9]}}}{\sigma_{\mathrm{FH[10]C[9]}}}w_{\mathrm{Sci}} + \frac{\sigma_{\mathrm{SCu}}}{\sigma_{\mathrm{FCu}}}w_{\mathrm{Fe}}}{w_{\mathrm{Sci}}+w_{\mathrm{Fe}}} \pm 1/\sqrt{w_{\mathrm{Sci}} + w_{\mathrm{Fe}}}$ $\frac{\sigma_{\mathrm{SH[10]C[9]}}}{\sigma_{\mathrm{FH[10]C[9]}}} = \frac{10\sigma_{(\mathrm{R-F})\mathrm{H}}+9\sigma_{(\mathrm{R-F})\mathrm{C}}}{10\sigma_{\mathrm{FH}}+9\sigma_{\mathrm{FC}}}$ $\sigma_{\mathrm{H}}, \sigma_{\mathrm{C}}, \sigma_{\mathrm{Cu}}$ from [115] $w_{\mathrm{Sci}} = 206.4\mathrm{mg/cm^2}$ $w_{\mathrm{Fe}} = 40.8\mathrm{mg/cm^2}$
$\mathrm{P_{Rtgt}}$	0.06 ± 0.018	Reaction rate for the whole target (15 mm) obtained with Atima (uncertainties set to 3%)
$\mathrm{P_{Rbtgt}}$	0.039± 0.012	Probability that a uranium reacts before the target, calculated using the Atima list of materials between the cave's entrance and the target (see A.1).
$\mathrm{P_{Sbtgt}} = \frac{\sigma_{\mathrm{Ssci}}}{\sigma_{\mathrm{Rsci}}}$	0.470 ± 0.064	$\frac{\sigma_{\mathrm{Ssci}}}{\sigma_{\mathrm{Rsci}}} = \frac{\frac{\sigma_{\mathrm{SH[10]C[9]}}}{\sigma_{\mathrm{RH[10]C[9]}}}w_{\mathrm{Sci}} + \frac{\sigma_{\mathrm{SCu}}}{\sigma_{\mathrm{RCu}}}w_{\mathrm{Fe}}}{w_{\mathrm{Sci}}+w_{\mathrm{Fe}}} \pm 1/\sqrt{w_{\mathrm{Sci}} + w_{\mathrm{Fe}}}$ $\frac{\sigma_{\mathrm{SH[10]C[9]}}}{\sigma_{\mathrm{RH[10]C[9]}}} = \frac{10\sigma_{(\mathrm{R-F})\mathrm{H}}+9\sigma_{(\mathrm{R-F})\mathrm{C}}}{10\sigma_{\mathrm{RH}}+9\sigma_{\mathrm{RC}}}$ $\sigma_{\mathrm{H}}, \sigma_{\mathrm{C}}, \sigma_{\mathrm{Cu}}$ from [115] $w_{\mathrm{Sci}} = 206.4\mathrm{mg/cm^2}$ $w_{\mathrm{Fe}} = 40.8\mathrm{mg/cm^2}$

Table A.3: *Correction factors for the fission cross-section calculation.*

A.5 Total fission cross section uncertainties

The first step is to calculate the total fission cross-section for each run. To do so, for each 12 spills in the run (3000 incomings for each spill) the fission cross-section is calculated with the formula described in sections 3.8.3 for Method 1 and 3.8.4 for Method 2. Any measurement has the contribution of two uncertainties: type A uncertainty (the one associated with the statistical analysis of a series of observations) and type B uncertainty (any other uncertainty that is not based on statistics) [116]. Type B uncertainties are often calculated using assumptions based on previous knowledge of the matter or reasonable assignment of the probability distributions of a given variable. For example, to calculate the number of fissions coming from the scintillator, a cut in the Z position of the reaction's vertex should be defined around the scintillator peak shown in Fig. 3.41. However, the probability distribution of this cut is in principle unknown, so an estimation should be made. Since in Fig. 3.41 it can be seen that the tail of the counts coming from the scintillator is rather long to the left, a reasonable margin of variation for the left cut could be chosen between the known position of the scintillator in the setup and the end of the setup. This contribution to the uncertainty could be calculated separately from the Type A uncertainty and then combined by performing the quadratic mean with the Type B uncertainty to obtain the combined uncertainty as $\sigma_C = \sqrt{\sigma_A^2 + \sigma_B^2}$. Another way to calculate the combined uncertainty is to let the parameters vary within its probability distribution margins for each subset of data so that after several subsets, the distribution would have been broadened by both the type A and B uncertainties. This last one was the procedure followed in this work, and the final distribution for the total fission cross-section is displayed in Fig. A.7 for run 221 as an example.

Since each spill has approximately the same number of counts (around 3000), the mean is estimated as the regular arithmetic mean for a selection of events, as described in A.1, with a standard deviation of A.2 and an uncertainty of the mean of A.3. In these formulas, N corresponds with the number of groups of 12 spills, x_i corresponds to the different fission cross-section for each group of spills, and $\overline{x}$ to the mean value of the fission cross-section for that run.

$$\overline{x} = \frac{\sum_{i=0}^{N} x_i}{N} \tag{A.1}$$

$$\sigma(x) = \sqrt{\frac{1}{N-1}\sum_{i=0}^{N}(x_i - \overline{x})^2} \tag{A.2}$$

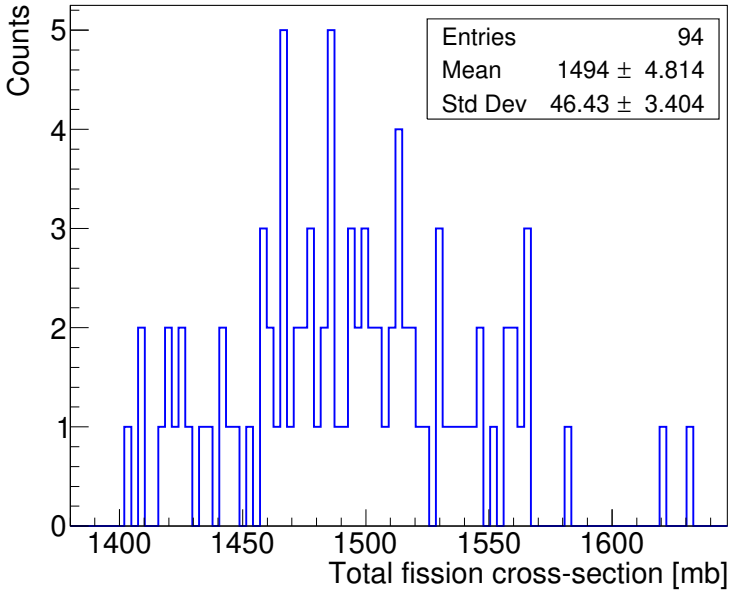

Figure A.7: *Total fission cross-section distribution for the run 221.*

$$\sigma(\overline{x}) = \sqrt{\frac{1}{N}\frac{1}{N-1}\sum_{i=0}^{N}(x_i - \overline{x})^2} \tag{A.3}$$

Finally, 5 mean values with their uncertainties are obtained for the 5 runs, as shown in table A.4.

Run	Fission cross-section [mb] Method 1	Fission cross-section [mb] Method 2
209	1540 ±10 (101)	1542 ±10 (103)
216	1513 ±14 (53)	1519 ±14 (52)
217	1516 ±7 (46)	1523 ±7 (46)
221	1494 ±5 (46)	1500 ±5 (47)
223	1478 ±8 (59)	1485 ±8 (60)
Average	1511 ±13	1516 ±12

Table A.4: *Fission cross-section results for 5 experimental runs. The uncertainties of each run correspond to the uncertainty of the mean, and the value in parenthesis corresponds to the standard deviation of the distribution.*

To obtain a final value for the total fission cross-section, the average of the 5 runs must be computed. Since this time the 5 subsets of data have different statistics (each run has a different number of spills), the mean should be calculated as the weighted average mean, as shown in Eq. A.4 (left). In this formula, the value of the measurement (x_i) is multiplied by a weighting factor (w_i), which in this case is defined as the statistics of each run divided by the total statistics, as shown in A.4 (right). The uncertainty associated with the weighted average mean

is shown in Eq. A.5.

$$\overline{x} = \sum_{i=0}^{N} w_i x_i, \quad w_i = \frac{n_{run}}{n_{total}} \tag{A.4}$$

$$\sigma(\overline{x}) = \sqrt{\sum_{i=0}^{N} w_i^2 x_i^2} \tag{A.5}$$

However, experimental uncertainties could be underestimated due to not taking into account all sources of error. Therefore, the uncertainty in the weighted mean should be corrected to account for a too large χ^2. The correction that must be made is shown in Eq. A.6 [117], where χ is the reduced chi-squared, as seen in Eq. A.7. The σ_i in this equation corresponds to the uncertainties of the mean for each run on table A.4.

$$\sigma(\overline{x})_{corrected} = \sigma(\overline{x})\chi \tag{A.6}$$

$$\chi = \sqrt{\frac{1}{N}\sum_{i=0}^{N}\left(\frac{(x_i - \overline{x})^2}{\sigma_i}\right)} \tag{A.7}$$

A.6 Residues

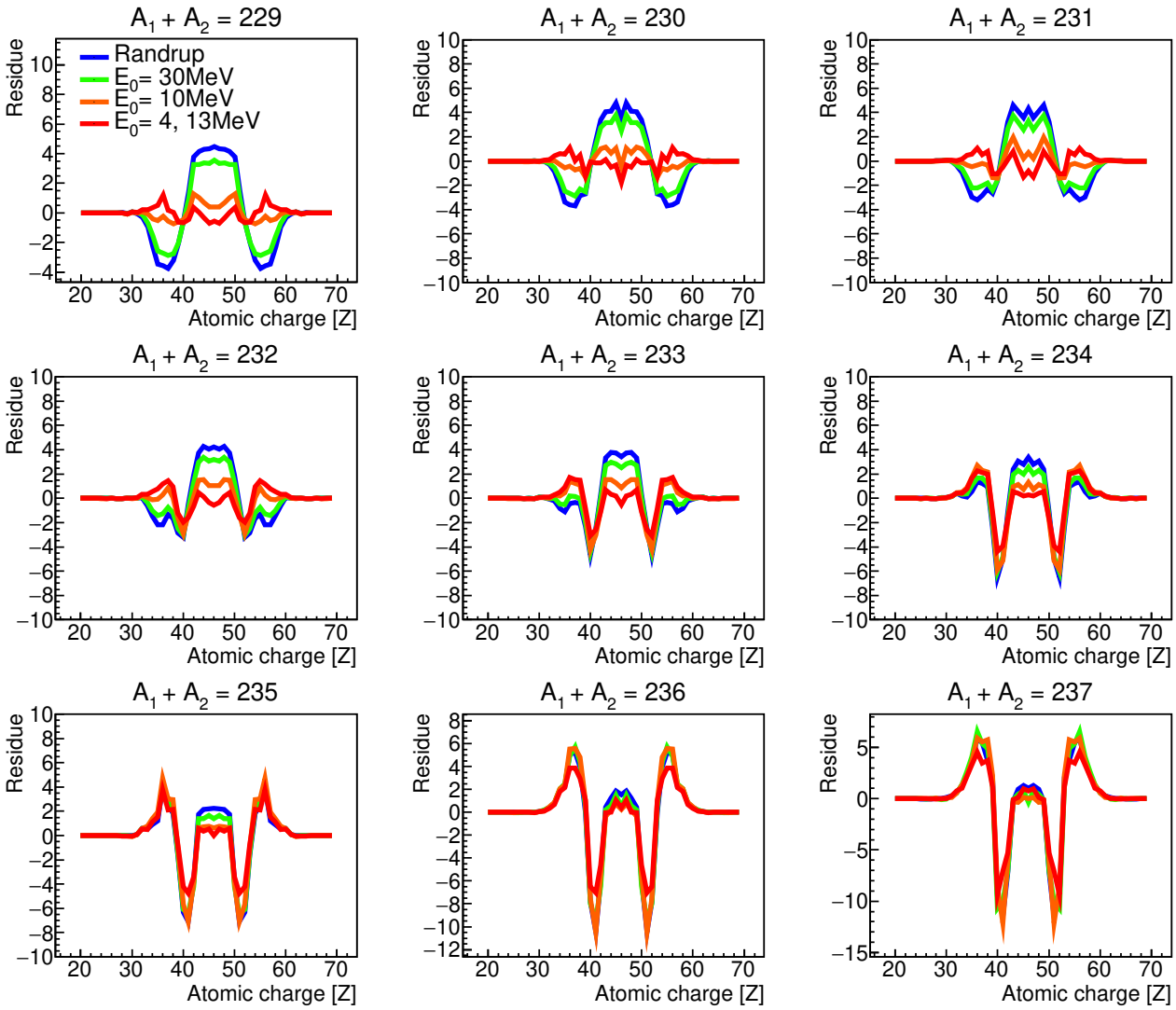

Figure A.8: *Residues from Fig. 4.14 (experimental values - function). The blue line corresponds to the Woods-Saxon function proposed by Randrup [17] with* $E_0 = 15MeV$ *and* $E_1 = 20MeV$*. The other lines correspond to the exponential* $S(E^*) = E^*/E_0 MeV$*, with* $E_0 = 30$ *MeV for the green line and* $E_0 = 10$ *for the orange line. The red line is a combination of* $E_0 = 4$ *MeV for excitation energies lower 20MeV and* $E_0 = 14MeV$ *for higher*

A.7 Velocities reconstruction

The total velocity is calculated as V = ToF/L, being 'ToF' the time of flight of the fission fragment and 'L' the reconstructed total path length. To decompose the velocity on its three spatial coordinates, the horizontal angle given by the Twin (θ_{Twin}) and the ToF Wall (θ_{Tof}) displayed in Fig. A.9, are required. θ_{Twin} is the angle between the Z component of the velocity and the total velocity projection in the ZX plane, and there should be an anti-correlation between the θ_{Twin} angle of both fission fragments, as shown in A.10 (a). The angle ϕ between V_{XY} and V_Y can be calculated as $\mathrm{arctg}\,(\mathrm{tg}\theta_{\mathrm{Tof}}/\mathrm{sen}\theta_{\mathrm{Twin}})$ and the correlation between the ϕ angles of both fission fragments should be coplanar, as the one displayed in A.9 (b). Then, θ_{Tof} is calculated as $\theta_{\mathrm{Tof}} = \mathrm{arcsen}\,(\mathrm{Y}_{\mathrm{Tof}}/\mathrm{L})$, using the Y position in the ToF Wall and the total length.

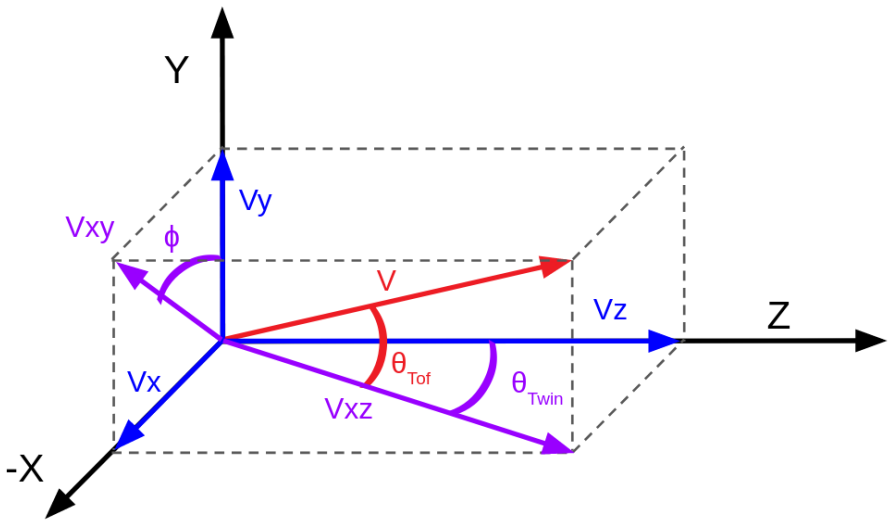

Figure A.9: *Velocity decomposition on the 3 coordinates of the laboratory frame.*

Then, the three velocity components are calculated as shown in Eq. A.8, deduced from Fig. A.9 . To obtain the velocities in the center of mass reference system (CM), the Lorentz transformation equations shown in Eq. A.8 are employed. The velocities (Vx, Vy, Vz) are in the laboratory frame, and (Vx′, Vy′, Vy′) in the CM frame. The variable 'u' is the velocity of the fissioning system, and γ_u is its corresponding Lorentz's Factor. Since the velocity of the fissioning system is unknown, the mean value of the Vz distribution is used instead.

$$\mathrm{Vx} = \mathrm{V}\cos(\theta_{\mathrm{Tof}})\mathrm{sen}(\theta_{\mathrm{Twin}}), \quad \mathrm{Vy} = \mathrm{V}\mathrm{sen}(\theta_{\mathrm{Tof}}), \quad \mathrm{Vz} = \mathrm{V}\cos(\theta_{\mathrm{Tof}})\cos(\theta_{\mathrm{Twin}}) \tag{A.8}$$

$$Vx' = \frac{Vx}{\gamma_u \left(1 - \frac{uVz}{c^2}\right)}, \qquad Vy' = \frac{Vy}{\gamma_u \left(1 - \frac{uVz}{c^2}\right)} \qquad Vz' = \frac{Vz - u}{1 - \frac{uVz}{c^2}} \tag{A.9}$$

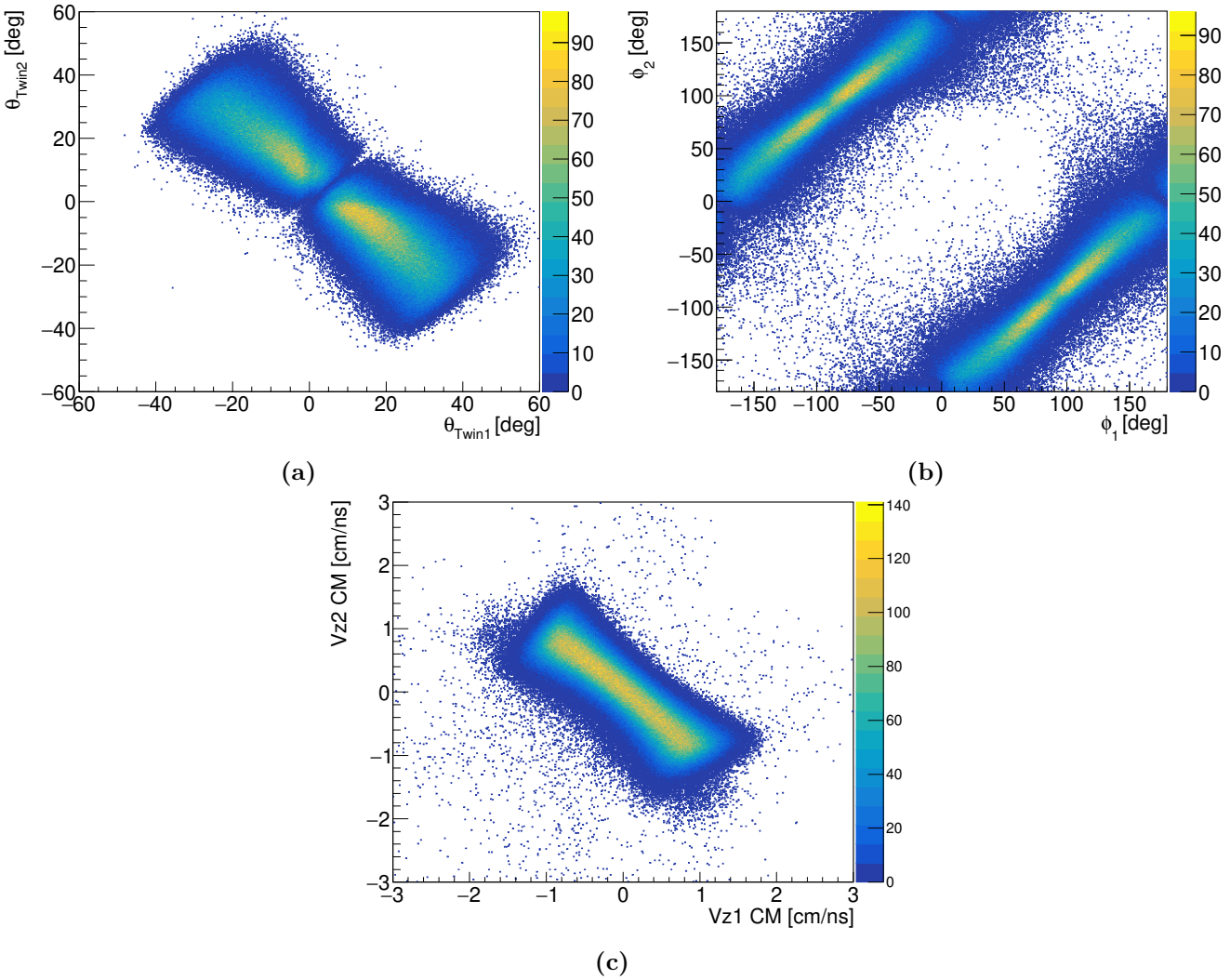

Figure A.10: *(a) Correlation of the horizontal angle measured by the Twin MUSIC of the two fission fragments. (b) Correlation of the ϕ angle of the two fission fragments. (c) Correlation of the velocities in Z and center of mass reference system for the two fission fragments.*

Fig. A.10 (c) shows the correlation between the Z component of the velocity in the center of mass of the two fission fragments. They are anti-correlated, since due to the conservation of the momentum, the higher the velocity of one fission fragment, the lower the other. It can be seen, however, that the distribution is rather broad, due to the lack of information on the angular distribution of the beam at the entrance of the experimental area.

A.8 Yields tables

Table A.5: $Z_{sum} = 91, A_{sum} = 225, 226$

Z	Yield(Z) 200%	Stat. Error
25	0.01	0.01
26	0.04	0.02
27	0.03	0.01
28	0.07	0.02
29	0.17	0.03
30	0.28	0.04
31	0.5	0.05
32	0.9	0.07
33	1.46	0.08
34	2.48	0.11
35	3.83	0.13
36	5.18	0.16
37	6.62	0.17
38	7.46	0.19
39	7.61	0.19
40	8.44	0.2
41	9.11	0.2
42	10.71	0.22
43	11.2	0.23
44	11.83	0.23
45	12.19	0.24
46	12.19	0.24
47	11.83	0.23
48	11.2	0.23
49	10.71	0.22
50	9.11	0.2
51	8.44	0.2
52	7.61	0.19
53	7.46	0.19
54	6.62	0.17
55	5.18	0.16
56	3.83	0.13
57	2.48	0.11
58	1.46	0.08
59	0.9	0.07
60	0.5	0.05
61	0.28	0.04
62	0.17	0.03
63	0.07	0.02
64	0.03	0.01
65	0.04	0.02
66	0.01	0.01

Table A.6: $Z_{sum} = 91, A_{sum} = 227, 228$

Z	Yield(Z) 200%	Stat. Error
25	0.02	0.01
26	0.03	0.02
27	0.04	0.02
28	0.07	0.02
29	0.14	0.03
30	0.28	0.04
31	0.5	0.06
32	0.93	0.07
33	1.63	0.1
34	3.1	0.13
35	4.68	0.16
36	6.29	0.19
37	7.17	0.2
38	8.06	0.21
39	8.56	0.22
40	8.79	0.22
41	9.12	0.22
42	9.26	0.23
43	9.82	0.23
44	10.64	0.24
45	10.98	0.25
46	10.98	0.25
47	10.64	0.24
48	9.82	0.23
49	9.26	0.23
50	9.12	0.22
51	8.79	0.22
52	8.56	0.22
53	8.06	0.21
54	7.17	0.2
55	6.29	0.19
56	4.68	0.16
57	3.1	0.13
58	1.63	0.1
59	0.93	0.07
60	0.5	0.06
61	0.28	0.04
62	0.14	0.03
63	0.07	0.02
64	0.04	0.02
65	0.03	0.02
66	0.02	0.01

Table A.7: $Z_{sum} = 91, A_{sum} = 229, 230$

Z	Yield(Z) 200%	Stat. Error
26	0.01	0.01
27	0.04	0.02
28	0.05	0.02
29	0.07	0.03
30	0.26	0.05
31	0.43	0.06
32	1.01	0.09
33	1.86	0.12
34	3.88	0.17
35	5.55	0.2
36	7.79	0.23
37	8.46	0.24
38	9.61	0.26
39	8.81	0.25
40	8.65	0.25
41	8.56	0.24
42	8.58	0.24
43	8.53	0.24
44	9.02	0.25
45	8.92	0.25
46	8.92	0.25
47	9.02	0.25
48	8.53	0.24
49	8.58	0.24
50	8.56	0.24
51	8.65	0.25
52	8.81	0.25
53	9.61	0.26
54	8.46	0.24
55	7.79	0.23
56	5.55	0.2
57	3.88	0.17
58	1.86	0.12
59	1.01	0.09
60	0.43	0.06
61	0.26	0.05
62	0.07	0.03
63	0.05	0.02
64	0.04	0.02
65	0.01	0.01

Table A.8: $Z_{sum} = 91, A_{sum} = 231, 232$

Z	Yield(Z) 200%	Stat. Error
26	0.02	0.02
29	0.08	0.03
30	0.18	0.05
31	0.4	0.07
32	1.42	0.12
33	2.34	0.16
34	4.74	0.22
35	6.69	0.26
36	8.94	0.3
37	9.75	0.31
38	10.9	0.33
39	10.4	0.32
40	8.97	0.3
41	7.88	0.28
42	6.69	0.26
43	6.51	0.26
44	7.1	0.27
45	7.06	0.27
46	7.06	0.27
47	7.1	0.27
48	6.51	0.26
49	6.69	0.26
50	7.88	0.28
51	8.97	0.3
52	10.4	0.32
53	10.9	0.33
54	9.75	0.31
55	8.94	0.3
56	6.69	0.26
57	4.74	0.22
58	2.34	0.16
59	1.42	0.12
60	0.4	0.07
61	0.18	0.05
62	0.08	0.03
65	0.02	0.02

Table A.9: $Z_{sum} = 91, A_{sum} = 233, 234$

Z	Yield(Z) 200%	Stat. Error
26	0.02	0.02
27	0.04	0.03
28	0.04	0.03
29	0.08	0.04
30	0.16	0.06
31	0.34	0.08
32	1.4	0.15
33	2.58	0.21
34	5.5	0.3
35	7.99	0.36
36	11.16	0.43
37	11.61	0.43
38	12.45	0.45
39	12	0.44
40	9.21	0.39
41	7.16	0.34
42	4.85	0.28
43	4.54	0.27
44	4.81	0.28
45	4.16	0.26
46	4.16	0.26
47	4.81	0.28
48	4.54	0.27
49	4.85	0.28
50	7.16	0.34
51	9.21	0.39
52	12	0.44
53	12.45	0.45
54	11.61	0.43
55	11.16	0.43
56	7.99	0.36
57	5.5	0.3
58	2.58	0.21
59	1.4	0.15
60	0.34	0.08
61	0.16	0.06
62	0.08	0.04
63	0.04	0.03
64	0.04	0.03
65	0.02	0.02

Table A.10: $Z_{sum} = 91, A_{sum} = 235, 236$

Z	Yield(Z) 200%	Stat. Error
27	0.04	0.04
30	0.33	0.11
31	0.55	0.14
32	1.17	0.2
33	2.43	0.28
34	5.53	0.43
35	10.02	0.57
36	11.96	0.63
37	13.05	0.65
38	13.02	0.65
39	13.31	0.66
40	11.02	0.6
41	6.3	0.46
42	3.56	0.34
43	2.43	0.28
44	2.72	0.3
45	2.65	0.3
46	2.65	0.3
47	2.72	0.3
48	2.43	0.28
49	3.56	0.34
50	6.3	0.46
51	11.02	0.6
52	13.31	0.66
53	13.02	0.65
54	13.05	0.65
55	11.96	0.63
56	10.02	0.57
57	5.53	0.43
58	2.43	0.28
59	1.17	0.2
60	0.55	0.14
61	0.33	0.11
64	0.04	0.04

Table A.11: $Z_{sum} = 91, A_{sum} = 237, 238$

Z	Yield(Z) 200%	Stat. Error
29	0.18	0.13
30	0.18	0.13
31	0.54	0.22
32	1.16	0.33
33	2.23	0.45
34	5.52	0.7
35	10.76	0.98
36	11.83	1.03
37	13.69	1.11
38	13.07	1.08
39	13.87	1.12
40	11.12	1
41	8.45	0.87
42	3.03	0.52
43	2.41	0.47
44	1.16	0.33
45	0.89	0.29
46	0.89	0.29
47	1.16	0.33
48	2.41	0.47
49	3.03	0.52
50	8.45	0.87
51	11.12	1
52	13.87	1.12
53	13.07	1.08
54	13.69	1.11
55	11.83	1.03
56	10.76	0.98
57	5.52	0.7
58	2.23	0.45
59	1.16	0.33
60	0.54	0.22
61	0.18	0.13
62	0.18	0.13

Table A.12: $Z_{sum} = 91, A_{sum} = 225, 226$

A	Yield(A) 200%	Stat. Error
72	0.11	0.03
73	0.1	0.03
74	0.14	0.03
75	0.22	0.04
76	0.25	0.04
77	0.32	0.04
78	0.38	0.05
79	0.49	0.05
80	0.54	0.05
81	0.64	0.06
82	0.89	0.07
83	0.97	0.07
84	1.19	0.08
85	1.33	0.08
86	1.51	0.09
87	1.86	0.09
88	2.06	0.1
89	2.28	0.1
90	2.42	0.11
91	2.64	0.11
92	2.52	0.11
93	2.75	0.11
94	2.77	0.11
95	2.79	0.12
96	2.72	0.11
97	2.82	0.12
98	3.02	0.12
99	3.07	0.12
100	3.38	0.13
101	3.66	0.13
102	3.98	0.14
103	3.93	0.14
104	4.27	0.14
105	4.3	0.14
106	4.18	0.14
107	4.68	0.15
108	4.66	0.15
109	4.53	0.15
110	4.62	0.15
111	4.87	0.15
112	4.82	0.15

Table A.13: $Z_{sum} = 91, A_{sum} = 225, 226$

A	Yield(A) 200%	Stat. Error
113	4.97	0.15
114	4.74	0.15
115	4.82	0.15
116	4.65	0.15
117	4.56	0.15
118	4.6	0.15
119	4.39	0.14
120	4.43	0.14
121	4.09	0.14
122	4.07	0.14
123	4.11	0.14
124	3.79	0.13
125	3.45	0.13
126	3.17	0.12
127	2.99	0.12
128	3.04	0.12
129	2.66	0.11
130	2.83	0.12
131	2.73	0.11
132	2.76	0.11
133	2.66	0.11
134	2.56	0.11
135	2.58	0.11
136	2.3	0.11
137	2.14	0.1
138	2	0.1
139	1.71	0.09
140	1.39	0.08
141	1.35	0.08
142	1.03	0.07
143	0.93	0.07
144	0.73	0.06
145	0.58	0.05
146	0.53	0.05
147	0.43	0.05
148	0.34	0.04
149	0.31	0.04
150	0.25	0.04
151	0.13	0.03
152	0.11	0.03
153	0.14	0.03

Table A.14: $Z_{sum} = 91, A_{sum} = 227, 228$

A	Yield(A) 200%	Stat. Error
73	0.13	0.03
74	0.11	0.03
75	0.15	0.03
76	0.19	0.04
77	0.27	0.04
78	0.3	0.04
79	0.43	0.05
80	0.48	0.05
81	0.87	0.07
82	0.93	0.07
83	1.04	0.08
84	1.3	0.09
85	1.48	0.09
86	1.79	0.1
87	1.86	0.1
88	2.16	0.11
89	2.31	0.12
90	2.92	0.13
91	2.94	0.13
92	2.8	0.13
93	3	0.13
94	2.75	0.13
95	2.94	0.13
96	3.02	0.13
97	3.09	0.13
98	3.12	0.13
99	2.94	0.13
100	3.08	0.13
101	3.31	0.14
102	3.51	0.14
103	3.64	0.14
104	3.66	0.14
105	3.64	0.14
106	3.9	0.15
107	3.91	0.15
108	3.91	0.15
109	4.1	0.15
110	4.3	0.16
111	4.05	0.15
112	4.19	0.15
113	4.47	0.16
114	4.25	0.15

Table A.15: $Z_{sum} = 91, A_{sum} = 227, 228$

A	Yield(A) 200%	Stat. Error
115	4.47	0.16
116	3.91	0.15
117	4.31	0.16
118	4.17	0.15
119	3.85	0.15
120	3.99	0.15
121	3.96	0.15
122	3.7	0.14
123	3.62	0.14
124	3.73	0.15
125	3.48	0.14
126	3.46	0.14
127	3.24	0.14
128	2.95	0.13
129	3.11	0.13
130	2.98	0.13
131	3.05	0.13
132	2.91	0.13
133	2.83	0.13
134	2.98	0.13
135	2.85	0.13
136	2.9	0.13
137	2.92	0.13
138	2.63	0.12
139	2.13	0.11
140	2.1	0.11
141	1.89	0.1
142	1.56	0.1
143	1.47	0.09
144	1.1	0.08
145	1.02	0.08
146	0.84	0.07
147	0.7	0.07
148	0.45	0.05
149	0.29	0.04
150	0.36	0.05
151	0.17	0.03
152	0.23	0.04
153	0.1	0.03
154	0.13	0.03
155	0.1	0.03

Table A.16: $Z_{sum} = 91, A_{sum} = 229, 230$

A	Yield(A) 200%	Stat. Error
74	0.1	0.03
75	0.11	0.03
76	0.16	0.04
77	0.21	0.04
78	0.18	0.04
79	0.29	0.05
80	0.5	0.06
81	0.66	0.07
82	0.98	0.09
83	1.17	0.09
84	1.48	0.1
85	1.78	0.11
86	1.86	0.12
87	2.27	0.13
88	2.59	0.14
89	2.74	0.14
90	2.82	0.14
91	3.33	0.15
92	3.36	0.16
93	3.51	0.16
94	3.57	0.16
95	3.53	0.16
96	3.32	0.15
97	3.32	0.15
98	2.87	0.14
99	3.05	0.15
100	3.31	0.15
101	2.91	0.14
102	3.06	0.15
103	2.82	0.14
104	3.27	0.15
105	3.23	0.15
106	3.38	0.16
107	3.38	0.16
108	3.08	0.15
109	3.32	0.15
110	3.56	0.16
111	3.47	0.16
112	3.42	0.16
113	3.75	0.16
114	3.55	0.16

Table A.17: $Z_{sum} = 91, A_{sum} = 229, 230$

A	Yield(A) 200%	Stat. Error
115	3.38	0.16
116	3.72	0.16
117	3.62	0.16
118	3.37	0.16
119	3.52	0.16
120	3.51	0.16
121	3.25	0.15
122	3.17	0.15
123	3.19	0.15
124	3.43	0.16
125	3.23	0.15
126	3.11	0.15
127	2.97	0.15
128	2.95	0.15
129	2.94	0.15
130	3.27	0.15
131	2.95	0.15
132	3.09	0.15
133	3.21	0.15
134	3.48	0.16
135	3.48	0.16
136	3.61	0.16
137	3.34	0.15
138	3.46	0.16
139	2.92	0.14
140	2.83	0.14
141	2.7	0.14
142	2.47	0.13
143	2.09	0.12
144	1.82	0.12
145	1.57	0.11
146	1.31	0.1
147	1.14	0.09
148	0.75	0.08
149	0.6	0.07
150	0.38	0.06
151	0.2	0.04
152	0.19	0.04
153	0.21	0.04
154	0.12	0.03

Table A.18: $Z_{sum} = 91, A_{sum} = 231, 232$

A	Yield(A) 200%	Stat. Error
77	0.19	0.05
78	0.18	0.05
79	0.43	0.07
80	0.52	0.08
81	0.62	0.08
82	0.95	0.1
83	1.18	0.11
84	1.57	0.13
85	1.7	0.13
86	2.38	0.16
87	2.55	0.16
88	2.63	0.17
89	3.43	0.19
90	3.63	0.19
91	3.67	0.19
92	3.17	0.18
93	3.71	0.2
94	3.96	0.2
95	4.28	0.21
96	4.18	0.21
97	3.97	0.2
98	3.73	0.2
99	3.31	0.19
100	3.08	0.18
101	2.91	0.17
102	3.04	0.18
103	2.92	0.17
104	2.57	0.16
105	2.57	0.16
106	2.62	0.17
107	2.48	0.16
108	2.43	0.16
109	2.66	0.17
110	2.48	0.16
111	2.62	0.17
112	2.9	0.17
113	2.78	0.17
114	2.6	0.16
115	2.58	0.16
116	2.86	0.17

Table A.19: $Z_{sum} = 91, A_{sum} = 231, 232$

A	Yield(A) 200%	Stat. Error
117	2.78	0.17
118	2.67	0.17
119	2.87	0.17
120	2.71	0.17
121	2.48	0.16
122	2.58	0.16
123	2.54	0.16
124	2.45	0.16
125	2.54	0.16
126	2.57	0.16
127	2.53	0.16
128	2.87	0.17
129	2.71	0.17
130	3.22	0.18
131	2.82	0.17
132	3.22	0.18
133	3.52	0.19
134	3.96	0.2
135	4	0.2
136	4.15	0.21
137	4.32	0.21
138	3.84	0.2
139	3.38	0.19
140	3.43	0.19
141	3.47	0.19
142	3.45	0.19
143	3.26	0.18
144	2.62	0.17
145	2.27	0.15
146	2.24	0.15
147	1.51	0.13
148	1.28	0.12
149	1.05	0.11
150	0.9	0.1
151	0.51	0.08
152	0.48	0.07
153	0.29	0.06
154	0.19	0.05
155	0.14	0.04

Table A.20: $Z_{sum} = 91, A_{sum} = 233, 234$

A	Yield(A) 200%	Stat. Error
77	0.1	0.04
78	0.15	0.05
79	0.26	0.07
80	0.35	0.08
81	0.5	0.09
82	0.88	0.12
83	1.24	0.15
84	1.35	0.15
85	1.99	0.18
86	2.07	0.19
87	2.5	0.2
88	3.55	0.24
89	3.64	0.25
90	4.04	0.26
91	3.94	0.26
92	4.56	0.27
93	3.83	0.25
94	4.69	0.28
95	4.62	0.28
96	4.45	0.27
97	4.89	0.28
98	4.4	0.27
99	4.43	0.27
100	4.09	0.26
101	3.59	0.24
102	3.24	0.23
103	2.7	0.21
104	2.08	0.19
105	2.29	0.2
106	1.62	0.17
107	1.96	0.18
108	1.88	0.18
109	1.7	0.17
110	1.85	0.18
111	1.61	0.16
112	1.81	0.17
113	1.83	0.18
114	1.66	0.17
115	1.78	0.17
116	1.45	0.16

Table A.21: $Z_{sum} = 91, A_{sum} = 233, 234$

A	Yield(A) 200%	Stat. Error
117	1.62	0.17
118	1.59	0.16
119	1.67	0.17
120	1.89	0.18
121	1.64	0.17
122	1.69	0.17
123	1.86	0.18
124	1.51	0.16
125	2.15	0.19
126	1.8	0.17
127	1.77	0.17
128	1.93	0.18
129	2.21	0.19
130	2.31	0.2
131	3.08	0.23
132	3.35	0.24
133	3.66	0.25
134	4.53	0.27
135	4.77	0.28
136	4.12	0.26
137	5.09	0.29
138	4.45	0.27
139	4.39	0.27
140	4.26	0.26
141	4.42	0.27
142	4.07	0.26
143	4.13	0.26
144	3.89	0.25
145	3.39	0.24
146	3.01	0.22
147	2.29	0.2
148	2.08	0.19
149	1.64	0.17
150	1.15	0.14
151	1.15	0.14
152	0.58	0.1
153	0.4	0.08
154	0.35	0.08
155	0.2	0.06
156	0.12	0.05

Table A.22: $Z_{sum} = 91, A_{sum} = 235, 236$

A	Yield(A) 200%	Stat. Error
77	0.2	0.08
79	0.13	0.07
80	0.26	0.1
81	0.42	0.12
82	0.36	0.11
83	1.14	0.2
84	1.01	0.18
85	1.68	0.24
86	2.1	0.27
87	2.46	0.29
88	3.33	0.33
89	4.14	0.37
90	4.11	0.37
91	4.33	0.38
92	3.95	0.36
93	5.33	0.42
94	5.37	0.42
95	4.53	0.39
96	4.79	0.4
97	5.21	0.41
98	5.08	0.41
99	4.37	0.38
100	5.43	0.42
101	5.53	0.43
102	3.88	0.36
103	2.98	0.31
104	2.3	0.28
105	1.85	0.25
106	1.88	0.25
107	1.56	0.23
108	1.2	0.2
109	0.88	0.17
110	1.26	0.21
111	1.1	0.19
112	0.78	0.16
113	0.94	0.18
114	1.01	0.18
115	0.88	0.17
116	1.07	0.19
117	1.04	0.19
118	0.88	0.17

Table A.23: $Z_{sum} = 91, A_{sum} = 235, 236$

A	Yield(A) 200%	Stat. Error
119	1.07	0.19
120	0.81	0.17
121	1.07	0.19
122	0.88	0.17
123	1.01	0.18
124	1.04	0.19
125	1.01	0.18
126	1.1	0.19
127	0.91	0.18
128	1.46	0.22
129	1.72	0.24
130	1.56	0.23
131	2.3	0.28
132	2.75	0.3
133	3.2	0.33
134	4.88	0.4
135	6.05	0.45
136	4.4	0.38
137	5.11	0.41
138	4.88	0.4
139	5.11	0.41
140	4.43	0.38
141	4.88	0.4
142	5.79	0.44
143	3.91	0.36
144	4.62	0.39
145	4.3	0.38
146	4.11	0.37
147	3.78	0.35
148	2.62	0.3
149	2.46	0.29
150	1.56	0.23
151	1.36	0.21
152	1.14	0.2
153	0.65	0.15
154	0.42	0.12
155	0.26	0.1
156	0.23	0.09
158	0.1	0.06
159	0.17	0.08

Table A.24: $Z_{sum} = 91, A_{sum} = 237, 238$

A	Yield(A) 200%	Stat. Error
79	0.36	0.18
81	0.54	0.22
82	0.54	0.22
83	1.07	0.31
84	0.45	0.2
85	0.89	0.29
86	1.34	0.35
87	2.67	0.49
88	1.96	0.42
89	3.29	0.55
90	4.72	0.65
91	3.56	0.57
92	5.43	0.7
93	4.45	0.63
94	5.43	0.7
95	4.72	0.65
96	4.81	0.66
97	6.05	0.74
98	4.36	0.63
99	4.09	0.61
100	5.43	0.7
101	5.96	0.73
102	5.78	0.72
103	4.54	0.64
104	3.65	0.57
105	3.03	0.52
106	2.05	0.43
107	1.61	0.38
108	1.43	0.36
109	1.16	0.33
110	0.72	0.26
111	0.36	0.18
112	1.07	0.31
113	0.36	0.18
114	0.36	0.18
115	0.36	0.18
116	0.45	0.2
117	0.63	0.24
118	0.18	0.13
119	0.27	0.16

Table A.25: $Z_{sum} = 91, A_{sum} = 237, 238$

A	Yield(A) 200%	Stat. Error
120	0.45	0.2
121	0.63	0.24
122	0.36	0.18
123	0.36	0.18
124	0.36	0.18
125	0.81	0.27
126	0.72	0.26
127	0.54	0.22
128	0.72	0.26
129	1.61	0.38
130	1.43	0.36
131	1.52	0.37
132	2.85	0.51
133	3.74	0.58
134	4.45	0.63
135	4.89	0.66
136	6.14	0.74
137	5.78	0.72
138	4.54	0.64
139	4.09	0.61
140	5.43	0.7
141	5.52	0.7
142	4.18	0.61
143	5.07	0.68
144	5.25	0.69
145	4.89	0.66
146	4.54	0.64
147	4.72	0.65
148	3.47	0.56
149	1.78	0.4
150	2.94	0.52
151	1.52	0.37
152	1.52	0.37
153	0.36	0.18
154	0.81	0.27
155	0.63	0.24
156	0.81	0.27
158	0.18	0.13
159	0.18	0.13
161	0.18	0.13

Table A.26: $Z_{sum} = 92, A_{sum} = 229$

Z	Yield(Z) 200%	Stat. Error
30	0.28	0.06
31	0.39	0.06
32	0.84	0.09
33	1.17	0.11
34	2.06	0.14
35	2.98	0.17
36	5.29	0.22
37	5.87	0.23
38	7.82	0.27
39	8.4	0.28
40	8.8	0.29
41	8.82	0.29
42	10.11	0.31
43	10.01	0.31
44	10.48	0.31
45	10.89	0.32
46	11.35	0.32
47	10.89	0.32
48	10.48	0.31
49	10.01	0.31
50	10.11	0.31
51	8.82	0.29
52	8.8	0.29
53	8.4	0.28
54	7.82	0.27
55	5.87	0.23
56	5.29	0.22
57	2.98	0.17
58	2.06	0.14
59	1.17	0.11
60	0.84	0.09
61	0.39	0.06
62	0.28	0.06

Table A.27: $Z_{sum} = 92, A_{sum} = 230$

Z	Yield(Z) 200%	Stat. Error
29	0.11	0.04
30	0.16	0.04
31	0.39	0.07
32	0.77	0.09
33	1.31	0.12
34	2.4	0.16
35	3.2	0.18
36	5.61	0.24
37	6.03	0.25
38	8.62	0.29
39	8.56	0.29
40	9.97	0.31
41	9.4	0.31
42	9.46	0.31
43	9.3	0.3
44	9.49	0.31
45	10.53	0.32
46	9.46	0.31
47	10.53	0.32
48	9.49	0.31
49	9.3	0.3
50	9.46	0.31
51	9.4	0.31
52	9.97	0.31
53	8.56	0.29
54	8.62	0.29
55	6.03	0.25
56	5.61	0.24
57	3.2	0.18
58	2.4	0.16
59	1.31	0.12
60	0.77	0.09
61	0.39	0.07
62	0.16	0.04
63	0.11	0.04

Table A.28: $Z_{sum} = 92, A_{sum} = 231$

Z	Yield(Z) 200%	Stat. Error
29	0.11	0.04
30	0.23	0.05
31	0.34	0.06
32	0.63	0.08
33	1.15	0.11
34	2.54	0.16
35	3.51	0.19
36	6.26	0.25
37	6.9	0.27
38	9.53	0.31
39	9.47	0.31
40	10.05	0.32
41	9.42	0.31
42	9.26	0.31
43	9.11	0.31
44	8.6	0.3
45	8.28	0.29
46	9.24	0.31
47	8.28	0.29
48	8.6	0.3
49	9.11	0.31
50	9.26	0.31
51	9.42	0.31
52	10.05	0.32
53	9.47	0.31
54	9.53	0.31
55	6.9	0.27
56	6.26	0.25
57	3.51	0.19
58	2.54	0.16
59	1.15	0.11
60	0.63	0.08
61	0.34	0.06
62	0.23	0.05
63	0.11	0.04

Table A.29: $Z_{sum} = 92, A_{sum} = 232$

Z	Yield(Z) 200%	Stat. Error
30	0.13	0.04
31	0.29	0.06
32	0.92	0.11
33	1.33	0.13
34	2.82	0.18
35	3.98	0.22
36	7.08	0.29
37	8.19	0.31
38	10.34	0.34
39	10.12	0.34
40	10.56	0.35
41	9.18	0.32
42	8.17	0.31
43	7.54	0.29
44	7.74	0.3
45	7.63	0.3
46	7.94	0.3
47	7.63	0.3
48	7.74	0.3
49	7.54	0.29
50	8.17	0.31
51	9.18	0.32
52	10.56	0.35
53	10.12	0.34
54	10.34	0.34
55	8.19	0.31
56	7.08	0.29
57	3.98	0.22
58	2.82	0.18
59	1.33	0.13
60	0.92	0.11
61	0.29	0.06
62	0.13	0.04

Table A.30: $Z_{sum} = 92, A_{sum} = 233$

Z	Yield(Z) 200%	Stat. Error
30	0.18	0.05
31	0.28	0.06
32	0.65	0.09
33	1.45	0.14
34	3.07	0.2
35	4.39	0.23
36	8.24	0.32
37	8.7	0.33
38	11.59	0.38
39	11.1	0.37
40	11.46	0.37
41	9.21	0.34
42	7.42	0.3
43	6.58	0.29
44	6.36	0.28
45	6.29	0.28
46	6.14	0.28
47	6.29	0.28
48	6.36	0.28
49	6.58	0.29
50	7.42	0.3
51	9.21	0.34
52	11.46	0.37
53	11.1	0.37
54	11.59	0.38
55	8.7	0.33
56	8.24	0.32
57	4.39	0.23
58	3.07	0.2
59	1.45	0.14
60	0.65	0.09
61	0.28	0.06
62	0.18	0.05

Table A.31: $Z_{sum} = 92, A_{sum} = 234$

Z	Yield(Z) 200%	Stat. Error
30	0.13	0.05
31	0.34	0.07
32	0.94	0.12
33	1.5	0.15
34	3.41	0.22
35	5.15	0.27
36	8.96	0.36
37	9.52	0.37
38	12.55	0.42
39	11.1	0.4
40	12.34	0.42
41	9.45	0.37
42	7.35	0.33
43	5.34	0.28
44	4.84	0.27
45	4.46	0.25
46	5.22	0.28
47	4.46	0.25
48	4.84	0.27
49	5.34	0.28
50	7.35	0.33
51	9.45	0.37
52	12.34	0.42
53	11.1	0.4
54	12.55	0.42
55	9.52	0.37
56	8.96	0.36
57	5.15	0.27
58	3.41	0.22
59	1.5	0.15
60	0.94	0.12
61	0.34	0.07
62	0.13	0.05

Table A.32: $Z_{sum} = 92, A_{sum} = 235$

Z	Yield(Z) 200%	Stat. Error
31	0.22	0.07
32	0.94	0.13
33	1.47	0.16
34	3.58	0.25
35	4.82	0.29
36	10.36	0.42
37	9.73	0.41
38	13.04	0.47
39	11.51	0.44
40	14.75	0.5
41	10.21	0.42
42	6.5	0.33
43	4.53	0.28
44	3.43	0.24
45	3.27	0.24
46	3.33	0.24
47	3.27	0.24
48	3.43	0.24
49	4.53	0.28
50	6.5	0.33
51	10.21	0.42
52	14.75	0.5
53	11.51	0.44
54	13.04	0.47
55	9.73	0.41
56	10.36	0.42
57	4.82	0.29
58	3.58	0.25
59	1.47	0.16
60	0.94	0.13
61	0.22	0.07

Table A.33: $Z_{sum} = 92, A_{sum} = 236$

Z	Yield(Z) 200%	Stat. Error
30	0.11	0.05
31	0.26	0.08
32	0.72	0.13
33	1.42	0.18
34	3.74	0.29
35	4.9	0.33
36	10.05	0.47
37	11.38	0.49
38	14.23	0.55
39	12.73	0.52
40	15.01	0.57
41	9.75	0.46
42	6.76	0.38
43	3.32	0.27
44	2.16	0.22
45	2.41	0.23
46	2.16	0.22
47	2.41	0.23
48	2.16	0.22
49	3.32	0.27
50	6.76	0.38
51	9.75	0.46
52	15.01	0.57
53	12.73	0.52
54	14.23	0.55
55	11.38	0.49
56	10.05	0.47
57	4.9	0.33
58	3.74	0.29
59	1.42	0.18
60	0.72	0.13
61	0.26	0.08
62	0.11	0.05

Table A.34: $Z_{sum} = 92, A_{sum} = 237$

Z	Yield(Z) 200%	Stat. Error
30	0.17	0.07
31	0.34	0.1
32	0.77	0.15
33	1.76	0.23
34	3.65	0.33
35	5.8	0.41
36	10.44	0.55
37	10.98	0.56
38	14.85	0.65
39	13.41	0.62
40	14.6	0.65
41	10.21	0.54
42	6.74	0.44
43	2.47	0.27
44	1.67	0.22
45	1.48	0.21
46	1.25	0.19
47	1.48	0.21
48	1.67	0.22
49	2.47	0.27
50	6.74	0.44
51	10.21	0.54
52	14.6	0.65
53	13.41	0.62
54	14.85	0.65
55	10.98	0.56
56	10.44	0.55
57	5.8	0.41
58	3.65	0.33
59	1.76	0.23
60	0.77	0.15
61	0.34	0.1
62	0.17	0.07

Bibliography

[1] J. Alcaraz et al. "The alpha magnetic spectrometer silicon tracker: Performance results with protons and helium nuclei". In: *Nucl. Instrum. Methods Phys. Res. A* 593 (2008), p. 376.

[2] H. Alvarez Pol et al. "Performance analysis for the CALIFA Barrel calorimeter of the R^3B experiment". In: *Nucl. Instrum. Methods Phys. Res. A* 767 (2014), p. 453.

[3] J. Chadwick. "Possible Existence of a Neutron". In: *Nature* 129 (1932), p. 312.

[4] E. Fermi. "Possible Production of Elements of Atomic Number Higher than 92". In: *Nature* 133 (1934), 898–899.

[5] I. Noddack. "On Element 93". In: *Zeitschrift fur Angewandte Chemie* 47 (1934), p. 653.

[6] L. Meitner and O. R. Frisch. "Disintegration of Uranium by Neutrons: a New Type of Nuclear Reaction". In: *Nature* 143 (1939), 239–240.

[7] J. L. Rodríguez-Sánchez et al. "Complete characterization of the fission fragments produced in reactions induced by ^{208}Pb projectiles on proton at 500AMeV". In: *Phys. Rev. C* 91 (2015), p. 064616.

[8] E. Pellereau et al. "Accurate isotopic fission yields of electromagnetically induced fission of ^{238}U measured in inverse kinematics at relativistic energies". In: *Phys. Rev. C* 95 (2017), p. 054603.

[9] J. L. Rodríguez-Sánchez et al. "Presaddle and postsaddle dissipative effects in fission using complete kinematics measurements". In: *Phys. Rev. C* 94 (2016), p. 061601.

[10] A. Chatillon et al. "Experimental study of nuclear fission along the thorium isotopic chain: From asymmetric to symmetric fission". In: *Phys. Rev. C* 99 (2019), p. 054628.

[11] A. Chatillon et al. "Evidence for a New Compact Symmetric Fission Mode in Light Thorium Isotopes". In: *Phys. Rev. Lett.* 124 (2020), p. 202502.

[12] K.-H. Schmidt et al. "Relativistic radioactive beams: A new access to nuclear-fission studies". In: *Nucl. Phys. A* 665 (2000), p. 221.

[13] D. Ramos et al. "Insight into excitation energy and structure effects in fission from isotopic information in fission yields". In: *Phys. Rev. C* 99 (2019), p. 024615.

[14] K. R. Kean. "Validation of the multinucleon transfer method for the determination of the fission barrier height". In: *Phys. Rev. C* 100 (2019), p. 014611.

[15] Y. Ayyad et al. "Dissipative effects in spallation-induced fission of ^{208}Pb at high excitation energies". In: *Phys. Rev. C* 91 (2015), p. 034601.

[16] J. L. Rodríguez-Sánchez et al. "Light charged particles emitted in fission reactions induced by protons on ^{208}Pb". In: *Phys. Rev. C* 94 (2016), p. 034605.

[17] J. Randrup et al. "Energy dependence of fission-fragment mass distributions from strongly damped shape evolution". In: *Phys. Rev. C* 88 (2013), p. 064606.

[18] K.-H. Schmidt and B. Jurado. "Entropy driven excitation energy sorting in superfluid fission dynamics". In: *Phys. Rev. Lett* 104 (2010), p. 212501.

[19] N. Bohr and J. A. Wheeler. "The mechanism of nuclear fission". In: *Phys. Rev.* 56 (1939), p. 426.

[20] J.-F. Martin. "Coulex fission of ^{234}U, ^{235}U, ^{237}Np, and ^{238}Np studied within the SOFIA experimental program". PhD thesis. Université Paris-Sud, 2014.

[21] N. K. Skobelev. "On the Possibility of Delayed Fission of Nuclei in the Region of Superheavy Transuranium Elements". In: *Phys. Rev. C* 81 (2018), 455–462.

[22] M. Caamaño et al. "Isotopic yield distributions of transfer- and fusion-induced fission from ^{238}U + ^{12}C reactions in inverse kinematics". In: *Phys. Rev. C* 88 (2013), p. 024605.

[23] N. Bohr. "Neutron capture and nuclear constitution". In: *Nature* 137 (1936), p. 344.

[24] W. M. Elsasser. "Sur le principe de Pauli dans les noyaux". In: *J. Phys. Radium* 4 (1933), pp. 549–556.

[25] M.G. Mayer. "On closed shells in nuclei". In: *Phys. Rev.* 74 (1948), p. 235.

[26] O. Haxel, J.H.D. Jensen, and H.E. Suess. "On the 'magic numbers' in nuclear structure". In: *Phys. Rev.* 75 (1949), p. 1766.

[27] M.G. Mayer. "Nuclear configurations in the spin-orbit coupling model. I. empirical evidence". In: *Phys. Rev.* 78 (1950), p. 16.

[28] K.S. Krane. *Introductory nuclear physics*. Wiley, 1988.

[29] Roger D. Woods and David S. Saxon. "Diffuse Surface Optical Model for Nucleon-Nuclei Scattering". In: *Phys. Rev.* 95 (1954), pp. 577–578.

[30] S.G. Nilsson. "Binding states of individual nucleons in strongly deformed nuclei". In: *Dan Mat Fys Medd* 29 (1955), p. 16.

[31] V.M. Strutinsky. "Shell effects in nuclear masses and deformation energies". In: *Nuclear Physics A* 95 (1967), pp. 420–442.

[32] S. Polikanov et al. In: *Zh. Eksp. Teor Fiz* 42 (1962), p. 1464.

[33] V. Metag. "Spectroscopic properties of fission isomers". In: *Physics reports* 65 (1980), pp. 1–41.

[34] Ichikawa, Takatoshi and Iwamoto, Akira and Möller, Peter and Sierk, Arnold J. "Contrasting fission potential-energy structure of actinides and mercury isotopes". In: *Phys. Rev. C* 86 (2012), p. 024610.

[35] V. F. Weisskopf and D. H. Ewing. "On the Yield of Nuclear Reactions with Heavy Elements". In: *Phys. Rev.* 57 (1940), p. 472.

[36] H. A. Bethe. "Nuclear Physics". In: *Rev. Mod. Phys.* 9 (1937), p. 69.

[37] H.A. Kramers. "Brownian motion in a field of force and the diffusion model of chemical reactions". In: *Physica.* 7 (1940), pp. 284–304.

[38] Shambhu Nath Sharma and Hirenkumar G. Patel. "The Fokker-Planck Equation". In: 2010. URL: https://api.semanticscholar.org/CorpusID:6734228.

[39] A. Gavron et al. "Time Scale of Fission at High Angular Momentum". In: *Phy. Rev. Lett* 48 (1982), p. 835.

[40] H.A. Weidenmüller. "Transport theories of heavy-ion reactions". In: *Prog. Part. Nucl. Phys.* 3 (1980), pp. 49–126.

[41] P. Grangé, L. Jun-Qing, and H.A. Weidenmüller. "Induced nuclear fission viewed as a diffusion process: Transients". In: *Phys. Rev. C* 27 (1983), p. 2063.

[42] K.H. Bhatt, P. Grangé, and B. Hiller. "Nuclear friction and lifetime of induced fission". In: *Phys. Rev. C* 33 (1986), p. 954.

[43] B. Jurado et al. "Time evolution of the fission-decay width under the influence of dissipation". In: *Phys. Lett. B* 553 (2003), pp. 186–190.

[44] B. Jurado et al. "A critical analysis of the modelling of dissipation in fission". In: *Nucl. Phys. A* 747 (2005), p. 14.

[45] B. Jurado et al. "Transient Effects in Fission from New Experimental Signatures". In: *Phys. Rev. Lett* 93 (2004), p. 072501.

[46] J. W. Negele, S. E. Koonin, P. Möller, J. R. Nix, and A. J. Sierk. "The self-consistent single-particle model in nuclear physics". In: *Phys. Rev. C* 17 (1978), p. 1098.

[47] H.J. Mang. "The self-consistent single-particle model in nuclear physics". In: *Physics Reports* 18 (1975), p. 325.

[48] H. Goutte, J. F. Berger, P. Casoli, and D. Gogny. "Microscopic approach of fission dynamics applied to fragment kinetic energy and mass distributions in ^{238}U". In: *Phys. Rev. C* 71 (2005), p. 024316.

[49] J. Weber et al. "Fission of $_{228}$Ra". In: *Phys. Rev. C* 13 (1976), p. 2413.

[50] W. Lang et al. "Nuclear charge and mass yields for ^{235}U(n_{th}, f) as a function of the kinetic energy of the fission products". In: *Nucl. Phys. A* 345 (1980), p. 34.

[51] H. C. Britt et al. "Fission of $_{255-256}$Es, $_{255-257}$Fm, and ^{258}Md at moderate excitation energies". In: *Phys. Rev. C* 30 (1984), p. 559.

[52] B. M. A. Swinton-Bland et al. "Mass-asymmetric fission of ^{205,207,209}Bi at energies close to the fission barrier using proton bombardment of ^{204,206,208}Pb". In: *Phys. Rev. C* 102 (2020), p. 054611.

[53] A. C. Berriman et al. "Isotopic yield distributions of transfer- and fusion-induced fission from ^{238}U + ^{12}C reactions in inverse kinematics". In: *Phys. Rev. C* 105 (2022), p. 064614.

[54] A. Chatillon et al. "Influence of proton and neutron deformed shells on the asymmetric fission of thorium isotopes". In: *Phys. Rev. C* 106 (2022), p. 024618.

[55] Meng Wang et al. "The AME 2020 atomic mass evaluation (II). Tables, graphs and references". In: *Chinese Phys. C* 45 (2021), p. 030003.

[56] Aumann T., Bertulani C. A., Duer M., Galatyuk T., Obertelli A., Panin V., Rodríguez-Sánchez J. L., Roth R. and Stroth J. "Nuclear structure opportunities with GeV radioactive beams at FAIR". In: *Phil. Trans. R. Soc. A.* 382 (2024), p. 20230121.

[57] U. Brosa, S. Grossmann and A. Müller. "Nuclear scission". In: *Phys. Rep* 197 (1990), p. 167.

[58] A. N. Andreyev et al. "Nuclear fission: a review of experimental advances and phenomenology". In: *Rep. Prog. Phys* 81 (2018), p. 016301.

[59] U. Brosa, S. Grossmann and A. Müller. "Four Channels in the Fission of ^{252}Cf". In: *Z. Naturforsch* 41 (1986), 1341–1346.

[60] B. D. Wilkins, E. P. Steinberg and R. R. Chasman. “Scission-point model of nuclear fission based on deformed-shell effects”. In: *Phys. Rev. C* 14 (1976), p. 1832.

[61] C. Böckstiegel et al. “Nuclear-fission studies with relativistic secondary beams: Analysis of fission channels”. In: *Nucl. Phys. A* 802 (2008), 12–25.

[62] G. Scamps and C. Simenel. “Impact of pear-shaped fission fragments on mass-asymmetric fission in actinides”. In: *Nature* 564 (2018), p. 382.

[63] B. Bucher et al. “Direct evidence of octupole deformation in neutron-rich ^{144}Ba.” In: *Phys. Rev. Lett* 116 (2016), p. 112503.

[64] B. Bucher et al. “Direct evidence for octupole deformation in ^{146}Ba and the origin of large E1 moment variations in reflection-asymmetric nuclei”. In: *Phys. Rev. Lett* 118 (2017), p. 152504.

[65] K. Nishio et al. “Excitation energy dependence of fragment-mass distributions from fission of ^{180,190}Hg formed in fusion reactions of ^{36}Ar + ^{144,154}Sm”. In: *Phys. Lett. B* 748 (2015), 89–94.

[66] U. Moselle and H. W. Schmitt. “Fragment-Shell Influences in Nuclear Fission”. In: *Phys. Rev. C* 4 (1971), p. 2185.

[67] A. V. Voinov et al. “Nuclear excitations at constant temperature”. In: *Phys. Rev. C* 79 (2009), p. 031301.

[68] T. von Egidy and D. Bucurescu. “Systematics of nuclear level density parameters”. In: *Phys. Rev. C* 72 (2005), p. 044311.

[69] A. A. Naqvi, F. Käppeler, F. Dickmann, and R. Müller. “Fission fragment properties in fast-neutron-induced fission of ^{237}Np”. In: *Phys. Rev. C* 34 (1986), p. 218.

[70] G. N. Kniajeva et al. “Neutron and gamma-ray emission in the proton, neutron and gamma ray emission in the proton induced fission of ^{238}U and ^{242}Pu”. In: *Nucl. Phys. A* 734 (2004), E25–E28.

[71] K.-H. Schmidt and B. Jurado. “Inconsistencies in the description of pairing effects in nuclear level densities”. In: *Phys. Rev. C* 86 (2012), p. 044322.

[72] B. Jurado and K.-H. Schmidt. “The even-odd effect in fission-fragment Z yields - a new kind of nuclear clock”. In: *EPJ Web of Conferences* 62 (2013), p. 07003.

[73] B. L. Tracy et al. “Rb and Cs Isotopic Cross Sections from 40-60-Mev-Proton Fission of ^{238}U, ^{232}Th and ^{235}U”. In: *Phys. Rev. C* 5 (1972), p. 222.

[74] S. Steinhäuser et al. “Odd-even effects observed in the fission of nuclei with unpaired protons”. In: *Nucl. Phys. A* 634 (1998), 89–111.

[75] B. Bouzid et al. “The nature of dynamics of the last stages of the fission process”. In: *J. Phys. G: Nucl. Part. Phys.* 24 (1998), p. 1029.

[76] F. Rejmund, A.V. Ignatyuk, A.R. Junghans and K.-H. Schmidt. “Pair breaking and even-odd structure in fission-fragment yields”. In: *Nucl. Phys. A* 678 (2000), 215–234.

[77] M. Caamaño et al. “Evidence for the predominant influence of the asymmetry degree of freedom on the even-odd structure in fission-fragment yields”. In: *J. Phys. G* 38 (2011), p. 035101.

[78] https://doi.org/10.48550/arXiv.1007.0741.

[79] M.L. Pumo. "The s-process nucleosynthesis in massive stars: current status and uncertainties due to convective overshooting". In: Mar. 2012. ISBN: 978-953-51-0473-5. DOI: 10.5772/34308.

[80] E.M. Burbidge, G.R. Burbidge, W.A. Fowler and F.Hoyle. "Synthesis of the Elements in Stars". In: *Rev. Mod. Phys* 29 (1957), p. 547.

[81] F. Käppeler, R. Gallino, S. Bisterzo, and W. Aoki. "The s process: nuclear physics, stellar models, and observations". In: *Rev. Mod. Phys* 83 (2011), 157–193.

[82] J. W. Truran et al. "Rapid neutron capture in supernova explosions". In: *Astrophys. Space Sci.* 1 (1968), pp. 129–146.

[83] T. A. Thompson. "Magnetic protoneutron star winds and r-process nucleosynthesis". In: *Astrophys. J. Lett* 585 (2003), L33–L36.

[84] B. P. Abbott et al. "GW170817: observation of gravitational waves from a binary neutron star inspiral". In: *Phys. Rev. Lett* 119 (2017), p. 161101.

[85] D. Kasen et al. "Origin of the heavy elements in binary neutron-star mergers from a gravitational-wave event". In: *Nature* 551 (2017), 80–84.

[86] Daniel M. Siegel. "r-Process nucleosynthesis in gravitational-wave and other explosive astrophysical events". In: *Nature Reviews Physics* 4 (2022).

[87] N. Vassh et al. "Using excitation-energy dependent fission yields to identify key fissioning nuclei in r-process nucleosynthesis". In: *J. Phys. G: Nucl. Part. Phys.* 46 (2019), p. 065202.

[88] J.-F. Lemaître, S. Goriely, A. Bauswein, H.-T. Janka. "Fission fragment distributions and their impact on the r-process nucleosynthesis in neutron star mergers". In: *Phys. Rev. C* 103 (2021), p. 025806.

[89] A. Turkevich and J. B. Niday. "Radiochemical Studies on the Fission of ^{232}Th with Pile Neutrons". In: *Phys. Rev.* 84 (1951), p. 52.

[90] G. Siegert, H. Wollnik, J. Greif, R. Decker, G. Fiedler, and B. Pfeiffer. "Nuclear charge distribution of fission products from ^{235}U (n_{th}),f of the masses 79 to 100". In: *Phys. Rev. C* 14 (1976), p. 1864.

[91] W. Lang, H.-G. Clerc, H. Wohlfarth, H. Schrader and K.-H. Schmidt. "Nuclear charge and mass yields for ^{235}U (n_{th}, f) as a function of the kinetic energy of the fission products". In: *Nucl.Phys.A* 345 (1980), p. 34.

[92] O. Chamberlain and E. Segrè. "Proton-Proton Collisions within Lithium Nuclei". In: *Phys. Rev.* 87 (1952), 81–83.

[93] M. Yosoi. "Structure and decay of the s-hole state in ^{11}B studied via the ^{12}C(p, 2p) ^{11}B* reaction". In: *Phys. Lett. B* 551 (2003), 255–261.

[94] T. Noro et al. "Experimental study of (p, 2p) reactions at 392 MeV on ^{12}C, ^{16}O, ^{40}Ca and ^{208}Pb nuclei leading to low-lying states of residual nuclei". In: *Prog. Theor. Exp. Phys* 2020 (2020), p. 093D02.

[95] V. Panin et al. "Exclusive measurements of quasi-free proton scattering reactions in inverse and complete kinematics". In: *Phys. Lett. B* 753 (2016), 204–210.

[96] K. Boretzky et al. "NeuLAND: The high-resolution neutron time-of-flight spectrometer for R^{3}B at FAIR". In: *Nucl. Instrum. Method Phys. Res. A* 1014 (2021), p. 165701.

[97] https://github.com/R3BRootGroup/R3BRoot.

[98] https://fy.chalmers.se/ f96hajo/ucesb/.

[99] https://irfu.cea.fr/dphn/Spallation/incl.html.

[100] A.V. Ignatyuk, G.A. Kudyaev, A. Junghans, M. de Jong, H.-G. Clerc and K.-H. Schmidt. "Analysis of dissipative effects in nuclear fission observed in the fragmentation of ^{238}U projectiles". In: *Nucl. Phys. A* 593 (1995), 519–534.

[101] W. D. Myers and W. J. Swiatecki. "The Nuclear Droplet Model for Arbitrary Shapes". In: *Annals of Physics* 84 (1974), 186–210.

[102] J. B. Natowitz et al. "Caloric curves and critical behavior in nuclei". In: *Phys. Rev. C* 65 (2002), p. 034618.

[103] J. L. Rodríguez-Sánchez et al. "Hypernuclei formation in spallation reactions by coupling the Liège intranuclear cascade model to the deexcitation code ABLA". In: *Phys. Rev. C* 105 (2022), p. 014623.

[104] L. G. Moretto. "Statistical emission of large fragments: a general theoretical approach". In: *Nucl. Phys. A* 247 (1975), p. 211.

[105] W. Hauser and H. Feshbach. "The Inelastic Scattering of Neutrons". In: *Phys. Rev* 87 (1952), p. 366.

[106] D. Mancusi, R. J. Charity and J. Cugnon. "Unified description of fission in fusion and spallation reactions". In: *Phys. Rev. C* 82 (2010), p. 044610.

[107] Davide Mancusi et al. "Elusiveness of evidence for multifragmentation in 1-GeV proton-nucleus reactions". In: *Phys. Rev. C* 84 (2011), p. 064615.

[108] J.P. Bondorf. "Statistical multifragmentation of nuclei". In: *Physics Reports* 257 (1995), 133–221.

[109] G. García-Jiménez. "Proton-Induced Fission and Spallation Reactions in Inverse Kinematics: Insights from CALIFA Calorimeter Reconstruction". PhD thesis. University of Santiago de Compostela, 2024.

[110] https://repository.gsi.de/record/68035/files/FG-S-FRS-05.pdf.

[111] https://indico.gsi.de/event/5496/contributions/25455/attachments/18598/23317/FPGA_TDC.pdf.

[112] M. Bernas et al. "Fission-residues produced in the spallation reaction ^{238}U + p at 1 AGeV". In: *Nucl. Phys. A* 725 (2003), 213–253.

[113] "Technical Report for the Design, Construction and Commissioning of The CALIFA Barrel: The R^{3}B CALorimeter for In Flight detection of γ-rays and high energy charged pArticles experiment". In: (2011).

[114] Yiman Yan. "Study of fission of exotic actinides by relativistic reactions". PhD thesis. Université Paris-Saclay, 2016.

[115] B. Jurado. "New signatures on dissipation at small deformations from studies of fission induced by peripheral heavy- ion collisions at relativistic energies". PhD thesis. GSI, 2002.

[116] ISO. *Evaluation of measurement data - Guide to the expression of uncertainty in measurement*. JCGM, 2020.

[117] https://en.wikipedia.org/wiki/Weighted_arithmetic_mean.

[118] K.-H. Schmidt et al. "High-precision measurement of total fission cross sections in spallation reactions of ^{208}Pb and ^{238}U". In: *Phys. Rev. C* 87 (2013), p. 034601.

[119] A. A. Kotov et al. "Energy dependence of proton induced fission cross sections for heavy nuclei in the energy range 200−1000 MeV". In: *Phys. Rev. C* 74 (2006), p. 034605.

[120] https://www-nds.iaea.org/exfor/.

[121] J. L. Rodríguez-Sánchez. "Proton-induced fission cross sections on ^{208}Pb at high kinetic energies". In: *Phys. Rev. C* 90 (2014), p. 064606.

[122] J. L. Rodríguez-Sánchez. "Constraining the level density using fission of lead projectiles". In: *Phys. Rev. C* 92 (2015), p. 044612.

[123] B. Jurado. "Transient Effects in Fission Evidenced from New Experimental Signatures". In: *Phys. Rev. Lett* 93 (2004), p. 072501.

[124] J. L. Rodríguez-Sánchez. "Pre- and postsaddle fission dynamics using lead on proton reactions in complete kinematic measurements". PhD thesis. University of Santiago de Compostela, 2015.

[125] M. Feijoo Rodríguez. "Fission dynamics investigated in inverse kinematics in reactions induced by relativistic ^{236}U projectiles." PhD thesis. University of Santiago de Compostela, 2021.

[126] C. Schmitt. "Fragmentation of spherical radioactive heavy nuclei as a novel probe of transient effects in fission". In: *Phys. Rev. C* 81 (2010), p. 064602.

[127] S.I. Mulgin et al. "Shell effects in the symmetric-modal fission of pre-actinide nuclei". In: *Nucl. Phys. A* 640 (1998), 375–388.

[128] M. Zöller. "Untersuchung der neutroneninduzierten Spaltung von ^{238}U im Energiebereich von 1 MeV bis 500 MeV". PhD thesis. Technischen Hochchule Darmstadt, 1995.

[129] F. Vivès et al. "Investigation of the fission fragment properties of the reaction ^{238}U(n,f) at incident neutron energies up to 5.8 MeV". In: *Nucl. Phys. A* 662 (2000), 63–92.

[130] et al D. Ramos. "Isotopic fission-fragment distributions of ^{238}U, ^{239}Np, ^{240}Pu, ^{244}Cm, and ^{250}Cf produced through inelastic scattering, transfer, and fusion reactions in inverse kinematics". In: *Phys. Rev. C* 97 (2018), p. 054612.

[131] Arjan Koning et al. *JEFF Report 21: The JEFF-3.1 Nuclear Data Library*. Jan. 2006. ISBN: 92-64-02314-3.

[132] C. Böckstiegel et al. "Nuclear-fission studies with relativistic secondary beams: Analysis of fission channels". In: *Nucl. Phys. A* 802 (2008), 12–25.

[133] J. Pereira et al. "Comprehensive analysis of fission-reaction properties in the nuclear spallation of ^{238}U(1 GeV/nucleon) on deuterium". In: *Phys. Rev. C* 75 (2007), p. 044604.

[134] D. Hilscher and H. Rossner. "Dynamics of nuclear fission". In: *Ann. Phys. Fr* 17 (1992), 471–552.

[135] M. Mager. "ALPIDE, the Monolithic Active Pixel Sensor for the ALICE ITS upgrade". In: *NIM A* 824 (2016), p. 434.

This work was partially supported by the Spanish "Ministerio de Ciencia e Innovación", under the grant FPI:PRE2018-085934.

This study is about nuclear fission, discovered in 1939 by Lise Meitner and Otto Hahn. In the research presented in this work, the quasi-free (p, 2p) reactions are combined for the first time with the study of fission in inverse kinematics, using state-of-the-art detectors developed by the R3B (Reactions with Relativistic Radioactive Beams) collaboration. To do so, uranium beams (238) are accelerated to impinge on a liquid hydrogen target at 540 MeV/u. This novel experimental technique would provide full kinematics measurements by obtaining the excitation energy for the fissioning nuclei and identifying the mass, charge, and kinetic energy of the two fission fragments simultaneously. The versatility of this technique allows the study of characteristic fission phenomena at both low and high excitation energies.